STRUCTURAL STUDIES OF THE MECHANISM BY WHICH BCL-2 AND BECLIN PROTEINS REGULATE AUTOPHAGY AND APOPTOSIS

A Dissertation
Submitted to the Graduate Faculty
of the
North Dakota State University
of Agriculture and Applied Science

By

Minfei Su

In Partial Fulfillment of the Requirements
for the Degree of
DOCTOR OF PHILOSOPHY

Major Department:
Chemistry and Biochemistry

July 2016

Fargo, North Dakota

North Dakota State University
Graduate School

Title

STRUCTURAL STUDIES OF THE MECHANISM BY WHICH BCL-2 AND BECLIN PROTEINS REGULATE AUTOPHAGY AND APOPTOSIS

By

Minfei Su

The Supervisory Committee certifies that this ***disquisition*** complies with North Dakota State University's regulations and meets the accepted standards for the degree of

DOCTOR OF PHILOSOPHY

SUPERVISORY COMMITTEE:

Dr. Sangita Sinha
Chair

Dr. Mukund Sibi

Dr. Bin Guo

Dr. Glenn Dorsam

Approved:

July 6, 2016
Date

Dr. Gregory Cook
Department Chair

ABSTRACT

Autophagy and apoptosis are catabolic pathways essential for homeostasis in all eukaryotes. While autophagy usually promotes cell-survival by enabling degradation and recycling of damaged macromolecules, apoptosis is the canonical programmed cell death pathway. Dysfunction of autophagy and apoptosis is implicated in diseases like cancers, cardiac disease, and infectious disease. Beclin homologs are key for autophagy as they are core components of class III phosphatidylinositol 3-kinase autophagosome nucleation and maturation complexes. Anti-apoptotic Bcl-2s inhibit apoptosis through binding and antagonizing pro-apoptotic Bcl-2s. Anti-apoptotic Bcl-2s also down-regulate autophagy by binding to the Bcl-2 homology domain 3 (BH3D) of Beclin homologs, thereby enabling crosstalk between apoptosis and autophagy. The central goal of my doctoral research is to understand the structure-based mechanism of selected Bcl-2s and Beclin homologs in the regulation of autophagy and apoptosis.

γ-Herpesviruses are common human pathogens that encode viral Bcl-2s to facilitate viral reactivation and oncogenic transformation. M11, a viral Bcl-2, and Bcl-X_L, a cellular Bcl-2, bind with comparable affinities to the Beclin 1 BH3D. By assessing the impact of different Beclin 1 BH3D mutations on binding to M11 and Bcl-X_L, we developed a cell-permeable inhibitory peptide that targets M11, but not Bcl-X_L. The mechanism by which this peptide specifically binds to M11 was elucidated by determining the X-ray crystal structure of the peptide:M11 complex.

Our attempts to investigate the role of other Bcl-2s in these pathways were unsuccessful. In one project, we were unable to express and purify BALF1, another viral Bcl-2. In another, no interaction was detected between purified samples of the anti-apoptotic Bcl-2 homolog Mcl-1, and the autophagy protein Atg12, that had previously been shown to bind.

We also delineated the domain architecture of Beclin 2, a novel Beclin homolog and attempted to express and purify different Beclin 2 constructs for structural studies. We successfully purified and solved the X-ray crystal structure of the Beclin 2 coiled-coil domain (CCD), showing it is a curved, anti-parallel, meta-stable coiled-coil homodimer with seven pairs of non-ideal packing residues. In general, mutating the non-ideal packing residues to leucines enhanced Beclin 2 CCD homodimerization, but also weakened its binding to Atg14 CCD.

ACKNOWLEDGEMENTS

I would like to express my sincere gratitude to my advisor Dr. Sangita Sinha for all her guidance, support, and encouragement throughout my graduate studies. Without her, this work would not have been possible.

I would also like to thank my committee members, Dr. Mukund Sibi, Dr. Bin Guo and Dr. Glenn Dorsam for their advice and direction.

I would like to thank our collaborator, Dr. Christopher Colbert here at North Dakota State Univerity, not only for his collaboration, but also for all his continuous advice and support. I would also like to thank our other collaborator Dr. Beth Levine group at University of Texas Southwestern Medical Center, Dr. David Neau at NE-CAT, APS, Argonne, Dr. Ruslan Sanishvili at GMCA, APS, Argonne, and Dr. Srinivas Chakravarthy st Bio-CAT, APS, Argonne, for their collaboration.

Additionally, I would like to thank all the members in the Sinha group, including Yang Mei, Yue Li, Karen Glover, Shreya Mukhopadhyay, Srinivas Dasanna, Marion Okondo, Tanner Huebner, Vishnuveni Leelaruban, and Samuel Wyatt, and Colbert group, including Jaime Jensen Shane Wyborny and Benjamin LeVahn, who made my graduate experience both enjoyable and productive through daily advice, assistance, and relaxation.

This research was supported and funded by NIH grant R21 AI078198, NIH grant R03 NS090939, NSF grant MCB 1413525, NSF grant HRD-0811239, and P30 GM103332-01 to Dr. Sangita Sinha, and North Dakota EPSCoR doctoral dissertation award for Minfei Su and Dr. Sangita Sinha.

DEDICATION

This dissertation is dedicated to my parents,

for their endless love, understanding, support, encouragement and inspiration.

TABLE OF CONTENTS

LIST OF TABLES

LIST OF FIGURES

LIST OF ABBREVIATIONS

AEBSF	4-(2-Aminoethyl) benzenesulfonyl fluoride hydrochloride
APAF-1	Apoptotic protease-activating factor 1
Atg	Autophagy-related protein
BARAD	β-α repeat, autophagy-specific domain
Bcl-2BD	Bcl-2 binding domain
BH3D	Bcl-2 homology 3 domain
BIM_S, BIM_L and BIM_{EL}	BIM-short, BIM-long and BIM-extra long
BSA	Bovine serum albumin
Calpain	Calcium-dependent, non-lysosomal, cysteine protease
CB1R	Cannabinoid receptor 1
$CC_{1/2}$	Pearson correlation coefficient between random half-datasets
CCDs	Coiled-coil domains
CD	Circular dichroism
Co-IP	Co-immunoprecipitation
DISC	Death-inducing signaling complex
D_{max}	Maximum particle dimension
DMEM	Dulbecco's Modified Eagle Medium
DOR	Opioid receptor δ1
DS	Double-substituted
EAA	Essential amino acids
E. coli	*Escherichia coli*
EBSS	Earle’s balanced salt solution

EBV.....Epstein Barr virus

EDTA.....Ethylenediaminetetraacetic acid

ESI-MS .....Electrospray ionization mass spectrometry

FADD.....Fas-associated death domain

FHD.....Flexible helical domain

GASP1 .....G protein-coupled receptor-associated sorting protein 1

GFP .....Green fluorescent protein

GPCR.....G protein-coupled receptors

GST.....Glutathione S-transferase

HEPES .....4-(2-hydroxyethyl)-1-piperazineethanesulfonic acid

HIV .....Human immunodeficiency virus

I(0).....Scattering intensity at zero-angle

IDR.....Intrinsically disordered region

IEX.....Ion-exchange chromatography

IMAC .....Immobilized metal affinity chromatography

IPTG.....Isopropyl β-D-1-thiogalactopyranoside

ITC .....Isothermal titration calorimetry

K_a .....Association constant

K_d .....Dissociation constant

KSHV.....Kaposi's sarcoma-associated HV

LB .....Luria Bertani

MBP .....Maltose-binding protein

mNOXA.....Mouse NOXA

MMP .....Mitochondrial membrane permeability

MR .....Molecular replacement

NCS.....Non-crystallographic symmetry

NEAA .....Non-essential amino acids

NMR .....Nuclear magnetic resonance

p53.....Tumor protein 53

PCR.....Polymerase chain reaction

PDB.....Protein data bank

PEST sequences.....Peptide sequences that are rich in proline, glutamic acid, serine, and threonine

P(r) function.....pairwise-distance distribution function

PI3KC3 .....Class III phosphotidylinositol-3-kinase

PVDF .....Polyvinylidenedifluoride

R_{free}.....Free R-factor

R_{work} .....Working R-factor

Rg.....Radius of gyration

ROS.....Reactive oxygen species

SAXS .....Small-angel X-ray scattering

SDS-PAGE .....Sodium dodecyl sulfate polyacrylamide gel electrophoresis

SEC .....Size exclusion chromatography

SUMO.....Small ubiquitin-like modifier

TAT.....Trans-activating HIV-1 transcriptional activator protein transduction domain

TCEP.....Tris(2-carboxyethyl)phosphine

TLS .....Translation-libration-screw

T_m.....Melting temperature

TM.....Transmembrane domain

TNF .....Tumor necrosis factor

TRAIL .....Tumor necrosis factor-related apoptosis-inducing ligand

UVRAG .....UV radiation resistance associated gene

WT .....Wild type

ΔG .....Change in the Gibbs free energy

ΔH .....Change in enthalpy

ΔS.....Change in entropy

ρ.....Pearson correlation coefficient

θ.....Degree of ellipticity

γHV .....γ-herpesviruse

CHAPTER 1. INTRODUCTION

1.1. Introduction to autophagy

Autophagy is a cell-survival pathway conserved in all eukaryotes. It involves the selective degradation of cellular components, including long-lived proteins, protein aggregates, damaged cytoplasmic organelles and intracellular pathogens. Basal levels of autophagy are required for cellular homeostasis. Autophagy is up regulated to recycle nutrients and energy under stress conditions; including intracellular stress such as that caused by accumulation of damaged proteins and organelles and high bioenergetic demands; and extracellular stress such as nutrition deprivation, hypoxia, and infection. It allows lower eukaryotes to survive starvation, while in mammals, it is thought to be involved in many physiological and pathophysiological processes, including anti-aging mechanisms, differentiation and development, immunity, and elimination of microorganisms (Levine and Klionsky, 2004, Mizushima, 2007, Levine and Kroemer, 2008, Sinha et al., 2008).

Autophagy is a highly regulated process executed by effector proteins called Autophagy-related (Atg) proteins (Figure 1.1). The first committed step of autophagy is vesicle nucleation in which macromolecular assemblies selected for degradation are surrounded by isolation membranes called phagophores. The vesicle nucleation process is executed by a protein complex whose core comprises the class III phosphotidylinositol-3-kinase (PI3KC3) which catalyzes phosphorylation of phosphotidylinositol to phosphotidylinositol 3-phosphate; the PI3KC3 regulatory subunit (p150), a myristylated serine/threonine kinase that phosphorylates PI3KC3 and recruits it to the membrane; Bcl-2 interacting protein (Beclin 1), which appears to be a protein interaction hub, and Atg14. This PI3KC3 complex is named as PI3KC3 Complex I, while Complex II which includes UV radiation resistance associated gene (UVRAG) instead of Atg14,

mediates autophagosome maturation (Levine and Klionsky, 2004, Kihara et al., 2001b, Itakura et al., 2008, Itakura and Mizushima, 2009). More recently, Ambra 1 has been identified as a positive regulator of autophagy and interacts with Beclin1 (Fimia et al., 2007).

Membranes comprising the nascent phagophore are enlarged, and then fused at their edges to form multi-layered vesicles called autophagosomes. Two ubiquitin-like conjugation systems are involved in this process. In one system, Atg12, a protein with an ubiquitin-like fold is covalently conjugated to Atg5, catalyzed by the activity of the E1-like enzyme Atg7 and the E2-like enzyme Atg10. The Atg12-Atg5 then forms a larger multimeric complex with Atg16. In the other system, another ubiquitin-like protein, Atg8, is conjugated to phosphatidylethanolamine, by the sequential action of a protease Atg4, a E1-like enzyme Atg7 and a E2-like enzyme Atg3 (Ichimura et al., 2000, Maiuri et al., 2007b, Mizushima et al., 1999, Ohsumi, 2001).

The outer membrane of autophagosomes eventually fuses with lysosomes to create autophagolysosomes. This stage involves some Atg8 paralogs, multiple WD repeat domain, phosphoinositide interacting Atg18 paralogs, Atg2A which binds to Atg18, the transmembrane protein, Atg9, SNX 18 which causes autophagosome tubulation as well as small G-proteins that power this process. Inside the autophagolysosome, the contents of the autophagosome are degraded by lysosomal enzymes (Levine and Klionsky, 2004, Levine and Kroemer, 2008, Sinha et al., 2008, Sinha and Levine, 2008), after which the degradation products are recycled by the cell.

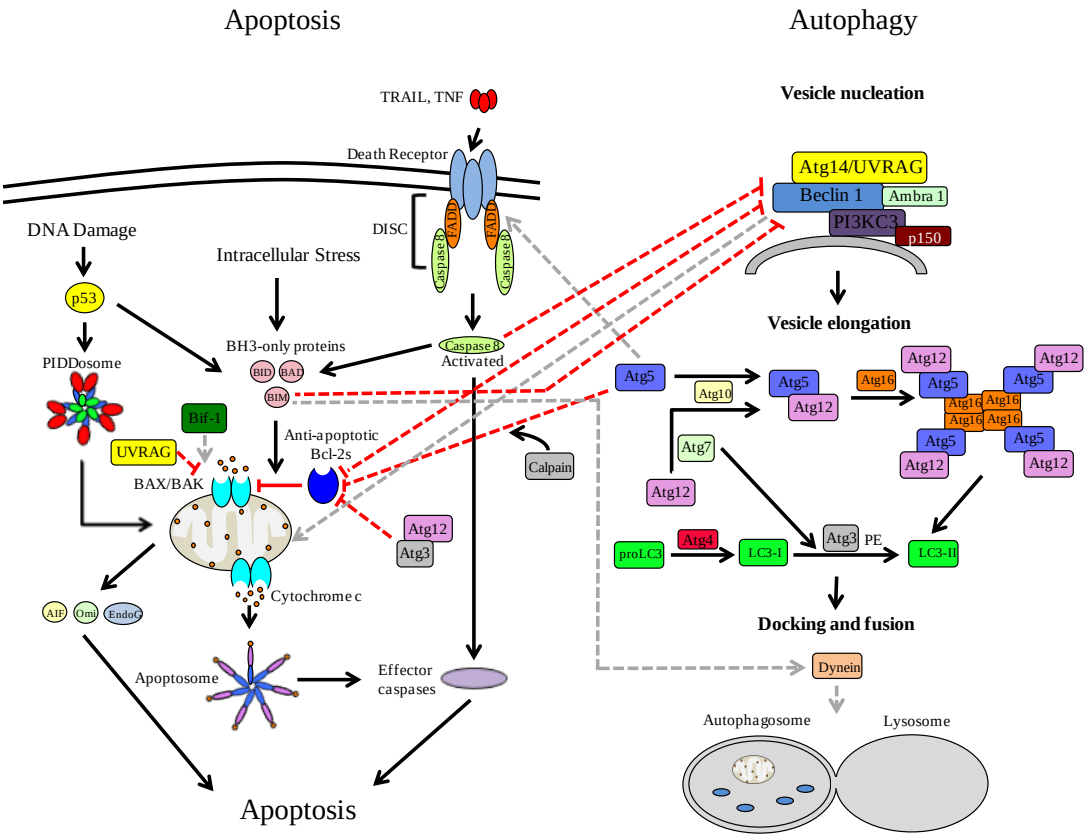

Figure 1.1: Crosstalk between autophagy and apoptosis. Various proteins involved at the different points of crosstalk are shown and labeled. Lines denote interactions or processes, with solid lines corresponding to intra-pathway processes and dashed lines corresponding to inter-pathway connections. Red lines denote inhibitory interactions, while lines with arrows indicate facilitating interactions (Su et al., 2013).

1.2. Introduction to apoptosis

In contrast to autophagy, apoptosis is the best-known mechanism of programmed cell death. It is recognized by distinct morphological characteristics of cells, e.g. cellular shrinkage with nuclear chromatin condensation and nuclear fragmentation. It functions as a homeostatis mechanism to maintain cell populations as well as a defense mechanism in the presence of toxic agents. Apoptosis can be triggered by diverse cellular signals. These include intracellular signals produced in response to cellular stresses, such as the increased intracellular Ca^{2+} concentration, oxidative damage caused by reactive oxygen species (ROS) (Annunziato et al., 2003) and

hypoxia (Shimizu et al., 1996). Extrinsic inducers of apoptosis include bacterial pathogens (Weinrauch and Zychlinsky, 1999), toxins (Uchida et al., 1999), nitric oxide (Brune, 2003), growth factors (Rajah et al., 1997), and hormones (Yaoita and Nakajima, 1997).

Depending on the apoptosis-inducing signal, two different apoptosis pathways have been identified: the intrinsic pathway characterized by mitochondrial outer membrane permeabilization and the release of mitochondrial cytochrome c; and the extrinsic pathway, which is initiated by death-receptor stimulation. There is overlap between these pathways as the extrinsic pathway usually also activates the intrinsic pathway, and both pathways resulting in the recruitment and activation of cysteine-aspartic acid proteases (caspases) (Elmore, 2007, Taylor et al., 2008). Intracellular apoptotic signals trigger the intrinsic pathway, starting with the activation of different Bcl-2 homology 3 domain (BH3D) -only proteins. Activated BH3D-only proteins bind to anti-apoptotic Bcl-2 proteins, preventing them from binding to and inhibiting the multi-BH domain pro-apoptotic Bcl-2 proteins, BAX and BAK. This allows homodimerization of BAX and/or BAK in the outer mitochondrial membrane, forming channels that increase mitochondrial membrane permeability (MMP) to permit the release of cytochrome c as well as other apoptosis effectors. Cytochrome c then associates with apoptotic protease-activating factor 1 (APAF-1) and caspase-9 to form a complex called the apoptosome. The apoptosome activates effector caspases leading to cell death (Byrne and Ojcius, 2004, Giansanti et al., 2011). The extrinsic pathway starts with the stimulation of sets of death receptors uponbinding of their specific ligands, like tumor necrosis factor-related apoptosis-inducing ligand (TRAIL) and tumor necrosis factor (TNF). The binding of ligands causes trimerization of the death receptors, resulting in clustering of their death domains and recruiting Fas-associated death domain (FADD), caspases 8 to form the death-inducing signaling complex (DISC) (Pennarun et al.,

2010). Caspase 8 activated inside the DISC can then promote cell death either by activating effector caspases or by cleaving BH3D-only protein BID to initiate mitochondria-dependent apoptosis (Byrne and Ojcius, 2004, Giansanti et al., 2011).

1.3. The molecular crosstalk between autophagy and apoptosis

Since both autophagy and apoptosis play multiple, essential roles in cellular homeostasis, it is perhaps not surprising that there is extensive crosstalk between them that enables co-regulation of these pathways. Nodes of crosstalk include the Beclin 1 – Bcl-2 interaction(Liang et al., 1998); caspase-mediated Beclin 1 cleavage (Wirawan et al., 2010, Rohn et al., 2011, Li et al., 2011); UVRAG – Bax interaction(Yin et al., 2011); Atg12-Atg3 conjugation (Radoshevich et al., 2010); Atg5 – FADD interaction (Radoshevich et al., 2010); Calcium-dependent, non-lysosomal, cysteine protease (Calpain)-cleaved Atg5-regulated apoptosis (Yousefi et al., 2006); and tumor protein 53 (p53)-mediated cross-regulation (Crighton et al., 2006, Feng et al., 2005).

1.3.1. Bcl-2 proteins

The Bcl-2 familyof proteins are important regulators of both apoptosis and autophagy (Su et al., 2013). The first identified member of this family, *bcl-2*, was discovered at the chromosomal breakpoint of t(14;18), which is the molecular hallmark of follicular B cell lymphoma (Tsujimoto et al., 1985, Bakhshi et al., 1985). This is the first identified oncogene that functions in preventing programmed cell death instead of promoting proliferation (Hockenbery et al., 1990). Since then, the Bcl-2 family has expanded significantly. More than twenty Bcl-2 proteins have now been identified. Bcl-2 family of proteins contains up to four BH domains called BH1, BH2, BH3, and BH4. The Bcl-2 family of proteins can be divided into three subfamilies: the anti-apoptotic Bcl-2 proteins,the multi-BH domain pro-apoptotic Bcl-2 proteins and BH3-only Bcl-2 proteins (Figure 1.2) (Czabotar et al., 2014).

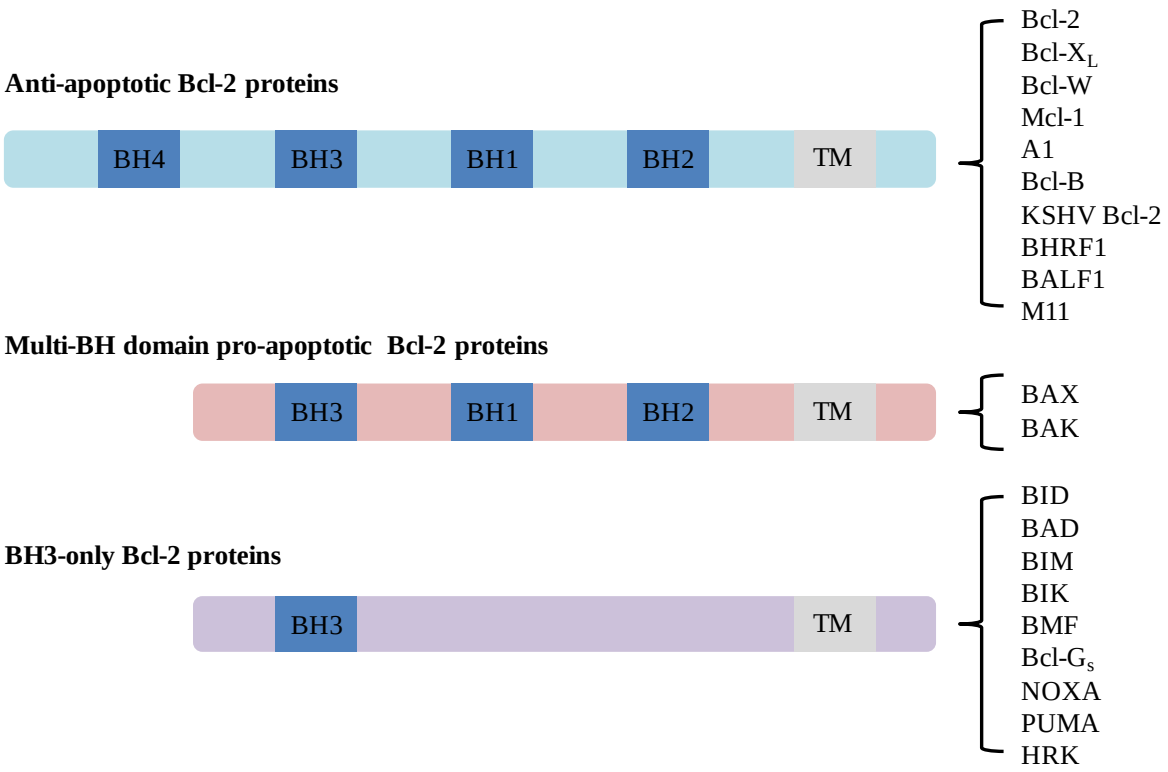

Figure 1.2: The Bcl-2 family proteins.

The anti-apoptotic Bcl-2 proteins contain all four BH domains (Figure 1.2). Most members also contain transmembrane domains (TM) and therefore, are typically associated with membranes. The anti-apoptotic Bcl-2 proteins block apoptosis by binding to the multi-BH domain pro-apoptotic Bcl-2 protein BAX and/or BAK to prevent their oligomerization, which would otherwise result in the formation of channels in mitochondrial membranes to permit the release of cytochrome c as well as other apoptosis effectors (Taylor et al., 2008).The BH1, BH2, and BH3 domains of the anti-apoptotic proteins form a hydrophobic groove on the protein surface which binds to the BH3D from a pro-apoptotic binding partner. The hydrophobic groove formed by BH1, BH2 and BH3 domains may be further stabilized by the BH4D (Sattler et al., 1997, Day et al., 2008, Sinha et al., 2008, Ku et al., 2011, Wang et al., 2007). The BH4D may be

removed by caspase-mediated proteolytic cleavage, changing an anti-apoptotic Bcl-2 protein to a pro-apoptotic Bcl-2 protein (Cheng et al., 1997b).

Unlike the anti-apoptotic Bcl-2 proteins, which contain all four BHDs, the multi-BH domain pro-apoptotic Bcl-2 proteins lack the BH4D at their N-terminus. As noted, both BAX and BAK execute their pro-apoptotic functions in the outer mitochondrial membrane. The homodimerization of BAX and BAK forms channels that increase MMP to permit the release of cytochrome c as well as other apoptosis effectors. Over-expression of BAX or BAK has been shown to promote apoptosis (Pastorino et al., 1998, Tong et al., 2004). $BAX^{-/-}/BAK^{-/-}$ double-knockout cells are resistant to various apoptotic stimuli that act through disruption of mitochondrial function (Wei et al., 2001). Surprisingly, the structures of BAX and BAK reveal a 3D structure very similar to the anti-apoptotic Bcl-2 proteins (Suzuki et al., 2000, Moldoveanu et al., 2006). The BH1, BH2 and BH3 domains of BAX and BAK assembles the almost the same structure formed by the BH1, BH2 and BH3 domains of anti-apoptotic Bcl-2 proteins. As mentioned earlier, in anti-apoptotic Bcl-2 proteins, the hydrophobic groove formed by the BH1, BH2 and BH3 domains is responsible for binding to the BH3D of pro-apoptotic proteins. In the BAX structure, the TM of BAX comprises an α helix which is located in this hydrophobic groove in a manner similar to the way the BH3Ds of pro-apoptotic Bcl-2 proteins bind to the anti-apoptotic Bcl-2 proteins, although in an opposite orientation. The BH4D which comprises the first α helix in most anti-apoptotic Bcl-2 proteins is not present in BAX and BAK based on amino acid sequence predictions. However, a similar α-helix formed by the residues before BH3D is present in both BAX and BAK structure (Suzuki et al., 2000, Moldoveanu et al., 2006).

The BH3-only Bcl-2 proteins, as indicated by their name, contain only BH3Ds. The TM is present in only some of the BH3-only Bcl-2 proteins, like BIK and HRK. Numerous studies

have shown that the BH3-only proteins execute their pro-apoptotic function through binding to the anti-apoptotic Bcl-2 proteins to release BAX and BAK from anti-apoptotic Bcl-2 proteins, thereby removing inhibition of apoptosis (Boyd et al., 1995, O'Connor et al., 1998, Zha et al., 1997, Willis et al., 2005). However, the BH3-only proteins may have additional roles in regulating apoptosis. In an *in vitro* study using BH3D-containing peptides derived from different BH3-only proteins to induce mitochondrial release of cytochrome c in purified mouse mitochondria, the BH3-derived peptide can be classified into two different groups based on their functions. One group, including BH3D-derived peptides of BID and BIM, can directly activate BAX to dimerize and release cytochrome c from mitochondria. The other group, including BH3D-derived peptides of BAD and BIK do not directly activate BAK. Instead, they bind to anti-apoptotic Bcl-2 to displace BID-like peptides (Letai et al., 2002). But since a BH3D-derived peptide instead of the full-length proteins were used in this study, the suggested multiple functions of BH3-only Bcl-2 proteins in regulating apoptosis need to be further confirmed by investigating full-length proteins *in vivo*. Multiple structural studies of BH3-only Bcl-2 proteins bound to anti-apoptotic Bcl-2 proteins or pro-apoptotic multi-domain Bcl-2 proteins have demonstrated that the BH3D of BH3-only Bcl-2 proteins forms a single α-helix upon binding to the hydrophobic groove of the binding partners (Follis et al., 2013, Czabotar et al., 2013, Rajan et al., 2015).

1.3.2. The Beclin 1–Bcl-2 interaction

Beclin 1 was first discovered as a protein that interacts with the anti-apoptotic Bcl-2 (Liang et al., 1998), and only later shown to associate with PI3KC3 and p150, to form the vesicle nucleation complex essential for autophagy (Kihara et al., 2001a, Stack et al., 1993). Thus, the

Beclin 1–Bcl-2 interaction was the first established molecular connection between autophagy and apoptosis.

Beclin 1 contains a BH3D which is required and sufficient for bindingto Bcl-2 (Sinha et al., 2008), Bcl-X_L (Oberstein et al., 2007) and viral Bcl-2 proteins (Ku et al., 2008a, Sinha et al., 2008). This interaction appears to help maintain autophagy at levels essential for normal cellular homeostasis, while mutations in Beclin 1 that block the interaction with Bcl-2 prevent Bcl-2 from inhibiting autophagy and promoting cell death (Pattingre et al., 2005a). Thus, the Beclin 1–Bcl-2 interaction provides an important node of crosstalk between apoptosis and autophagy (Feng et al., 2007).

1.3.3. Caspase-mediated Beclin 1 cleavage

The role of Beclin 1 in the interplay between apoptosis and autophagy can also be regulated by caspases. Caspase-mediated cleavage of Beclin 1 decreases cellular levels of Beclin 1 and consequently reduces levels of autophagy (Rohn et al., 2011). To date, three caspase cleavage sites have been identified in Beclin 1: D133, D146 and D149 (Wirawan et al., 2010, Rohn et al., 2011, Li et al., 2011). In one study (Wirawan et al., 2010), growth factor depletion, initially up-regulated autophagy inside Ba/F3 cells (a murine hematopoietic cell line). However, sustained growth factor withdrawal reduced levels of autophagy and activated apoptosis. Further, after apoptosis was activated, Beclin 1 was found to be cleaved at D133 and D149. The resultant Beclin 1 fragment was incapable of mediating autophagy. Instead, the C-terminal fragments were found to localize to the mitochondria and sensitize Ba/F3 cells to growth factor deprivation-induced apoptosis. Interestingly, in a separate study using HCT116 cells (Li et al., 2011), Beclin 1 fragments generated by caspase-mediated cleavage at D133 and D146 during apoptosis were not able to induce either autophagy or apoptosis.

1.3.4. BIM and its role in different autophagy stages

BIM is a potent pro-apoptotic protein. It may occur as three splice isoforms: BIM-short, BIM-long and BIM-extra long (BIM_S, BIM_L and BIM_{EL}, respectively). Different isoforms have different cellular functions. BIM_S and BIM_{EL} mainly function in apoptosis while BIM_L has a more important role in autophagy (Ruppert et al., 2012). BIM expression is up-regulated by growth factor withdrawal, mediated via inhibition of ERK1/2 and PKB signaling, the consequent dephosphorylation of the Forkhead Box O transcription factor, resulting in up-regulation of BIM transcription (Fu and Tindall, 2008, Yang et al., 2008)

BIM triggers apoptosis by binding via its BH3D to Bcl-2; preventing it from binding to and inhibiting BAX and BAK and consequently activating the intrinsic apoptotic pathway that leads to cell death (Rahmani et al., 2012). Serum or growth factor triggered activation of ERK1/2 causes BIM_{EL} phosphorylation, releasing anti-apoptotic Bcl-2 homologs. Phosphorylated BIM_{EL} is recognized by E3 ubiquitin ligase, resulting in BIM_{EL} ubiquitination and proteosomal destruction (Ewings et al., 2007b, Ewings et al., 2007a). As a result, cellular BIM_{EL} levels are reduced, apoptosis is inhibited and cells can survive.

BIM, especially BIM_{EL}, appears to inhibit autophagy independent of apoptosis activation, and this regulation occurs via diverse interactions of BIM with different proteins at multiple stages of autophagy. For instance, recently it was shown that BIM can directly interact with Beclin 1; and this interaction occurs at a site different from the Beclin 1–Bcl-2 binding region. BIM-mediated regulation of autophagy is Beclin 1-dependent, and can be disrupted by starvation (Luo et al., 2012). Additionally, previous studies have demonstrated that BIM_L is sequestered by dynein in healthy cells, and dissociated upon an apoptotic stimulus (Puthalakath et al., 1999). The interaction of BIM_L with dynein facilitates the loading, and perhaps fusion and positioning

of lysosomes.Thus, it is inferred that the absence of BIM leads to impairment of the later degradative phase of autophagy (Ruppert et al., 2012).

1.3.5. Interaction of UVRAG with BAX

UVRAG forms a heterodimer with Beclin 1 via the coiled-coil domains (CCDs) of both proteins and this interaction disrupts the homodimerization of Beclin 1, suggesting this how UVRAG activate autophagy (Noble et al., 2008). Binding of Bcl-2 to Beclin 1reduces the affinity of Beclin 1 for UVRAG, consequently inhibiting autophagy (Noble et al., 2008). UVRAG is essential for the localization of PI3KC3 to the preautophagosomal structure and endosome (Itakura and Mizushima, 2009).

UVRAG has been shown to function as an unusual BAX suppressor to regulate apoptosis (Yin et al., 2011). The UVRAG C2 domain is responsible for binding BAX. UVRAG over-expression and increased interaction with BAX inhibits the exposure of the BAX N-terminus, and the consequent mitochondrial translocation of BAX, MMP and cytochrome c release, preventing apoptosis. Consistently, in human tumor cells such as HL60 and HCT116, suppression of UVRAG expression significantly increases apoptosis and decreases autophagy. Further, knockout of UVRAG in autophagy deficient $Atg5^{-/-}$ mouse embryonic fibroblasts enhances doxorubicin-induced apoptosis. Therefore, it appears that UVRAG has a direct role in apoptosis regulation, which is independent of its role in autophagy.

1.3.6. Interaction of UVRAG with Bif-1

Bif-1, a member of endophilin B protein family, activates the conformational change of pro-apoptotic proteins BAX/BAK and the subsequent release of cytochrome c and caspase 3 during apoptosis (Takahashi et al., 2005). It has also been shown to bind via its Srchomology 3

domain to the N-terminal poly-proline region of UVRAG. This interaction, as well the Bif-1 BAR domain, facilitates autophagosome formation.

1.3.7. Atg12–Atg3 conjugation

As previously mentioned, the ubiquitin-like protein Atg12 is covalently conjugated to Atg5, and this conjugation is essential for autophagosome expansion. Unlike most other known ubiquitin-like proteins, for more than 10 years, Atg5 was the only known target of Atg12. However in 2010, Atg3, the E2 enzyme involved in conjugation phosphatidylethanolamine to Atg8, the other ubiquitin-like autophagy protein; was shown to be a novel target of Atg12 (Radoshevich et al., 2010). Surprisingly, disruption of Atg12-Atg3 conjugation did not affect starvation-induced autophagy, but rather affected apoptosis regulation. Apoptosis induced by mitochondrial-uncoupling-agents was reduced in cells lacking Atg12-Atg3 conjugation. This protection was shown to also correlate with increased expression of the anti-apoptotic protein Bcl-X_L. Further, Bcl-X_L inhibitors were able to induce a similar level of apoptosis in cells expressing either wild-type (WT) ATG3 or mutant ATG3 incapable of ATG12-ATG3 complex formation (Radoshevich et al., 2010).

1.3.8. Atg5–FADD interaction

In addition to the conjugation of Atg5 to Atg12, which is essential for autophagy, more recently, a yeast two-hybrid screen showed that Atg5 also interacts with FADD (Pyo et al., 2005). This study also showed that certain stimuli, such as IFN-γ, up-regulate Atg5 expression, resulting in autophagosome accumulation and cell death. In Atg5-overexpressing cells treated with IFN-γ, autophagosomes start to accumulate, then aggregate and fuse to form bigger vesicles. Eventually, most of the cells harboring aggregated vacuoles shrink and die. Atg5 mutants that cannot conjugate to Atg12 inhibit both IFN-γ-induced cell death and vacuole

formation. However, Atg5-overexpression in FADD-deficient cells is insufficient for cell death, although vacuole formation is unaffected. Moreover, the autophagy inhibitor 3-MA suppresses both Atg5-mediated vacuole formation and cell death, but the caspase inhibitor Z-VAD-fmk inhibits only cell death. Taken together, these findings indicate that, in addition to its key function in autophagy, Atg5 may also have important roles in the regulation of apoptosis. Further, contrary to expectations, in this study, cell death appears to occur due to apoptosis rather than elevated autophagy, and depends on the interaction of Atg5 and FADD.

1.3.9. Calpain-mediated Atg5 cleavage

Calpains have been reported to cleave Atg5, and the cleaved Atg5 appears to provoke apoptotic cell death (Yousefi et al., 2006). The cleavage product, an N-terminal Atg5 fragment with a relative molecular mass of 24 kD, is shown to translocate from cytosol to mitochondria. Both full-length Atg5 and truncated Atg5 are present in cells undergoing apoptosis. However, only the truncated Atg5 coimmunoprecipitates with the antiapoptotic protein Bcl-X_L, triggers cytochrome c release and caspase activation.Thus, truncated Atg5 appears to function as a pro-apoptoticprotein that inhibits anti-apoptotic Bcl-2 homologs, resulting in the activation of the mitochondria-dependent apoptosis. Meanwhile, the truncated Atg5 loses its autophagy-inducing activity.

1.3.10. p53: A master regulator of autophagy and apoptosis

p53, encoded by the TP53 gene, is a tumor suppressor (Matlashewski et al., 1986). Stress-induced DNA or protein damage triggers repair mechanisms or programmed cell death, depending on the severity of the damage (Crighton et al., 2003). The response to DNA damage is regulated by p53, which plays a central role in cell cycle arrest and cell death.

p53 has been shown to activate both extrinsic and intrinsic apoptotic pathways (Maiuri et al., 2007b). In the extrinsic pathway, nuclear p53 increases the expression of APO-1/Fas (the receptor of pro-apoptotic molecules) (Muller et al., 1998) and the TRAIL receptor (DR4/5) (Kuribayashi and El-Deiry, 2008); while cytoplasmic p53 activates caspases 8 and 3. In the intrinsic apoptotic pathway, nuclear p53 activates the expression of the pro-apoptotic proteins PUMA, NOXA, BAX and BID, leading to increased MMP, cytochrome c release, and activation of caspase-9 and caspase-8 (Reuter et al., 2008). Meanwhile, cytoplasmic p53 translocates to the mitochondria and forms a complex with Bcl-2/Bcl-X_L to liberate the proapoptotic proteins BAX and BAK (Moll et al., 2005). p53 also activates the expression of APAF-1, a key component of the apoptosome (Moroni et al., 2001).

Cytoplasmic and nuclear p53 have contradictory roles in regulating autophagy. Cytoplasmic p53 inhibits autophagy through the activation of mTOR signaling via the inactivation of AMP kinase (Feng, 2010), while nuclear p53 activates autophagy by transcriptional activation of DRAM, which promotes the formation of autophagolysosomes (Crighton et al., 2006). In p53-induced apoptosis, the knock-down of DRAM leads to a decrease in cell death. In tumors with WT p53, DRAM mRNA is down-regulated compared to tumors containing mutated p53, perhaps to mitigate the apoptosis-inducing function of p53 and facilitate survival of cancer cells (Crighton et al., 2006). In contrast to cytoplasmic p53, nuclear p53 activates kinases like Cdc42/JNK1, triggering Bcl-2 phosphorylation at T56, S70, T74, and S87. Phosphorylated Bcl-2 cannot bind to Beclin 1, allowing Beclin 1 to promote autophagy (Sui et al., 2011, Thomas et al., 2000)[123, 124]. Thus, nuclear p53 promotes autophagy.

1.3.11. The regulation of autophagy by anti-apoptotic viral Bcl-2 homologs

Homologs of the anti-apoptotic cellular Bcl-2 proteins are encoded by all γ-herpesviruses (γHV) (Sinha et al., 2008, Russo et al., 1996, Afonso et al., 2001); as well as some other viruses like African swine fever virus and fowlpox virus (Subramanian et al., 1984, Brun et al., 1998, Afonso et al., 2000). Viral Bcl-2 proteins are thought to sustain host cell viability by preventing cell death, in order to maximize viral replication (Tarodi et al., 1994, Wang et al., 1999). Further, viral Bcl-2 proteins contribute to establishment of latency, the emergence from latency and the establishment of chronic, persistent infections (de Lima et al., 2005, Cuconati and White, 2002).

γHVs, including important human pathogens such as Epstein Barr virus (EBV), Kaposi's sarcoma-associated HV (KSHV), and the murine γHV68, are associated with lymphoproliferation and cancer. EBV is implicated in the pathogenesis of a number of human malignancies of epithelial and lymphoid origin, and a number of lymphoproliferative diseases in immunocompromised hosts (Cabras et al., 2005, Bellows et al., 2002); while KSHV is involved in the etiology of Kaposi sarcoma tumors (Muralidhar et al., 2000). EBV encodes two Bcl-2 homologs: BHRF1 and BALF1. BHRF1 binds to BH3D-containing pro-apoptotic proteins, including BIM, BID, PUMA and BAK. BHRF1 expression renders a mouse model of Burkitt lymphoma untreatable (Kvansakul et al., 2010). Unexpectedly, the other γHVBcl-2 encoded by EBV, BALF1, fails to protect cells against apoptosis. Instead, it appears to inhibit the anti-apoptotic activity of BHRF1 (Bellows et al., 2002). KSHV encoded Bcl-2 was also shown to bind to the BH3Ds of BAX and BAK with affinities significantly lower than cellular Bcl-2 proteins (Huang et al., 2002). However, in a separate study, KSHV Bcl-2 fails to heterodimerize with cellular BAX and BAK proteins, although its overexpression leads to the inhibition of Sindbis Virus-induced apoptosis (Cheng et al., 1997a). Murine γHV68 also encodes an anti-

apoptotic Bcl-2 homolog, M11, that inhibits apoptosis induced by anti-Fas antibody and by TNF-α (Wang et al., 1999). Despite low sequence conservation between the various cellular and viral Bcl-2 homologs, including BHRF1, KSHV Bcl-2 and M11, all those with known 3D-structures share the same fold, indicating that they are homologs. Further, all of them appear to bear a hydrophobic surface groove that is responsible for binding to the BH3D of other proteins such as various pro-apoptotic proteins and the autophagy effector, Beclin 1 (Huang et al., 2002, Kvansakul et al., 2010, Sinha et al., 2008).

Therefore, it is not surprising that γHV Bcl-2 proteins have now been shown to bind to the Beclin 1 BH3D to function as potent autophagy inhibitors. KSHV Bcl-2 was shown to block Beclin 1-dependent autophagy in both yeast and mammalian cells (Pattingre et al., 2005a). Subsequently, γHV68 M11 was shown to also bind to Beclin 1 and inhibit autophagy. Structures of M11 in complex with the Beclin 1 BH3D, show that the Beclin 1 BH3D binds to the hydrophobic surface groove on M11 (Sinha et al., 2008), similar to the mode by which various BH3Ds have been shown to bind to cellular Bcl-2 proteins. M11 also binds to most pro-apoptotic proteins except BAD, BIK (Ku et al., 2008b). Thus, M11 inhibits both apoptosis and autophagy by binding to BH3Ds from pro-apoptotic proteins and the pro-autophagic protein, Beclin 1 (Sinha et al., 2008, Ku et al., 2008a). However, unlike the cellular Bcl-2 proteins, the inhibitory activity of γHVBcl-2 proteins does not appear to be down-regulated by cellular phosphorylation, allowing them to constitutively inhibit autophagy and apoptosis (Wei et al., 2008a).

1.4. Overview of methods used in this research

1.4.1. Protein X-ray crystallography

Protein X- ray crystallography is used to determine the three-dimensional molecular structure of a crystallized protein at the atomic resolution. Currently, X-ray crystallography is the

most favored technique for structure determination of proteins and other biological macromolecules. Amongst nearly 120000 structures deposited in the Protein Data Bank (PDB) to date, 107000 are X-ray crystal structures (www.rcsb.org).

In order to determine the X-ray crystal structure of a protein, firstly, a high quality protein crystal needs to be grown. Currently, this is often the most challenging and time consuming step in protein crystallographic studies, and is also the least well understood (Smyth and Martin, 2000). Nevertheless, to start with, the protein sample used for growing crystals needs to be pure, homogeneous, and stable. This high-quality protein can then be used to grow protein crystals. In general, the principle of crystallization is to bring the protein solution to supersaturation, which is a thermodynamically unstable state. This induces some of the protein to come out of the solution, either to form crystal nuclei that may further grow into larger crystals, or as precipitation. Crystallization and precipitation are competing processes, and crystallization can only happen if conditions such as protein purity, concentration and structure, temperature, pH, precipitants and additives favor crystallization, rather than precipitation (McRee, 1993, Rhodes, 1993). Vapor diffusion is the most widely used method for protein crystallization, while microbatch and microdialysis have also been successfully used to grow protein crystals (Chayen, 1998).

After high-quality protein crystals are obtained, the X-ray diffraction data then can be recorded by exposing the crystals to a monochromatic X-ray beam. The X-ray can either be generated from an in-house laboratory source from electrons striking a copper anode, or from accelerating electrons in a synchrotron storage ring (Smyth and Martin, 2000). For protein X-ray crystallography, the more powerful synchrotron is most often used in order to obtain high-resolution diffraction data. At synchrotron, the data is usually collected by exposing the crystal

repeatedly to the X-ray beam, while rotating the crystals. X-ray diffraction occurs when the X-ray interacts with the electrons of the atoms inside the crystal. The X-rays are scattered by the electrons. When the scattered waves add up, they either get stronger, or weaker and may even cancel each other. These waves are registered as spots of different intensity on the X-ray detector (Massa, 2004). Therefore, each exposure generates an X-ray diffraction pattern that contains diffraction spots known as reflections, corresponding to a diffracted X-ray beam registered by the X-ray detector (Figure 1.3).

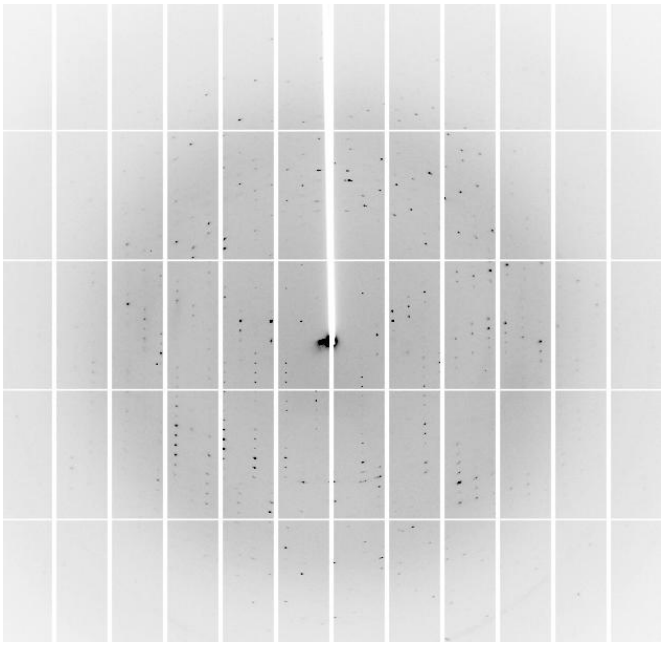

Figure 1.3: X-ray diffraction image of a crystal of Beclin 2 CCD taken at 24-ID NE-CAT at Advanced Photon Source, Argonne National Laboratory, Argonne, IL.

The diffraction data is then processed to determine the space group, unit cell parameters and the orientation of the crystal in the beam, which results in each spot on the diffraction image being assigned an index consisting of three integers: h, k, and l, called the Miller indices. Next, the intensity of each spot on the diffraction image is measured. Although this cannot be deconvoluted at this stage, the intensity of each spot is a result of both, the amplitude of the

diffracted waves and their phase relation (Smyth and Martin, 2000). A full data set might consist of hundreds of diffraction images, and equivalent diffracted spots from each image are merged and scaled. During scaling, intensities of symmetry related reflections whose intensities are expected to be identical (within acceptable experimental error) are averaged. All symmetry-related reflections are then merged into a unique set of reflections (Smyth and Martin, 2000). The quality of the data set can be assessed by Pearson correlation coefficient (ρ) between random half-data sets ($CC_{1/2}$)

$$\rho_{X,Y} = cov\frac{(X,Y)}{\sigma_X \sigma_Y} = E\frac{[(X-\mu_X)(Y-\mu_Y)]}{\sigma_X \sigma_Y}$$

where *X* and *Y* are the two variables from each random half-data set, respectively, *cov* is the covariance, σ_X and σ_y are the standard deviation of *X* and *Y* respectively, *E* is the expectation and μ_X and μ_y are the mean of *X* and *Y* respectively. $CC_{1/2}$ values of 0.5 and above are considered acceptable.

The next step is to use the high-quality data to calculate the three-dimensional electron density map into which the protein structure can be built. The electron density *ρ(x,y,z)* is calculated using a Fourier transformation:

$$\rho_{(xyz)} = \left(\frac{1}{V}\right)\sum_{\mathrm{h}}\sum_{\mathrm{k}}\sum_{\mathrm{l}} F_{(hkl)} \exp[-2\pi i(hx+ky+lz)]$$

where h,k,l are the miller indices, x,y,z are fractional coordinates of the unit cell, and V is the volume of the unit cell. *F*(*hkl)* is the structure factor for each X-ray reflection *hkl* , and includes information about both the amplitude and the phase of that reflection, as expressed below:

$$F_{(hkl)} = \sum_{j=1}^{N} f_j \exp[2\pi i(hx_j + ky_j + lz_j) = \left|F_{(hkl)}\right|\exp(i\varphi_{(hkl)}),$$

where f_j is the individual atomic scattering factor for atom j, $|F_{(hkl)}|$ is the amplitude, and $\varphi_{(hkl)}$ is the relative phase of the diffracted X-rays.

Therefore,

$$\rho_{(xyz)} = \left(\frac{1}{V}\right)\sum_{h}\sum_{k}\sum_{l}|F_{hkl}|\exp[-2\pi i(hx+ky+lz)+i\varphi_{(hkl)}]$$

While the square of amplitude $|F_{(hkl)}|$ is proportional to the measured intensity, the phase $\varphi_{(hkl)}$ cannot be determined directly.

Fortunately, there are several methods that can be used to solve the phasing problem, including molecular replacement (MR), multi-wavelength anomalous diffraction, single-wavelength anomalous dispersion, and multiple isomorphous replacement (Smyth and Martin, 2000). All the structures in this research were solved by MR.

In MR the unknown structure of a protein is solved by using the known atomic structure of a homologous protein. This known structure is computationally placed in all possible permutations of different orientations and positions in the crystal unit cell of the protein whose structure is to be solved, and the theoretical diffraction pattern from each permutation calculated and compared to the experimental diffraction to identify the orientation and position that produces the best match to the experimental diffraction. This MR model is then used to calculate the phases for each reflection. The calculated phases together with the measured diffraction amplitudes are then used to calculate the initial electron density map. The atomic structure of the unknown protein is then built into this electron density map.

The measured amplitude is used to supply information for refining the model to more closely resemble the target structure (Evans and Mccoy, 2008). In order to improve the phases and the interpretation of the electron density map, refinement is usually carried out in a cyclic

process together with model rebuilding to gradually improve the model through statistical adjustment of the atomic coordinates to better fit both, the experimental diffraction data and established geometric constraints. To evaluate the refinement process, the R-factor is usually used as an indicator of the agreement between the built model and the experimental X-ray diffraction data.

$$R = \frac{\Sigma \left| |F_{obs}| - |F_{calc}| \right|}{\Sigma |F_{obs}|}$$

where |Fobs| is the observed amplitudes from the experimental diffraction data and |Fcalc| is the calculated amplitude from the model.

The free R-factor, or R_{free}, is commonly used as a cross-validation method (Brunger, 1992). R_{free} is calculated from a small fraction (usually 5%) of data, which is set aside and never used in the refinement. The comparison between the values of the working R-factor (R_{work}) and R_{free} indicates the extent to which the data is overfitted and also provides information about the quality of model and data. During refinement, the decrease of both R_{work} and R_{free} is more important than the actual value. However, as a general guide, the final value of R_{free} should be somewhere close to 10% of the resolution of the structure, and the difference between R_{work} and R_{free} should be < 5%.

The maximum likelihood method is widely used in refinement (Murshudov et al., 1997). The basic idea of maximum likelihood is that the best model is one that is most consistent with observed data. Consistency between the model and observed data is measured statistically by comparing the theoretical diffraction data calculated from the model with the experimentally observed diffraction data. The model becomes better if it is changed to make the observation more probable. Maximum likelihood also uses restraints to ensure the model agrees with

established chemical parameters such as bond distances, angles and torsions and temperature factors (B-factors). Simulated annealing is another method commonly used to refine structures. In simulated annealing, the model is "heated" to add random thermal motion to each atom, then slowly cooled and refined. The random thermal motion reduces the probability of a model being trapped in the wrong local minimum, and therefore is more useful in the early stages of refinement (Brunger et al., 1997). Non-crystallographic symmetry (NCS) restraints are also useful for refinement, providing more than one copy of the same molecule in the asymmetric unit. TLS (translation-libration-screw) refinement, which provides a good approximation of anisotropy with much fewer parameters is also frequently used (Winn et al., 2001). Lastly, in addition to R_{work} and R_{free}, during refinement and rebuilding of the model, other criteria are also used to judge the quality of the model based on our knowledge of the structure of macromolecules. These includes deviations from ideality of bond lengths, bond angles, violations of dihedral, and chirality restraints, temperature factors, Ramachandran plot, peptide orientation, rotamer analysis, residue real-space electron-density fit and close contacts.

1.4.2. Small-angle X-ray scattering (SAXS)

Although X-ray crystallography can provide detailed, atomic-resolution, structural information of a protein, only the low-energy conformation trapped during crystallization can be determined using this method. SAXS, is a complementary method that can provide structural information about shape, assembly state, aggregation and folding of a protein in solution in the 50 Å to 10 Å resolution range. This method can also be used to obtain the structural information about flexibly linked domains, which often cannot be studied by X-ray crystallography, since they do not crystallize (Putnam et al., 2007).

In a typical SAXS experiment, a purified protein sample in solution is exposed to the X-ray source and the elastic scattering of X-rays is recorded at very low angles (0.1 - 10 °). The scattering curve of the protein is obtained by subtraction of the buffer from the sample, and is typically represented as scattered intensity I as a function of the magnitude of the scattering vector q.

$$q = \frac{4\pi \sin\theta}{\lambda}$$

where 2θ is the scattering angle and λ is the wavelength of the incident X-ray beam (Putnam et al., 2007). Structural information about the protein sample can then be obtained by analyzing the SAXS data recorded for that sample.

The linearity of the Guinier plot (Figure 1.4), which is a plot of Ln(I) vs. q^2, at low q regions where $q \times R_g \leq 1.3$, indicates that the sample is monodispersed in solution. If the Guinier plot is frown or smile, the protein sample contains aggregated particles. The linear fit of Guinier plot at this low q region enables estimation of the radius of gyration (Rg), scattering intensity at zero-angle(I(0)) of the protein sample.The slope of linear fit equals $-R_g^2/3$, and intercept at 0 on the x-axis equals to $e^{(I(0))}$. R_g is the average root-mean-square distance from the center of density of the molecule, weighted by the scattering length density (Kikhney and Svergun, 2015). Therefore, a protein with a compact shape will have a smaller R_g than an extended protein of the same molecular weight.

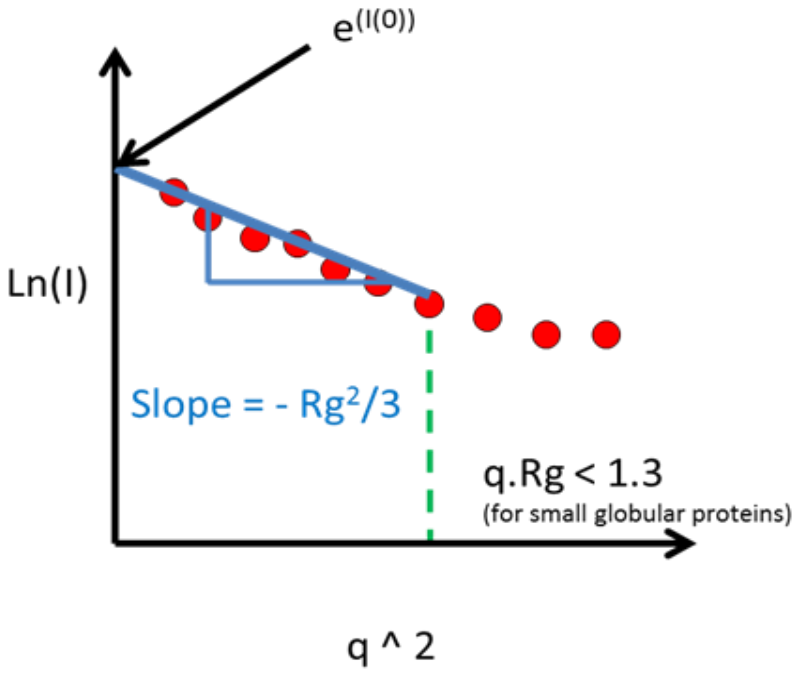

Figure 1.4: A sample Guinier plot. This figure is obtained from the website (http://psldc.isis.rl.ac.uk/Guinier/Guinier%20plot.htm).

The pairwise-distance distribution function, or P(r) function, describes the distribution of distances between electrons in the scattering particles in the sample. P(r) can be calculated through a Fourier transform of the scattering curve:

$$P(r) = \frac{r}{2\pi^2}\int_0^\infty I(q)q\sin(qr)dq$$

where r is all possible intra-particle distances, and I(q) is the intensity as a function of the magnitude of the scattering vector q.

Maximum particle dimension (D_{max}),which is the radius of the protein at the longest dimension,is the value of r at P(r) equals to zero (Putnam et al., 2007). The shape of the P(r) curve (Figure 1.5) also provides information about the shape of the protein. A symmetrical bell-shape curve indicates that the protein has a solid spherical shape, while an asymmetrical curve with a tail to the right corresponds to a long rod shape.

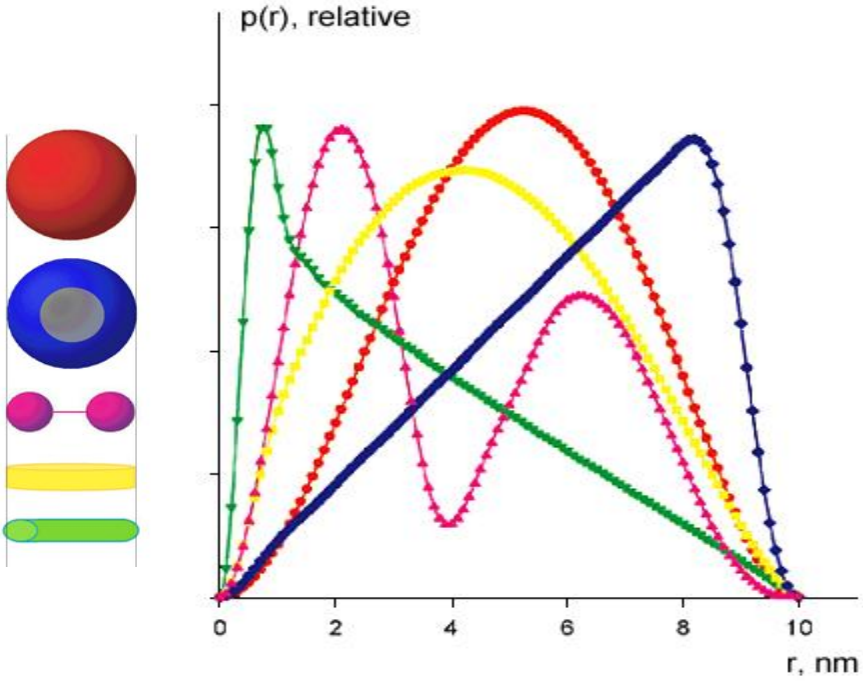

Figure 1.5: The P(r) curves correspond to proteins with different shapes. This figure is obtained from the website (http://www.saxier.org/forum/viewtopic.php?t=663).

The Kratky plot (Figure 1.6), which is the plot of $I(q) \times q^2$ vs. q, can be used to assess the folding state of a protein. For a well-folded single-domain protein, the Kratky plot will have a bell-shape at the low q region and converges to the starting point on the $I(q) \times q^2$ axis at high q. A well-folded multi-domain protein will have additional peaks or shoulders at the low q region and converges to starting point on the $I(q) \times q^2$ axis at high q. But if a protein is not well-folded, the Kratky plot does not converge to the starting point on the $I(q) \times q^2$ axis at high q (Kikhney and Svergun, 2015).

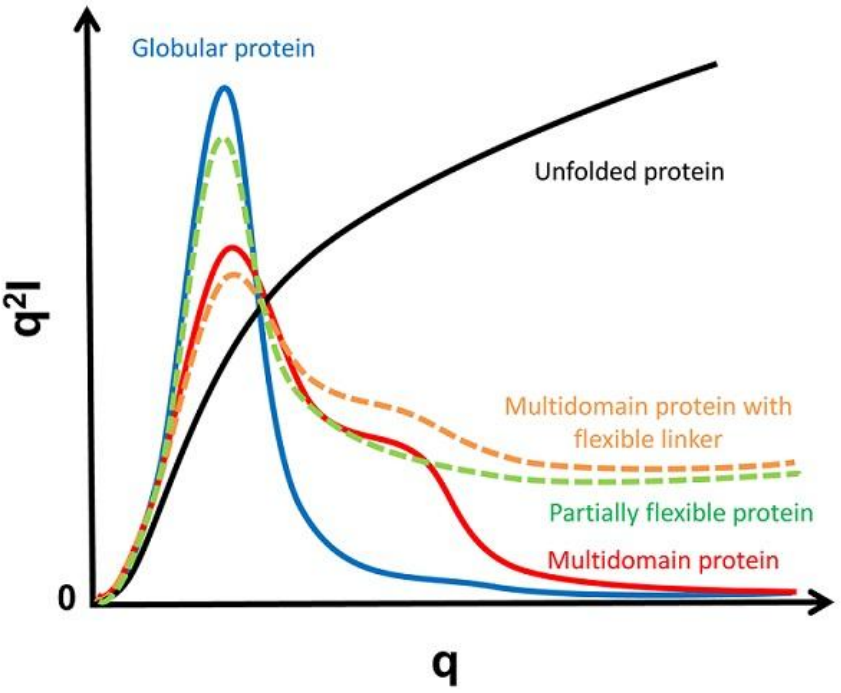

Figure 1.6: The Kratky plots correspond to proteins with different folding states. This figure is obtained from the website (https://www-ssrl.slac.stanford.edu/~saxs/analysis/assessment.htm).

There are also programs available for calculating an *ab initio* molecular envelope of a protein sample from the scattering profiles. Perhaps, the most common program is DAMMIN (Franke and Svergun, 2009), which creates *ab initio* molecular envelopes starting form a random configuration, followed by simulating annealing and application of a non-compactness penalty, to identify a compact "dummy" beads configuration that yields a scattering pattern that fits the experimental data (Franke and Svergun, 2009). Components with known atomic structure can then be fitted into this the molecular envelope either manually or using available SAXS modeling programs, which can provide information such as the arrangement of individual proteins/domains in a large complex/protein and the oligomerization state of a protein. The theoretical X-ray scattering curve can be calculated from the constructed model and its fit to the

experimental scattering curve can be used to validate the constructed model (Schneidman-Duhovny et al., 2010).

1.4.3. Isothermal titration calorimetry(ITC)

ITC directly characterize the thermodynamics of a binding event by monitoring the heat released or absorbed during a binding event. As chemical interactions are often associated with a heat exchange with the environment, this makes ITC a convenient method to quantify thermodynamics of the interaction. Further favorable features of ITC are that it is a label-free technique, it doesn't require immobilization of ligand or protein, and it uses relatively small amounts of materials (García-Fuentes et al., 2011).

Currently, there are two ITC machines that are widely used: the VP-ITC or iTC-200 from Microcal and Nano ITC from TA instruments. The latter was used in this study. These instruments can determine dissociation constants in a wide range from 10^{-9} M to 10^{-4} M (García-Fuentes et al., 2011). For these modern ITC instruments, the measuring unit is composed of two identical cells, the sample cell and reference cell, made of a highly efficient thermally conducting and chemically inert material, and sensitive thermopile circuits used to detect temperature differences between the two cells. Before the experiment, constant power is applied to the reference cell, which directs a feedback circuit to activate a heater located on the sample cell to maintain equal temperature between the two cells. During an experiment, when a molecule is titrated into the sample cell, causing heat to be absorbed or released, the heating power supplied to the sample cell will decrease or increase accordingly, in order to keep the sample and reference cells at equal temperatures. The heat change is then simply calculated by integrating the heater power over the time (sec) of the measurement (Freyer and Lewis, 2008).

In a typical ITC experiment, the molecule that can be concentrated to the highest molar concentration is loaded in the syringe, and titrated into the cell which contains the binding partner (Figure 1.7A). Each injection of the syringe into the cell enables interaction of the two molecules, resulting in a positive or negative signal (Figure 1.7B). During data analysis, the area of each peak is integrated and plotted versus the molar ratio of the molecule in the syringe to the molecule in the cell (Figure 1.7B). This titration curve is then fitted to a binding model to extract the enthalpy of interaction (ΔH), the association constant (K_a) and stoichiometry (Figure 1.7B). ΔH is represented by the distance between the two asymptotic lines of the binding curve corresponding to the minimal and maximal heat formation. The slope at the inflection point of the binding curve reflects K_a. The molar ratio at the inflection point of the binding curve determines the reaction stoichiometry. The change in the Gibbs free energy (ΔG) and change in entropy (ΔS) of the reaction can be calculated from ΔH, K_a and reaction temperature (Nunez et al., 2012).

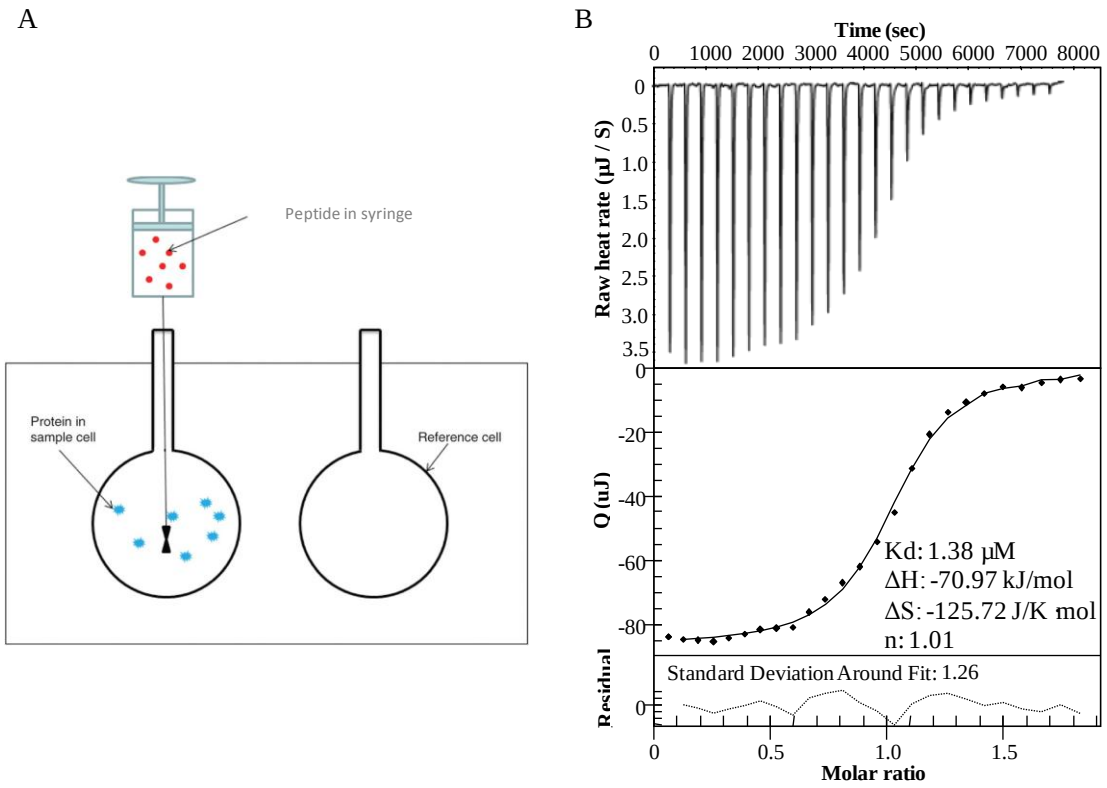

Figure 1.7: ITC experimental setup (A) (Zhou et al., 2011) and the ITC titration raw data and data analysis for Beclin 1 BH3D binding to M11 (B).

For good ITC experiment design, a C-value in the 10-100 range needs to be achieved. The C value is defined as the product of K_a times the molar concentration of the molecule in the sample cell times stoichiometry (Wiseman et al., 1989). To accurately determine the binding parameters, it is important to obtain a sigmoidal binding curve, which is dependent on the C-value (Wiseman et al., 1989). Therefore, simulations are important in optimizing an ITC experiment and in achieving a balance between detectable heats and a sigmoidal binding curve. However, in many cases, the intrinsic property of the binding reaction makes it difficult to reach a good C-value. For instance, it may not be possible to obtain the required concentration of the molecule in the sample cell because the protein of interest is not stable at high concentrations.

1.4.4. Circular dichroism (CD)

CD, an absorption spectroscopy method based on the difference in the absorption of left-handed and right-handed circularly polarized light, is often used to investigate structural aspects of optically active chiral molecules (Greenfield, 2006b). CD is usually reported in molar ellipticity in degrees cm^2 $dmol^{-1}$, where degree of ellipticity (θ) is defined as the tangent of the ratio of the minor to major elliptical axis (Sreerama and Woody, 2004).

CD can be used to determine the secondary structure of proteins. In the far UV range (below 250 nm) of CD, the energy of the electronic transitions contributed from the protein backbone dominates, and the geometric relation between amide groups in different secondary structures determines the characteristic CD spectra of different secondary structures (Figure 1.8) (Sreerama and Woody, 2004).

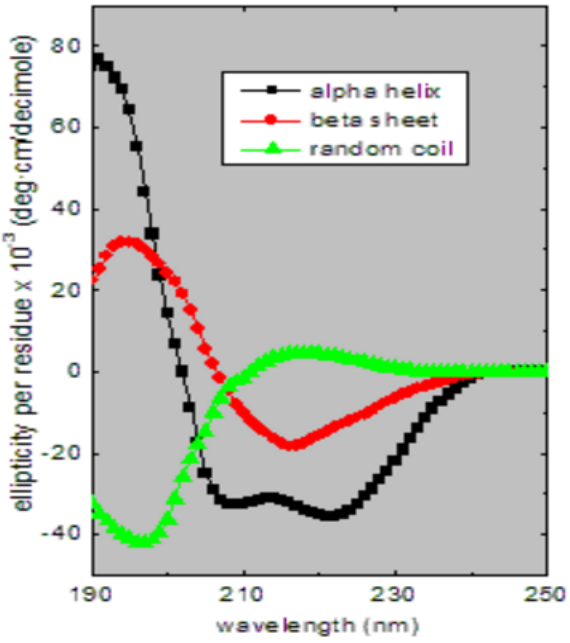

Figure 1.8: CD spectra of polypeptides with representative secondary structures. This figure is obtained from the website (http://www.ap-lab.com/circular_dichroism.htm).

CD spectra of typical all α-helical proteins have two negative bands at 208 nm and 222 nm respectively, and a positive band at 193 nm. CD spectra of proteins consisting of only β-sheets have a positive band at 195 nm and a negative band at 218 nm. Lastly, CD spectra of completely disordered proteins have a negative band near 195 nm and very low ellipticity above 210 nm. The predominant secondary structure of proteins of unknown structure can be determined by comparing the CD spectrum of a sample of that protein to standard CD spectra (Figure 1.8). Moreover, the secondary structure content of the protein can be estimated by analyzing the CD spectrum using programs such as the CDPro program package (Sreerama et al., 2001)

CD can also be used to study the thermal stability of folded proteins, which have a significant proportion of α-helices and/or β-strands. When the protein unfolds upon heating, it loses these highly ordered structures, resulting in a change in the CD spectra. Therefore, monitoring the change of the molar ellipticity at a particular wavelength that is characteristic of the most prevalent secondary structure in that protein, as a function of temperature reflects the unfolding process. For example, for an all α-helical protein, the CD spectrum in the far UV range has two negative bands at 208 nm and 222 nm (Figure 1.8). During the thermal unfolding process, the protein starts to lose its ordered α-helical conformation and becomes disordered. Therefore, its CD spectrum changes from the typical α-helical CD spectrum to the random coil spectrum, which has almost zero molar ellipticity at 222 nm (Figure 1.8). Hence, the thermal unfolding process can be studied by monitoring the change of molar ellipticity at the wavelength 222 nm. In order to study the thermal unfolding of a protein with unknown secondary structure composition, a CD spectrum in the far UV range needs to be first recorded, to determine the wavelength that has maximal absolute ellipticity. If a protein has maximal absolute ellipticity at

two wavelengths, the unfolding study is usually performed at higher wavelength in order to reduce the signal to noise ratio (Greenfield, 2006a). If the unfolding is reversible, after the unfolding curve is obtained, the melting temperature (T_m) can be calculated by fitting the unfolding curve with an appropriate algorithm. However, if the unfolding is irreversible due to the protein aggregation at higher temperatures, the unfolding curve may be perturbed by the kinetics of aggregation, preventing determination of the T_m (Greenfield, 2006a).

1.5. Specific aims of this study

Given the extensive molecular crosstalk between apoptosis and autophagy that enables co-regulation of the two pathways, it is very important to understand the mechanism of crosstalk between these pathways. The goal of this dissertation, entitled "STRUCTURAL STUDIES OF THE MECHANISM BY WHICH BCL-2 AND BECLIN PROTEINS REGULATE AUTOPHAGY AND APOPTOSIS", is to obtain a structure-based understanding of the biological function of selected Bcl-2s and Beclin homologs the regulation of autophagy and apoptosis. The specific aims of this research are:

1. To design a peptide that specifically binds to and blocks the down-regulation of autophagy by γHV68 M11, but not human Bcl-2 homologs.
2. To investigate the structure of EBV-encoded BALF1, which appears to be a second Bcl-2 homolog encoded by EBV.
3. To investigate the binding of Bcl-2 homolog, Mcl-1, to Atg12, an important autophagy protein.
4. To study the domain architecture of Beclin 2, a newly discovered mammalian paralog of Beclin 1, and to elucidate the structure of the Beclin 2 CCD.

5. To characterize the interaction of the Beclin 2 CCD with the Atg14 CCD, and identify Beclin 2 residues important for binding to Atg14.

CHAPTER 2. DEVELOPMENT OF A PEPTIDE INHIBITOR THAT SPECIFICALLY BLOCKS THE DOWN-REGULATION OF AUTOPHAGY BY VIRAL BCL-2 OF MURINE γ-HERPESVIRUS 68

2.1. Introduction

2.1.1. γHVs encode Bcl-2 homologs

γHVs are common human pathogens that infect ~95% of all adults. EBV, first isolated from Burkitt's lymphoma, has been detected in several malignant tumors originating in both lymphoid and epithelial tissues (Roizman). EBV is also the causative agent for infectious mononucleosis, and may be responsible for chronic fatigue syndrome. KSHV is associated with Kaposi sarcoma tumors, which show a high incidence among immunocompromised individuals, such as patients with human immunodeficiency virus (HIV) infection and transplant recipients. Another mammalian γHV, murine γHV68 does not infect humans, but provides a tractable model for studying γHV infections in vivo. A murine model has been developed to study the mechanisms and pathogenesis of γHV induction of lympho-proliferative disease (Tarakanova et al., 2005). All γHVs encode homologs of the anti-apoptotic, cellular Bcl-2 proteins (Cuconati and White, 2002, Gangappa et al., 2002) suggesting that these proteins play an important role in the pathogenesis of these viruses.

The anti-apoptotic γHV Bcl-2 homologs appear to be critical for viral reactivation from latency and replication in immunocompromised hosts (Gangappa et al., 2002, Hardwick, 1998, Benedict et al., 2002). Thus, they play important roles in latent and chronic infection. One mechanism by which γHV Bcl-2 homologs may accomplish these physiological functions is by the down-regulation of apoptosis. KSHV Bcl-2 blocks apoptosis stimulated by overexpression of BAX or v-cyclinor by Sindbis virus infection (Sarid et al., 1997, Ojala et al., 1999); however, in

cellular assays, it does not appear to heterodimerize with pro-apoptotic Bcl-2 family members, such as BAX and BAK (Cheng et al., 1997c). EBV encodes a Bcl-2 homolog, BHRF1, which is expressed as an early lytic cycle protein, has anti-apoptotic activity, heterodimerizes with BAX and BAK and also disrupts the differentiation of epithelial cells (Henderson et al., 1993, Foghsgaard and Jaattela, 1997, Marshall et al., 1999, Theodorakis et al., 1996). The γHV68 Bcl-2 homolog, M11, has been shown to down-regulate apoptosis induced by Fas, TNFα, and Sindbis virus infection (Wang et al., 1999, Loh et al., 2005). More recently it has been shown that KSHV Bcl-2 and γHV68 M11 also down-regulate autophagy in cell culture by binding to an essential autophagy effector, Beclin 1 (Pattingre et al., 2005b, Ku et al., 2008a, Sinha et al., 2008). M11 is the only γHV Bcl-2 that has been demonstrated to play a role during infection in vivo (Loh et al., 2005, Gangappa et al., 2002). Thus, the γHV and cellular Bcl-2 homologs are dual regulators of autophagy and apoptosis, and serve as a node of crosstalk between these pathways (Wei et al., 2008b, Levine et al., 2008, Maiuri et al., 2007b, Kang et al., 2011).

2.1.2. Cellular and γHVBcl-2 homologs

Although human cellular Bcl-2 paralogs share less than 50% sequence identity, known human and murine Bcl-2 ortholog pairs share >85% sequence identity. All anti-apoptotic Bcl-2 homologs have similar three-dimensional structures, consisting of a central hydrophobic α-helix surrounded by six or seven amphipathic helices (Muchmore et al., 1996). Previous structural and mutagenic analyses demonstrated that the amphipathic, α-helical Bcl-2 homology 3 domains (BH3Ds) of pro-apoptotic proteins bind to a hydrophobic surface groove on Bcl-2 homologs (Loh et al., 2005, Liu et al., 2003, Petros et al., 2000, Sattler et al., 1997, Huang et al., 2002, Huang et al., 2003), with the hydrophobic face of the helix buried in a hydrophobic groove on the surface of the Bcl-2 homolog. Different Bcl-2 homologs have widely varying affinities for

BH3 domains from different pro-apoptotic proteins (Sinha et al., 2008, Huang et al., 2002, Huang et al., 2003, Chen et al., 2005, DeBartolo et al., 2012). The molecular determinants that enforce these varying specificities are not well understood.

2.1.2.1. Bcl-X_L

Bcl-X_L is a human cellular Bcl-2 protein encoded by *BCL2L1* which mapped to chromosome 20q11.21. In addition to Bcl-X_L (233 residues), Bcl-Xs (170 residues) is also encoded by *BCL2L1* due to mRNA splicing. Unlike BCL-X_L which contains four BH domains and a TM, Bcl-Xs only contains the BH3D, BH4D and TM (Boise et al., 1993). Notably, *bcl-x_L* is the dominant mRNA species expressed in embryonic and adult tissues (Gonzalez-Garcia et al., 1994).

The X-ray crystal structure of Bcl-X_L (PDB code: 1MAZ) demonstrates that Bcl-X_L is composed of two central hydrophobic α-helices (α5 and α6) and five surrounding amphipathic α-helices (Figure 2.1A) (Muchmore et al., 1996). A 60-residue loop connecting α1 and α2 is too flexible to be seen in the crystal structure. Similar to other anti-apoptotic Bcl-2 proteins, Bcl-X_L also contain a hydrophobic groove on the surface (Figure 2.1B) and is occupied by an α-helix upon interacting with other BH3D-containing proteins (Figure 2.1C & D) (PDB code: 2P1L) (Oberstein et al., 2007).As shown in Figure 2.1C, the most significant changes in the Bcl-X_L structure upon binding to the Beclin 1 BH3D are observed in α2 to α4 helices and the loops connecting them. Upon binding, the 3 residues in the loop connecting α2 and α3 helices become helical to add about one extra helix turn to the α2 helix. Meanwhile, the α3 helix changes to loop and moved away from the hydrophobic groove. In addition, α4 helix of Bcl-X_L moves toward the hydrophobic groove and the 3 residues in the loop connecting α3 and α4 helices becomes helical to add about one extra helix turn to the α4 helix.

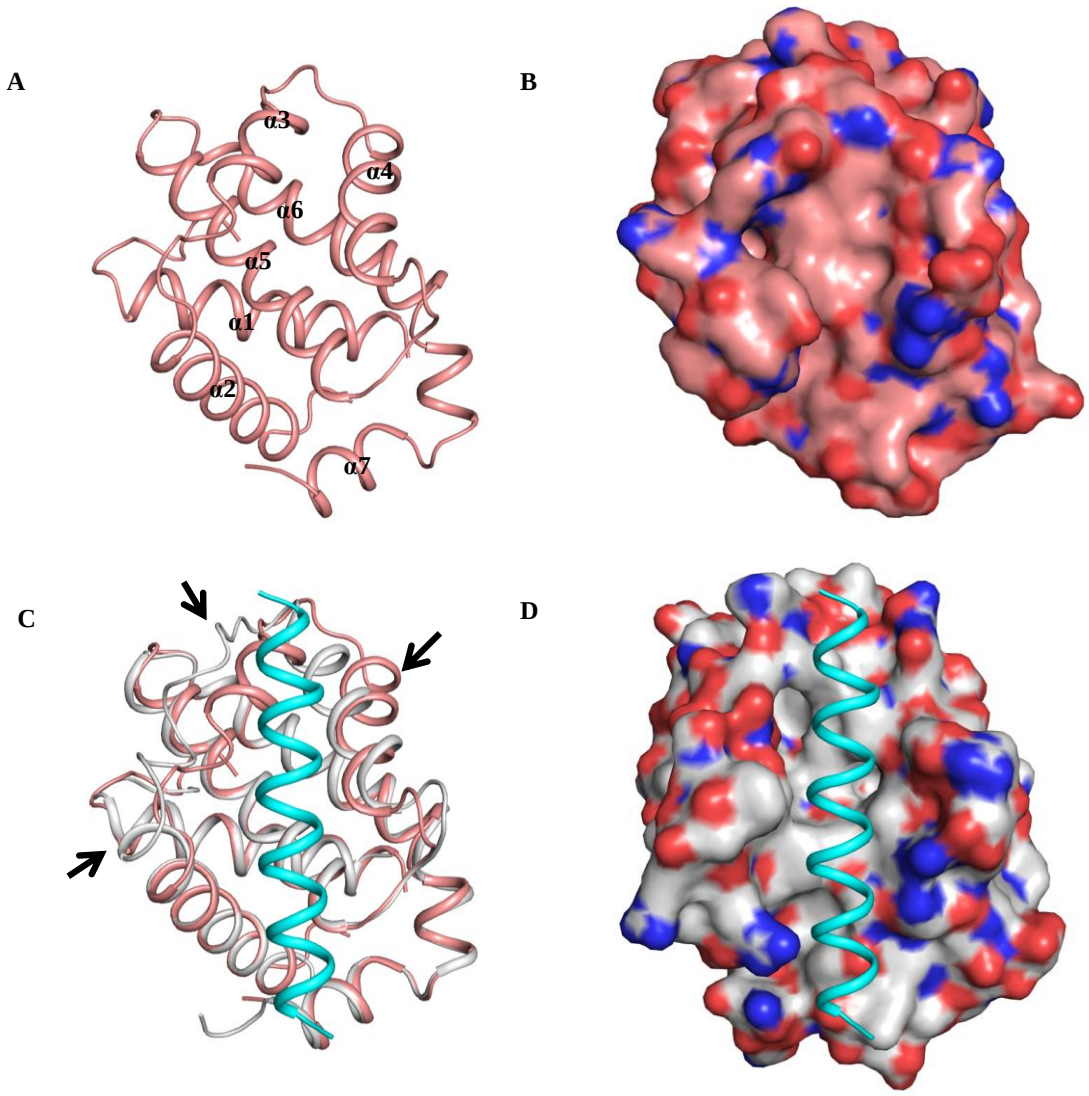

Figure 2.1: X-ray crystal structure of unbound Bcl-X_L and Bcl-X_L in complex with Beclin 1 BH3D. (A) Bcl-X_L shown in ribbon presentation. Each α-helix is labeled. (B) Bcl-X_L shown in surface presentation. Atoms are colored by type: oxygen red, nitrogen blue, sulfur yellow and carbon pink. (C) Superimposition of unbound Bcl-X_L with Bcl-X_L:Beclin 1 BH3D complex. Each structure is colored as such: Bcl-X_L (pink), Bcl-X_L (grey):Beclin 1 BH3D (cyan). Black arrows pointed to the regions of Bcl-X_L change the most between the unbound and bound Bcl-X_L structures. (D) Bcl-X_L:Beclin 1 BH3D complex. Bcl-X_L is shown in surface presentation and Beclin 1 BH3D is shown in ribbon presentation.

As noted, anti-apoptotic Bcl-2 proteins inhibit apoptosis by binding to the BH3D of BAX and/or BAK. Interestingly, in healthy cells, BAK is only associated with Bcl-X_L and Mcl-1 but not Bcl-2, Bcl-W, or A1. When BH3-only proteins that can bind to both Mcl-1 and Bcl-X_L, Noxa

for example, are activated and bind to Mcl-1 and Bcl-X_L, BAK is released and induces cell death (Willis et al., 2005). Bcl-X_L can also bind to BAX. The binding of Bcl-X_L to BAX constantly re-translocates mitochondrial BAX to cytosol, leading to the inhibition of BAX- mediated apoptosis (Edlich et al., 2011).

The anti-apoptotic Bcl-X_L can also be converted to a pro-apoptotic molecule by caspase-mediated cleavage. Bcl-X_L is cleaved after residue D61 in the loop region that connects α1 and α2 helices, during cell death induced by IL-3 withdrawal or virus infection. The resulting C-terminal fragment lacking the BH4D can potently induce cell death (Clem et al., 1998).

Bcl-X_L can also be phosphorylated at S62, which is also located in the loop connecting the α1 and α2 helices. This JNK-mediated phosphorylation of Bcl-X_L can be induced by microtubule inhibitors, such as taxol, 2-methoxyestradiol, and vinblastine (Basu and Haldar, 2003, Upreti et al., 2008). Co-immunoprecipitation (Co-IP) results indicate that unlike WT Bcl-X_L which can bind to BAX, phosphorylated Bcl-X_L can no longer bind to BAX. Furthermore, phosphor-mimic Bcl-X_L fails to protect cells against BAX-mediated apoptosis (Upreti et al., 2008). Thus, phosphorylation of Bcl-X_L at S62 abrogated its binding to BAX, leading to the inhibition of its anti-apoptotic function.

2.1.2.2. M11

M11 is an anti-apoptotic Bcl-2 protein encoded by murine γHV68 (Virgin et al., 1997). M11 has been shown to inhibit Fas- and TNF-induced apoptosis (Wang et al., 1999) and function in contributing to viral latency amplification in infected lymphoid tissue (de Lima et al., 2005). Although M11 and cellular anti-apoptotic Bcl-2 proteins share low sequence identity, the 171-residue-long M11 contains all four BH domains, as well as the TM (Loh et al., 2005).

The Nuclear Magnetic Resonance (NMR) structure of M11 (PDB code: 2ABO) (Loh et al., 2005) that includes all four BH domains, demonstrates that M11 has a three-dimensional structure similar to cellular anti-apoptotic Bcl-2 proteins (Figure 2.2 A & B). It also contains two central α-helices α5 and α6, surrounded by five amphipathic α-helices. Different from Bcl-X_L, the loop region connecting α1 and α2 comprises only 12 residues, which is much shorter than the 60-residue-long loop in Bcl-X_L (Figure 2.2A). Similar to the cellular anti-apoptotic Bcl-2 proteins, M11 contains a hydrophobic groove on its surface and is responsible for binding to BH3Ds of other BH3D-containing proteins, Beclin 1 for example (Figure 2.2 B, C & D) (Sinha et al., 2008). The superimposition of M11 and the M11:Beclin 1 BH3D complex indicates that the α3 helix moves away from hydrophobic groove to open the hydrophobic groove for binding to the Beclin 1 BH3D. Most of the residues in the α3 helix change into loop. The first 2 residues combined with the residues of the loop connecting α2 andα3 become helical and add an extra helix turn to the α2 helix.

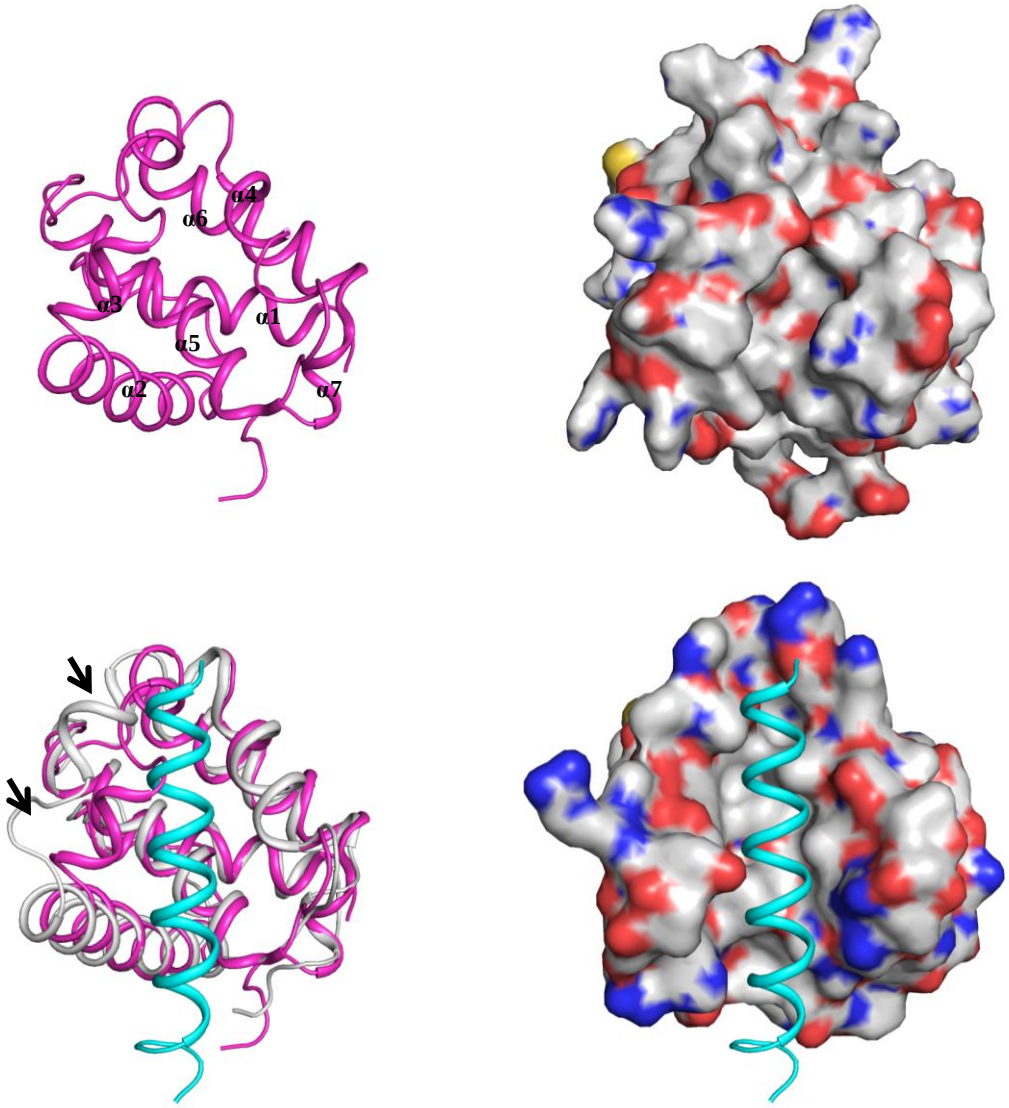

Figure 2.2: NMR structure of unbound M11 and X-ray crystal structure of M11 in complex with Beclin 1 BH3D. (A) Ligand-free M11is shown in magenta ribbon. Each α-helix is labeled. (B) M11 is shown in surface presentation with atoms colored by type: oxygen red, nitrogen blue, sulfur yellow and carbon grey. (C) Superimposition of unbound M11with M11:Beclin 1 BH3D complex. Each structure is colored as such: ligand-free M11 (magenta), M11(grey):Beclin 1 BH3D (cyan). Black arrows pointed to the regions of M11 that change the most between the unbound and bound M11 structures. (D) M11:Beclin 1 BH3D complex. M11 is shown in surface presentation and Beclin 1 BH3D is shown in ribbon presentation.

Similar to cellular Bcl-2 proteins, M11 has also been shown to bind to both BAK and BAX. ITC measurements show that M11 binds to BH3D of BAX and BAK with 0.69 μM and

0.08 μM affinity, respectively (Ku et al., 2008a). M11 has been shown to inhibit BAX-mediated cell death as effectively as Bcl-2 (Loh et al., 2005). M11 also binds to most of the BH3Ds of BH3-only Bcl-2 proteins, including BIM, NOXA, BID, BMF, PUMA, and HRK, with a binding affinity stronger than 1 μM by ITC measurements (Ku et al., 2008a).

In a study that aims to determine if viral Bcl-2 proteins can be converted into pro-apoptotic proteins, similar to the cellular anti-apoptotic Bcl-2 proteins, five herpesvirus Bcl-2 homologs, including M11, BHRF1, KSHV Bcl-2, HVS Bcl-2 and BHV4 Bcl-2, were tested for their susceptibility to caspases. Surprisingly, only M11 can be cleaved by caspase. However, unlike the caspase cleavage products of cellular Bcl-2 proteins, which become pro-apoptotic proteins, the cleavage product of M11 does not show any pro-apoptotic function (Bellows et al., 2000). Consistently, no phosphorylation of M11 is reported so far. Therefore, herpesvirus Bcl-2 homologs may escape negative regulation by caspase cleavage or phosphorylation and retain their anti-apoptotic functions to maintain the latency infection in host cells.

2.1.3. Beclin 1 BH3D

Beclin 1 is the key regulator of autophagy and also provides multiple points of crosstalk between autophagy and apoptosis. The 450-amino acid protein Beclin 1 contains an intrinsically disordered region (IDR, residues 1-140) (Mei et al., 2014, Lee et al., 2016), a BH3D (residues 105-130) (Oberstein et al., 2007, Sinha et al., 2008, Sinha and Levine, 2008, Ku et al., 2008a), a flexible helical domain (FHD, residues 141-171) (Mei et al., 2016a), a CCD (residues 175-265) (Li et al., 2012), and a β-α repeat, autophagy-specific domain (BARAD, residues 248-450) (Huang et al., 2012, Noda et al., 2012).

Beclin 1 was initially discovered as a Bcl-2 interacting protein (Liang et al., 1998). In the same study, yeast two-hybrid assays were used to show that residues 88 to 150 of Beclin 1 are

sufficient for the interaction with anti-apoptotic Bcl-2 proteins Bcl-2 and Bcl-X_L. Deletion of these residues from Beclin 1 significantly weakens its interaction with the two Bcl-2 proteins. Therefore, residues 88 to 150 of Beclin 1 were named the Bcl-2-binding domain (Bcl-2BD). Subsequently, sequence alignments of the Beclin 1 Bcl-2BD with multiple BH3Ds from known Bcl-2 family members identified a conserved BH3D in Beclin 1 (residues 105-130) within the Bcl-2BD (Oberstein et al., 2007, Feng et al., 2007).A typical BH3D is defined as a four-turn, amphipatic α-helix with a sequence motif of: Hy-X-X-X-Hy-K/R-X-X-Sm-D/E-X-Hy (Hy: hydrophobic residues; Sm: small residues, typically glycine) (Sinha and Levine, 2008). The corresponding conserved residues in Beclin 1 BH3D are: L112, L116, K117, G120, D121 and F123.

Beclin 1 binds selectively to Bcl-2 and Bcl-X_L, while it binds only weakly or not at all to other cellular Bcl-2 paralogs, including Mcl-1, A1 and Bcl-W (Pattingre et al., 2005a, Liang et al., 1998, Erlich et al., 2007). The Beclin 1 BH3D is the primary determinant of binding to cellular and γHV Bcl-2 homologs (Ku et al., 2008a, Sinha et al., 2008, Erlich et al., 2007, Feng et al., 2007, Oberstein et al., 2007, Sinha and Levine, 2008), binding to different Bcl-2 homologs with affinities in the micromolar range, for example with a K_d of ~ 54 μM to KSHV Bcl-2 (Sinha et al., 2008) and ~9 μM to Bcl-2 (Mei et al., 2014).

Ever since the identification of the Beclin 1 BH3D, many independent studies have been carried out to determine its structure both, when bound to Bcl-2 proteins, and independent of binding (Feng et al., 2007, Oberstein et al., 2007, Ku et al., 2008a, Sinha et al., 2008, Mei et al., 2014). Half of the BH3D (residues 105-115) was predicted to be an IDR while the other half (residues 116–128) was predicted to be an Anchor region (Mei et al., 2014). An Anchor region comprises sequences flanking or overlapping IDRs predicted to be stabilized in secondary

structures upon binding to a globular protein partner (Dosztanyi et al., 2009). The whole Beclin 1 BH3D is indeed disordered in an unbound state as supported by both CD and NMR results (Mei et al., 2014).

The binding pattern of Beclin 1 BH3D to anti-apoptotic Bcl-2 proteins is very similar to those of well-known BH3Ds. To date, four atomic structures of Beclin 1 BH3D in complex with anti-apoptotic Bcl-2 proteins are available in the PDB, including two Beclin 1 BH3D:Bcl-X_L structures (one X-ray crystal structure and one NMR structure) (Feng et al., 2007, Oberstein et al., 2007) and two Beclin 1 BH3D:M11 X-ray crystal structures (Ku et al., 2008a, Sinha et al., 2008). Superimposition of structures of Beclin 1 BH3D:M11 (PDB code: 3DVU) (Sinha et al., 2008), Beclin 1 BH3D:Bcl-X_L (PDB code: 2P1l) (Oberstein et al., 2007) indicates that the Beclin 1 BH3D forms an α-helix when bound to a hydrophobic groove on the surface of Bcl-2 proteins (Figure 2.3). The conserved Beclin 1 BH3D hydrophobic residues L112, L116, and F123 are buried and pack against the hydrophobic grooves of Bcl-2 proteins. The conserved G120-D121 pair packs against residues lining the hydrophobic groove of the Bcl-2: G86-R87 of M11 and G138-R139 of Bcl-X_L. This G-R pair is highly conserved amongst anti-apoptotic Bcl-2 proteins. Furthermore, side chains of all the conserved BH3D residues in both complexes point in the same direction.

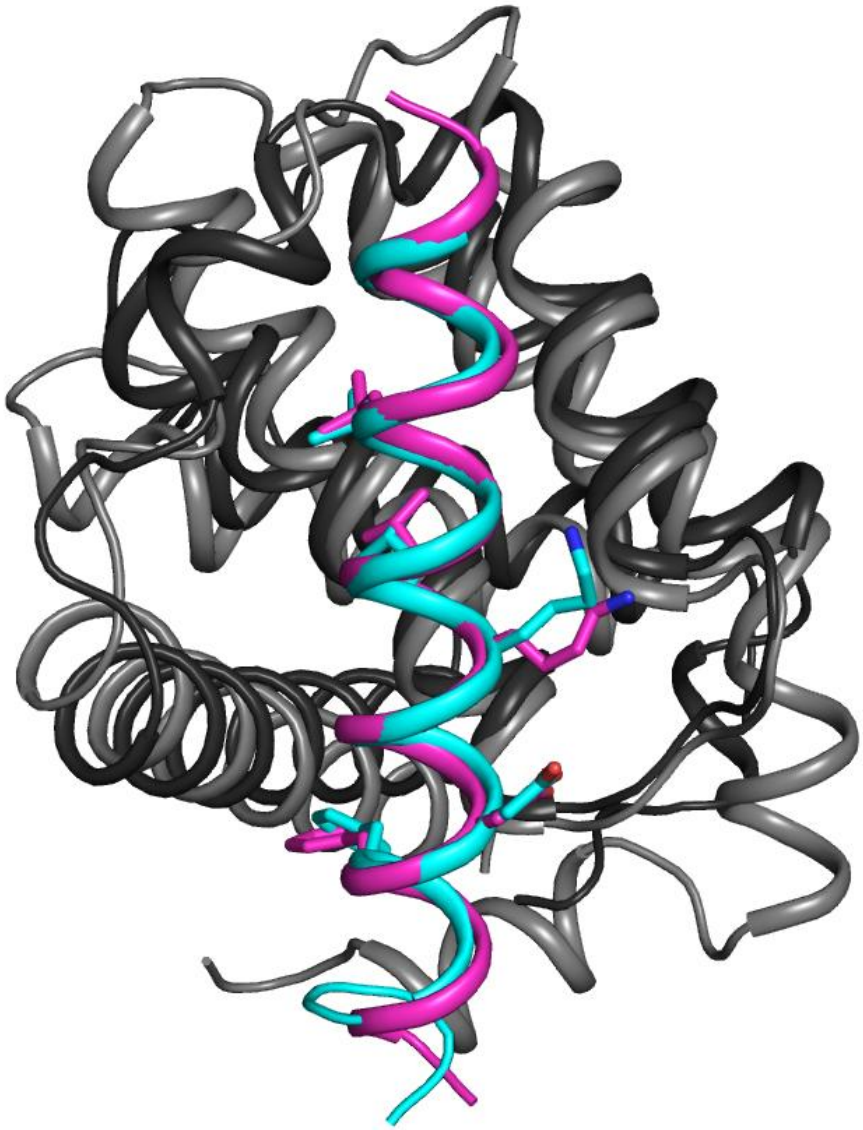

Figure 2.3: Superimposition of structures of Beclin 1 BH3D:M11 and Beclin 1 BH3D:Bcl-X_L Each structure is colored as such: Beclin 1 BH3D (cyan):M11 (dark grey) and Beclin 1 BH3D (magenta): Bcl-X_L (medium grey). Side chains of Beclin 1 BH3D residues L112, L116, K117, D121 and F123 were shown in atomic details.

Various mutagenesis studies, in combination with binding assays, have been done and the results agree well with the structures: Beclin 1 BH3D is both necessary and sufficient for its interaction with anti-apoptotic Bcl-2 proteins and the Anchor contains most of the residues involved in binding to Bcl-2 proteins. ITC experiments showed the Beclin 1 Bcl-2BD binds to

Bcl-X_L with 2.3 uM affinity (Oberstein et al., 2007), while Beclin 1 BH3D binds to Bcl-X_L with ~ 2 uM affinity (Feng et al., 2007, Oberstein et al., 2007). Thus, the additional sequences flanking the BH3D in the Bcl-2BD do not increase binding to Bcl-X_L. The Beclin 1 mutation L116Q, D121A and F123A nearly abrogates the interaction between Beclin 1 and Bcl-X_L as indicated by pull-down assays (Feng et al., 2007). As expected, the conserved residues of the Beclin 1 BH3D are also important for interacting with M11. Co-IP assays demonstrate that L116A and F123A mutations completely abrogate the interaction between Beclin 1 and M11. L112A also reduces the binding of Beclin 1 to M11 (Sinha et al., 2008). Residues lining the hydrophobic groove of M11 also impact its interaction with BH3D-containing proteins. Two M11 double mutants, G86A+R97A and Y60A+L74A, failed to interact with Beclin 1 in Co-IP assays (Sinha et al., 2008). A triple mutation S85A+G86A+R87A of M11 prevented its binding to BAX and BAK in Co-IP assays (Ku, Woo et al. 2008).

As noted, the interactions between Beclin 1 and anti-apoptotic Bcl-2 proteins mediated by Beclin 1 BH3D are important for autophagy regulation. Both cellular and viral anti-apoptotic Bcl-2 proteins inhibit Beclin 1-dependent and starvation-induced autophagy. Mutations either within Bcl-2 proteins or the Beclin 1 BH3D that decrease or abrogate their interactions rescue starvation-induced autophagy (Pattingre et al., 2005a, Sinha et al., 2008). The Bcl-2-mediated inhibition of Beclin 1-dependent autophagy is regulated via two mechanisms: competitive binding of other BH3D-containing proteins or BH3D mimics to anti-apoptotic Bcl-2 proteins; or disruption of Beclin 1:Bcl-2 interaction by phosphorylation.

BAD is a BH3-only protein that is activated by serum withdrawal. The amount of endogenous BAD that co-immunoprecipitates with Bcl-X_L increases within one hour upon starvation, while the amount of endogenous Beclin 1 that co-imminoprecipitates with Bcl-X_L

decreases (Maiuri et al., 2007a). Upon siRNA silencing of endogenous BAD expression, starvation-induced autophagy was decreases accordingly. Similarly, a BH3D mimetic compound ABT737, competitively disruptsthe interaction between Beclin 1 and Bcl-X_L or Bcl-2, releasing Beclin 1 from Bcl-2 protein down-regulation, and stimulates autophagy (Maiuri et al., 2007a).

Upon starvation, Bcl-2 can be phosphorylated by JNK-1 at residues T69, S70 and S87, which are located in a non-structured loop between BH4 and BH1 domain. The phosphorylated Bcl-2 then dissociates from the Beclin 1:Bcl-2 complex.When the non-phosphorylatable Bcl-2 mutant T69A+S70A+S87A was expressed instead of WT Bcl-2, starvation-induced dissociation of Beclin 1:Bcl-2 complex was inhibited, leading to the down-regulation of autophagy (Wei et al., 2008b). T119 within the Beclin 1 BH3D is also phosphorylated by ROCK1 upon starvation.This phosphorylation also promotes the dissociation of the Beclin 1:Bcl-2 complex. Inhibition of ROCK1 activity increases the interaction between Beclin 1 and Bcl-2, resulting in the down-regulation of starvation-induced autophagy (Gurkar et al., 2013). Thus, upon starvation, multiple proteins may phosphorylate both Beclin 1 and Bcl-2 proteins leading to the disruption of their interaction in order to enable autophagy induction.

2.1.4. NOXA BH3D

The BH3D of the BH3-only Bcl-2 protein mouse NOXA (mNOXA) has been shown to bind to M11 with a K_d of 132 nM (Ku et al., 2008a). The BH3D of human NOXA is highly selective for Mcl-1, binding with a K_d of 24 nM. It binds 7.5-fold more weakly to A1, but does not bind detectably to the other cellular Bcl-2 proteins, including Bcl-2, Bcl-$X_L$and Bcl-W (Chen et al., 2005). The human and mouse NOXA BH3Ds share 42% identity and 50% similarity (Chen et al., 2005), with three mNOXA residues L27, G31 and D32, which have previously been shown to be highly conserved amongst other BH3Ds (Sinha and Levine, 2008), also conserved in

human NOXA (Chen et al., 2005). Therefore, the mNOXA BH3 domain may also bind highly selectively to Mcl-1, but not to other cellular Bcl-2 proteins. The mouse NOXA BH3D has been shown to bind to a hydrophobic surface groove of Mcl-1 (Day et al., 2008), but no atomic structural information is available yet for the interactions between M11 and NOXA BH3D.

2.1.5. In this study

The hypothesis behind this study was that despite the similar general mode of binding of the Beclin 1 BH3D and potentially mNOXA BH3D, to viral M11 and cellular Bcl-2 proteins, the BH3D binding grooves of these homologs are lined by different residues, which results in different atomic details of interaction and different thermodynamic contributions from each BH3D residue's interactions, that would lead to differential affinities for mutant BH3D-derived peptides. Further, based on the promiscuity of M11 relative to Bcl-X_L or Mcl-1 for different BH3Ds that has been previously reported (Loh et al., 2005, Sinha et al., 2008, DeBartolo et al., 2012, Huang et al., 2002, Huang et al., 2003, Chen et al., 2005), we expected that a systematic mutagenesis approach would enable us to find a peptide that binds to M11, but does not bind to the cellular Bcl-2 homologs which have a more stringent binding specificity (Sinha et al., 2008).

We used ITC to confirm the binding of mNOXA BH3 domain to M11. Further, Size-Exclusion Chromatography (SEC) was employed to determine if mNOXA and M11 can form a stable complex in solution. However, we were not able to grow crystals of this complex.

We used cellular assays to identify Beclin 1 mutations that selectively abrogate down-regulation of autophagy by Bcl-X_L, but not M11, then used ITC to identify a peptide that binds selectively to M11, but not to Bcl-X_L. Further, we determined the X-ray crystal structure of this selective peptide bound to M11 in order to elucidate the mechanism by which it binds to M11. Lastly, we demonstrate that a cell-permeable version of this selective peptide serves as an M11-

specific inhibitor that abrogates M11-mediated down-regulation of autophagy in cells. These combined results help explain the atomic bases of the differential specificity of M11 and Bcl-X_L, and provide a unique tool to target M11-BH3D interactions *in vivo*. This information is key to the rational design of inhibitors that selectively target M11, which will be valuable in studying its interactions and roles in cell culture and *in vivo*.

2.2. Materials and methods

2.2.1. Bcl-X_L expression construct creation

The double mutant variant of Bcl-X_L (N52D, N66D) was created by two rounds of site-directed mutagenesis using the QuikChange II Site-Directed Mutagenesis Kit (Agilent Technologies). To create the N52D Bcl-X_L, the sense primer S1 and antisense primer A1 were designed to introduce the point mutation during the polymerase chain reaction (PCR) and their sequences were listed in Table 2.1. The reagents used for 50 μL of PCR reaction were as follows: 5 μL of 10 × reaction buffer, 1 μL of 10 mM dNTPs mixture, 2 μL of 10 ng/μL template, 2.5 μL of each 50 ng/μL primers, and 1 μL of 2.5 U/μL *Pfu Ultra* HF DNA polymerase and 37 μL nuclease-free H_2O. The PCR was performed on the GeneAmp PCR System 9700 (Life Technologies) for 12 cycles under the following experimental conditions: initial denaturation at 95 ℃ for 30 sec, denaturation at 95 ℃ for 30 sec, annealing at 55 ℃ for 1 min, extension at 68 ℃ for 6 min, final extension at 68 ℃ for 7 min, and then hold at 4 ℃. 1 μL of DpnI was then added to the reaction product to digest the template DNA at 37 ℃ for 1 hour. 2 μL of the digeation product was transformed into chemically competent Top10 cells. A single colony of the recombinant *Escherichia coli* (*E. coli)* cells was inoculated in 5 mL Luria Bertani (LB) medium supplemented with 100 μg/ml Ampicillin and grown overnight at 37 ℃. The plasmid was isolated using E.Z.N.A. Plasmid Mini Kit I (Omega Bio-tek). The N52D mutation was

confirmed by sequencing at MCLAB. The N66D mutation was created in the same manner and the primers S2 and A2 were used for introducing mutation and their sequences are listed in Table 2.1.

After creation of the double mutant variant of Bcl-X_L, PCR was employed to amplify the cDNA sequence corresponding to Bcl-X_L(residues 1-208, N52D and N66D) lacking the C-terminal transmembrane helix and simultaneously add EcoRI restriction site and NotI resitrction site along with the His_6-tag to the sense and antisense chains, respectively. The sense and antisense primers were named as S3 and A3 and their sequences were listed in Table 2.1. The reagents used for 50 μL of PCR reaction were as follows: 5 μL of 10 × *Taq* DNA polymerase buffer, 1 μL of 10 mM dNTPs mixture, 2.5μL of 20 ng/μL template, 5 μL of each 5 μM primers, and 0.5 μL of 5 U/μL *Taq* DNA polymerase and 31 μL nuclease-free H_2O. The PCR was performed on the GeneAmp PCR System 9700 (Life Technologies) for 35 cycles under the following experimental conditions: initial denaturation at 94 ℃ for 3 min, denaturation at 94 ℃ for 1 min, annealing at 65 ℃ for 1 min, extension at 72 ℃ for 1 min, final extension at 72 ℃ for 5 min, and then hold at 4 ℃. The PCR amplified DNA was purified using E.Z.N.A.Gel Extraction Kits (Omega Bio-tek).

To create the overhang, the purified PCR product and *p*ET 29b vector were subjected to restriction digestion. The reagents used for the 20 μL restriction digestion reaction were: 2 μg of the PCR product or *p*ET 29b vector, 2μL of 10 × Bovine serum albumin (BSA), 2 μL of 10 × NEBuffer 3, 1 μL of EcoRI (20 U/μL), 1 μL of NotI (10 U/μL), and nuclease-free H_2O to bring the volume to 20 μL. The reaction mixture was incubated at 37 ℃ for 2 hour followed by heat inactivation at 60 ℃ for 20 min. The digestion products were gel purified using E.Z.N.A. Gel Extraction Kits (Omega Bio-tek).

For the annealing reaction, vector was mixed with PCR product with a molar ratio of 1:6 and the reagents used for a 20 μL ligation reaction were: 2 μL of 10 × T4 DNA Ligase reaction buffer, 1 μL of T4 DNA Ligase (400 U/μL), and nuclease-free H_2O to bring the volume to 20 μL. The reaction mixture was incubated at 16 ℃ for overnight. The reaction mixture was used to transform chemically competent Top10 cells. A single colony of the recombinant *E. coli* cells was inoculated in 5 mL LB medium supplemented with 50 μg/ml Kanamycin and grown overnight at 37 ℃. The recombinant plasmid was isolated using E.Z.N.A. Plasmid Mini Kit I (Omega Bio-tek). The cloning of the coding regions of the Bcl-X_L (residues 1-208, N52D and N66D) with a C-terminal His_6-tag in the *p*ET 29b vector was confirmed by sequencing at MCLAB.

Another set of site-directed mutagenesis was used to remove the S-tag and thrombin site originally present in the *p*ET 29b vector in the same manner as above so that the final construct only encodes Bcl-X_L (residues 1-208, N52D and N66D) with a C-terminal His_6-tag.

Table 2.1: Summary of primers used for Bcl-X_L expression construct creation.

Primers	**5' to 3'**
S1	CCCCAGTGCCATCGATGGCAACCCATCCTG
A1	CAGGATGGGTTGCCATCGATGGCACTGGGG
S2	CAGCCCCGCGGTGGATGGAGCCACTGCGCA
A2	TGCGCAGTGGCTCCATCCACCGCGGGGCTG
S3	GCG GCGGAATTCATGTCTCAGAGCAACCGGGAGCTGGTGGTTGAC
A3	GCGGCGGCGGCCGCTTTAGTGGTGGTGGTGGTGGTGTTCCTGGCCCTTT CGGCTCTCGGC
S4	GAAGGAGATATACATATGTCTCAGAGCAACCGGGAGC
A4	GCTCCCGGTTGCTCTGAGACATATGTATATCTCCTTC

2.2.2. Protein expression and purification

For the overexpression of His_6-tagged Bcl-X_L (residues 1−208, N52D, N66D), *E. coli* L21(DE3)*p*LysS chemically competent cells were transformed with the *p*ET 29b-Bcl-X_L (residues 1−208, N52D, N66D)-His_6 plasmid. The transformed cells were grown in agar plate supplemented with 50 µg/µL Kanamycin and 35 µg/µL Chloramphenicol. A signal colony was picked and grown in 5 ml LB media supplemented with 50 µg/µL Kanamycin and 35 µg/µL Chloramphenicol at 37 ℃ for overnight. The next day, the 5 ml overnight culture was used to inoculate 200 ml of LB supplemented with 50 µg/µL Kanamycin and 35 µg/µL Chloramphenicol, and grown at 37 ℃ for 4 hours to make the secondary culture. Each 30 ml secondary culture was then used to inoculate 1 L LB media supplemented with 50 µg/µL Kanamycin and 35 µg/µL Chloramphenicol and further grown at 37 ℃ until optical density of 0.6-0.8 was reached at 600 nm. At this point, the overexpression of Bcl-X_L was induced with 0.5 mM Isopropyl β-D-1-thiogalactopyranoside (IPTG). The cells were further grown at 20 ℃ with shaker speed of 220 rpm for 18 hours.

The cells were harvested by centrifugation at 4000 rpm for 20 minutes at 4 ℃ and stored at -80 ℃ until usage. For Bcl-X_L purification, all chromatography was performed using AKTA purifier (GE healthcare Life Sciences). The pellet of 6 L culture was suspended in 200 ml lysis buffer comprising 25 mM 4-(2-hydroxyethyl)-1-piperazineethanesulfonic acid (HEPES), pH 7.5, 100 mM NaCl, 25 mM Imidazole, 2 mM 2-mercaptoethanol and 3 tablets of cOmplete protease inhibitor cocktail (Roche). The cells were lysed by sonication and the crude extract was centrifuged at 20000 g for 40 min at 4 ℃ to remove the cellular debris. The resulting supernatant was loaded onto two tandem 5 mL His-Trap HP columns (GE Healthcare). The column was washed with 15 column volumes of wash buffer comprising 25 mM HEPES, pH 7.5, 100 mM

NaCl, 25 mM Imidazole, 2 mM 2-mercaptoethanol, to remove contaminating protein weakly bound to the column. The remaining protein bound to the column was eluted with 10 column volume of elution buffer comprising 25 mM HEPES, pH 7.5, 100 mM NaCl, 250 mM Imidazole, 2 mM 2-mercaptoethanol. The purity of Bcl-X_L eluted from HisTrap columns in different fractions were evaluated using sodium dodecyl sulfate polyacrylamide gel electrophoresis (SDS-PAGE). All fractions containing Bcl-X_L were collected and further purified by Ion-Exchange Chromatography (IEX) using a Mono Q HR 10/10 column (GE Healthcare). The sample for IEX was prepared by diluting 80 mg of proteins with non-salt buffer comprising of 25 mM HEPES, pH 7.5, 2 mM 2-mercaptoethanol, to lower the NaCl concentration in the final protein solution to than 50 mM. The diluted protein was then load onto Mono Q HR 10/10 column and washed with 50 ml low-salt buffer comprising 25 mM HEPES, pH 7.5, 50 mM NaCl, 2 mM 2-mercaptoethanol. A 100 ml linear gradient ranging from 50-500 mM NaCl in 25 mM HEPES, pH 7.5 and 2 mM 2-mercaptoethanol, was used to elute Bcl-X_L. The purity of Bcl-X_L eluted from MonoQ columns in different fractions were evaluated using SDS-PAGE. Fractions contains only Bcl-X_L were pooled together and finally purified with SEC using a preparative 16/600 Superdex 200 column (GE Healthcare). The column was pre-equilibrated with the SEC buffer comprising 25 mM HEPES, pH 7.5, 100 mM NaCl, 2 mM 2-mercaptoethanol. 4.5 ml of 9.8 mg/ml protein was loaded onto the 16/600 Superdex 200 column and eluted with SEC buffer at 1 ml/min flow rate. The purity of Bcl-X_L eluted from SEC was evaluated using SDS-PAGE. Fractions from the single peak corresponding to Bcl-X_L were pooled together, concentrated to 5 mg/ml, and stored in 200 ul aliquots in -80 ℃.

M11 (residues 1−136)-His_6 was overexpressed in *E. coli* BL21(DE3)*p*LysS cells in the same manner as Bcl-X_L. For M11 purification, all chromatography were also performed using

AKTA purifier (GE healthcare Life Sciences). Soluble protein in the cell lysate was purified to homogeneity by Immobilized Metal Affinity Chromatography (IMAC) using two tandem 5 mL His-Trap HP columns (GE Healthcare) followed by SEC using a preparative 16/600 Superdex 200 column (GE Healthcare) in the same manner as Bcl-X_L, except different buffer composition was used for M11. The IMAC wash buffer was comprised of 25 mM HEPES, pH 7.5, 250 mM NaCl, 25 mM Imidazole, 2 mM 2-mercaptoethanol, while the IMAC elution buffer was comprised of 25 mM HEPES, pH 7.5, 250 mM NaCl, 250 mM Imidazole, 2 mM 2-mercaptoethanol. The SEC buffer is comprised of 50 mM HEPES, pH 7.5, 250 mM NaCl, 2mM 2-mercaptoethanol. After SEC, fractions from the single peak corresponding to M11 were pooled together, concentrated to 10 mg/ml, and stored in 200 ul aliquots in -80 ℃.

2.2.3. Peptide synthesis

mNOXA BH3D and various Beclin 1 BH3D-derived peptides were chemically synthesized and HPLC purified to > 95% purity, with peptide purity confirmed by electrospray mass spectrometry (RSSynthesis/Protein Chemistry Technology Core at the University of Texas Southwestern Medical Center, Dallas). The sequences of these peptides are summarized in Table 2.2.

Table 2.2: Summary of amino acid sequences of various BH3D-derived peptides.

Peptide	**N- to C-terminus**
mNOXA	RAELPPEFAAQLRKIGDKVYCTWSAP
Beclin 1 BH3D:	
WT	GSGTMENLSRRLKVTGDLFDIMSGQT
L112A	GSGTMENASRRLKVTGDLFDIMSGQT
L116A	GSGTMENLSRRAKVTGDLFDIMSGQT
K117A	GSGTMENLSRRLAVTGDLFDIMSGQT
G120E	GSGTMENLSRRLKVTEDLFDIMSGQT
D121A	GSGTMENLSRRLKVTGALFDIMSGQT
F123A	GSGTMENLSRRLKVTGDLADIMSGQT
G120E+D121A (DS peptide)	GSGTMENLSRRLKVTEALFDIMSGQT

2.2.4. ITC

ITC was performed using a Low Volume Nano ITC (TA Instruments). For all ITC experiments, samples were loaded into separate dialysis cassettes, and co-dialyzed into ITC buffer. The ITC buffer for all experiments was comprised of 25 mM HEPES, pH 7.5, 100 mM NaCl and 2 mM β-mercaptoethanol. ITC was performed at 25 °C with 25 injections of 2 μL each. Data were analyzed using NanoAnalyze Software (TA Instruments) with an independent model. The poor solubility of the D121A peptide in aqueous buffers necessitated a different solubilization and data analysis protocol for ITC.The D121A peptide was mixed into ITC buffer to a concentration of 1 mM and rocked at room temperature overnight. Despite this, a significant fraction of the peptide remained insoluble. This insoluble fraction was pelleted by centrifugation at 13,000 × g for 10 min. The supernatant was collected and co-dialyzed with M11 or Bcl-X_L, as described above and then used for ITC. Stoichiometry was forced to 1 during data analysis, and the concentration of the D121A peptidewas estimated from the fit.

2.2.5. Crystallization

The M11+double-substituted (DS) peptide complex was crystallized at 20 ℃ by hanging-drop vapor diffusion from a 1:1 mixture of protein stock (5 mg/ml complex in 20 mM HEPES, pH 7.5, 100 mM NaCl, 1 mM Tris(2-carboxyethyl)phosphine (TCEP) and well solution (2.5 M $(NH_4)_2SO_4$ and 8% v/v 2-propanol). Plate-shaped crystals were harvested and cryoprotected in a cryosolution consisting of 2.5 M $(NH_4)_2SO_4$ and 25% v/v glycerol, and then immediately flash-frozen in liquid N_2.

2.2.6. Data collection, structure solution and refinement

Diffraction intensities from these crystals were recorded at 100 K using 1 sec exposures over 0.5 ℃crystal rotation per image, on a 4 × 4 tiled MARmosaic CCD detector (Rayonix) at a crystal-to-detector distance of 250 mm at beamline 23ID-D of GMCA@APS, ANL, Chicago. The data used to solve the structure were collected at an X-ray wavelength of 0.97934 Å in a 360 °sweep from a single crystal. Data were processed using HKL2000 (Otwinowski and Minor, 1997). Data statistics are summarized in Table 2.4.

Crystals belonged to the space group C2 with unit cell parameters of a = 70.6 Å, b = 140.8 Å, c = 54.0 Å and β = 127.8 °. The crystals contained two copies of the M11+DS peptide complex per asymmetric unit. The positions and orientations of the two M11 (1-136) molecules, monomer A and B, were determined by MR using HKL3000/MOLREP (Kissinger et al., 1999) and a search model extracted from PDB code: 3DVU, consisting of a single M11 monomer with flexible loop residues 52-73 removed. A helix corresponding to the Beclin 1 BH3 domain (from PDB code: 3DVU, chain C), with D121 mutated to Ala, was manually placed into appropriate density next to monomer A using the program Coot (Emsley et al., 2010). A Glu side chain was built into clear electron density at position 120 after the first cycle of refinement. This defined

the structure of the DS peptide. The NCS operator required to superimpose M11 monomer A onto B was used to place a second copy of the DS peptide into appropriate density next to monomer B. The model was refined in the program Refmac5 (Brunger et al., 1998) using imperfect two-fold NCS restraints (Table 2.5).The final model is deposited in PDB with accession code 4MI8. Bcl-2–peptide interactions in different structures were analyzed using PISA (Krissinel and Henrick, 2007).

2.2.7. Autophagy assay

Quantification of fluorescent autophagosomes in MCF7 cells co-transfected with GFP-LC3 (1.6 μg), Beclin 1 (1.2 μg), and either Bcl-X_L (1.2 μg) or M11 (1.2 μg) expression plasmids (4μg total plasmid) was performed using an inverted Axio Observer (Zeiss). Cells were cultured in Dulbecco's Modified Eagle Medium (DMEM) with 10% fetal calf serum (growth medium) in 8-well slides (Millipore) and transfected at 80% confluency with Lipofectamine (Invitrogen). After transfection, cells were either starved overnight in Earle's balanced salt solution (EBSS, starvation medium), or grown in nutrient-rich media with the addition of 2 ×EAA (essential amino acids) and 2 ×NEAA (nonessential amino acids). The number of GFP-LC3 puncta per GFP-LC3 positive cell was assessed by counting a minimum of 50 cells via Image ProPlus for duplicate samples per condition in three independent experiments. The significance of alterations in autophagy levels were determined by a two-tailed, heteroscedastic student's t-test, wherein $p \leq 0.05$ is considered significant. The effect of a potential inhibitory peptide was investigated by comparing autophagy levels in the absence or presence of 30 μM control or inhibitory peptides. The author would like to thank Ms.Yang Mei in the Sinha Lab, NDSU, for performing all the autophagy assays in this study.

2.2.8. Western blot

Expression levels of Flag-tagged Beclin 1, Bcl-X_L and M11 in MCF7 cells were verified by western blot analysis using commercial mouse monoclonal anti-Flag M2-peroxidase antibody (Sigma). As a loading control, the levels of Actin in MCF7 cell lysates were detected with mouse anti-Actin (Chemicon). The author would like to thank Ms.Yang Mei in the Sinha Lab, NDSU, for performing all the western blots in this study.

2.3. Results

2.3.1. Expression and purification results of M11 and Bcl-X_L

In order to obtain enough pure and homogeneous M11 and Bcl-X_L protein for the usage of various binding assays and crystallography experiments in this study, we expressed and purified M11 and Bcl-X_L in the hundred-milligram scale. M11 (residues 1-136) was expressed in *E. coli* BL21(DE3)*p*LysS cells, and soluble protein in the cell lysate was purified to homogeneity by IMAC using two tandem 5 mL His-Trap HP columns followed by SEC using a preparative 16/600 Superdex 200 column. The final SEC purification results were shown in Figure 2.4. As indicated by the SDS-PAGE results, the sample loaded onto the SEC contained mostly M11 protein along with other contaminant proteins. The contaminant proteins were eluted off the column earlier than M11 and formed Peak 1 and Peak 2 in the SEC profile (Figure 2.4). Peak 3 contained only M11 as indicated by single bands on the SDS-PAGE gel. The apparent molecular weight of M11 estimated from the elution volume of the Peak 3 from SEC is 8.4kD, which is significantly smaller than the theoretical molecular weight of M11 monomer (16.6 kD) calculated from the amino acid sequence. This indicates that M11 may have a tendency to stick to Superdex column. The fractions corresponding exclusively to the third peak without the overlap of the second peak were pooled together and concentrated to 10 mg/ml and saved in 200

μL aliquots in -80 ℃ for the use of all the ITC and crystallization experiments. The final yield of purified M11 obtained from the one liter of the bacterial culture was 20 mg.

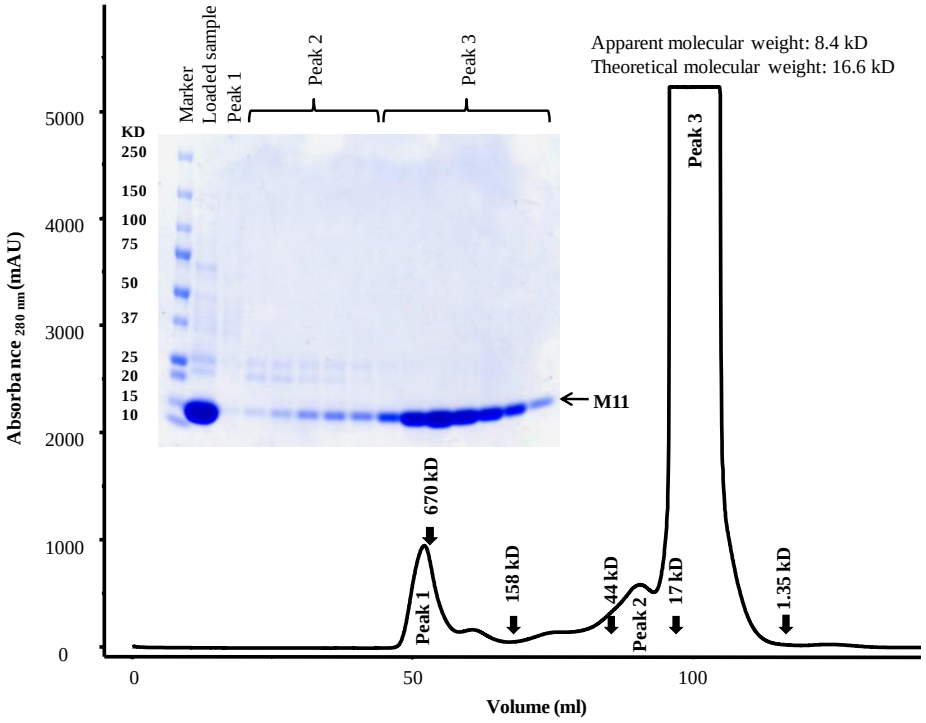

Figure 2.4: Size-exclusion chromatogram and the corresponding SDS-PAGE of M11 (residues 1-136)-His_6.

The Bcl-X_L (residues 1−208, N52D, N66D)-His_6 was also expressed in *E. coli* BL21(DE3)*p*LysS cells, and soluble protein in the cell lysate was purified to homogeneity by IMAC using two tandem 5 mL His-Trap HP columns followed by IEX using a Mono Q HR 10/10 column and SEC using a preparative 16/600 Superdex 200 column. The final SEC purification results are shown in Figure 2.5. The single peak on SEC and single band on SDS-PAGE gels indicate the high purity of Bcl-X_L. The apparent molecular weight of Bcl-X_L calculated based on the elution volume from SEC is 22.3 kD, which is very similar to the theoretical molecular weight of the Bcl-X_L monomer calculated from the amino acid sequence. This indicates that the Bcl-X_L construct used in this study is purified as a well-folded globular

monomer. The final yield of the purified Bcl-X_L obtained from the one liter of the bacterial culture was 9 mg.

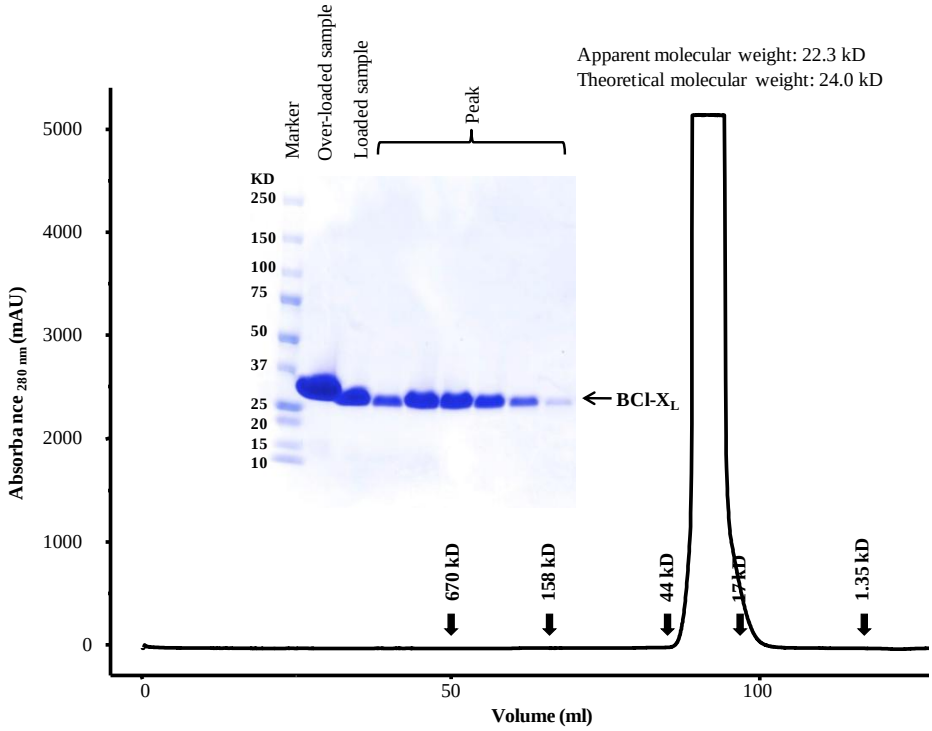

Figure 2.5: Size-exclusion chromatogram and the corresponding SDS-PAGE of Bcl-X_L (residues 1-208, N52D, N66D)-His_6.

2.3.2. Studies of M11 binding to mNOXA BH3D

ITC was employed to study the interactions between M11 and mNOXA BH3D. The peptide corresponding to the mNOXA BH3D was chemically synthesized and its sequence was listed in Table 2.2. As indicated by the ITC results (Figure 2.6), M11 binds to mNOXA BH3D tightly with a dissociation constant (K_d) of 0.80 μM. The binding of M11 to mNOXA is enthalpy-favored but entropy-disfavored, as indicated by the both negative enthalpy and entropy changes. mNOXA BH3D has been shown to bind to Mcl-1 at a stoichiometry of one (Czabotar et al., 2007). Therefore, as it is not possible to accurately determine the precise concentration of the

peptide, the stoichiometry of mNOXA BH3D binding to M11 was forced to one by adjusting the concentration of the mNOXA BH3D peptide during data fitting. .

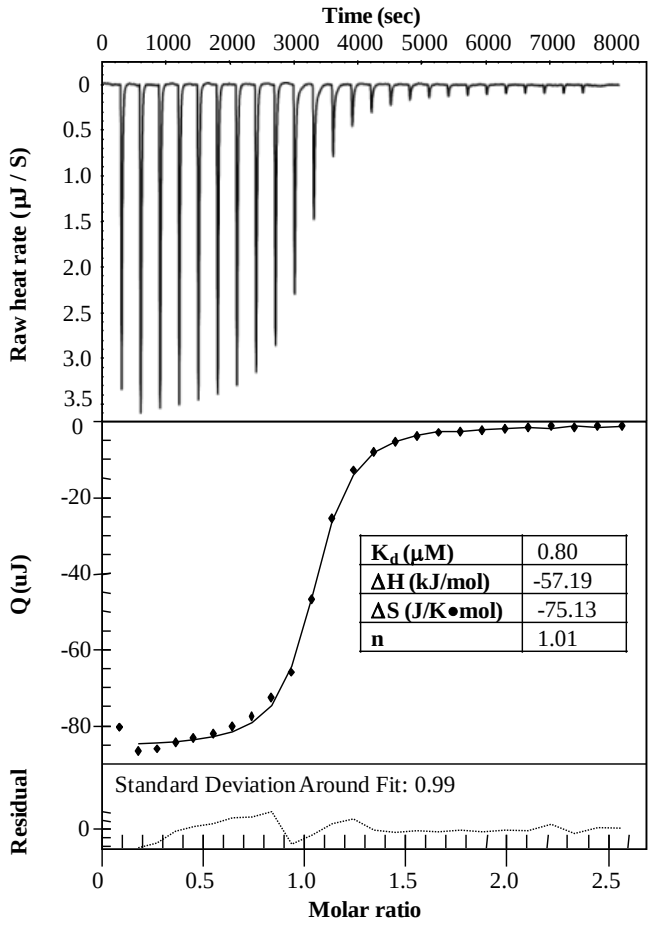

Figure 2.6: ITC titration profile of mNOXA with M11.

Next, we determined whether M11 and mNOXA BH3D peptide form a stable complex in solution using SEC. Purified M11 (11 mg/ml) and mNOXA BH3D peptide were mixed at 1:2 molar ratio and rocked at 4 ℃ for 30 min. The mixture was then applied to a Superdex 200 10/300 GL column in tandem with a Superdex 75 10/300 GL column. Compared to the SEC profile of M11 alone, a single peak with a left-shift corresponding to a increased molecular weight of 3.1 kD, which is very close to the molecular weight of mNOXA BH3D of 2.9 kD, was observed for the SEC profile of M11:mNOXA BH3D mixture, indicating M11 and mNOXA

BH3D can form a stable complex at 1:1 stoichiometry in solution (Figure 2.7). The fractions from the single peak corresponding to M11:mNOXA BH3D complex were pooled and concentrated to 4.3 mg/ml and used for crystallization experiments.

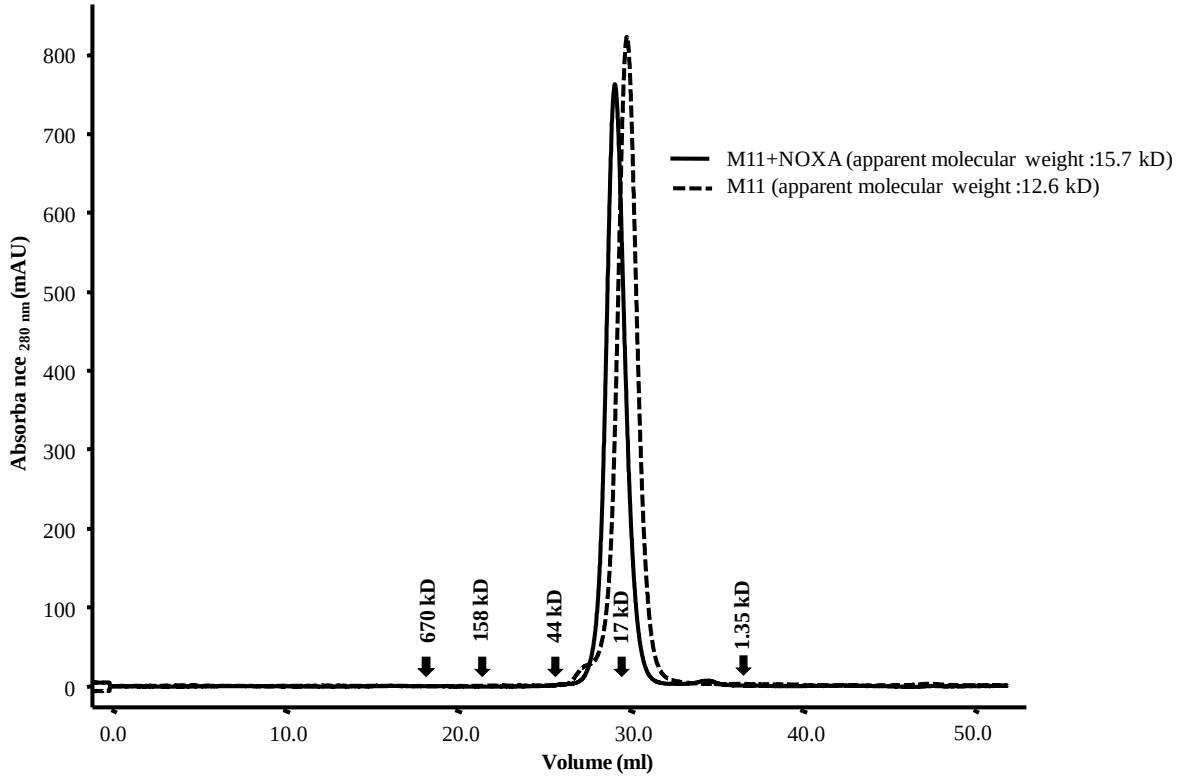

Figure 2.7: Size-exclusion chromatograms of M11 alone and M11:mNOXA BH3D.

In order to elucidate the structural details of the M11:mNOXA BH3D interacttion, we attempted to determine the X-ray crystal structure of the M11:mNOXA BH3D peptide complex. Three different matrix crystallization screens, including Grid Screen Salt HT (Hampton research), Index HT (Hampton research), and Wizard cryo (Emerald Biosystems) crystallization screens were used to identify potential crystallization conditions. Each screen contains 96 different reservoir solution compositions. In addition, three different protein:reservoir ratios, 3:1, 1:1 and 1:3, were screened for each of the reservoir solution compositions at 4 ℃. Thus, a total of

288 different conditions were screened for the crystallization of the M11:mNOXA BH3D peptide complex. However, no crystals were observed in any of the crystallization conditions.

Therefore, we focused subsequent efforts on the M11 and Bcl-X_L mediated down-regulation of autophagy through interaction with Beclin 1.

2.3.3. Selection of Beclin 1 residues important for binding to both M11 and Bcl-X_L

Both Beclin 1 and Bcl-X_L are highly conserved between human and mice. Human and mouse Beclin 1 orthologs are 99% identical and their BH3Ds are 100% identical. Similarly, human and murine Bcl-X_L orthologs are 97% identical, while residues lining the BH3D-binding groove are 100% identical (Figure 2.8). Therefore, there is no difference in the binding of different BH3Ds, particularly the Beclin 1 BH3D, to mouse or human Bcl-$X_L$orthologs.

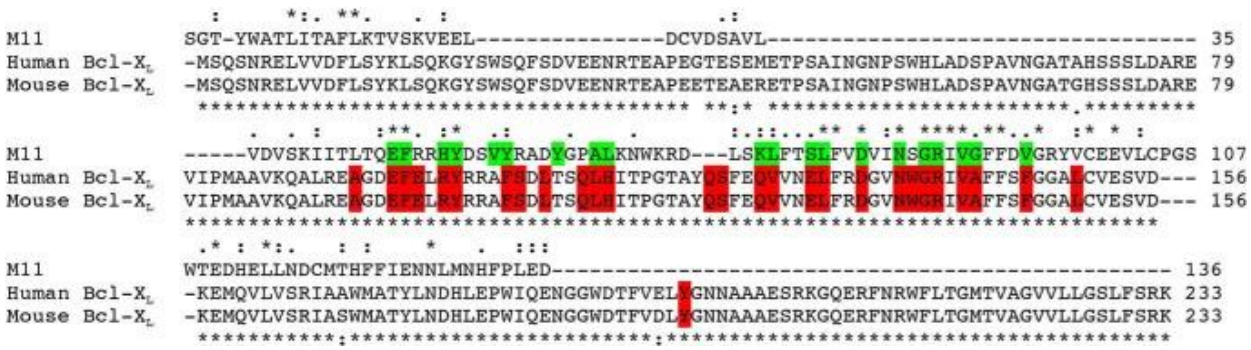

Figure 2.8: Sequence alignment of γHV Bcl-2 and Bcl-X_L homologs.The top sequence is γHV68 M11 while the lower sequences are human and mouse Bcl-X_L as indicated. Numbers after each alignment block indicate the last residue of each sequence in that block. Green or red backgrounds indicate residues lining the BH3D binding groove in either M11 or Bcl-X_L, respectively. Sequence conservation between all three homologs is indicated above the sequence alignment, while that between human and mouse Bcl-X_L is indicated below the alignment. Asterisks denote invariant residues, double dots indicate highly similar residues and single dots indicate similar residues.

In contrast, M11 and Bcl-X_L share only 16.2% sequence identity (Figure 2.8), although they also have similar functions, three-dimensional structures and modes of binding. A comparison of complex structures of the Beclin 1 BH3D bound to M11 (Ku et al., 2008a, Sinha et al., 2008) or Bcl-X_L (Oberstein et al., 2007, Feng et al., 2007) demonstrates that each

interaction involves the same twelve Beclin1 residues (Figure 2.9) and buries 978 $Å^2$ and 1052 $Å^2$ respectively of surface area from each molecule at the interface, as calculated using PISA (Krissinel and Henrick, 2007). Amongst these twelve Beclin 1 BH3 domain residues, the six that have the most extensive interactions (Figure 2.9) are also highly conserved amongst other BH3Ds (Sinha and Levine, 2008). Therefore these were selected for mutagenesis. Of these six residues, L112, L116 and G120 are completely buried; F123 is partially buried; the aliphatic part of the K117 side chain hydrophobically packs against M11 residues D81 and R87, while the amino group makes polar and charged interactions; and G120 and D121 interact with a Gly-Arg pair conserved in most Bcl-2 homologs, including Bcl-X_L and M11 (Ku et al., 2008a, Sinha et al., 2008, Oberstein et al., 2007, Feng et al., 2007, Sinha and Levine, 2008). This Gly-Arg pair, especially the Arg, has been shown to contribute significantly to the interaction of many Bcl-2 homologswith diverse BH3Ds (Loh et al., 2005, Moroy et al., 2009). G120 is packed against the conserved Bcl-2 Gly-Arg main chain, while the BH3 domain D121 makes a bidentate salt bridge with the conserved Bcl-2 Arg. Therefore, L112, L116, K117, G120, D121 and F123 were selected for further investigation in this study.

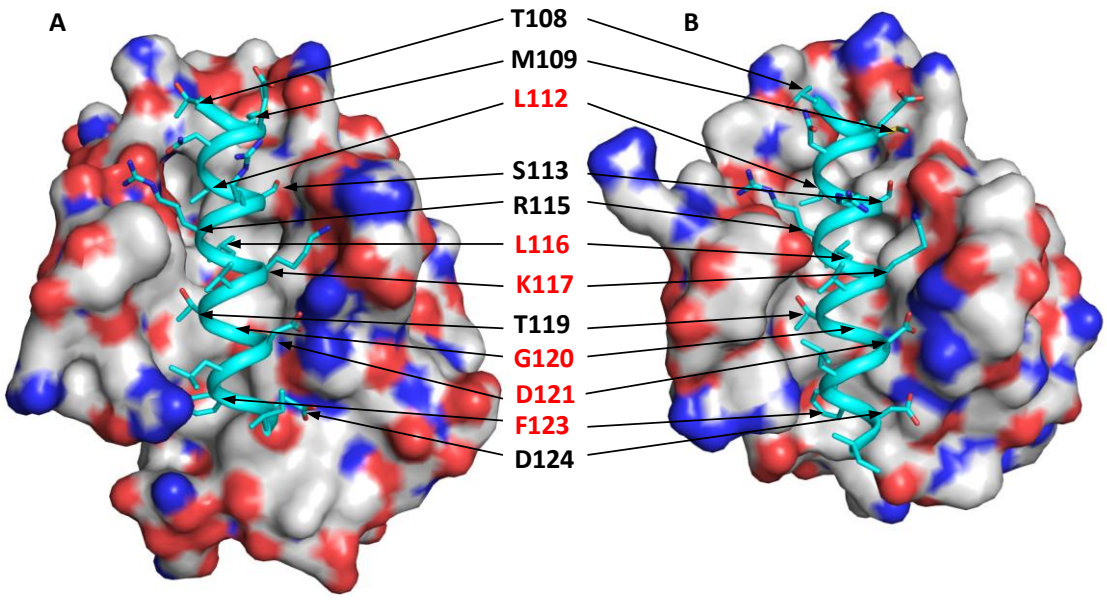

Figure 2.9: Comparison of the WT Beclin 1 BH3 domain bound to (A) Bcl-X_L (PDB code: 2PIL) and (B) M11 (PDB code: 3DVU). Each complex is shown in a superimposable view with Bcl-X_L and M11 shown as molecular surface colored by atom type: oxygen red, nitrogen blue, sulfur yellow and carbon light grey. In each complex structure, the WT BH3D is rendered as cyan ribbon and residues are displayed in stick. The twelve BH3D residues involved in binding to both Bcl-$X_L$and M11 are labeled, with the residues selected for mutagenesis highlighted in red. This and all other molecular figures were prepared with the program Pymol.

The Beclin 1 BH3 domain binds with a very similar, moderate binding affinity of ~1.5 μM to both M11 and Bcl-X_L (Figure 2.10A & B and Table 2.3). Further, for both interactions, the favorable ΔG is due to enthalpic contributions, rather than due to entropic contributions, which are negative in each case (Table 2.3). We showed that the Beclin 1 BH3D is disordered in solution, and that BH3D residues 116-127 appear to serve as an "Anchor" that nucleates concomitant folding and binding of the Beclin 1 BH3 domain to Bcl-2, and includes most of the residues important for binding to Bcl-2 (Mei et al., 2014). Therefore, the negative entropy change likely reflects BH3D desolvation and increased structure upon binding, which proceeds despite the negative entropy change, due to enthalpic compensation.

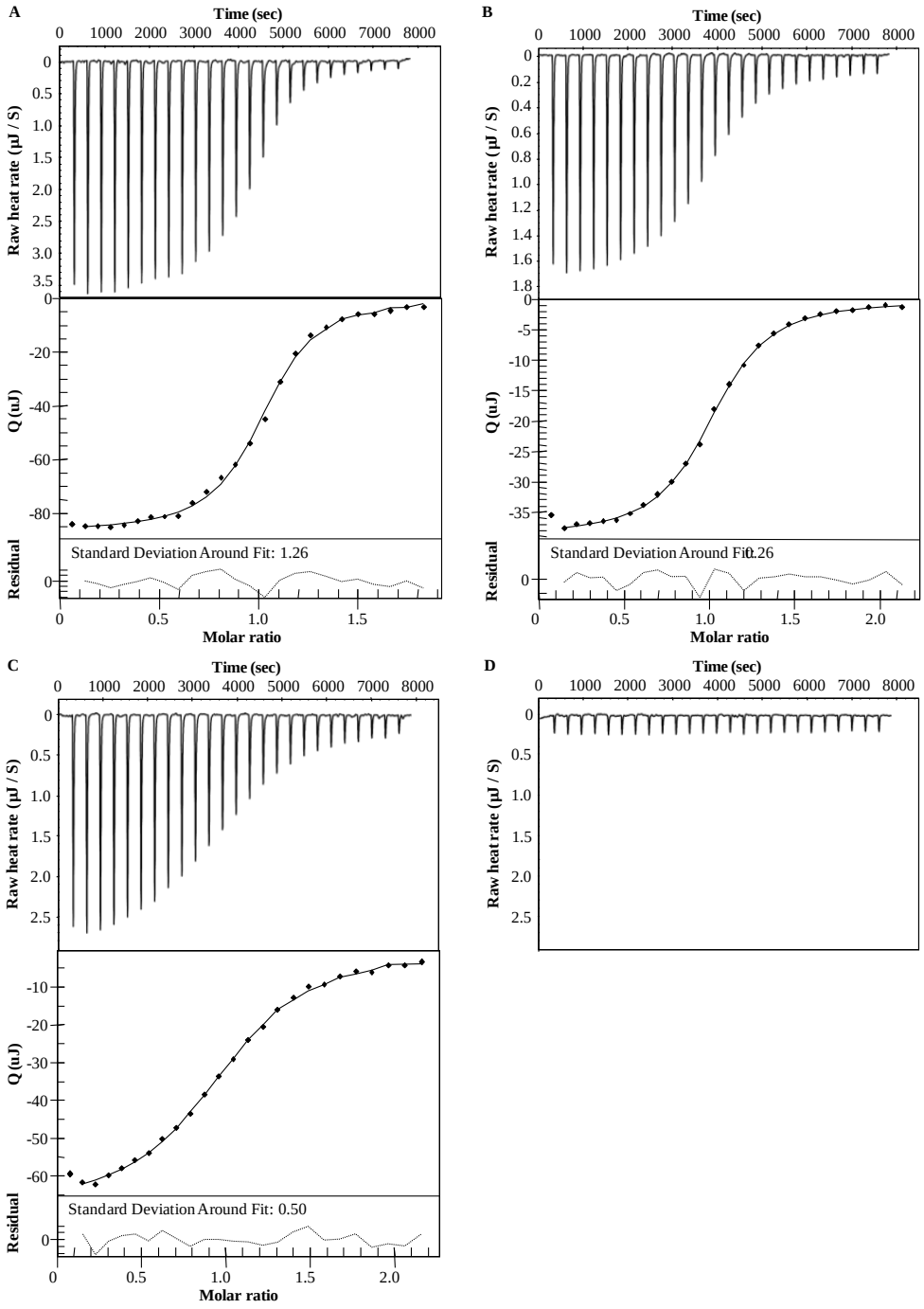

Figure 2.10: ITC titration profiles of WT Beclin 1 BH3D-derived peptide to M11 (A) and Bcl-X_L and G120E+D121A Beclin 1 BH3D-derived peptide to M11 (C) and Bcl-X_L (D).

Table 2.3: Thermodynamic parameters for binding of various Beclin 1 BH3D-derived peptides to M11 and Bcl-X_L.

Peptide	M11				Bcl-X_L			
	Kd (μM)	ΔH (kJ/mol)	ΔG (kJ/mol)	ΔS (J/K mol)	Kd (μM)	ΔH (kJ/mol)	ΔG (kJ/mol)	ΔS (J/K mol)
WT	1.38 ± 0.41	-70.97 ± 6.39	-33.51 ± 0.71	-125.72 ± 22.53	1.95 ± 0.19	-43.57 ± 1.44	-32.58 ± 0.23	-36.89 ± 4.53
L112A	4.33 ± 0.86	-47.36 ± 1.53	-30.63 ± 0.53	-56.14 ± 4.10	109.71 ± 3.10	-42.36 ± 1.07	-22.59 ± 0.07	-66.34 ± 3.84
L116A	177.62 ± 16.95	-36.40 ± 4.64	-21.40 ±0.24	-50.33 ± 16.36	No Binding	-------	-------	-------
K117A	0.66 ± 0.17	-69.08 ± 3.05	-35.32 ± 0.67	-113.29 ± 11.74	18.93 ± 4.15	-37.66 ± 3.72	-26.99 ± 0.58	-35.83 ± 11.52
G120E	36.49 ± 8.10	-52.17 ± 5.81	-25.36 ± 0.52	-89.97 ± 20.91	No Binding	-------	-------	-------
D121A	1.33 ± 0.72	-58.54 ± 12.21	-33.74 ± 1.23	-83.13 ± 45.04	No Binding	-------	-------	-------
F123A	5.20 ± 1.53	-59.36 ± 2.72	-30.20 ± 0.74	-97.84 ± 11.61	407.56 ± 75.68	-30.70 ± 8.28	-19.36 ± 0.46	-38.04 ± 29.34
G120E +D121A	6.43 ± 0.15	-62.34 ± 2.72	-29.62 ± 0.06	-109.81 ± 9.28	No Binding	-------	-------	-------

Despite the general overall similarity in the interaction of the Beclin 1 BH3D with M11 and Bcl-X_L described above, the specific interactions of each BH3D residue with the different residues lining the binding groove of the two homologs is different, suggesting that each BH3D residue will have a different thermodynamic contribution to the overall binding. Indeed, despite the similar ΔG of binding to M11 and Bcl-X_L, the magnitudes of the entropic and enthalpic contributions to binding are different, with ΔH for binding to M11 being ~2-fold higher, and TΔS being ~4-fold lower than that for binding to Bcl-X_L (Table 2.3). This supports the hypothesis that the different binding interactions of each BH3D residue dictatea different thermodynamic contribution to the overall similar affinity of binding in the interaction with M11 and Bcl-X_L. Thus, the similar interactions of the Beclin 1 BH3 domain with M11 and Bcl-X_L provide a good

model system for a detailed mutational and thermodynamic analysis elucidating how differences in the binding determinants of M11 and Bcl-$X_L$can translate to differential affinities for various BH3D-containing proteins, despite a similar overall mode of binding.

2.3.4. Specific Beclin 1 mutations abrogate autophagy down-regulation by Bcl-$X_L$but not M11

Based on the analysis above, we created the following single mutant Beclin 1 constructs: L112A, L116A, K117A, G120E and F123A. The D121A mutant was not investigated using cellular assays because our previously published results show that M11 binds to a Beclin 1 G120A+D121A mutant (Sinha et al., 2008). Expression of all Beclin 1 mutants was comparable to that of WT Beclin 1 in both starvation and nutrient-rich conditions (Figure 2.11A). Bcl-X_L and M11 also had comparable expression in both starvation and nutrient-rich conditions.

Assays to monitor autophagy levels were performed using MCF7 cells, which express low levels of Beclin 1 and do not show starvation-induced increases in autophagy unless Beclin 1 is ectopically expressed (Pattingre et al., 2005b, Liang et al., 1999, Liang et al., 2001, Furuya et al., 2005) (Figure 2.11).This allows the effect of Beclin 1 mutants to be assayed in the absence of endogenous Beclin 1. Earlier studies have utilized multiple diverse methods to conclusively demonstrate that in starvation conditions cellular and γHV Bcl-2 homologs, including Bcl-X_L and γHV68 M11, reduce autophagic flux by binding to Beclin 1 (Pattingre et al., 2005a, Ku et al., 2008a, Sinha et al., 2008, Maiuri et al., 2007a, Erlich et al., 2007, Wei et al., 2008a, Pattingre et al., 2009). Therefore, here we monitored autophagy levels simply by quantifying the change in cellular localization of a green fluorescent protein (GFP)-tagged, transiently expressed mammalian autophagy-specific marker, LC3 (GFP-LC3) from a diffuse cytoplasmic distribution to localized punctae corresponding to autophagosomal structures (Figure 2.11).

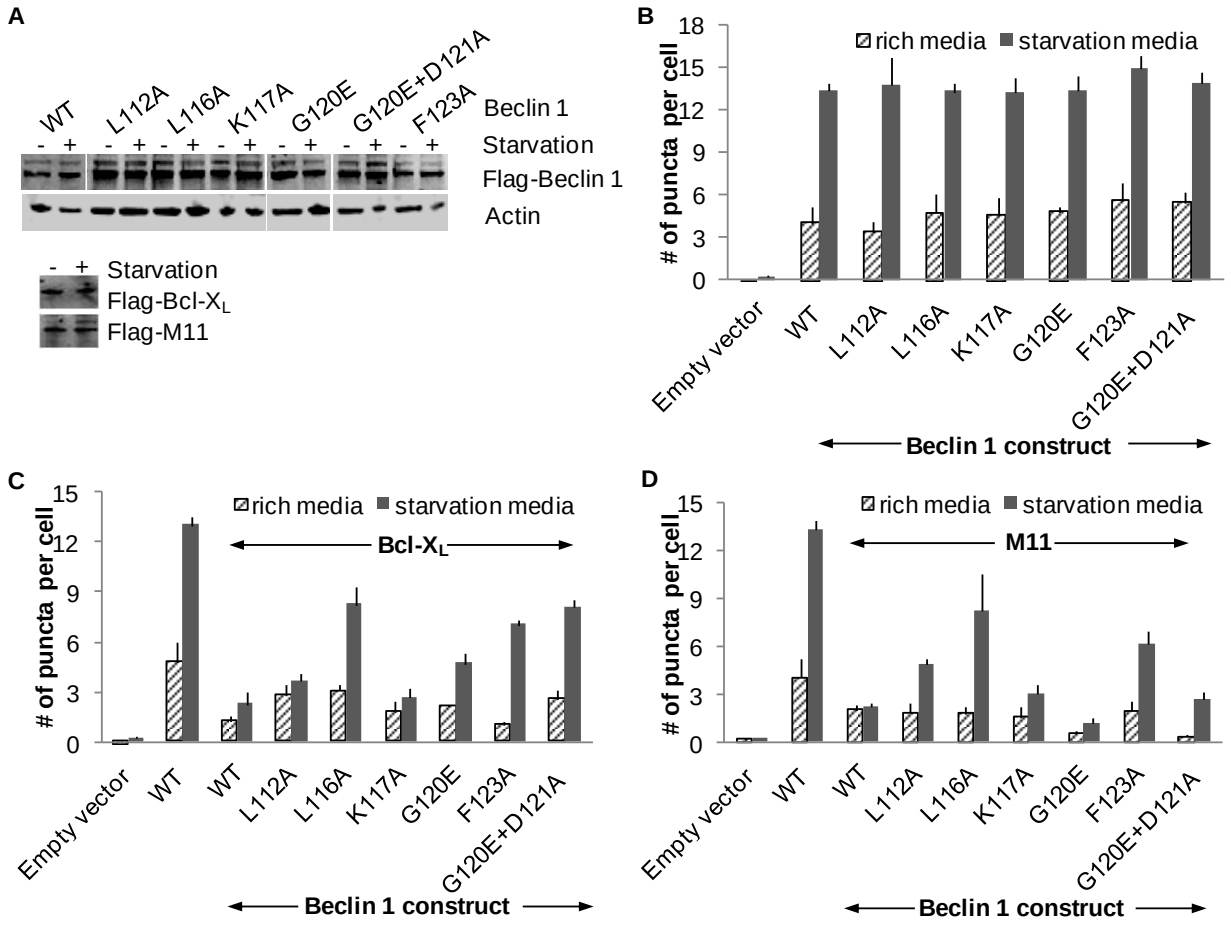

Figure 2.11: Effect of different Beclin 1 mutations on down-regulation of autophagy by Bcl-X_L or M11. (A) Western blots of MCF7 cell extracts indicating comparable expression levels of WT and mutant Flag-tagged Beclin 1 constructs, and of Bcl-X_L, and M11 in starvation and nutrient-rich conditions, with Actin as a loading control. (B-D) Bar graphs representing light microscopy quantification of the number of discrete GFP-LC3 puncta per cell in GFP-positive MCF7 cells co-transfected with GFP-LC3, WT or mutant Beclin 1 as indicated below the x-axis and either (B) No Bcl-2 homolog (C) Bcl-X_L or (D) M11.

Transient expression of Beclin 1 in MCF7 cells led to a marked increase in autophagy upon starvation ($p = 0.00060$ for starved versus nutrient-rich cells; Figure 2.11 B-D). Basal autophagy levels in nutrient-rich media are typically much lower and less consistent than in starvation conditions, therefore here we focus on the autophagy levels observed in starvation

conditions. The levels of autophagy mediated by each Beclin 1 mutant tested was comparable to that mediated by WT Beclin 1 (ranging between p = 0.10915 to 0.93428 for mutants versus WT Beclin 1; Figure 2.11B).

The transient co-expression of either Bcl-X_L or M11 was used to assay the ability of these homologs to down-regulate autophagy upon expression of each Beclin 1 single mutant (Figure 2.11). Starvation-induced, Beclin 1-dependent autophagy is significantly down-regulated by expression of either Bcl-X_L (p = 0.00033 for Bcl-X_L versus empty vector; Figure 2.11C) or M11 (p = 0.00434 for M11 versus empty vector; Figure 2.11D), as has been previously shown (Pattingre et al., 2005a, Ku et al., 2008a, Sinha et al., 2008). We find that M11 down-regulates starvation-induced autophagy at least as potently as Bcl-X_L (Figure 2.11C-D), and in general, Beclin 1 BH3D mutations are less deleterious for the M11-mediated down-regulation of Beclin 1-dependent autophagy.

Under starvation conditions, Bcl-X_L down-regulates autophagy mediated by the K117A Beclin 1 mutant as effectively as that mediated by WT Beclin 1 (p = 0.5043 for mutant versus WTBeclin 1; Figure 2.11C). However, Bcl-X_L–mediated down-regulation of autophagy is less pronounced upon expression of L112A (p = 0.06209 for mutant versus WT Beclin 1) or G120E (p = 0.01190 for mutant versus WT Beclin 1) Beclin 1 mutants (Figure 2.11C). Amongst the Beclin 1 single mutants, the most significant abrogation of Bcl-X_L–mediated down-regulation of autophagy was observed upon expression of the mutants F123A (p = 0.00246 for mutant versus WT Beclin 1) and L116A (p = 0.00212 for mutant versus WT Beclin 1; Figure 2.11C).

Similar to Bcl-X_L, expression of the Beclin 1 K117A mutant (p = 0.15725 for mutant versus WTBeclin 1) did not affect M11-mediated down-regulation of autophagy (Figure 2.11D). M11–mediated autophagy down-regulation is significantly weaker upon expression of the

mutants F123A ($p = 0.01070$ for mutant versus WT Beclin 1) and L112A ($p = 0.00065$ for mutant versus WT Beclin 1). The most significant abrogation of M11–mediated autophagy down-regulation is observed when L116A mutant Beclin 1 was expressed ($p = 0.04316$ for mutant versus WT Beclin 1).

Surprisingly however and contrary to expectations from structural analysis, M11 effectively down-regulates autophagy upon expression of the G120E single mutant ($p = 0.03131$ for mutant versus WT Beclin 1). Despite the previous cellular co-immunoprecipitation assays showing that a Beclin 1 G120A+D121A mutant binds to M11 (Sinha et al., 2008), we expected that the mutation of G120 to the large and negatively-charged Glu residue would disrupt binding to both Bcl-X_L and M11, consequently abrogating the down-regulation of autophagy by these Bcl-2 homologs. However, our data indicate that unlike Bcl-X_L (Figure 2.11C), the M11 binding site accommodates the Glu side chain, allowing M11 to effectively down-regulate autophagy mediated by G120E Beclin 1 (Figure 2.11D).

Therefore, we further examined the role of D121 in the context of the G120E mutation by assaying the ability of Bcl-X_L and M11 to down-regulate autophagy mediated by a G120E+D121A Beclin 1 double mutant. As expected, expression of the G120E+D121A double mutant resulted in abrogation of Bcl-X_L-mediated autophagy down-regulation ($p = 0.00079$ for double mutant versus WT Beclin 1), comparable to the effect seen upon expression of the L116A mutant Beclin 1 (Figure 2.11C).However, in complete contrast to Bcl-X_L, M11 effectively down-regulates autophagy mediated by the G120E+D121A Beclin 1 double mutant ($p = 0.22842$ for double mutant versus WT Beclin 1; Figure 2.11D). Thus, the G120E mutation enables selective inhibition of autophagy by M11.

2.3.5. Identification of peptides that bind to M11, but not to Bcl-X_L

We used ITC to quantify and compare binding of a systematic set of Beclin 1 BH3D-derived peptides whose residues are numbered according to the Beclin 1 sequence. In general, each residue substitution impacted binding to Bcl-X_L more than to M11, with the different substitutions having very diverse thermodynamic effects on binding to either M11 or Bcl-X_L (Table 2.3). All substitutions weakened binding to Bcl-X_L, but not to M11, and the binding affinity was generally consistent with results monitoring the effect of these mutations on down-regulation ofautophagy by Bcl-X_L and M11. The L112A substitution weakened binding to Bcl-X_L to barely detectable levels, but reduced binding to M11 by only ~3-fold. Similarly, the F123A substitution weakened binding to Bcl-X_L by ~200-fold, and to M11 by ~4-fold, although the equivalent mutation in Beclin 1 had a more dramatic impact on the down-regulation of cellular autophagy by M11, suggesting that this mutation is more deleterious in the context of full-length Beclin 1 interactions in the cell (Figure 2.11D). Interestingly, although relative to the WT BH3D, the K117A peptide bound with ~10-fold weaker affinity to Bcl-X_L, it actually bound with ~2-fold tighter affinity to M11 (Table 2.3). Lastly, no single substitution abolished binding to M11, but three single substitutions, L116A, G120E and D121A, completely abrogated binding to Bcl-X_L. The L116A and G120E substitutions were also the most deleterious for binding to M11, reducing binding affinity for M11 more than 120-fold and 26-fold, respectively (Table 2.3), but binding to M11 seems unaffected by the D121A substitution.

Contrary to initial expectations based on the structure of the WT BH3D bound to M11, but consistent with the cellular autophagy assays, the G120E and D121A peptides are still able to bind to M11 (Table 2.3). Therefore, we quantified and compared the ability of a G120E+D121A peptide (DS peptide) to bind to Bcl-X_L and M11. Consistent with our cellular experiments in the

previous section, the DS peptide does not bind to Bcl-X_L, but importantly, it binds to M11 with ~5.7-fold better affinity compared to the G120E peptide, and only ~4.7-fold weaker affinity compared to the WT BH3 domain (Figure 2.10 C & D and Table 2.3). Thus, in the context of the G120E substitution, the removal of the carboxylate group at the 121 position improves binding.

We also employed SEC to study the formation of M11:DS peptide complex in solution. M11 and DS peptide were mixed at 1: 1.5 molar ratio and rocked at 4 ℃ for 30 min. The mixed sample was then loaded onto a Superdex 200 10/300 GL column in tandem with a Superdex 75 10/300 GL column. As indicated by the SEC profile (Figure 2.12), the M11:DS peptide sample formed a single peak, but was left-shifted compared to the SEC profile of M11 alone. A small peak close to the 1.35 kD marker stayed the same in both SEC profiles of M11:DS peptide and M11-alone, which was most likely formed by the small-molecule contaminants in the M11 protein sample. The apparent molecular weight of the M11:DS peptide peak estimated from the void volume of the summit of that peak was 26.6 kD, which is close to the molecular weight of the dimer of the M11:DS peptide. However, unlike the SEC profile of M11:mNOXA complex (Figure 2.7), which had the ideal gaussian distribution, the peak of M11:DS peptide is unsymmetrical with a tail on the left. This indicated the peak may contain a mixture of M11:DS peptide and M11-alone, which is not surprising since M11 binds to the DS peptide with only a moderate affinity of 6.4 μM, 8-fold weaker compared to its binding affinity with mNOXA BH3D peptide. Nevertheless, the fractions from the single peak of M11:DS peptide were pooled together and concentrated to 5 mg/ml and used for crystallization experiments.

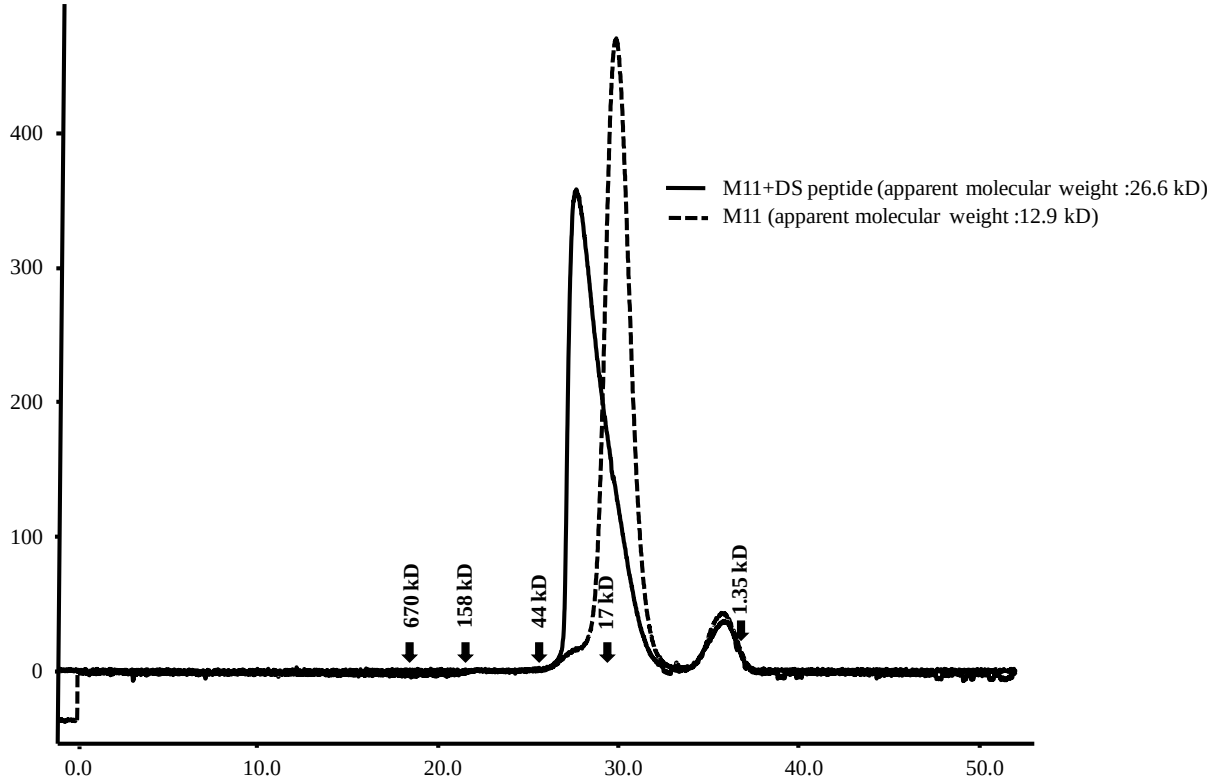

Figure 2.12: Size-exclusion chromatograms of M11 alone and M11:DS peptide.

2.3.6. Structure of the DS peptide bound to M11

In order to elucidate the mechanism by which M11 is able to bind the DS peptide, we crystallized M11:DS peptide complex (Figure 2.13) to determine its X-ray crystal structure. The best M11:DS peptide complex crystal were produced at 20 ℃ by hanging drop vapor diffusion methods, from a 1:1 mixture of protein solution (5mg/ml in 20 mM HEPES, pH 7.5, 100 mM NaCl, 1 mM TCEP) and well solution (2.5 M $(NH_4)_2SO_4$ and 8 % v/v 2-propanol). Plate-shaped crystals grew to 100×50×10 in 3 days (Figure 2.13).

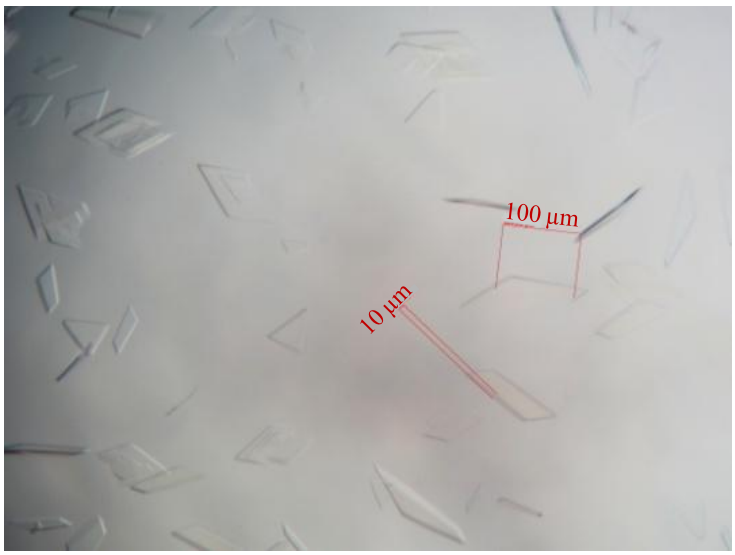

Figure 2.13: Typical M11:DS peptide complex crystals.

The crystals were then harvested and cryoprotected in a cryosolution consisting of 2.5 M $(NH_4)_2SO_4$ and 25% v/v glycerol, and then immediately flash-frozen in liquid N_2. The data used to solve the M11:DS peptide structure were collected at an X-ray wavelength of 0.97934 Å in a 360 °sweep from a single crystalat at beamline 23ID-D of GMCA@APS, ANL, Chicago. Data were processed using HKL2000 (Otwinowski and Minor, 1997) and the data statistics were summarized in Table 2.4.

Table 2.4: Summary of crystallographic data statistics.

Wavelength (Å)	0.97934
Data range (Å)	2.1-50.00 (2.1-2.14)
Mosaicity	0.329-0.633
Unique reflections	24082
Avg. multiplicity	3.8 (3.1)
Completeness (%)	99.4 (91.9)
$^{\ddagger}R_{sym}$ (%)	4.9 (44.7)
I/σ_I	9.2 (2.9)

Values in parentheses pertain to the outermost shell of data.

$^{\ddagger}R_{sym} = \sum_{h,i} |I_{h,i}-\langle I_h \rangle| / \sum_{h,i} I_{h,i}$.

The X-ray crystal structure of the M11:DS peptide complex was solved to 2.1 Å resolution by molecular replacement using a search model extracted from M11: Beclin 1 BH3D complex (PDB code: 3DVU). The detailed procedures of molecular replacement and structure refinement were described in the methods section and the crystallographic refinement statistics were summarized in Table 2.5.

Table 2.5: Summary of crystallographic refinement statistics.

Model:	
M11 residues (Monomer A)	135
M11 residues (Monomer B)	136
Beclin 1 DS peptide (Chain C)	20
Beclin 1 DS peptide (Chain D)	22
Water molecules	133
Sulfate molecules	4
Data Range (Å)	50-2.1
‡R_{work} (%)	16.0
‡R_{free} (%)	22.4
Average B-values ($Å^2$)	34.7
Main Chain	26.7
Side Chain	28.7
Water	48.0
All Atoms	34.7
B-factor RMSDs between bonded atoms:	
Main chain	2.332
Side Chain	4.026
RMSDs from target values:	
Bond Lengths (Å)	0.020
Bond Angles (°)	1.985
Dihedral Angles (°)	21.33
Improper Angles (°)	1.91
Cross-validated sigma coordinate error (Å)	0.24
Ramachandran outliers	0

‡R factor= $\sum_{h,} |F_{obs}-|F_{calc}|/\sum_{h}|F_{obs}|$. Test set for R_{free} consisted of 5.5 % of data.

As shown in Figure 2.14A, residues altered in the DS peptide, E120 and A121, have very well defined electron density. Both the DS peptide (Figure 2.14A) and the WT BH3D (Figure 2.14B) bind by a similar mode within the M11 hydrophobic surface groove. The two complexes superimpose with an RMSD of 0.451 Å over 148 Cα atoms, indicating that they are fairly similar, although the superposition is somewhat worse than that of the two complexes within the asymmetric units of structures of either the M11:DS peptide complex (0.162 Å) or the WT BH3D complex (0.031 Å). Despite this similarity of interaction, the surface area of each molecule buried in the interaction interface is significantly reduced in the M11:DS peptide complex, to 868 $Å^2$, compared to 978 $Å^2$ in the M11:WT BH3 domain complex. This reduced buried surface area likely accounts for the reduced binding affinity of the DS peptide, and is the result of the substantial main chain shifts and side chain movements in the bound DS peptide relative to the WT BH3D,as well as subtle compensatory side chain changes in M11 that facilitate binding of the DS peptide.

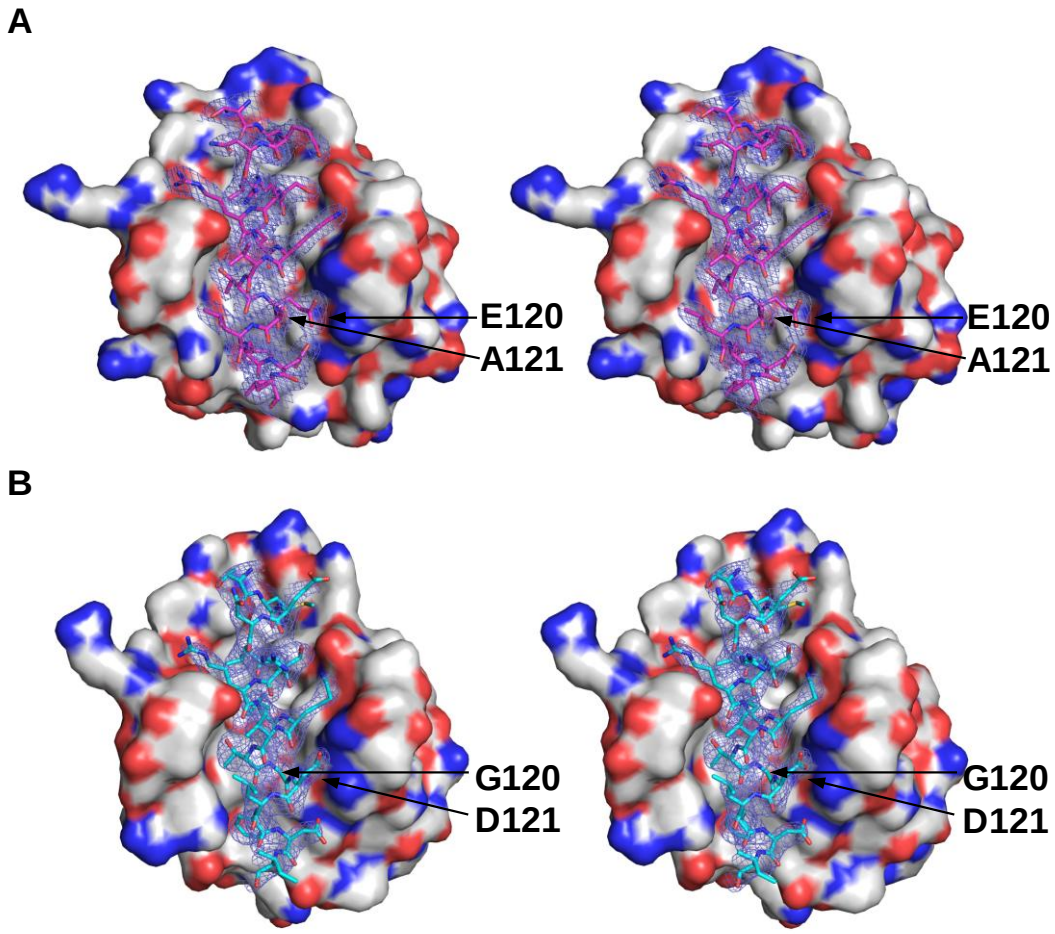

Figure 2.14: Stereo view of complexes of M11 bound to DS peptide **(**A**)** and WT BH3 domain (B**)** (PDB code: 3DVU). Atoms are colored by type as in Figure 2.6, with M11 shown as molecular surface, whereas the DS peptide (magenta carbons) and WT BH3D (cyan carbons) are displayed in atomic detail. The blue mesh represents the electron density contoured at 1 σ above the mean for a 1.6 Å radius around the peptide atoms from the $2F_o - F_c$ map at 2.1 Å for the DS peptide and at 2.5 Å for the WT BH3 domain complexes. Labels indicate residues substituted in the DS peptide.

Separate superimpositions of the M11 molecule in each complex indicate that there is limited conformational change in the M11 structure (Figure 2.15A), with RMSDs of 0.38 Å over 130 Cα atoms.This superposition is slightly worse than superposition of two M11 subunits within the asymmetric unit of either the M11:DS peptide complex (0.17 Å) or the WT BH3D complex (0.03 Å), but lies within experimental error for these structures. Maximal M11

conformational change is seen not at the BH3D binding groove, but rather at the flexible α1-α2 loop which is distant from the binding site; however this change is similar to conformational variation in this loop between different copies of the same complex present in the asymmetric unit of each crystal. Therefore, the conformational changes in this flexible loop do not relate to the binding of different peptides to M11.

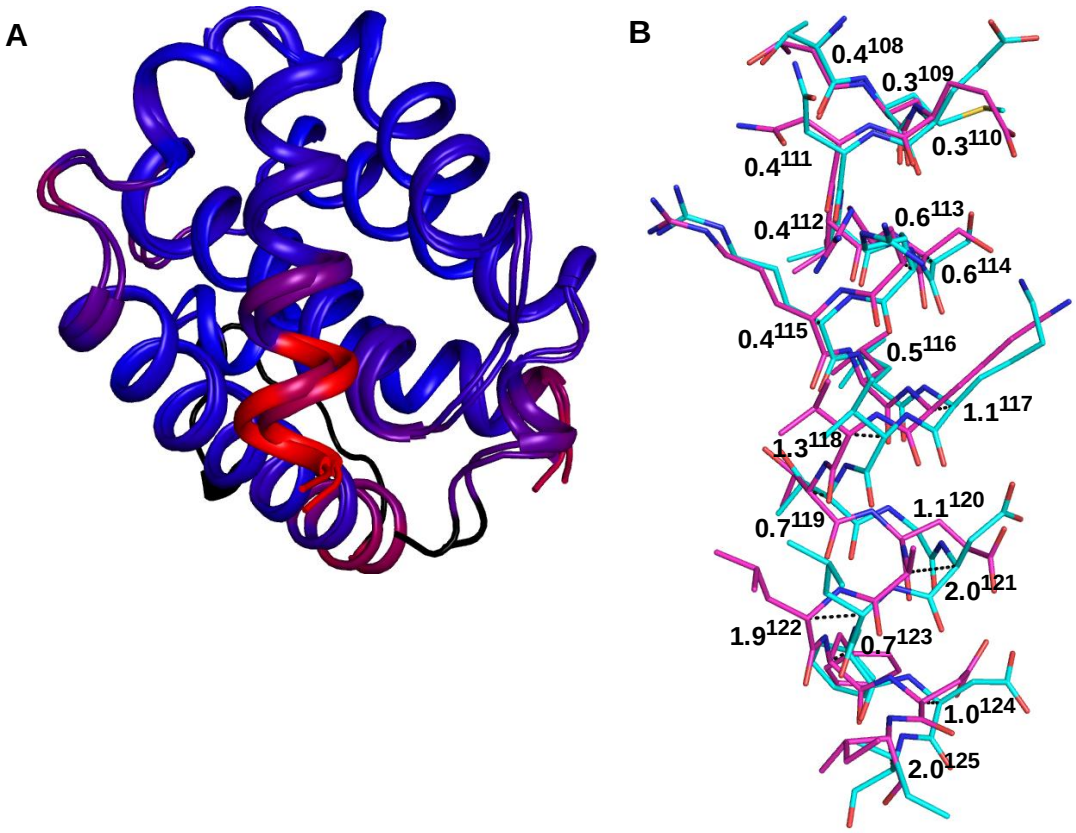

Figure 2.15: Superposition of complexes of M11 bound to DS peptide and WT BH3D. (A) M11-DS peptide and M11-WT BH3 domain (PDB code: 3DVU) are aligned and colored by RMSD, with colors from blue to red corresponding to the range of pairwise RMSDs from a minimum of 0.07 to a maximum of 4.30. The M11 flexible loop located on the M11 face opposite the BH3 domain-binding groove was not included in these calculations and is colored black. Besides this loop, the most significant shift between the two complexes is observed in the C-terminal half of the peptide, as indicated by the red color. (B) pairwise Cα shifts between DS peptide (magenta) and WT BH3 domain (cyan). Atoms are color-coded as in Figure 2.6. Pairwise shifts between the WT BH3D and DS peptide are displayed in Å, with superscript numbers denoting residue numbers relative to the Beclin 1 BH3D.

In contrast to M11, significant changes are seen between the bound DS peptide and WT BH3D conformations (Figure 2.15B). The bound WT and DS peptides superimpose with an RMSD of 0.99Å over 18 Cα atoms, with the comparatively poorer alignment chiefly attributable to the shifted positions of residues 117-125. The identical N-terminal halves of the two peptides superimpose fairly well between the WT BH3D and DS peptide structures, with an RMSD of 0.38 Å over 9 Cα atoms. However, superposition of the C-terminal half is poorer,with an RMSD of 1.35 Å over 9 Cα atoms. Thus, binding to M11 is enabled by significant shifts of the DS peptide main chain, especially of its C-terminal half (Figure 2.15), relative to WT BH3D.

2.3.7. Differences in the interactions of M11 with the DS peptide or the WT BH3D

Peptide amino acids corresponding to BH3D residues L112 and L116 bind in similar locations in the DS peptide and WT BH3D complexes, with pairwise differences in the Cα positions being 0.4 Å and 0.5 Å, respectively (Figure 2.15B). The packing of L112 is virtually identical in each complex, with L112 being sandwiched between M109 and L116 which are approximately one helical turn away on each side within the peptide, and surrounded by a hydrophobic pocket lined by M11 residues Y60, A63and L74. Similarly, in each complex L116 is packed into a hydrophobic pocket lined by M11 residues F48, Y60, L78, and V94, although there are some subtle differences in the atomic details of the interaction (Figure 2.16).

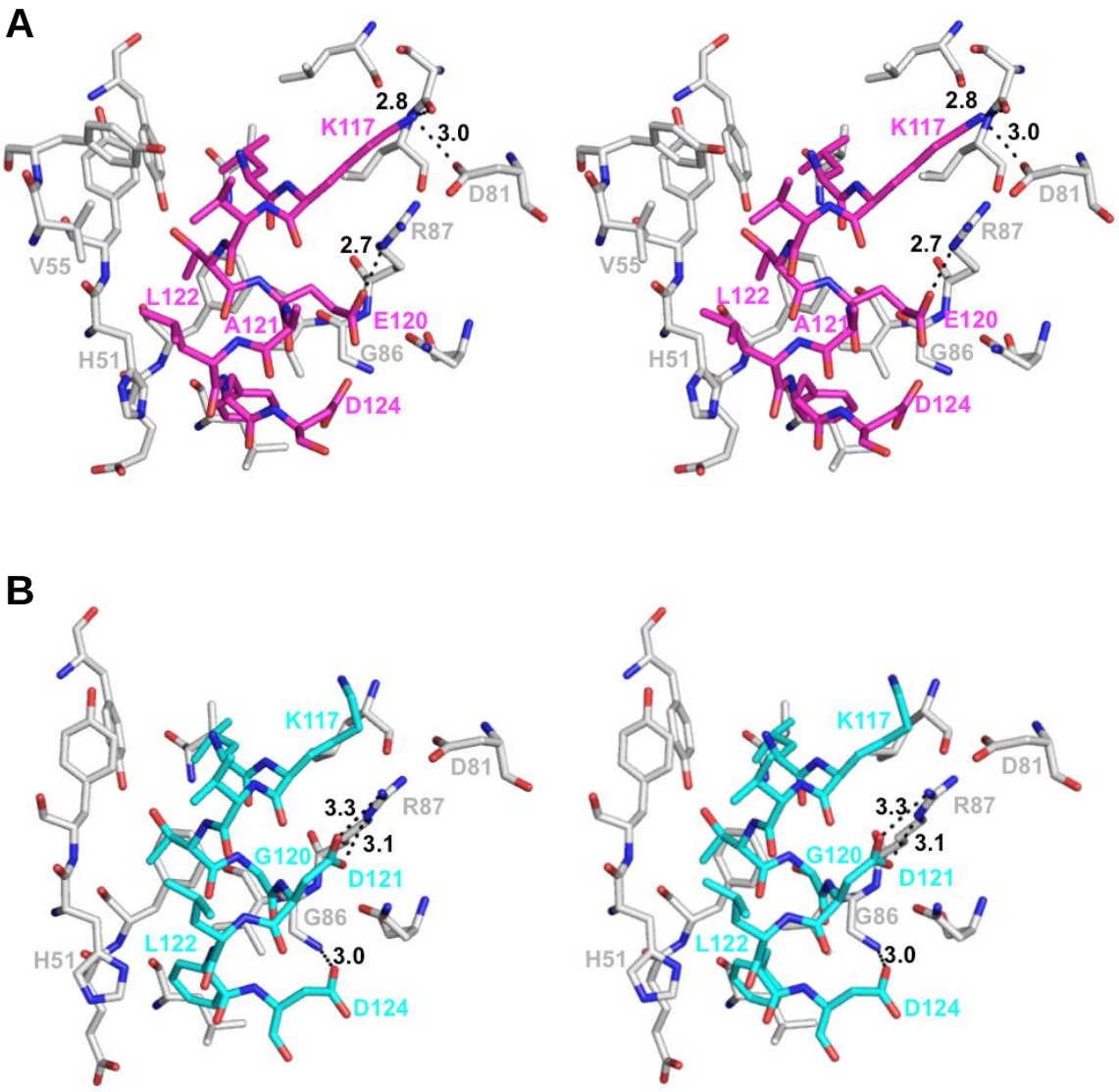

Figure 2.16: Stereo view showing details of M11 residue interactions with the DS peptide (A) and the WT BH3 domain (B) (PDB code: 3DVU). Bond lengths are shown for polar interactions. Atoms are color-coded as in Figure 2.9, and residue labels are color-coded by molecule.

Starting at K117, there are incrementally increasing shifts in the DS peptide residue positions relative to those in the WT BH3D. The pairwise shift at K117 Cα is 1.1 Å (Figure 2.15B), which enables additional interactions between K117 and M11 in the DS peptide complex. The aliphatic part of K117 packs against the aliphatic parts of M11 D81 and R87 in both complexes (Figure 2.16), but in the DS peptide complex also interacts with M11 L78 and

S77 (Figure 2.16A). Further, while the K117 amino group does not make any interactions in the WT complex (Figure 2.16B), in the DS complex it electrostatically bonds with the M11 D81 carboxylate and hydrogen bonds the S77 hydroxyl (Figure 2.16A). Similarly, the next peptide residue, V118, is solvent exposed and does not interact with M11 in the WT BH3D complex, but a 1.3 Å Cα shift (Figure 2.15B) at this position in the DS peptide complex results in packing against M11 Y56 (Figure 2.16A). The following residue, T119, has a smaller Cα shift between the WT BH3D and DS peptide (Figure 2.15), and maintains similar, but slightly different, interactions in both complexes, with the aliphatic parts of the side chain packed against M11 residues F48, Y52 and the H51 main chain (Figure 2.16).

The next two residues are altered in the DS peptide: E120 and A121, compared to G120 and D121 in the WT BH3D. The incremental shifts preceding these residues result in a shift of 1.1 Å at the E120 Cα from the WTBH3D G120 Cα position, and of a maximal shift of 2.0 Å at the Cα of residue 121. The Cα shift at residue 121 corresponds to approximately half a helical turn relative to the WT BH3D:M11 complex (Figure 2.15B). In the M11:WT BH3D complex (Figure 2.16B), the G120-D121 main chain packs in an anti-parallel manner against the main chain of two conserved M11 residues: G86 and R87. In contrast, in the M11:DS peptide complex (Figure 2.16A), E120 extends across the M11 hydrophobic groove, with the aliphatic part of the side chain packed against the M11 G86 main chain and the aliphatic parts of R87 and F48, to make one salt bridge with M11 R87. Thus, the M11 binding groove accommodates the larger Glu side chain, and stabilizes the altered E120 by electrostatic interactions with the conserved M11 R87. Further, while in the WT BH3D complex (Figure 2.16B) the D121 side chain is stabilized by packing against the aliphatic part of R87 and a bidentate salt bridge to M11 R87, in

the DS peptide complex (Figure 2.16A) A121 makes no contacts with M11, and is completely solvent exposed as a consequence of the main chain shifts.

L122, the peptide residue that follows the two altered residues, is also significantly shifted and has a completely different environment in the WT BH3D and DS peptide structures (Figure 2.16). In the WT peptide, L122 is solvent exposed and makes no contacts with M11 (Figure 2.16B) while in the DS peptide complex, it is shifted to pack against M11 H51 and V55 (Figure 2.16A) with this interaction being accommodated by a rotation of the H51 imidazole.

Pairwise Cα shifts between the M11-bound DS peptide and WT BH3D decrease to 0.7 Å at F123 (Figure 2.15), which allows the side chain to bind in equivalent M11 hydrophobic surface pockets comprised of residues L44, E47, F48, H51, G86 and V89 in each complex, but with an altered orientation of the F123 aromatic ring and subtly different interactions (Figure2.14 and 2.16).The relative shifts between WT BH3 domain and DS peptide are retained at the D124 Cα position (Figure 2.15). This allows the aliphatic part of the D124 side chain to pack against the M11 G86 Cα in both complexes. In addition, it packs against the aliphatic parts of M11 N84 in the WTBH3D complex, or against the peptide E120 in the DS peptide complex. Further, the D124 carboxylate group of the WT BH3 domain (Figure 2.16B) hydrogen bonds to the M11 G86 amide but a similar interaction is not seen in the DS peptide complex (Figure 2.16A).

Thus, the main chain shifts of the DS peptide enable the E120 – M11 R87 interaction and remove A121 from M11 interactions. It is likely that the improved binding of M11 to the DS peptide, relative to the G120E peptide, is due to the elimination of the competition between the G120E and D121 carboxylates for the M11 R87 interaction and the helix strain associated with the binding of the latter peptide.

2.3.8. A cell-permeable DS peptide selectively abrogates down-regulation of autophagy by M11, but not by Bcl-X_L

Lastly, we investigated whether the DS peptide would specifically prevent M11-mediated, but not Bcl-X_L-mediated down-regulation of Beclin 1-dependent autophagy. To make the peptide cell-permeable,the trans-activating HIV-1 transcriptional activator protein transduction domain (TAT), which is a cell penetrating peptide previously shown to facilitate entry of extended polypeptides into mammalian cells under the conditions used here (Shoji-Kawata et al., 2013), was attached via a diglycine linker to the N-terminus of the DS peptide (TAT-DS peptide). As a control we also assayed the effect of a TAT-BH3D fused peptide (TAT-WT peptide) on M11- and Bcl-X_L-mediated down-regulation of Beclin 1-dependent autophagy.

Treatment of Beclin 1-transfected MCF7 cells with the TAT-WT peptides did not significantly increase levels of autophagy in either nutrient-rich or starvation conditions (Figure 2.17). As expected, compared to untreated cells, TAT-WT peptide treatment markedly increases autophagy levels in cells that are transiently transfected with either M11 ($p = 0.00194$ for treated versus untreated cells; Figure 2.17) or Bcl-X_L ($p = 0.00007$ for treated versus untreated cells; Figure 2.17). This suggests that the TAT-WT peptide binds to both M11 and Bcl-X_L, preventing both Bcl-2 homologs from down-regulating Beclin 1-mediated autophagy.

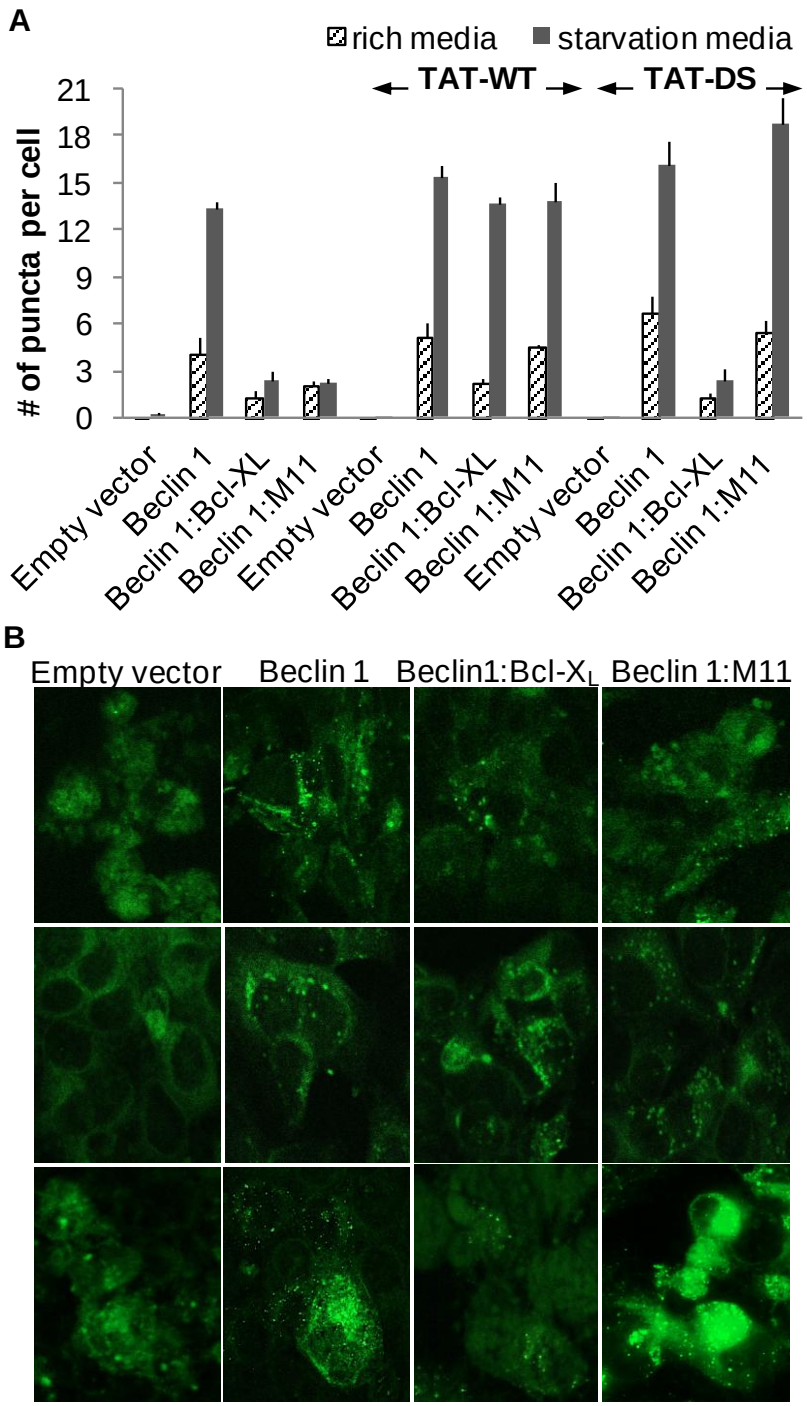

Figure 2.17: Effect of TAT-DS peptide treatment on down-regulation of autophagy by Bcl-X_L and M11. (A) light microscopy quantification of the number of discrete GFP-LC3 puncta per cell in GFP-positive MCF7 cells are co-transfected with GFP-LC3, WT Beclin 1, and either WT M11 or Bcl-X_L and then treated with either no peptide, TAT-WT, or TAT-DS peptide. (B) representative images of GFP-LC3 staining in these cells corresponding to cells that were untreated (top row), TAT-WT treated (middle row), and TAT-DS treated (bottom row).

TAT-DS peptide treatment of MCF7 cells that express Beclin 1, but not Bcl-X_L or M11, causes only an insignificant elevation in autophagy levels relative to untreated cells ($p = 0.20340$ for treated versus untreated cells; Figure 2.17).TAT-DS peptide treatment of cells that transiently express Bcl-X_L in addition to Beclin 1 had an insignificant effect compared to untreated cells ($p = 0.92294$ for treated versus untreated cells; Figure 2.17), presumably because the TAT-DS peptide does not bind to Bcl-X_L and so does not prevent Bcl-X_L from down-regulating autophagy. Strikingly however, TAT-DS peptide treatment of cells that transiently express M11 in addition to Beclin 1 markedly increases autophagy levels compared to untreated cells ($p = 0.042479$ for treated versus untreated cells; Figure 2.17), indicating that the TAT-DS peptide binds to M11, preventing M11 from down-regulating Beclin 1-mediated autophagy. Thus, the TAT-DS peptide inhibits M11-mediated down-regulation of autophagy, but not Bcl-X_L-mediated down-regulation of autophagy.

2.4. Discussion

In this chapter we have shown that despite the similar general mode of binding of the Beclin 1 BH3 domain to M11 and Bcl-X_L, the different residues lining the binding grooves of each homolog dictate differences in the atomic details and the thermodynamics of each interaction, and consequently affect biological function. We detailed the effect of mutations on binding of the BH3D to two different Bcl-2 homologs, which combined with our structural information, helps illuminate the atomic bases of the differential specificity of these homologs for different BH3D-containing binding partners. We found that, consistent with the promiscuity of M11 and specificity of Bcl-X_L for diverse BH3Ds, the M11 binding site accommodates more peptide residue substitutions than the binding sites of Bcl-$X_L$or Bcl-2 (Mei et al., 2014). These changes are accommodated chiefly by subtle M11 side chain conformational changes that allow

for more dramatic changes in the bound peptide, which enable alternate interactions with M11. Either the G120E or D121A mutation is sufficient for preventing binding to Bcl-X_L or Bcl-2 (Mei et al., 2014), suggesting that unlike for M11, Bcl-2 and Bcl-X_L cannot accommodate a large side chain at the G120 position and that the salt bridge formed with R87 of Bcl-X_L is critical for binding in Bcl-X_L and Bcl-2, but not for M11. Based on superimpositions of the complexes of M11:DS peptide, M11:WT BH3D and Bcl-X_L:WT BH3 domain, it appears that the peptide shifts observed in the first complex that enable the G120E to interact with R87 in the M11 complex, would not be easily accommodated in Bcl-X_L. For instance, an obvious steric clash occurs between the L122 main chain of the shifted DS peptide and the Bcl-X_L R100, whose conformation is stabilized by salt bridge networks (Maity et al., 2013). This information adds significantly to our understanding of interactions between Bcl-2 homologs and BH3D containing proteins, explaining how mutated or diverse BH3Ds may be bound by one homolog and not another, thus also adding to our repertoire of information on protein-protein interactions in general.

Consistent with our expectations, we were able to exploit the subtle differences in binding by M11 and the Bcl-X_L to design specific inhibitors of M11 that abrogate M11 function in cells. Our results provide a tool to directly target M11:BH3D interactions in cellular studies. The selective peptide inhibitor identified in this study will be useful in studying the role of M11 at different stages of the γHV68 life-cycle, by treating virus-infected cells with the peptide at different time-points and assaying the effects on viral infection. In vivo studies in mice may require the development of more bio-stable small molecules. The structural information presented here will be invaluable for the future rational design of such small molecules that can selectively inhibit M11, but do not affect cellular Bcl-2 homologs. While a general M11-specific

inhibitor would help elucidate the general function of M11, a specific inhibitor that selectively inhibits only theγHV Bcl-2:Beclin 1 interaction would remove only the γHV blockade of autophagy, and therefore would be an extremely useful tool to study the role of autophagy in regulating γHV infections.

Lastly, we also elucidate methods that may allow us to identify determinants specific for binding to other Bcl-2 homologs, especially those from other γHVs such as KSHV and EBV. Such studies will provide basic mechanistic explanations about their ability to bind to diverse BH3D-containing proteins, and consequently their ability to differentially regulate various pathways, and may further enable us to design inhibitors that specifically target these proteins. Thus, this research will substantially assist and inform future research on the pathogenesis of infections caused by γHVs. Ultimately, such small molecule inhibitors may even form the basis of novel therapeutics to treat γHV infection, which currently cannot be cured, by promoting the autophagic degradation of viruses, apoptotic destruction of infected host cells, and/or restoration of the tumor suppressor activity of Beclin 1.

CHAPTER 3. CLONING, EXPRESSION AND PURIFICATION TRIALS OF BALF1

3.1. Introduction

Apoptosis is used by the infected cells as part of their antiviral response (Roulston et al., 1999). However, some viruses encode Bcl-2-like proteins (vBcl-2s) to regulate apoptosis during infection. EBV is a human γ-herpesvirus that presents as a widespread infection in the majority of the human population (Cabras et al., 2005). EBV infects oral epithelium, where it undertakes lytic replication, and resting B cells, where it establishes a largely latent infection for the life of the host. EBV is implicated in the pathogenesis of a number of human malignancies of epithelial and lymphoid origin, including nasopharyngeal carcinoma, gastric carcinoma, endemic Burkitt's lymphoma, Hodgkin's lymphoma, non-Hodgkin's lymphoma, and a number of lymphoproliferative diseases in immunocompromised hosts (Crawford, 2001). While members of γ-herpesvirus family carry one vBcl-2 gene in general, EBV appears to encode two Bcl -2 homologs, BALF1 and BHRF1 (Altmann and Hammerschmidt, 2005). BHRF1 clearly resembles Bcl-2 in its anti-apoptotic role (Henderson et al., 1993), whereas the function of BALF1 is controversial.

BALF1, first identified by Marshall et al.,was found to inhibit apoptosis and interact with pro-apoptotic Bcl-2 proteins, including BAX and BAK (Marshall et al., 1999). Later on, a second in-frame BALF1 methionine codon, which is 114 bp upstream of the previously identified BALF1 methionine codon, was discovered and the encoded protein was named BALF0 (Bellows et al., 2002). In the same study, BALF1 was found to co-immunoprecipitate with and antagonize the anti-apoptotic activity of BHRF1 and was not able to protect against Sindbis virus- or BAX-induced apoptosis (Bellows et al., 2002). BALF0 also antagonizes the anti-apoptotic activity of BHRF1, but it does not co-immunoprecipitate with BHRF1 (Bellows et

al., 2002). BALF0 was also found to be actively expressed in EBV-positive Burkitt lymphoma's cell lines and nasopharyngeal carcinoma biopsies and renders cells serum-independent, which suggests a prominent anti-apoptotic function for BALF0 during EBV-driven tumorigenesis (Cabras et al., 2005).

To date, it is not clear whether both BALF0 and BALF1 are expressed in the cells, nor are their functions in regulating apoptosis understood. Determination of the three-dimensional structure of BALF1 and BALF0 and a comparison with the structures of anti- and pro-apoptotic proteins, will provide unambiguous information regarding the exact function of BALF0 and BALF1.

In order to investigate the structure of BALF1, we attempted to clone the BALF1 gene (corresponding to residues 2-169), which includes the whole sequence of BALF1 except the C-terminal TM, into three expression vectors, including *p*MBP-Parallel, *p*GST-Parellel, and *p*His-Parallel, to express BALF (residues 2-169) as Maltose-Binding Protein (MBP)-, Glutathione S-transferase (GST)-, or His_6-tagged fusion protein, respectively. We successfully amplified BALF1 gene by PCR amplification. The PCR product and the three vectors were then digested by restriction enzymes BamHI and NotI. After ligation and transformation, in all the repeated trials, less than ten colonies were obtained for each of the ligation samples and none of the plasmids extracted from any colony contained the correct insert. TOPO TA cloning was then used to ligate the PCR product to the *p*CR 2.1-TOPO vector in order to test the double digestion efficiency. However, no colony grown after TOPO TA cloning contained the PCR product. Therefore, the cloning of BALF1 gene into *p*MBP-Parallel, *p*GST-Parellel, and *p*His-Parallel was not successful.

The expression and purification of the two BALF1 constructs, GST-BALF1 (residues 1-182) and BALF1 (residues 2-169)-His_6, that are available in Dr. Sangita Sinha's lab, were then tested in order to obtain stable BALF1 protein for further structural and biochemical studies. GST-BALF1 was degraded during expression and purification, and the three major components in the purified sample were confirmed to be the GST protein by western bolt, electrospray ionization mass spectrometry (ESI-MS) and Edman sequencing. The expression of BALF1 (residues 2-169)-His_6 was also not successful. No His_6-tagged protein was present in the protein eluted after SEC as demonstrated by western blot. The results of ESI-MS and Edman sequencing also suggested that no protein in the BALF1 (residues 2-169)-His_6 purified sample matches the molecular weight and amino acid sequence of intact or fragment of BALF1.

3.2. Materials and methods

3.2.1. BALF1 expression construct creation

In order to construct a series of BALF1 expression vectors for expressing BALF1 with different affinity tags, the "parallel" expression vectors (Sheffield et al., 1999), including *p*MBP-Parallel, *p*GST-Parallel, and *p*His-Parallel vectors were used to make BALF1 expression vectors with MBP, GST or His_6 tag. First, PCR was employed to amplify the cDNA sequence corresponding to BALF1 (residues 2-169) lacking the C-terminal TM, while simultaneously adding BamHI and NotI restriction sites to the sense and antisense chains, respectively. The sense and antisense primers were named as S1 and A1 and their sequences were listed in Table 3.1. The reagents used for 50 μL of PCR reaction were as follows: 5 μL of 10 × *Taq* DNA polymerase buffer, 1 μL of 10 mM dNTPs mixture, 2.5 μL of 10 ng/μL template, 5 μL of each 5 μM primers, and 0.5 μL of 5 U/μL *Taq* DNA polymerase, 6 μL of 25 mM $MgCl_2$ and 25μL nuclease-free H_2O. The PCR was performed on the GeneAmp PCR System 9700 (Life

Technologies) for 35 cycles under the following experimental conditions: initial denaturation at 94 ℃ for 3 min, denaturation at 94 ℃ for 1 min, annealing at 55 ℃ for 1 min, extension at 72 ℃ for 1 min, final extension at 72 ℃ for 5 min, and then hold at 4 ℃. The PCR products were gel purified using E.Z.N.A. Gel Extraction Kits (Omega Bio-tek).

To create the overhang for annealing, the purified PCR products, *p*MBP-Parallel, *p*GST-Parellel, and *p*His-Parallel vectors were subjected to restriction digestion. The reagents used for the 20 μL restriction digestion reaction were: 1 μg of the PCR product or vectors, 2 μL of 10 × BSA, 2 μL of 10 × NEBuffer 3, 1 μL of BamHI (20 U/μL), 1 μL of NotI (10 U/μL), and add nuclease-free H_2O to bring the volume to 20 μL. 1 uL of Antarctic Phosphatase was added to each reaction mixture, except the PCR fragment, after 2 hr digestion at 37 ℃. Continue digesting at 37 ℃ over night. The digestion products were gel purified using E.Z.N.A. Gel Extraction Kits (Omega Bio-tek).

For the annealing reaction, the vector was mixed with PCR product in a molar ratio of 1:6; with the reagents used for the 20 μL ligation reaction being: 10μL of 2 × T4 DNA Ligase reaction buffer, 1 μL of Quick T4 DNA Ligase, with nuclease-free H_2O added to bring the volume to 20 μL. The reaction mixture was incubated at room temperature for 5 min. 3 μL of ligation reaction mixture was transformed into chemically competent Top10 cells. The transformation mixture was then layered separately onto Ampicillin plates and the plates were incubated at 37 ℃ over night.

In order to increase the efficiency of PCR product digestion, TOPO TA cloning kit (Invitrogen) was also utilized in some of the cloning trials. The reagents used for TOPO TA cloning were as follows: 2 uLof PCR product, 1 uL of salt solution, 2 uL of ddH_2O, 1 uL of

TOPO vector. The reagents were then mixed gently and incubated for 5 minutes at room temperature.

A single colony of the recombinant *E. coli* cells was inoculated into 5 mL LB media supplemented with 100 µg/ml Ampicillin and grown overnight at 37 °C. The recombinant plasmid was isolated using E.Z.N.A. Plasmid Mini Kit I (Omega Bio-tek). The cloning of the coding regions of the BALF1 (residues 2-169) into the parallel vectors weretested by restriction digestion and gel electrophoresis and the plasmids containing the right-size DNA insertion were sent for sequencing at MCLAB.

Table 3.1: Summary of primers used for Bcl-X_L expression construct creation.

Primers	**5' to 3'**
S1	GCGGCGATGGATCCGAGGCCAGCCAAGTCTACAGATTCTGTGTTTGTG
A1	GCGGCGGCGGCCGCTTTACGTCACGGGGAACTGACGTCTCAGCGA

3.2.2. BALF1 expression and purification

Two BALF1 expression vectors, *p*GEX4T3-BALF1 (residues 1-182) and *p*ET21d-BALF1 (residues 2-169), were tested for expression and purification. *p*GEX4T3-BALF1 (residues 1-182) expresses BALF1 as GST-BALF1 (residues 1-182) and *p*ET21d-BALF1 (residues 2-169) expresses BALF1 as BALF1 (residues 2-169)-His_6. For the overexpression of both constructs, *E. coli* BL21(DE3)*p*LysS chemically competent cells were transformed with these plasmids. The transformed cells were grown in agar plate supplemented with 100 µg/µL Ampicillin and 35 µg/µL Chloramphenicol. A single colony was picked and grown overnight in 5 ml LB media supplemented with 100 µg/µL Ampicillin and 35 µg/µL Chloramphenicol at 37 ℃. The next day, the 5 ml overnight culture was used to inoculate 1 L of LB supplemented with 100 µg/µL Ampicillin and 35 µg/µL Chloramphenicol and further grown at 37 ℃ until optical

density of 0.6-0.8 was reached at 600 nm. At this point, overexpression of GST-BALF1 (residues 1-182) or BALF1 (residues 2-169)-His_6 was induced with 0.5 mM IPTG. The cells were grown further at 20 ℃ with a shaker speed of 220 rpm for 16-18 hours. The cells were harvested by centrifugation at 4700 rpm for 20 minutes at 4 ℃, and stored at -80 ℃ until usage.

The same purification procedures were used for purifying both GST-BALF1 (residues 1-182) and BALF1 (residues 2-169)-His_6. In general, the cell pellet from a 1 L culture was suspended in 50 ml lysis buffer comprising 25 mM HEPES, pH 8.0, 100 mM NaCl, 0.05% β-mercaptoethanol and a half-tablet of cOmplete protease inhibitor cocktail (Roche). The cells were lysed by sonication and the crude extract centrifuged at 18000 rpm for 50 min at 4 ℃ to remove the cellular debris. The resulting supernatant was loaded onto a gravity column containing 0.5 ml of glutathione sepharose resin (GE Healthcare) for GST-BALF1 (residues 1-182) purification, or Ni-NTA resin (Sigma-Aldrich) for BALF1(residues 2-169))-His_6 purification. After the supernatant passed through the column completely, the column was washed with 10 ml lysis buffer or 25 mM Imidazole in 10 ml lysis buffer to remove contaminating protein from glutathione sepharose resin or Ni-NTA resin, respectively. 1 ml wash fractions were collected. The glutathione sepharose resin or Ni-NTA resin was then eluted with 20 mM glutathione or 250 mM Imidazole in lysis buffer, respectively. Each 0.5 ml elution fraction was collected. Fractions collected along the purification process were analysis by SDS-PAGE. Elution samples were collected and further purified by SEC using a Superdex 200 10/300 GL column in tandem with a Superdex 75 10/300 GL column (GE Healthcare). The column was pre-equilibrated with SEC buffer comprising 25 mM HEPES, pH 8.0, 100 mM NaCl, 0.05% 2-mercaptoethanol. 800 μL of 1.3 mg/ml protein eluted from glutathione sepharose resin, or 750 ul of 0.4 mg/ml protein eluted from Ni-NTA resin was loaded onto the tandem SEC column and

eluted with SEC buffer at 0.5 ml/min flow rate. The purity of proteineluted from SEC was evaluated using SDS-PAGE.

3.2.3. Western blot

The expression of GST-BALF1 (residues 1-182) and BALF1 (residues 2-169)-His_6 was verified by western blot. In general, for the purified GST-BALF1 (residues 1-182) and BALF1 (residues 2-169)-His_6 samples, 15 μg of total protein was loaded into each well of a SDS-polyacrylamide gel. Protein bands separated on the SDS-polyacrylamide gel were transferred to polyvinylidenedifluoride (PVDF) membrane. Blot transfer was conducted under 360 mA for 2 hours. The membrane was then blocked with 5% nonfat dried milk at room temperature for 1 hour with shaking and was probed with anti-GST antibody and anti-His antibody for 1 hour at room temperature. Secondary detection was performed using peroxidase-conjugated goat anti-mouse IgG for 1 hour at room temperature and ECL Western Blotting Substrate (Pierce).

3.2.4. ESI-MS

The molecular weight of purified GST-BALF1 (residues 1-182) and BALF1 (residues 2-169)-His_6 samples was determined by ESI-MS at the Core Mass Spectrometry Facility in the Department of Chemistry and Biochemistry at North Dakota State University.

3.2.5. Edman sequencing

The expression of GST-BALF1 (residues 1-182) and BALF1 (residues 2-169)-His_6 protein were also verified by Edman degradation to sequence the N-terminal first five residues of each protein sample. For sequencing sample preparation, 15 μg protein of each sample were separated on SDS-polyacrylamide gels and transferred to PVDF membrane.Transfer buffer comprised of 10 mM CAPS, pH 11, 10% Methanol was used to avoid glycine contamination. Blot transfer was conducted under 360 mA for 2 hours. After blotting, the membrane was stained

with amido black for 2 min and then destained three times with 5% Acetic Acid. Bands of interest were then cut from the wet membrane and sent to Protein Chemistry Technology Core at University of Texas Southwestern Medical Center for Edman sequencing.

3.3. Results

3.3.1. Cloning of BALF1 into parallel expression vectors

In order to clone the gene of BALF1 (residues 2-169) in to three parallel expression vector (Sheffield et al., 1999), including *p*GST-Parallel (5037 kb), *p*HIS-Parallel (5549 kb), and *p*MBP-Parallel (6724 kb), to express BALF1 with GST tag, His_6 tag or MBP tag, PCR was first used to amplify the gene of interest and simultaneously add BamHI and NotI restriction sites to the sense and antisense strands, respectively. One single band of ~500 bp was detected by agarose gel electrophoresis, indicating a successful PCR amplification. The PCR fragment and three parallel plasmids were subjected to restriction digestion using BamHI and NotI. Uncut plasmid usually smears or presents as multiple bands on the agarose gels after electrophoresis due to the possibility of forming different types of supercoils, while the linearized plasmid usually forms a single band. As shown in Figure 3.1, all three plasmids samples after digestion mainly present as single bands with correct molecular sizes after electrophoresis, indicating a potential successful digestion. However, it is still possible the plasmids were cut by only one restriction enzyme, instead of two.

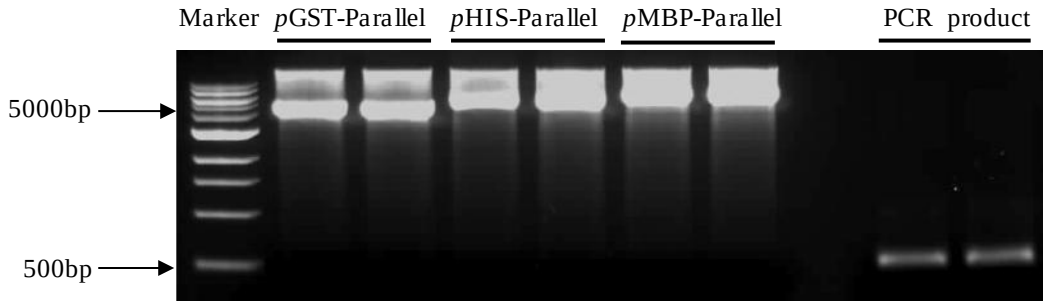

Figure 3.1: Digestion of three vectors and BALF1 PCR fragment using restriction enzymes BamHI and NotI.

The single bands from digestion samples of the three plasmids as well as the digested PCR products were cut out from the gel and DNA was extracted. After ligation and transformation, for repeated trials less than 10 colonies were grown for each of the ligation samples. Unfortunately, none of the plasmid extracted from the colony contains a DNA insert of 500 bp.

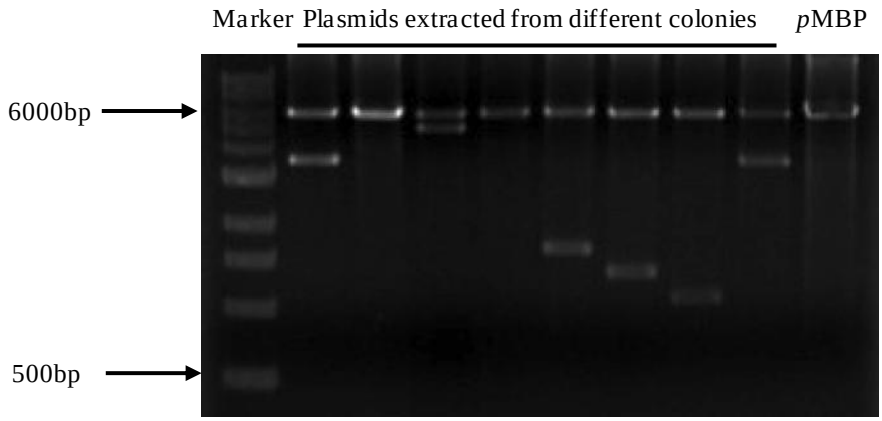

Figure 3.2: Screening of colonies with correct inserts through restriction digestion BamHI and NotI.

The TOPO TA cloning system was employed to first ligate the PCR product with the *p*CR 2.1-TOPO vector without the requirement of restriction digestion so that the efficiency of double restriction digestion can be verified by detecting a digestion product of 500 bp. Although

8 colonies were grown after ligation and transformation, restriction digestion with BamHI and NotI indicates that none of them contained a recombinant plasmid with an insert of 500 bp (Figure 3.3).

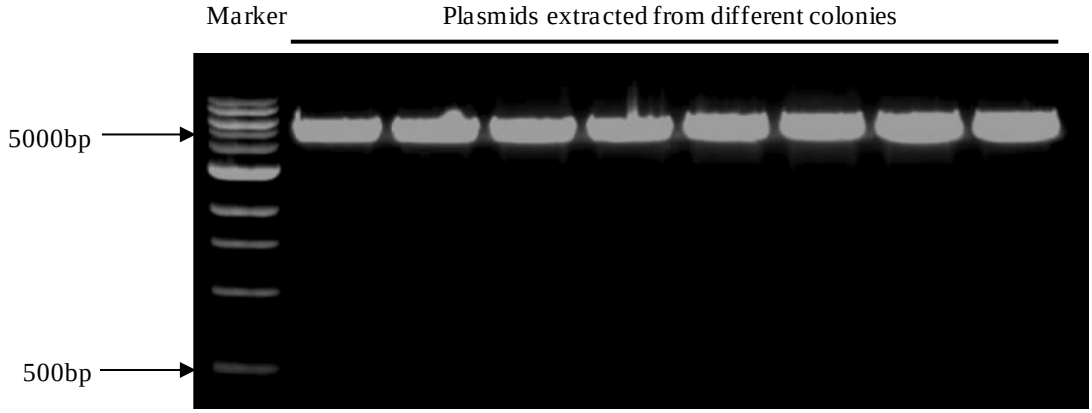

Figure 3.3: Screening of colonies with correct inserts through restriction digestion with BamHI and NotI.

3.3.2. Expression and purification of GST-BALF1 (residues 1-182) and BALF1 (residues 2-169)-His_6

Although cloning of BALF1 into the parallel plasmid was not successful, two BALF1 constructs, *p*GEX4T3-BALF1 (residues 1-182) and *p*ET21d-BALF1 (residues 2-169), were available in Dr. Sangita Sinha's lab. Then the two constructs that express BALF1 as GST-BALF1 (residues 1-182) and BALF1 (residues 2-169)-His_6 were used to express and purify BALF1. Both GST-BALF1 (residues 1-182) and BALF1 (residues 2-169)-His_6 were expressed in *E. coli* BL21(DE3)*p*LysS cells at 20 ℃ for 16-18 hrs after expression was induced with 0.5 mM IPTG. The soluble protein in the cell lysate was first purified by affinity chromatography using glutathione sepharose resin (GE Healthcare) for GST-BALF1 (residues 1-182) purification, or Ni-NTA resin (Sigma-Aldrich) for BALF1 (residues 2-169)-His_6 purification.

Protein eluted from affinity resin was further purified by SEC using a Superdex 200 10/300 GL column in tandem with a Superdex7510/300 GL column.

The molecular weight of GST-BALF1 (residues 1-182) is 47.2 kD. However, after glutathione affinity purification, as indicated by the SDS-PAGE results (Figure 3.4A), all the elution fractions contain at least three major protein populations with molecular weight smaller than 37 kD. The molecular weights of these three proteins are closer to that of GST (26 kD) than to the fusion protein. Nevertheless, the elution fractions were collected and analyzed by SEC (Figure 3.4B) to obtain more information on the purity, molecular weight and oligomerization state of the protein in the elution fractions. As shown in Figure 3.4B, three proteins elute under Peak 2 that elutes just a little after the 44 kD SEC marker. Of these three proteins, the one with the highest molecular weight of ~ 30 kD elutes mainly in the shoulder on the leading eadge of Peak 2. As the GST tag dimerizes in solution, the GST-BALF1 (residues 1-182) fusion protein is expected to be a dimer of molecular weight of 94.4 kD. However, the SEC chromatogram indicates that none of these three proteins has a molecular weight close to 94.4 kD.

Multiple bands were detected by SDS-PAGE after nickel affinity purification of BALF1 (residues 2-169)-His_6 (Figure 3.5A). As the molecular weight of BALF1 (residues 2-169)-His_6 is 20.5 kD, either of the two bands aligned with the 25 kD marker might be the protein of interest. This was monitored during the following SEC purification. As indicated by the SEC profile Figure 3.5B), both protein were eluted in Peak 2, which was eluted between the 17 kD and 44 kD marker. Therefore, both proteins could be the protein of interest.

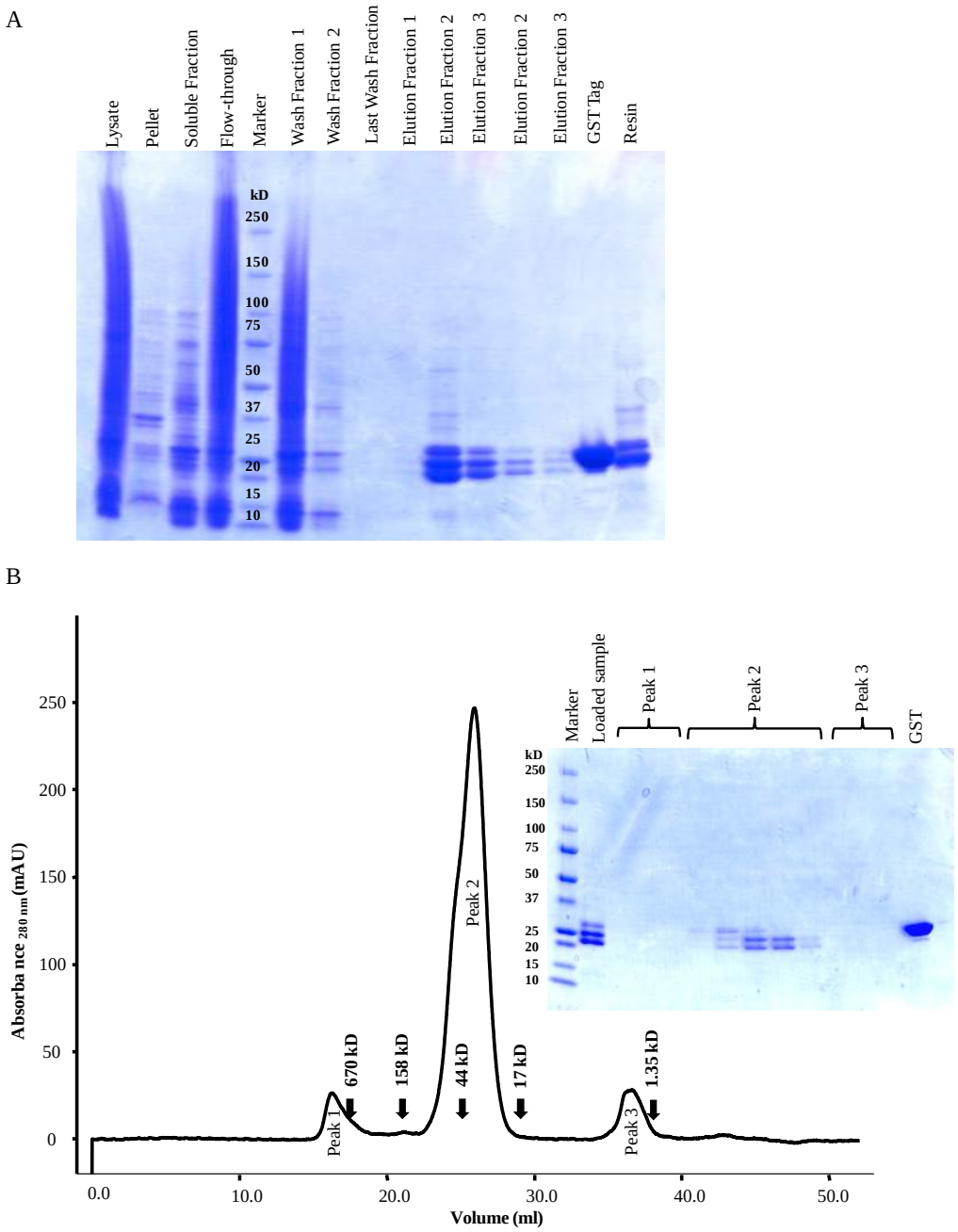

Figure 3.4: Purification of GST-BALF1 (residues 1-182). (A) SDS-PAGE analysis of protein samples collected during glutathione affinity purification. (B) Size-exclusion chromatogram and the corresponding SDS-PAGE analysis.

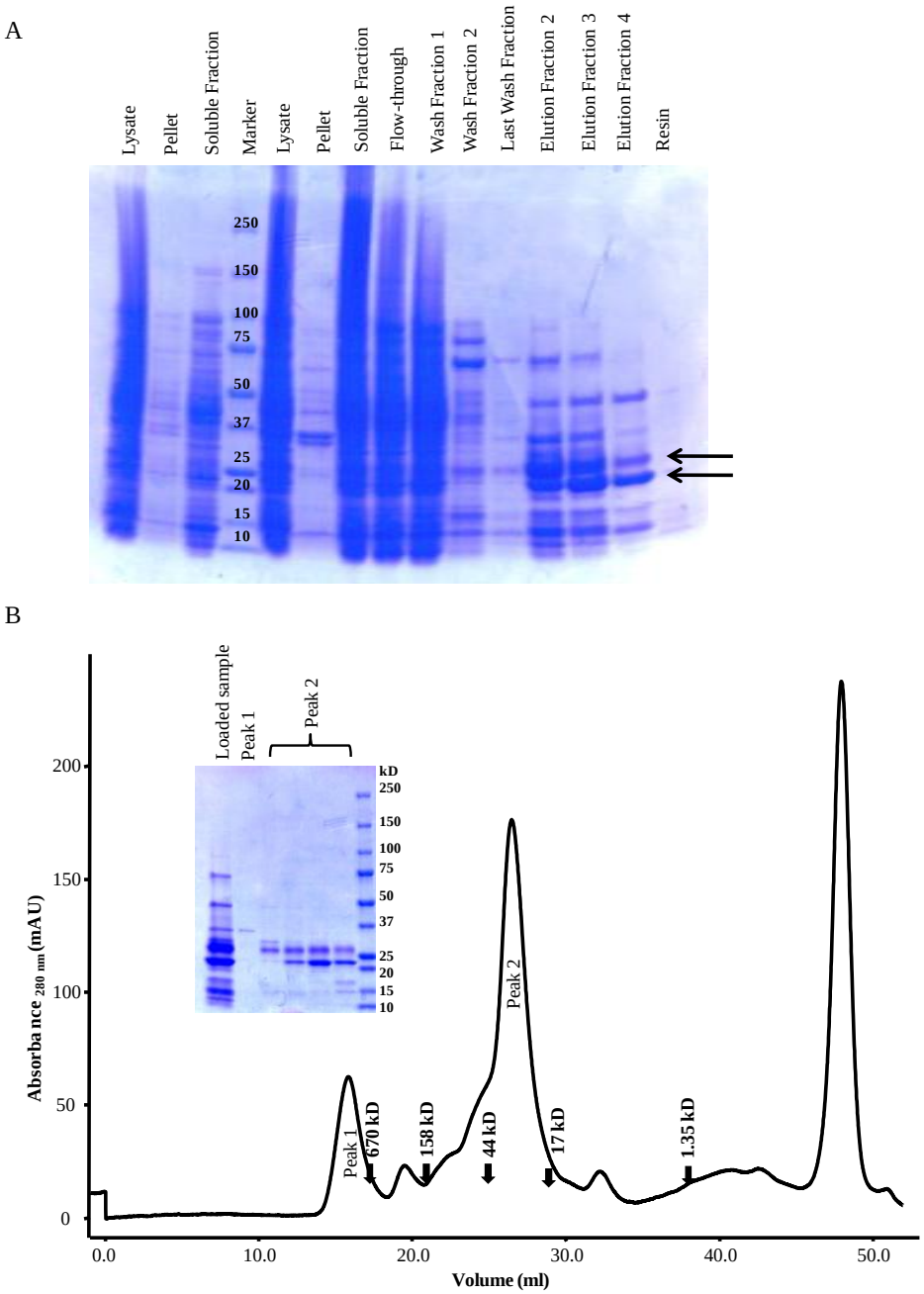

Figure 3.5: Purification of BALF1 (residues 2-169)-His_6. (A) SDS-PAGE analysis of protein fractions collected during nickel affinity purification. The two arrows indicate the two bands with molecular weight close to that of BALF1 (residues 2-169)-His_6. (B) Size-exclusion chromatogram and the corresponding SDS-PAGE analysis.

3.3.3. Detection of expression of GST-BALF1 (residues 1-182) and BALF1 (residues 2-169)-His_6

The affinity purification of GST-BALF1 (residues 1-182) and BALF1 (residues 2-169)-His_6 was assessed by western blot (Figure 3.6). For GST-BALF1 (residues 1-182), the elution fractions (Figure 3.4A) pooled together after glutathione affinity purification was used as the sample for western blot. While for BALF1 (residues 2-169)-His_6, the SEC fractions from Peak 2 (Figure 3.5B) were pooled together and used for western blot. As indicated by the western blot results (Figure 3.6), each of the three bands from the GST-BALF1 (residues 1-182) purification sample contains GST tag, while no band was detected from BALF1 (residues 2-169)-His_6 sample.

The same samples were then used for Edman sequencing and ESI-MS to further analyze components in the sample. The Edman sequencing results indicate that for GST-BALF1 (residues 1-182) sample, the first five residues of each of the three proteins are methionine, serine, proline, isoleucine and leucine. This sequence matches the first five residues of GST tag. While for BALF1 (residues 2-169)-His_6 sample, the first five residue of the protein with relative higher molecular weight are glycine/methionine, lysine, valine, alanine, and lysine. The first five residues for the other protein are glycine/valine/lysine/serine, leucine, isoleucine/glycine, lysine, and proline. Neither of these sequences matches the BALF1 sequence.

ESI-MS was performed on the same proteins sample as mentioned above. As shown in Figure 3.7A, there were four major species in the GST-BALF1 (residues 1-182) sample, including the proteins with molecular weight of 22632 Da, 22762 Da, 26159 Da, and 26759 Da. In contrast, for the BALF1 (residues 2-169)-His_6 sample (Figure 3.7B), there are four major species, including proteins with molecular weight of 23509 Da, 23524 Da, 23551 Da, and 23566

Da. These molecular masses don't agree with the molecular mass of any fragment of BALF1 (residues 2-169)-$His_{6.}$

In summary, all the three detection experiments indicate that GST-BALF1 (residues 1-182) was degraded during purification, or perhaps even earlier, during expression. Based on the ESI-MS analysis, the possible cleavage sites are after GST Y192, L193, P219, or BALF1 P3. Further, no BALF1 (residues 2-169)-His_6 was detected in the protein eluted after SEC.

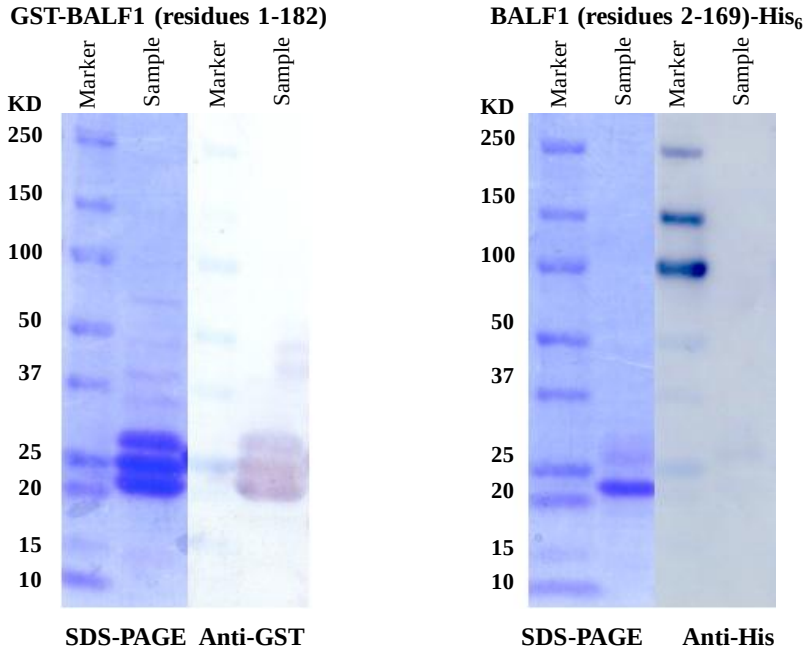

Figure 3.6: Detection of expression of GST-BALF1 (residues 1-182) and BALF1 (residues 2-169)-His_6 by western blot.

A

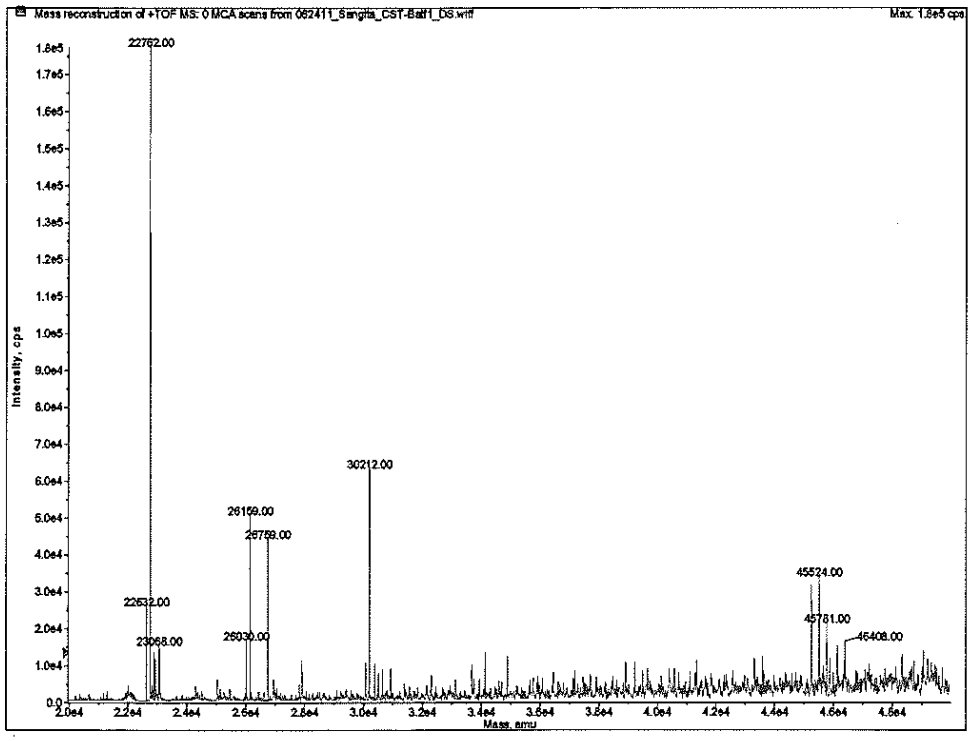

B

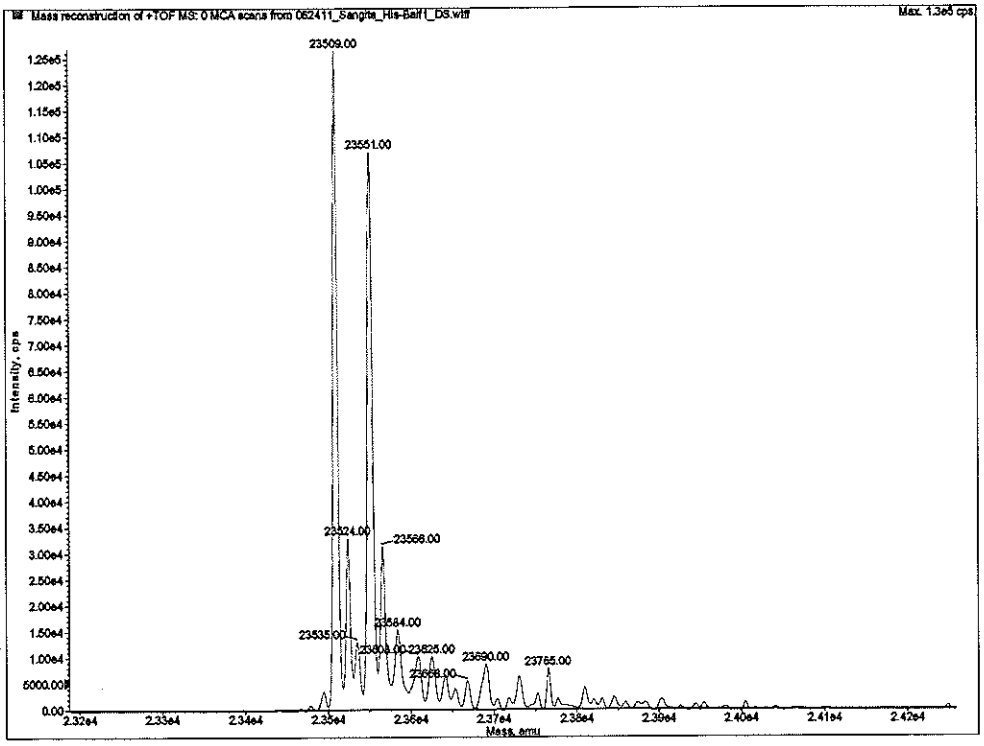

Figure 3.7: Electrospray ionization mass spectrum of (A) GST-BALF1 (residues 1-182) and (B) BALF1 (residues 2-169)-His_6.

3.4. Discussion

The degradation of GST-BALF1 (residues 1-182) and BALF1 (residues 1-169)-His_6 during expression and purification raise the possibility that the two proteins were not well-folded during expression. The inappropriately-folded protein is usually degraded by host protease to guarantee there is no accumulation of abnormal polypeptides within the cells (Baneyx and Mujacic, 2004). To date, successful expression of BALF1 in prokaryotic cells has not been reported. It is likely that BALF1 can only be folded properly when expressed in the eukaryotic expression systems, like insect cells.

As mentioned earlier, two BALF proteins, BALF0 and BALF1 may be encoded by the BALF gene. The currently available combined results suggest that it is highly possible that BALF1 is a multi-domain pro-apoptotic protein while BALF0 is more like an anti-apoptotic protein. Overexpression of multi-domain pro-apoptotic proteins can be highly toxic to the host cells (Donnelly et al., 2001), and therefore, the unsuccessful production of BALF1 may also be due to the toxicity of BALF1. With the rapid developments in biotechnology, there are some modified *E. coli* strains available now for tighter control of the expression of target proteins to overcome the toxicity of the proteins, like the BL21(DE3)*p*LysE strain (Invitrogen) which expresses higher levels of T7 lysozyme than the *p*LysS plasmid in BL21(DE3)*p*LysS. If BALF1 can be expressed in *E. coli*, compared to insect cells, the cultivation simplicity, rapidity and inexpensiveness makes *E. coli* a more competitive expression host.

While expressing BALF1 with different protein tags may help stabilize BALF1, first, the BALF1 gene needs to be cloned into the expression vector successfully. The newly developed cloning methods, Gibson assembly (Gibson et al., 2009), can be utilized to increase the cloning

efficiency. This method has been shown to successfully assemble multiple DNA fragments, regardless of fragment length or end compatibility (Gibson et al., 2009).

CHAPTER 4. PRELIMINARY STUDIES OF THE INTERACTION OF ATG12 AND MCL-1 IN AUTOPHAGY REGULATION

4.1. Introduction

4.1.1. Atg12

Atg12 was the first identified ubiquitin-like autophagy protein, and is involved in the ubiquitin-like conjugation system of autophagy (Geng and Klionsky, 2008). During the conjugation process, Atg12 is activated by an E1-like enzyme, Atg7, through forming a thioester bond between the Atg12 C-terminal G186 and Atg7 C507 (Tanida et al., 1999). The activated Atg12 is then transferred to an E2 enzyme, Atg10 (Shintani et al., 1999), and finally conjugated to the target protein Atg5 by making an isopeptide bond between Atg12 and K149 of Atg5 through an isopeptide bond (Mizushima et al., 1998). The Atg12-Atg5 conjugate then forms a larger multimeric complex with Atg16 through the homo-oligomerization of Atg16 (Mizushima et al., 1999). The formation of the Atg12-Atg5 complex is essential for autophagy, as mutating either Atg12 or Atg5 results in impaired autophagosome formation (Geng and Klionsky, 2008).

4.1.2. Mcl-1

Mcl-l (myeloid cell leukemia 1), an anti-apoptotic Bcl-2 protein, was isolated from the ML-1 human myeloid leukemia cell line during phorbol ester-induced differentiation. Mcl-1 is a relatively large protein of 350 residues compared to other anti-apoptotic Bcl-2 proteins which all contain less than 250 residues (Kozopas et al., 1993). In its large N-terminal region (residues 1-170), there are four PEST sequences (Thomas et al., 2010). PEST sequences are peptide sequences that are rich in proline, glutamic acid, serine, and threonine, and are associated with proteins that have short intracellular half-lives. Therefore, it is not surprising that Mcl-1 has a very short half-life, differing from other anti-apoptotic Bcl-2 proteins (Kozopas et al., 1993).

The NMR structure of Mcl-1 (residues 171-327; PDB code: 2MHS) shows that the structure of Mcl-1 lacking the large N-terminal region is very similar to the typical anti-apoptotic Bcl-2 structure (Figure 4.1A, B & C). A α1 helix, similar to the helix comprising the BH4D in other anti-apoptotic Bcl-2 protein, is formed by residues 173-191 of Mcl-1 (Figure 4.1A). Similar to Bcl-X_L, Mcl-1 also contains two central α-helices α5 and α6, surrounded by five amphipathic α-helices (Figure 4.1A) and a hydrophobic groove on the surface (Figure 4.1B). The superimposition of Mcl-1 with Bcl-X_L confirms that the two proteins have very similar three-dimensional structures (Figure 4.1C). Notably, in Bcl-X_L, there is a 60-residue loop connecting α1 and α2 and is not observed in the X-ray crystal structure. In Mcl-1, α1 and α2 is connected by smaller 11-residue loop and is characterized in the NMR structure. The hydrophobic groove of Mcl-1 is also responsible for binding to the BH3D of other BH3D-containing proteins such as BAX (Figure 4.1D). Comparing to the multi-BH domain pro-apoptotic Bcl-2 proteins, BAX for example, the BH1D, BH2D and BH3D of Mcl-1 assemble almost the same structure formed by BH1D, BH2D and BH3D of BAX (Suzuki et al., 2000). Although the BH4D is not predicted to be present in BAX, a similar α-helix that assembles the BH4D of anti-apoptotic Bcl-2 proteins is formed by the residues before BAX BH3D. The major difference between the structures of Mcl-1 and BAX is that the hydrophobic groove which is present on the surface of Mcl-1 is occupied by an α helix formed by the BAX TM domain in the BAX structure (Suzuki et al., 2000).

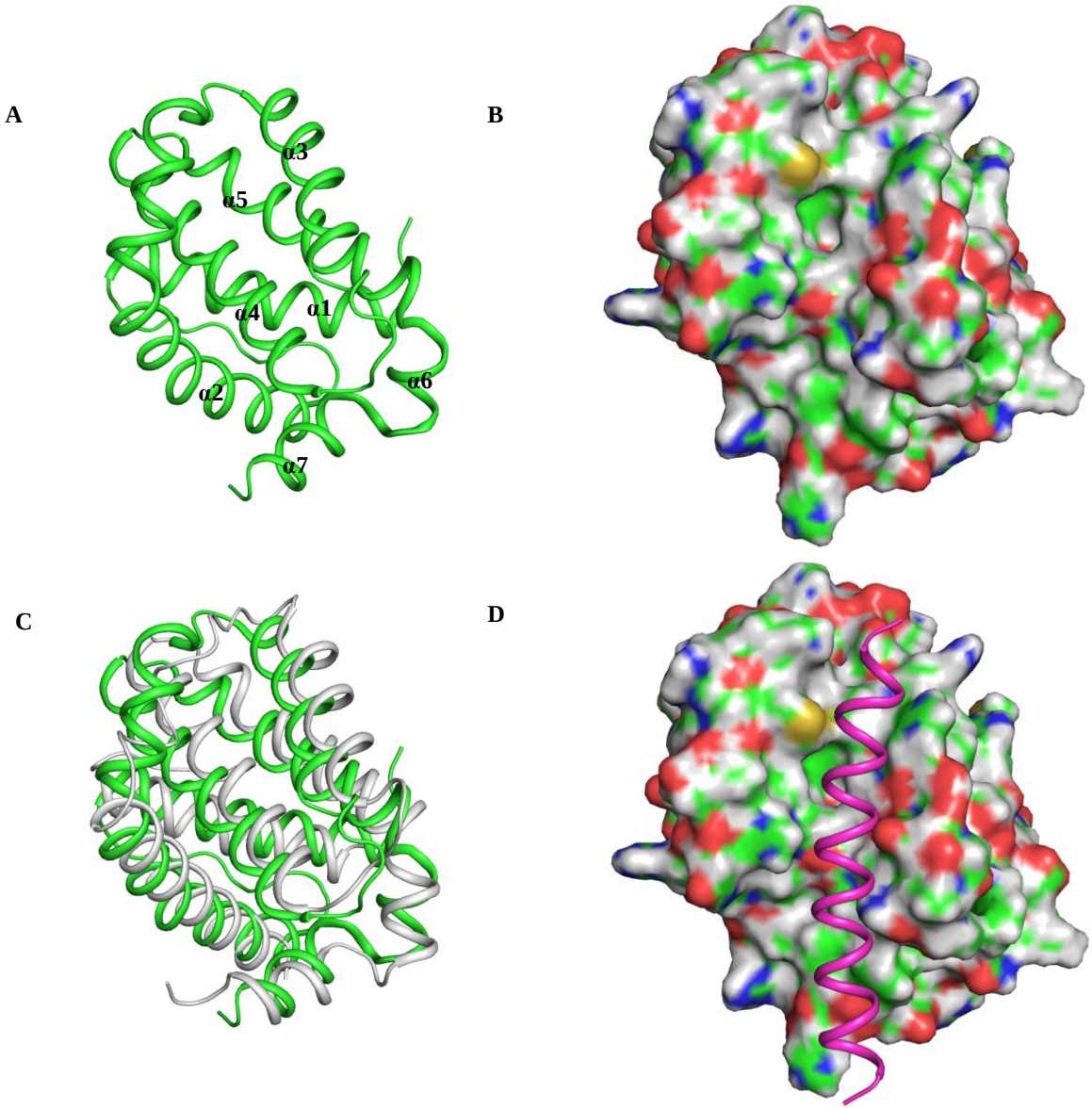

Figure 4.1: X-ray crystal structure of unbound Mcl-1 and Mcl-1 in complex with BAX BH3D. (A) Mcl-1 shown in ribbon presentation. Each α-helix is labeled. (B) Mcl-1 shown in surface presentation. Atoms are colored by type: oxygen red, nitrogen blue, sulfur yellow and carbon green. (C) Superimposition of Mcl-1(green) with Bcl-X_L(grey). (D) Mcl-1:BAX BH3D complex. Mcl-1 is shown in surface presentation and Beclin 1 BH3D is shown in ribbon presentation.

Similar to Bcl-X_L, Mcl-1 has been shown to bind to both BAX and BAK and inhibits BAX/BAK-induced cytochrome c release (Germain et al., 2008). However, Mcl-1 is unique among all the anti-apoptotic Bcl-2 homologs because it binds to a different subset of BH3D-only

proteins from Bcl-2, Bcl-X_L and Bcl-W. The NOXA BH3D binds highly selectively to Mcl-1, and 7.5-fold more weakly to A1, but does not bind to the other Bcl-2 proteins. The BH3Ds of BAD and BMF bind Mcl-1 more weakly than to any of the other anti-apoptotic Bcl-2 proteins. The BH3Ds of BIK, HRK, and Bid bind to Mcl-1 with similar affinity as to Bcl-2, but more weakly as compared to Bcl-X_L, Bcl-W, and A1. Mcl-1 only binds to the BH3Ds of BIM and PUMA with strong affinities comparable to all other anti-apoptotic Bcl-2 proteins (Chen et al., 2005).

Mcl-1 is also subjected to caspase-dependent cleavage, at two distinct sites, D127 and D157, within the PEST sequences, particularly during the progression of apoptosis. This specific cleavage of Mcl-1 has been shown to be important for TRAIL-induced apoptosis in Jurkat T cells, while Bcl-2 or Bcl-X_L is not affected. The C-terminal fragment of Mcl-1 becomes pro-apoptotic as a result of caspase-dependent cleavage (Weng et al., 2005). GrB also cleaves Mcl-1 at the same two sites and additionally at D117. The major Mcl-1 C-terminal fragment (residues 118–350) is generated by cleavage at D117, and has been shown to bind to BIM with lower affinity compared to full-length Mcl-1, thereby losing its function in inhibiting apoptosis (Han et al., 2005).

Mcl-1 is also subject to phosphorylation at multiple sites, including S64, T92, S121, S155, S159 and T163. S64 is phosphorylated by CDK1, CDK2 and JNK, which is required for Mcl-1 to interact with various pro-apoptotic Bcl-2 proteins. T92 is the target of ERK-1 and is phosphorylated in conjugation with T163. Phosphorylation of T92 and T163 by ERK has been reported to stabilize Mcl-1. S121 can be phosphorylated by JNK and p38 in conjugation with T163, resulting in a more stable Mcl-1. However, the function of phosphorylation at these two sites is still controversial. In one study, phosphorylation provides protection against TNFα-

induced apoptosis. But in a separate study, a double mutant S121A/T163A of Mcl-1 that disables phosphorylation, makes Mcl-1 more potent at inhibiting apoptosis induced by H_2O_2 treatment. S155 is the target of GSK-3 and is phosphorylated in conjugation with T163. Phosphorylation at these two sites leads to inhibition of the anti-apoptotic function of Mcl-1. S159 can also be phosphorylated by GSK, providing T163 is already phosphorylated by JNK. Phosphorylation of S159 significantly destabilizes and reduces cellular levels of Mcl-1, and impairs its interaction with BIM and its anti-apoptotic function. T163 is the target of ERK-1, GSK-3 and JNK. As noted, its phosphorylation is required for phosphorylating other residues (Thomas et al., 2010).

4.1.3. The Atg12:Mcl-1 interaction

In addition to its role in autophagy, recently, Atg12 was shown to be a positive mediator of apoptosis through interacting with anti-apoptotic Bcl-2 proteins (Rubinstein et al., 2011). Atg12 co-immunoprecipited with the anti-apoptotic Bcl-2 homolog, Mcl-1, and weakly with Bcl-2. Further, the interaction between Atg12 and Bcl-2 proteins was disrupted by the co-expression of the pro-apoptotic, BH3D-only protein BAD. Importantly, ABT-737, a BH3D-mimetic inhibitor that specifically targets Bcl-2/Bcl-X_L, but not Mcl-1 (Mazumder et al., 2012, van Delft et al., 2006), disrupted the Co-IP of Atg12 with Bcl-2, but not with Mcl-1 (Rubinstein et al., 2011). Mammalian Atg12 homologs were found to contain a potential BH3D-like sequence motif that is N-terminus to the ubiquitin-like fold of Atg12. This motif appears to be an abnormal BH3D, because although it contains conserved residues important for binding to the hydrophobic surface groove on Bcl-2 (Oberstein et al., 2007, Sinha et al., 2008), it also bears a proline, which would prevent it from forming an α-helix like other BH3Ds. Notably, Atg12 mutations within the BH3D-like motif did not affect Atg12-Atg5 conjugation, or its role in autophagy. Bcl-2 homologs bind to free Atg12, but not to Atg12-Atg5 conjugates. In addition to the BH3D-like

motif, binding of Mcl-1 to Atg12 was found to require a second Atg12 site comprising an adjacent loop (Rubinstein et al., 2011). Together, this information suggests that Atg12 may competitively bind to the hydrophobic grooves of anti-apoptotic Bcl-2 proteins, especially Mcl-1, preventing them from binding to multi-BH domain pro-apoptotic Bcl-2 proteins, thus triggering apoptosis.

4.1.4. In this study

In order to test the directed binding of Atg12 and Mcl-1 *in vitro*, we expressed and purified the well-folded and stable domains of Atg12 and Mcl-1 to homogeneity. Pull-down assay and ITC were then employed to study the interaction between Atg12 and Mcl-1 using purified proteins. An Atg12 BH3D-like motif-derived peptide was also tested for binding to Mcl-1 using ITC. No binding was observed between either Atg12 and Mcl-1 or Atg12 BH3D-like motif-derived peptide and Mcl-1. Although we did not observe any interaction, there are still questions need to be answered before we can make the conclusion that Atg12 doesn't bind to Mcl-1. The most obvious and important question is that whether the unstructured portions of Atg12 or Mcl-1 are required for the interaction.

4.2. Materials and methods

4.2.1. Atg12 expression and purification

The vector to express His_6-MBP-TEV-Atg12(residues 52-140)-intein-chitin binding domain fusion protein was a kind gift from Prof. Takanori Otomo at the Scripps Research Institute, La Jolla, California. This plasmid was transformed into *E. coli* BL21(DE3)*p*LysS chemically competent cells for the overexpression of His_6-MBP-TEV-Atg12(residues 52-140)-intein-chitin binding domain fusion protein. Transformed cells were grown in agar plates supplemented with 100 μg/μL Ampicillin and 35 μg/μL Chloramphenicol. A signal colony was

picked and grown in 5 ml LB media supplemented with 100 µg/µL Ampicillin and 35 µg/µL Chloramphenicol at 37 ℃ overnight. The next day, the 5 ml overnight culture was used to inoculate 50 ml of LB supplemented with 100 µg/µL Ampicillin and 35 µg/µL Chloramphenicol and grown at 37 ℃ for 2 hrs to make the secondary culture. 20 ml secondary culture was then used to inoculate 1 L LB media supplemented with 100 µg/µL Ampicillin and 35 µg/µL Chloramphenicol and further grown at 37 ℃ until optical density of 0.6-0.8 was reached at 600 nm. At this point, the overexpression of His_6-MBP-TEV-Atg12(residues 52-140)-intein-chitin binding domain fusion protein was induced with 0.2 mM IPTG. The cells were further grown at 18 ℃ with shaker speed of 220 rpm for 16 hours. Then the cells were harvested by centrifugation at 4000 rpm for 20 min at 4 ℃.

Cells harvested from 2 L culture were immediately suspended in 100 ml lysis buffer comprising 20 mM Tris, pH 8.0, 500 mM NaCl, 1 mM Ethylenediaminetetraacetic acid (EDTA) and 1 tablet of cOmplete protease inhibitor cocktail (Roche). The cells were lysed by emulsification and the crude extract centrifuged at 20000 g for 30 min at 4 ℃ to remove the cellular debris. The resulting supernatant was loaded onto a gravity column containing 20 ml of chitin resin (New England Biolabs). After the supernatant had completely passed through the column, the column was washed with 250 ml lysis buffer to remove contaminating protein. To induce on-column intein self-cleavage to release His_6-MBP-TEV-Atg12(residues 52-140) from the chitin binding tag, the column was further washed with 60 ml lysis buffer containing 50 mM Dithiothreitol, then incubated at 4 ℃ for overnight cleavage. The next day, the column was wash with 60 ml lysis buffer to wash off the cleaved His_6-MBP-TEV-Atg12(residues 52-140). All wash fractions containing His_6-MBP-TEV-Atg12(residues 52-140) were collected, concentrated to 2.8 mg/ml, and further purified by SEC using a Superdex 200 10/300 GL column in tandem

with a Superdex 75 10/300 GL column (GE Healthcare). The column was pre-equilibrated with the SEC buffer comprised of 20 mM Tris, pH 8.0, 100 mM NaCl, 2 mM 2-mercaptoethanol. 1.8 ml of 2.8 mg/ml protein was loaded onto the tandem SEC column and eluted with SEC buffer at 0.5 ml/min flow rate. The purity of His_6-MBP-TEV-Atg12(residues 52-140) eluted from SEC was evaluated using SDS-PAGE. Fractions from the single peak corresponding to His_6-MBP-TEV-Atg12(residues 52-140) were pooled together and concentrated to 3.2 mg/ml. Because His_6-MBP-TEV-Atg12(residues 52-140) tended to aggregate over time, the purified protein was immediately used for ITC experiments and pull-down assays.

4.2.2. Mcl-1 expression and purification

The vector that expresses His_6-MBP-TEV-Mcl-1(residues 172-327) was a kind gift from Prof. Amy E. Keating at Massachusetts Institute of Technology, Cambridge, Massachusetts. *E. coli* BL21(DE3)*p*LysS chemically competent cells were transformed with this plasmid for the overexpression of His_6-MBP-TEV-Mcl-1(residues 172-327). The transformed cells were grown in agar plate supplemented with 50 μg/μL Kanamycin and 35 μg/μL Chloramphenicol. A signal colony was picked and grown in 5 ml LB media supplemented with 50 μg/μL Kanamycin and 35 μg/μL Chloramphenicol at 37 ℃ overnight. The second day, the 5 ml overnight culture was used to inoculate 50 ml of LB supplemented with 50 μg/μL Kanamycin and 35 μg/μL Chloramphenicol, and grown at 37 ℃ for 2 hrs to make the secondary culture. Each 20 ml secondary culture was then used to inoculate 1 L LB media supplemented with 50 μg/μL Kanamycin and 35 μg/μL Chloramphenicol and further grown at 37 ℃ until an optical density of 0.6-0.8 was reached at 600 nm. At this point, overexpression of His_6-MBP-TEV-Mcl-1(residues 172-327) was induced with 0.5 mM IPTG. The cells were further grown at 20 ℃ with

a shaker speed of 220 rpm for 16-18 hrs. Then the cells were harvested by centrifugation at 4000 rpm for 20 min at 4 ℃ and stored at -80 ℃ until usage.

The cell pellet from 2 L culture was suspended in 100 ml lysis buffer comprised of 20 mM Tris, pH 8.0, 150 mM NaCl, 2 mM Dithiothreitol and 1 tablet of cOmplete protease inhibitor cocktail (Roche). The cells were lysed by sonication and the crude extract was centrifuged at 20000 g for 30 min at 4 ℃ to remove cellular debris. The resulting supernatant was loaded onto a gravity column containing 3 ml of amylose resin (New England Biolabs). After the supernatant has passed through the column completely, the column was washed with 40 ml lysis buffer to remove contaminating protein. On-column TEV cleavage was performed by adding 4 mg of GST-TEV to the column to remove the His_6-MBP tag from Mcl-1(residues 172-327). The amylose resin was resuspended to enable mixing, then incubated at 4 ℃ for overnight cleavage. The next day, this column was washed with lysis buffer to wash off the cleaved Mcl-1(residues 172-327). Wash fractions containing Mcl-1(residues 172-327) were pulled together and passed through 2 ml Ni-NTA resin (Sigma-Aldrich) to remove contaminating His_6-MBP. The flow-through was collected, concentrated to 7 mg/ml and further purified by SEC using a Superdex 200 10/300 GL column in tandem with a Superdex7510/300 GL column (GE Healthcare). The column was pre-equilibrated with the SEC buffer comprising of 50 mM HEPES, pH 7.5, 150 mM NaCl, 2mM 2-mercaptoethanol. 1ml of 7 mg/ml protein was loaded onto the tandem SEC column and eluted with SEC buffer at 0.5 ml/min flow rate. The purity of Mcl-1 (residues 172-327) eluted from SEC was evaluated using SDS-PAGE. Fractions from the single peak corresponding to Mcl-1 (residues 172-327) were pooled together, concentrated to 5.2 mg/ml, and stored in 100 ul aliquots in -80 ℃.

4.2.3. Peptide synthesis

Atg12 BH3D-like motif-derived peptides (amino acid sequence: EGDTKKKIDILLKAVGDTPIMKTKKW) were chemically synthesized and HPLC purified to > 95% purity, with peptide purity confirmed by electrospray mass spectrometry (RS Synthesis).

4.2.4. Pull-down assay

1 mg of His_6-MBP-TEV-Atg12 (residues 52-140) and 0.5 mg of Mcl-1 (residues 172-327) at a molar ratio of 1:1 was loaded on a column containing 1 ml of amylose resin (New England Biolads). After a good mixing, the column was incubated at 4 ℃ for 2 hours. The column was then washed with washing buffer comprised of 20 mM Tris, pH 8.0, 300 mM NaCl, 2 mM 2-mercaptoethanol, and fractions of 0.5 ml each were collected. The OD_{280} of each fraction was measured and the washing continued until OD_{280} reached ~0. The column was then eluted with 20 mM maltose in the wash buffer, and 0.5 ml fractions were collected. Elution was stopped when OD_{280} reached ~0. Each washing and elution fraction sample was evaluated using SDS-PAGE.

4.2.5. ITC

ITC was performed using a Low Volume Nano ITC (TA Instruments). Atg12 protein, Atg12 BH3D-like motif-derived peptide and Mcl-1 protein were loaded into separate dialysis cassettes, and co-dialyzed into ITC buffer comprised of 20 mM Tris, pH 8.0, 300 mM NaCl and 2 mM β-mercaptoethanol. ITC was performed at 25°C with 25 injections of 2 μL each.

4.3. Results

4.3.1. Expression and purification of Atg12

The X-ray crystal structureof 94-amino acid protein *Arabidopsis thaliana* Atg12 only contains residues 10-94, which indicates that the first 9 residues are unstructured (Suzuki et al.,

2005). Sequence alignment shows that residue 10-94 of *Arabidopsis thaliana* Atg12 aligns with residue 53-140 of human Atg12 (Suzuki et al., 2005). In fact, we showed that residues 1-49 of human Atg12 constitute an intrinsically disordered region (IDR) (Mei et al., 2014). Therefore, to express a well-folded human Atg12 for ITC, pull-down and potentially crystallization experiments, we used the expression construct containing only residues 52-140. This construct contains all the conserved residues in the Atg12 BH3D-like motif that are thought to be important for interacting with Mcl-1. The Atg12 was expressedas a His_6-MBP-TEV-Atg12 (residues 52-140)-intein-chitin binding domain fusion proteinin *E. coli*B L21(DE3)*p*LysS cells, and soluble protein in the cell lysate was first purified by chitin affinity resin. The chitin-binding domain was then removed by intein self-cleavage in a reducing environment. The resulting His_6-MBP-TEV-Atg12 (residues 52-140) was further purified to homogeneity by SEC using a Superdex 200 10/300 GL column in tandem with a Superdex 7510/300 GL column.The His_6-MBP can be removed by TEV cleavage. However, the resulting isolated Atg12 aggregates. Therefore, the His_6-MBP tag is important for stabilizing the Atg12 (residues 52-140) and was not cleaved for all the experiments. The final SEC purification is shown in Figure 4.2. SDS-PAGE (Figure 4.2) indicates that compared to the second lane on the gel that corresponds to the intact fusion protein, an additional band of ~50 kD is observed after the intein cleavage, which is most likely His_6-MBP-TEV-Atg12 (residues 52-140). The wash sample collected after intein cleavage mostly contains His_6-MBP-TEV-Atg12 (residues 52-140), and was concentrated (Figure 4.2 lane 4) and further purified by SEC. The resulting SEC profile contained 2 major peaks (Figure 4.2). Peak 1 that appeared in the void volume, did not contain any components dectectablebycoomassie blue stained SDS-PAGE gel. Peak 2, especially the center of the peak, contains fairly pure His_6-MBP-TEV-Atg12 (residues 52-140). The apparent molecular weight of

His_6-MBP-TEV-Atg12 (residues 52-140) calculated from the elution volume of Peak 2 is 41.5kD, which is a little smaller than the theoretical molecular weight of His_6-MBP-TEV-Atg12 (residues 52-140) (54.2kD) calculated from the amino acid sequence. The fractions from the center of Peak 2 were pooled together and concentrated to 3.2 mg/ml and used immediately for ITC and pull-down assays to avoid aggregation. The final yield of the purified Atg12 obtained from the one liter of the bacterial culture was 1.3 mg.

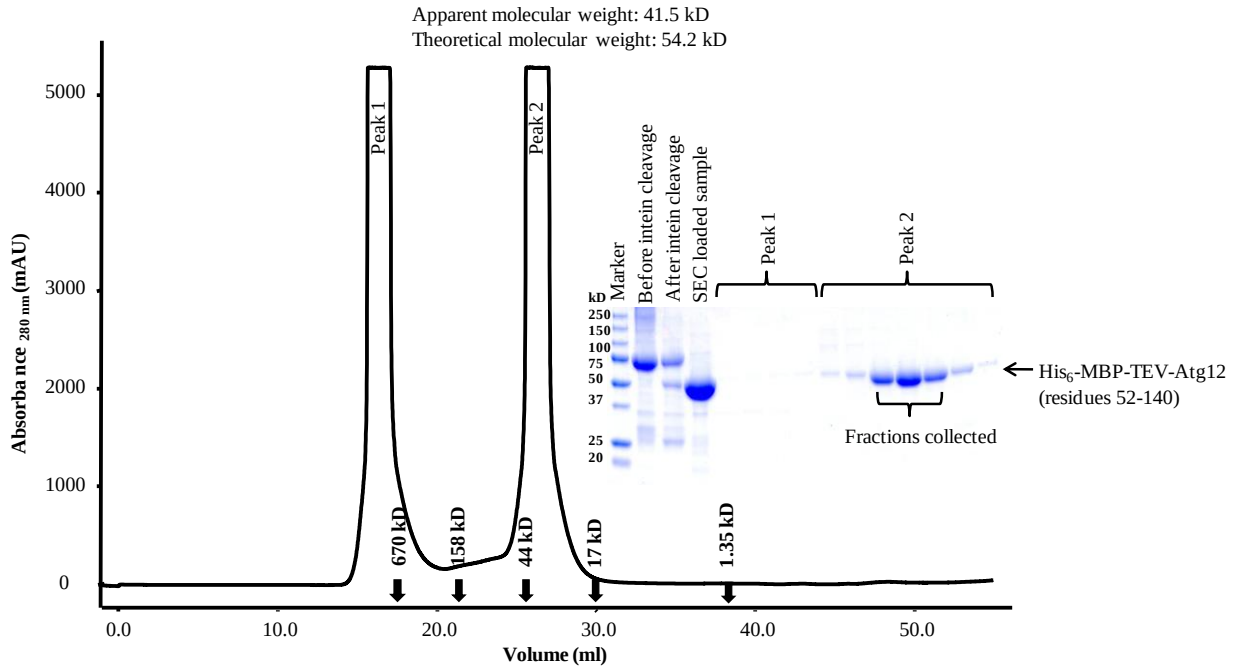

Figure 4.2: Size-exclusion chromatogram and the corresponding SDS-PAGE of His_6-MBP-TEV-Atg12 (residues 52-140).

4.3.2. Expression and purification of Mcl-1

As noted, Mcl-1 has a larger N-terminal region compared to other anti-apoptotic Bcl-2 proteins and four PEST sequences have been identified in this region (Thomas, Lam et al. 2010). PEST sequences are associated with proteins that have short intracellular half-lives. Therefore, studies require purified Mcl-1 protein usually use a Mcl-1 construct without the N-terminal region. Moreover, both NMR and X-ray structures of Mcl-1 demonstrated that Mcl-1without the

N-terminal region folds into structures of typical anti-apoptotic Bcl-2 homologs (Day et al., 2005, Liu et al., 2014, Czabotar et al., 2011, Liu et al., 2010, Day et al., 2008, Fire et al., 2010) and is sufficient for binding to BH3Ds of other Bcl-2 proteins, including BAX (Czabotar et al., 2011), BID (Liu et al., 2010), PUMA (Day et al., 2008), NOXA (Day et al., 2008), and BIM (Fire et al., 2010).

Therefore, in this study, to express and purify stable, soluble Mcl-1, we used a construct to express Mcl-1 (residues 172-327), which lacks the N-terminal region and C-terminal transmembrane domain. The His_6-MBP-TEV-Mcl-1 (residues 172-327) was expressed in *E. coli* BL21(DE3)*p*LysS cells. Soluble protein in the cell lysate was purified by amylose affinity chromatography, followed by His_6-MBP tag removal by TEV cleavage and nickel affinity chromatography. The resulting Mcl-1 (residues 172-327) was purified to homogeneity by SEC using tandem Superdex 200 10/300 GL and Superdex 75 10/300 GL columns. The final SEC purification results are shown in Figure 4.3. Two major peaks are observed in the SEC profile. Peak 1 was eluted before the void volume of the tandem Superdex column and contained contaminant proteins. Peak 2 contains pure Mcl-1 protein and the apparent molecular weight of Mcl-1 calculated from the elution volume is 14.9 kD, which is similar to the theoretical molecular weight of the Mcl-1 monomer calculated from the amino acid sequence. The fractions from Peak 2 were pooled together and concentrated to 5.2 mg/ml and stored in 200 μl aliquots at -80 ℃ until usage. The final yield of the purified Mcl-1 obtained from the one liter of the bacterial culture was 3 mg.

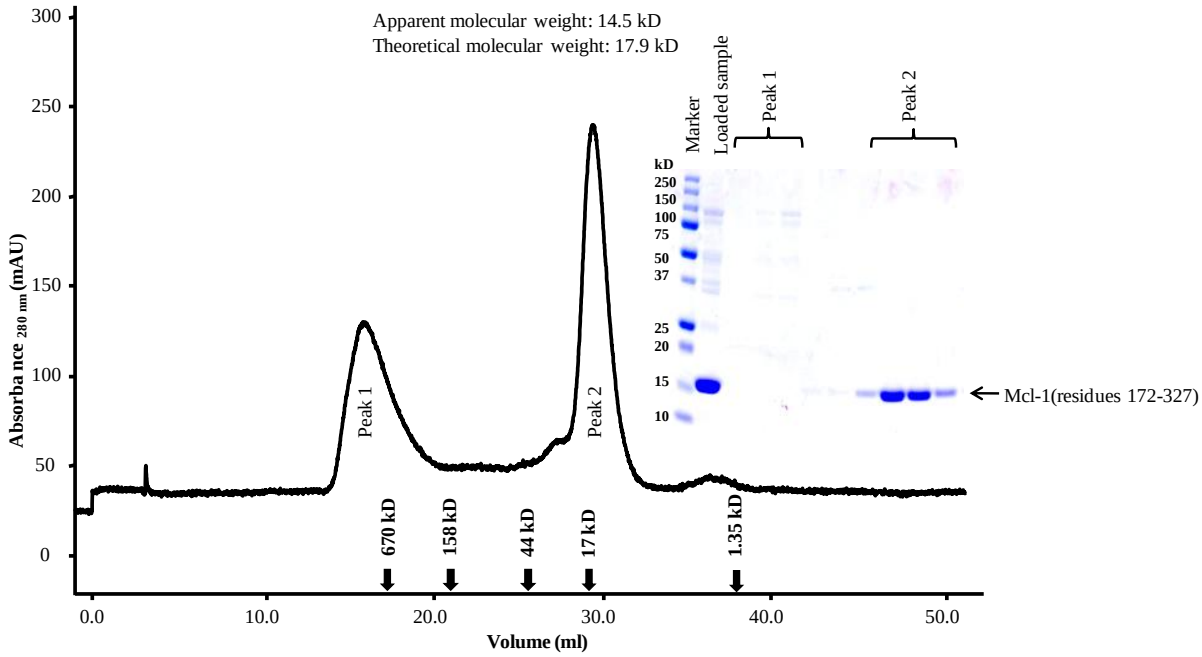

Figure 4.3: Size-exclusion chromatogram and the corresponding SDS-PAGE of Mcl-1 (residues 172-327).

4.3.3. Assaying Atg12 binding to Mcl-1 by pull-down assays

To assess whether purified Atg12 and Mcl-1 binds *in vitro*, MBP-based pull-down assays were performed and the results are shown in Figure 4.4. 1 mg His_6-MBP-TEV-Atg12 (residues 52-140) (Figure 4.4 Lane 1) and 0.5 mg Mcl-1(residues 172-327) (Figure 4.4Lane 2) were mixed at a 1:1.5 molar ratio by pipetting and then loaded on to a gravity column containing 1 ml amylose resin. After mixing thoroughly by pipetting, the column was incubated at 4 ℃ for 2 hours. The column was then washed until no protein could be detected in the wash fractions, and wash fractions 1 to 5 and the final wash were loaded in PAGE Lanes 4 to 10 (Figure 4.4). The column was eluted with 20 mM maltose and elution fractions 2 to 6 were loaded in Lanes 11 to 14 (Figure 4.4). SDS-PAGE was also used to test the resin after elution (Figure 4.4 Lane 15). As demonstrated in Figure 4.4, no Atg12 was removed by washing the resin, indicating that all Atg12 is bound to the amylose resin. However, all Mcl-1 was washed off within the first two

wash fractions (Figure 4.4 Lane 4-10). No Mcl-1 was present in the elution fractions (Figure 4.4 Lane 11-14) or stuck to the resin (Figure 4.4 Lane 15). In the elution fractions, only His_6-MBP-TEV-Atg12 (residues 52-140) was detected. Therefore, the pull-down assys indicate that purified Mcl-1 (residues 172-327) does not bind to His_6-MBP-TEV-Atg12 (residues 52-140) *in vitro*.

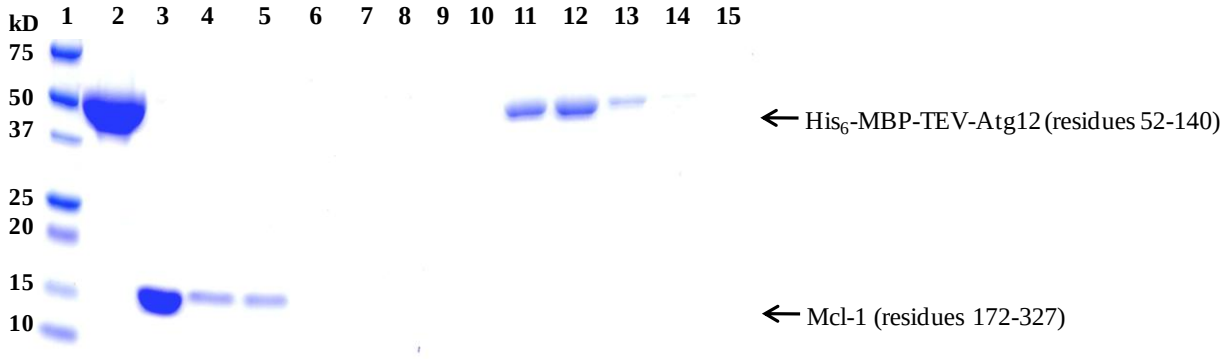

Lane 1: Marker
Lane 2: His_6-MBP-TEV-Atg12 (residues 52-140)
Lane 3: Mcl-1 (residues 172-327)
Lane 4-10: Wash fraction1 to 5 and 10
Lane 11-14: Elution fraction 2 to 6
Lane 15: Resin

Figure 4.4: Pull-down assay to assess the binding between Atg12 and Mcl-1.

4.3.4. Studies of Atg12 binding to Mcl-1 by ITC

Next, we used ITC to determine if purified Mcl-1 binds to purified Atg12 protein or chemically synthesized Atg12 BH3D-like peptide. For Mcl-1:Atg12 binding, 0.266 mM Mcl-1 (residues 172-327) protein were loaded into the syringe and titrated into 0.026 mM Atg12 in the cell. The ITC titration profile (Figure 4.5 A) indicates there is no detectable interaction between Mcl-1 (residues 172-327) and Atg12, as all peaks in the titration profile are similarly small, reflecting only dilution heat produced upon each injection. For testing of Atg12 BH3D-like peptide binding to Mcl-1, 0.85 mM peptide were loaded into syringe and titrated into 0.095 mM Mcl-1 (residues 172-327) in the cell. Similarly, only dilution heat was detected upon each

injection (Figure 4.5 B). Therefore, no interaction was detected between Atg12 BH3D-like peptide and Mcl-1 (residues 172-327). The ITC results together with the pull-down assay results suggest that neither purified Atg12 protein nor the Atg12 BH3D-like peptide was able to bind to purified Mcl-1 (residues 172-327) *in vitro*.

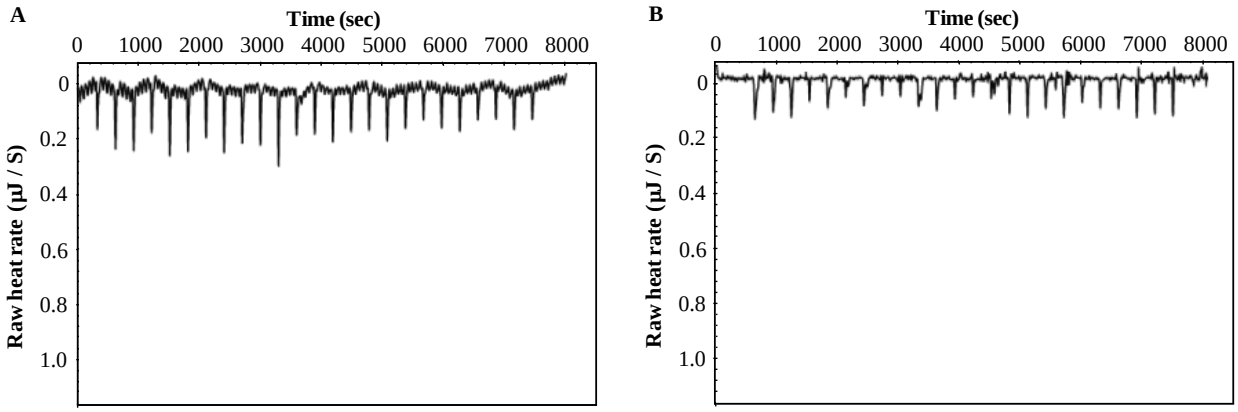

Figure 4.5: ITC titration profiles of Mcl-1 to Atg12 (A) and Atg12 BH3D-like motif-derived peptide (B).

4.4. Discussion

In this study, we tested binding of Atg12 to Mcl-1 using protein purified by pull-down assays and ITC. Since our ITC results indicate that the Atg12 BH3D-like peptide does not bind to Mcl-1, it is possible that the Atg12 IDR is also required for binding. BH3D-derived peptides have been shown to be sufficient for binding to various anti-apoptotic Bcl-2 proteins, including Mcl-1, and form α-helices upon binding (Oberstein et al., 2007, Sinha et al., 2008, Ku et al., 2008a, Chen et al., 2005). As noted, Atg12 BH3D-like motif contains a proline, which would prevent it from forming an α-helix like other BH3Ds. Therefore, unlike other BH3Ds, the Atg12 BH3D-like motif may not be sufficient for binding to Mcl-1. As only the IDR is missing in the construct used for binding assay in this study, it is very likely the IDR is involved in interacting with Mcl-1.

Although an interaction between the two proteins was previously indicated by Co-IP (Rubinstein et al., 2011), in our study, no interaction was detected by either pull-down assay or ITC. The most notable difference between the previous Co-IP assay and our study is that purified proteins that were used in our studies. Full-length Atg12 and Mcl-1 were expressed and used for cellular interaction assays (Rubinstein et al., 2011). However, for the *in vitro* binding assays performed in our study, in order to obtain well-folded and stable proteins, the Atg12 IDR and PEST sequences, as well as the TM of Mcl-1, were not included in the expression constructs. Therefore, if the interaction between Atg12 and Mcl-1 requires part or the whole IDR of Atg12 and/or PEST sequences of Mcl-1, no interaction would be detected using the Atg12 and Mcl-1 expressed in this study. Alternately, it is possible that the Atg14:Mcl-1 may not interact directly. CoIPs often result in identification of false positive interactions, especially when one of the binding partners is also involved in formation of a large protein complex (Solstad et al., 2008),

Therefore, for future studies, Co-IPs should be utilized to determine the minimal constructs of Atg12 and Mcl-1 that are required for the interaction. These constructs can then be used for ITC and pull-down assays. Moreover, if post-translational modifications are necessary for the interaction, instead of *E. coli* cells, yeast or mammalian cells should be used for expressing Atg12 and Mcl-1.

CHAPTER 5. INVESTIGATING THE STRUCTURE OF BECLIN 2

5.1. Introduction

Recently, Beclin 2, a 431-residue protein, that shares 57% of amino acid sequence identity with Beclin 1, was identified by bioinformatics analyses of the human gene database (He et al., 2013). Human *beclin 2* maps to chromosome 1q43 near the autophagy gene MAP1LC3C. Unlike the genomic organization of human *beclin 1* which contains 12 exons, *beclin 2* is intronless,

Beclin 2, like Beclin 1, has also been shown to regulate autophagy in both basal and starvation conditions. During normal growth conditions, when the expression of Beclin 2 in HeLa cells was knocked down by siRNA treatment, decreased numbers of GFP-LC3 puncta and a decreased ratio of LC3-II/LC3-I was observed, while levels of p62 stay the same. Upon amino acid starvation, siRNA knockdown of Beclin 2 expression leads to decreased numbers of GFP-LC3 puncta, decreased ratio of LC3-II/LC3-I, and decreased p62 degradation.

In addition to its function in autophagy, Beclin 2, but not Beclin 1, has been found to regulate endolysosomal trafficking and degradation of G protein-coupled receptors (GPCR). G protein-coupled receptor-associated sorting protein 1 (GASP1) interacts with several GPCRs, including the opioid receptor δ1 (DOR), the cannabinoid receptor 1 (CB1R), and β-adrenergic receptor, and is required for their agonist-induced lysosomal degradation. The N-terminal 1-88 residues of human Beclin 2 have been shown to interact with the C-terminal 899–1395 residues of GASP1 by both yeast two-hybrid and Co-IP assays. When the expression of Beclin 2 was knocked out by siRNA treatment in HEK293 cells, the endolysosomal trafficking and degradation of GPCRs that interact with GASP1 was blocked. Excess CB1R signaling has been reported to increase food intake, result in weight gain, and promote insulin resistance

(Maccarrone et al., 2010). Therefore it is not surprising that Beclin 2 heterozygous knockout mice have defective autophagy, increased levels of brain cannabinoid 1 receptor, elevated food intake, obesity and insulin resistance.

Although Beclin 2 and Beclin 1 are broadly similar in sequence and function, the differences in their sequence, detailed structure, interactions and mechanism result in their distinct roles in the cell. A structure-based understanding of this difference in mechanism is necessary to understand the mechanistic bases for the different biological functions of the Beclin paralogs and consequently, the reason that mammals have two paralogs of this protein.

In this study, the domain architecture of Beclin 2 was delineated by sequence alignment to Beclin 1 along with secondary structure predication. Different Beclin 2 expression constructs, containing full-length, multi-domain and single-domain of Beclin 2, were designed, expressed and purified to obtain proteins samples that can be used for structure determination by X-ray crystallography. The CCD of Beclin 2 was successfully crystallized and its X-ray crystal structure was determined, showing that it is an anti-parallel coiled-coil dimer in which two alpha-helices are coiled around each other. In contrast to the Beclin 1 CCD homodimer, which has a flat molecular surface, the Beclin 2 CCD is curved, with a 15 nm radius of curvature. The Beclin 2 CCD is a metastable dimer with 7 pairs of non-ideal packing interactions, which includes 4 pairs of charged residues and 3 pairs of bulky polar side chains.

5.2. Materials and methods

5.2.1. Delineating Beclin 2 domain architecture

Beclin 2 domain architecture was delineated using a combination of bioinformatics tools including the alignment of sequences of human Beclin 1 and Beclin 2 using ClustalW2 (Larkin et al., 2007); secondary structure prediction using Jpred (Cole et al., 2008); and sequence

analysis using the programs IUPred (Dosztanyi et al., 2005),PrDOS (Ishida and Kinoshita, 2007) and the VSL2B algorithm in the PONDR program suite (Obradovic et al., 2005, Peng et al., 2006) to identify IDRs.

5.2.2. Expression constructs creation

The author would like to thank Ms.Yue Li in the Sinha Lab, NDSU, for making all the expression constructs used in this Chapter.

The expression constructs of full-length Beclin 2 (residues 1-431) were created using the Gibson Assembly cloning method (Gibson et al., 2009). In general, to insert the cDNA sequence corresponding to Beclin 2 full-length between the EcoRI and XhoI restriction sites of *p*MBP parallel vector (Sheffield et al., 1999) so that full-length Beclin 2 would be expressed as a MBP-tagged fusion protein, PCR was first employed to amplify the cDNA sequence corresponding to Beclin 2 (residues 1-431). Complimentary sequences to the target *p*MBP parallel vector as well as the EcoRI and XhoI restriction sites sequences were also incorporated in the sense and antisense primers, respectively. The sense and antisense primers were named as S1 and A1 and their sequences are listed in Table 5.1. The reagents used for 50 μL of PCR reaction are as follows: 5 μL of 10 × *Pfu* Ultra AD DNA polymerase reaction buffer, 1 μL of 10 mM dNTPs mixture, 2 μL of 20 ng/μL template, 1 μL of each 25 μM primers, and 1 μL of 2.5 U/μL *Pfu* Ultra AD polymerase and 39 μL nuclease-free H_2O. PCR was performed on the GeneAmp PCR System 9700 (Life Technologies) for 25 cycles under the following experimental conditions: initial denaturation at 95 ℃ for 45 sec, denaturation at 95 ℃ for 30 sec, annealing at 67 ℃ for 45 sec, extension at 72 ℃ for 45 sec, final extension at 72 ℃ for 5 min, and then hold at 4 ℃. The PCR amplified DNA was gel purified using E.Z.N.A. Gel Extraction Kits (Omega Bio-tek).

The linearized *p*MBP parallel vector was prepared by restriction digestion. The reagents used for the 20 μL restriction digestion reaction were: 1 μg of vector, 2 μL of 10 × NEBuffer 2.1, 1 μL of EcoRI (20 U/μL), 1 μL of XhoI (20 U/μL), and 15 μL nuclease-free H_2O. The reaction mixture was incubated at 37 ℃ for 1 hour. The digestion products were gel purified using E.Z.N.A. Gel Extraction Kits (Omega Bio-tek).

For the assembly reaction, a 1:6 molar ratio of gel purified vector and PCR product was added to 15 ul of Gibson Assembly Master Mix for a 20 μL reaction. The reaction mixture was incubated at 50 ℃ for 1 hr. The DNA present in the reaction mixture was transformed into chemically competent Top10 cells. A single colony of the recombinant *E. coli* cells was inoculated into 5 mL LB media supplemented with 100 μg/ml Ampicillin and grown overnight at 37 ℃. The recombinant plasmid was isolated using E.Z.N.A. Plasmid Mini Kit I (Omega Bio-tek). The cloning of the coding regions of the Beclin 2 full-length in the *p*MBP parallel vector was confirmed by sequencing at MCLAB.

The expression plasmid for the Beclin 2 FHD-CCD-BARAD (residues 121-431) was created using the same Gibson Assembly as described above. The cDNA sequence corresponding to Beclin 2FHD-CCD-BARAD (residues 121-431) was inserted between the EcoRI and XhoI restriction sites of *p*MBP parallel vector. The sense (primer S2) and antisense (primer A2) primers used for making this construct are listed in Table 5.1

The Beclin 2 FHD-CCD (residues 121-250) expression construct was created by site-directed mutagenesis by inserting a stop codon after the residue 250 of the Beclin 2 FHD-CCD-BARAD expression construct using the QuikChange II Site-Directed Mutagenesis Kit (Agilent Technologies). To create the Beclin 2 FHD-CCD construct, the sense (primer S3) and antisense (primer A3) primers were designed to introduce the stop codon during PCR and their sequences

were listed in Table 5.1. The reagents used for 50 μL of PCR reaction were as follows: 5 μL of 10 × reaction buffer, 1 μL of 10 mM dNTPs mixture, 2 μL of 10 ng/μL template, 2.5 μL of each 50 ng/μL primers, and 1 μL of 2.5 U/μL *PfuUltra* AD DNA polymerase and 37 μL nuclease-free H_2O. The PCR was performed on the GeneAmp PCR System 9700 (Life Technologies) for 16 cycles under the following experimental conditions: initial denaturation at 95 ℃ for 30 sec, denaturation at 95 ℃ for 30 sec, annealing at 55 ℃ for 1 min, extension at 68 ℃ for 6 min, final extension at 68 ℃ for 7 min, and then hold at 4 ℃. 1 μL of DpnI was then added to the reaction product to digest the template DNA at 37 ℃ for 1 hr. 2 μL of the digeation product was transformed into chemically competent Top10 cells. A single colony of recombinant *E. coli* cells was inoculated in 5 mL LB media supplemented with 100 μg/ml Ampicillin and grown overnight at 37 ℃. The plasmid was isolated using E.Z.N.A. Plasmid Mini Kit I (Omega Bio-tek). The stop codon insertion was confirmed by sequencing at MCLAB.

To make the Beclin 2 CCD expression construct, the cDNA sequence corresponding to Beclin 2 CCD (residues 158-250) was inserted between the BamHI and NotI restriction sites of *p*MBP parallel vector using the same method as described in Chapter 2 for making the Bcl-X_L expression construct. The sense (primer S4) and antisense (primer A4) primers used for making this construct were listed in Table 5.1

Three different expression constructs of the Beclin 2 BARAD were created in order to determine the N-terminus of the most stable Beclin 2 BARAD construct. A construct wherein the Beclin 2 BARAD (residues 230-431) was inserted into the *p*MBP parallel vector was created using the Gibson Assembly method described above. The sense (primer S5) and antisense (primer A5) primers used for making the construct are listed in Table 5.1. Residues were either added to or removed from the Beclin 2 BARAD (residues 230-431) construct using the same

site-directed mutagenesis protocol described for creating the Beclin 2 FHD-CCD construct, to make the Beclin 2 (residues 223-431) and Beclin 2 (residues 254-431) respectively. The site-directed mutagenesis primers used for making Beclin 2 (residues 223-431) (primers S6 and A6) and Beclin 2 (residues 254-431) (primers S7 and A7) were listed in table 5.1.

Table 5.1: Summary of primers used for varius Beclin 2 expression construct creation.

Primers	5’ to 3’
S1	CTGTATTTTCAGGGCGCCATGGATCCGGAATTCATGTCTTCCATCCGCTTCCTG
A1	GGCCAGTGCCAAGCTTGGTACCGCATGCCTCGAGCTACTTTTGATACCTTGAGGCAAC
S2	CTGTATTTTCAGGGCGCCATGGATCCGGAATTCTGCACCGACAGTCTTTTAGAG
A2	GGCCAGTGCCAAGCTTGGTACCGCATGCCTCGAGCTACTTTTGATACCTTGAGGCAAC
S3	GCTGAAGGAAATCAACTAGTGTTTCACCGCCACG
A3	CGTGGCGGTGAAACACTAGTTGATTTCCTTCAGC
S4	GCGGCGGGATCCGGAGGCGGCGGCGCTGCGGGCGGAGCTGCGG
A4	GCGGCGGCGGCCGCCTAGTTGATTTCCTTCAGCCGGTCCCTCTG
S5	CTGTATTTTCAGGGCGCCATGGATCCGGAATTCGGGAACGTGGAGAACCAGCTG
A5	GGCCAGTGCCAAGCTTGGTACCGCATGCCTCGAGCTACTTTTGATACCTTGAGGCAAC
S6	CATGGATCCGGAATTCCTGGAACTGCTTGATCAGCTGGGGAACGTGGAGAAC
A6	GTTCTCCACGTTCCCCAGCTGATCAAGCAGTTCCAGGAATTCCGGATCCATG
S7	GCCATGGATCCGGAATTCGCCACGTTTGAGATCTGG
A7	CCAGATCTCAAACGTGGCGAATTCCGGATCCATGGC

5.2.3. Full-length Beclin 2 expression and purification

E. coli BL21(DE3)*p*LysS chemically competent cells were transformed with pMBP-Beclin 2 for the overexpression of MBP-Beclin 2. The transformed cells were grown on agar

plates supplemented with 100 µg/µL Ampicillin and 35 µg/µL Chloramphenicol. A single colony was picked and grown in 5 ml LB media supplemented with 100 µg/µL Ampicillin and 35 µg/µL Chloramphenicol at 37 ℃ overnight. The next day, the 5 ml overnight culture was used to inoculate 1 L LB supplemented with 100 µg/µL Ampicillin and 35 µg/µL Chloramphenicol, and grown at 37 ℃ until the optical density at 600 nm reached 0.6-0.8. At this point, the overexpression of MBP-Beclin 2 was induced with 0.5 mM IPTG. The cells were grown further at 30 ℃ with shaker speed of 220 rpm for 2 hrs, then harvested by centrifugation at 4000 rpm for 20 min at 4 ℃, and stored at -80 ℃ until usage.

The cell pellet from 1 L culture was suspended in 40 ml lysis buffer comprised of 20 mM Tris, pH 8.0, 300 mM NaCl, 10% Glycerol, 2 mM 2-mercaptoethanol, and 0.2 mM 4-(2-Aminoethyl) benzenesulfonyl fluoride hydrochloride (AEBSF). The cells were lysed by sonication and the crude extract was centrifuged at 20000 g for 30 min at 4 ℃ to remove the cellular debris. The resulting supernatant was loaded onto a gravity column containing 2 ml of amylose resin (New England Biolabs). After the supernatant had passed through the column completely, the column was washed with 40 ml lysis buffer to remove contaminating protein. 20 mM maltose in lysis buffer was used to elute the MBP-Beclin 2 and each 0.5 ml faction was collected until OD_{280} of elution sample reached ~0. The elution samples were analyzed using SDS-PAGE and all elution sample containing MBP-Beclin 2 were pooled together and concentrated to ~10 mg/ml. The protein was further purified by SEC using tandem Superdex 200 10/300 GL and Superdex 75 10/300 GL columns (GE Healthcare), that had been pre-equilibrated with the SEC buffer comprised of 20 mM Tris, pH 8.0, 300 mM NaCl, 10% Glycerol, 2 mM 2-mercaptoethanol. 400 µl of ~10 mg/ml protein was loaded onto the tandem SEC column and

eluted with SEC buffer at flow rate of 0.4 ml/min. The purity of samples eluted from SEC was evaluated using SDS-PAGE.

5.2.4. Beclin 2 FHD-CCD-BARAD expression and purification

MBP-Beclin 2 FHD-CCD-BARAD was expressed in *E. coli*BL21(DE3)*p*LysS cells in the same manner as MBP-Beclin 2. The cell pellet from 5 L culture was suspended in 250 ml lysis buffer comprising 20 mM Tris, pH 8.0, 150 mM NaCl, 2 mM 2-mercaptoethanol with 0.2 mM AEBSF added. The cells were lysed by emulsification and the crude extract was centrifuged at 20000 g for 40 min at 4 ℃ to remove the cellular debris. The resulting supernatant was loaded onto a gravity column containing 10 ml of amylose resin (New England Biolabs). After the supernatant had completely passed through the column, the column was washed with 100 ml lysis buffer to remove contaminating protein. 20 mM maltose in lysis buffer was used to elute MBP-Beclin 2 FHD-CCD-BARAD and 5 ml elution fractions were collected. The elution samples were analyzed using SDS-PAGE and all elution samples containing MBP-Beclin 2 FHD-CCD-BARAD were pooled together for further purification by IEX using a Mono Q HR 10/10 column (GE Healthcare). ~40 mg of protein were diluted with non-salt buffer comprised of 25 mM HEPES, pH 7.5, 2 mM 2-mercaptoethanol, to make the final NaCl concentration in the protein solution lower than 50 mM. The diluted protein was then load onto the Mono Q HR 10/10 column and washed with 40 ml low-salt buffer comprising 25 mM HEPES, pH 7.5, 50 mM NaCl, 2 mM 2-mercaptoethanol. A linear gradient of 150 ml of NaCl ranging from 50-500 mM in 25 mM HEPES, pH 7.5 and 2 mM 2-mercaptoethanol, was used to elute MBP-Beclin 2 FHD-CCD-BARAD. The purity of MBP-Beclin 2 FHD-CCD-BARAD eluted from MonoQ columns in different fractions were evaluated using SDS-PAGE. Fractions containing pure MBP-Beclin 2 FHD-CCD-BARAD were pooled, concentrated to ~5 mg/ml and further purified using a

Superdex 200 10/300 GL column in tandem with a Superdex 75 10/300 GL column (GE Healthcare). The column was pre-equilibrated with the SEC buffer comprised of 20 mM Tris, pH 8.0, 150 mM NaCl, 2 mM 2-mercaptoethanol. 1 ml of ~5 mg/ml protein was loaded onto the tandem SEC column and eluted with SEC buffer at a flow rate of 0.4 ml/min. The purity of samples eluted from SEC was evaluated using SDS-PAGE. SEC fractions containing the purest and most homogenous MBP-Beclin 2 FHD-CCD-BARAD were pooled together, concentrated to 4.5 mg/ml and stored in small aliquots in -80 ℃ until usage.

5.2.5. Beclin 2 FHD-CCD expression and purification

MBP-Beclin 2 FHD-CCD was expressed in *E. coli* BL21(DE3)*p*LysS cells in almost the same manner as MBP-Beclin 2. The only difference is that instead of expression at 37 ℃ for 2 hrs, MBP-Beclin 2 FHD-CCD was expressed at 20 ℃ for 16-18 hours. The cell pellet from a 6 L culture was suspended in 200 ml lysis buffer comprising 20 mM Tris, pH 8.0, 150 mM NaCl, 2 mM Dithiothreitol and 0.2 mM AEBSF. The cells were lysed by emulsification and the crude extract was centrifuged at 20000 g for 40 min at 4 ℃ to remove the cellular debris. The resulting supernatant was loaded onto a gravity column containing 15 ml of amylose resin (New England Biolabs). After the supernatant had completely passed through the column, the column was then washed with 150 ml lysis buffer to remove contaminating protein. 10 mg GST-TEV was then added to the column to perform an on-column TEV cleavage. After GST-TEV was mixed well with the resin by pipetting, the column was incubated at 4 ℃ overnight. The next day, the cleaved protein was washed off the column with lysis buffer and 5 ml wash factions were collected until OD_{280} of the wash fractions reached ~0. The wash fractions were analyzed using SDS-PAGE and all wash fractions containing Beclin 2 FHD-CCD were pooled together and further purified by IEX using a Mono Q HR 10/10 column (GE Healthcare). ~50 mg of protein

were diluted with non-salt buffer comprising 25 mM HEPES, pH 7.5, 2 mM 2-mercaptoethanol, to make the final NaCl concentration in the protein solution lower than 50 mM. The diluted protein was then loaded onto Mono Q HR 10/10 column and washed with 40 ml low-salt buffer comprised of 25 mM HEPES, pH 7.5, 100 mM NaCl, 2 mM 2-mercaptoethanol. A linear gradient of 150 ml NaCl ranging from 100-500 mM in 25 mM HEPES, pH 7.5 and 2 mM 2-mercaptoethanol, was used to elute the Beclin 2 FHD-CCD. The purity of the Beclin 2 FHD-CCD eluted from MonoQ columns in different fractions was evaluated using SDS-PAGE. Fractions containing pure Beclin 2 FHD-CCD were pooled, concentrated to ~8mg/ml and further purified using a Superdex 200 10/300 GL column in tandem with a Superdex 75 10/300 GL column (GE Healthcare). The column was pre-equilibrated with SEC buffer comprised of 20 mM Tris, pH 8.0, 150 mM NaCl and 2 mM 2-mercaptoethanol. 600 µl of 8 mg/ml protein was loaded onto the tandem SEC column and eluted with SEC buffer at a flow rate of 0.4 ml/min. The purity of samples eluted from SEC was evaluated using SDS-PAGE. SEC fractions containing the purest and most homogenous Beclin 2 FHD-CCD were pooled, concentrated to ~6 mg/ml and stored in small aliquots at -80 ℃ until needed.

5.2.6. Beclin 2 CCD expression and purification

MBP-Beclin 2 CCD was expressed in *E. coli* BL21(DE3)*p*LysS cells in the same manner as MBP-Beclin 2 FHD-CCD. The cell pellet from 6 L culture was suspended in 250 ml lysis buffer comprised of 20 mM Tris, pH 8.0, 150 mM NaCl, 2 mM Dithiothreitol with 0.2 mM AEBSF and 0.5 mM EDTA. The cells were lysed by emulsification and the crude extract was centrifuged at 20000 g for 40 min at 4 ℃ to remove the cellular debris. The resulting supernatant was purified by amylose affinity chromatography followed by on-column TEV cleavage, as described above for purifying the MBP-Beclin 2 FHD-CCD. All samples containing the Beclin 2

CCD were pooled and further purified by IEX using a Mono Q HR 10/10 column (GE Healthcare). ~50 mg of protein was load onto the Mono Q HR 10/10 column and washed with 40 ml low-salt buffer comprised of 20 mM Tris, pH 8.0, 50 mM NaCl, 2 mM 2-mercaptoethanol. A linear gradient of 150 ml of NaCl ranging from 50-500 mM in 20 mM Tris, pH 8.0 and 2 mM 2-mercaptoethanol was used to purify the Beclin 2CCD. The purity of the Beclin 2 CCD eluted from MonoQ columns in different fractions was evaluated using SDS-PAGE. Fractions containing pure Beclin 2 CCD were pooled, concentrated to ~7 mg/ml and further purified by SEC, using a tandem Superdex 200 10/300 GL and Superdex 75 10/300 GL column (GE Healthcare). The SEC column was pre-equilibrated with the SEC buffer comprised of 20 mM Tris, pH 8.0, 150 mM NaCl, 2 mM 2-Mercaptoethanol. 1 ml of 7 mg/ml protein was loaded onto the tandem SEC column and eluted with SEC buffer at a flow rate of 0.4 ml/min. The purity of samples eluted from SEC was evaluated using SDS-PAGE. SEC fractions containing the purest Beclin 2 CCD were pooled, concentrated to ~6 mg/ml and stored in small aliquots at -80 ℃.

5.2.7. Beclin 2 BARAD expression and purification

All three different MBP-Beclin 2 BARAD constructs, the MBP-Beclin 2 BARAD (residues 223-431), MBP-Beclin 2 BARAD (residues 230-431) and MBP-Beclin 2 BARAD (residues 254-431), were expressed in *E. coli* BL21(DE3)*p*LysS cells in a manner almost identical to that for MBP-Beclin 2, except that MBP-Beclin 2 BARAD was expressed at 15 ℃ for 16-18 hrs, instead of expression at 37 ℃ for 2 hrs as for MBP-Beclin 2.

To purify MBP-Beclin 2 BARAD (residues 223-431), the lysis buffer used comprised of 20 mM Tris, pH 8.0, 150 mM NaCl and 2 mM 2-mercaptoethanol. The MBP-Beclin 2 BARAD was purified by amylose affinity chromatography followed by SEC as described for purifying MBP-Beclin 2.

Purification of the MBP-Beclin 2 BARAD (residues 254-431) started with suspension of the cell pellet from a 6 L culture in 200 ml lysis buffer comprising 20 mM Tris, pH 8.0, 150 mM NaCl, 2 mM Dithiothreitol and 10 % Glycerol with 2 tablets of cOmplete protease inhibitor cocktail (Roche) added. The cells were lysed by emulsification and the crude extract was centrifuged at 20000 g for 40 min at 4 ℃ to remove the cellular debris. The resulting supernatant was purified by amylose affinity chromatography followed by on-column TEV cleavage as described for the purification of MBP-Beclin 2 FHD-CCD. All samples containing Beclin 2 BARAD (residues 254-431) were pooled together and further purified by IEX using a Mono Q HR 10/10 column (GE Healthcare). ~35 mg of protein was load onto Mono Q HR 10/10 column and washed with 40 ml low-salt buffer comprising of 20 mM Tris, pH 8.0, 50 mM NaCl, 2 mM 2-mercaptoethanol. A 35 ml linear gradient of NaCl ranging from 50-150 mM, followed by 30 ml of 150 mM NaCl and 40 ml of 500 mM NaCl in 20 mM Tris, pH 8.0 and 2 mM 2-mercaptoethanol, was used to purify the Beclin 2 BARAD (residues 254-431). The purity of Beclin 2 BARAD eluted from MonoQ columns in different fractions was evaluated using SDS-PAGE. Fractions containing pure Beclin 2 BARAD (residues 254-431) were pooled, concentrated to ~2 mg/ml and further purified using a Superdex 200 10/300 GL column in tandem with a Superdex 75 10/300 GL column (GE Healthcare). Column was pre-equilibrated with the SEC buffer comprised of 20 mM Tris, pH 8.0, 150 mM NaCl, 2 mM 2-mercaptoethanol. 1.2 ml of 2 mg/ml protein was loaded onto the tandem SEC column and eluted with SEC buffer at a flow rate of 0.4 ml/min. The purity of samples eluted from SEC was evaluated using SDS-PAGE. SEC fractions containing the purest Beclin 2 BARAD (residues 254-431) were pooled, concentrated to ~4mg/ml and stored in small aliquots at -80 ℃ until needed.

MBP-Beclin 2 BARAD (residues 230-431) was purified in a manner similar to the purification of MBP-Beclin 2 BARAD (residues 254-431), with only two differences: the lysis buffer used during cell lysis and NaCl gradient used during IEX. The lysis buffer used for MBP-Beclin 2 BARAD (residues 230-431) purification is comprised of 20 mMTris, pH 8.0, 150 mM NaCl, 2 mM Dithiothreitol. During IEX, a linear gradient of 150 ml of NaCl ranging from 50-500 mM in 20 mM Tris, pH 8.0 and 2 mM 2-mercaptoethanol, was used to purify Beclin 2 BARAD (residues 230-431).

5.2.8. Crystallization screening

In order to crystallize the Beclin 2 CCD, Beclin 2 FHD-CCD and Beclin 2 BARAD (residues 254-431) for X-ray crystallographic studies, the MCSG Suite (Microlytic) which includes four different matrix crystallization screens were used to identify potential crystallization conditions using a Crystal Gryphon 96-reservoir crystallization robot (Art Robbins Instruments). Each screen contains 96 different reservoir solution compositions. In addition, three different protein:reservoir ratios, 3:1, 1:1 and 1:3, were screened for each of the reservoir solution compositions at 20 ℃. Thus, a total of 384 different conditions were screen for the crystallization of the three proteins. To set up a 96 reservoir well, 3 protein well per reservoir well crystallization screening plate at three different protein:reservoir ratios, 3:1, 1:1 and 1:3, using the Crystal Gryphon 96-reservoir crystallization robot, the 96-syringe head of the robot quickly aspirates designed volumes of solutions from the 96-well matrix crystallization screen and then dispenses 65 µl of the solutions to each of the reservoir well and 0.125 µl, 0.25 µl, 0.375 µl to the protein well 1, 2, 3 of each reservoir, respectively. The nano dispenser aspirates the protein solution and dispenses 0.375 µl, 0.25 µl, 0.125 µl to the protein well 1, 2, 3 of each reservoir, respectively, to create the 3:1, 1:1 and 1:3 protein:reservoir ratios. The plate was then

sealed and incubated at 20 ℃. The crystallization screening plate was monitored for crystal growth under microscope every 24 hrs for the first 7 day and twice a week for another 3 weeks.

5.2.9. Crystallization and structure determination

Beclin 2 CCD was crystallized at 20 ℃ by hanging-drop vapor diffusion. The Beclin 2 CCD was crystallized from a 1:1 mixture of 5.5 mg/ml protein and reservoir solution comprised of 0.1 M Bis-Tris pH 6.5, 0.1 M NaCl and 1.5 M $(NH_4)_2SO_4$. Crystals were harvested and cryo-protected in cryosolutions comprising the reservoir solution and 25 % glycerol, then immediately flash-frozen in liquid N_2. All diffraction data were collected at 100 K at 24-ID NE-CAT at Advanced Photon Source, Argonne National Laboratory, Argonne, IL. Data were recorded in a 180° sweep from a single Beclin 2 CCD crystal, at 1 second exposure per 1 °crystal rotation per imageat a crystal-to-detector distance of 450 mm. The Beclin 2 CCD diffraction data were indexed and integrated using MOSFLM (Leslie and Powell, 2007). Various combinations of search models derived from the Beclin 1 CCD structure (PDB code: 3Q8T) were used as the search model for molecular replacement. Ultimately, the Beclin 2 CCD structure was solved by molecular replacement using half of the rat Beclin 1 CCD homodimer structure, comprising residues 217-265 of one chain and residues 174-219 of the partner chain, as the search model using Phaser-MR in the CCP4 Suite (Winn et al., 2011). The asymmetric unit contained two Beclin 2 CCD homodimers, AB and CD. Chain A included residues 160-200; chain B, residues 204-247; chain C, residues 160-200; and chain D, residues203-247. Buccaneer in the CCP4 Suite (Winn et al., 2011) was then used to autobuild the rest of the Beclin 2 CCD structure. Refinement was performed using PHENIX (Adams et al., 2010). Crystallographic data collection and refinement statistics are summarized in Table 5.2. All molecular figures were prepared using the PyMOL Molecular Graphics System (Schrodinger, 2010). Buried surface areawas analyzed

using PISA (Krissinel and Henrick, 2007). The final refined structure of Beclin 2 CCD is deposited in the PDB with code 5K7B.

5.3. Results

5.3.1. Domain architecture of Beclin 2

Beclin 1 and Beclin 2 likely have a very similar architecture based on their sequence similarity (56.6% sequence identity) and predicted Beclin 2 secondary structure. Based on this similarity and secondary structure predictions, Beclin 2 domain architecture (Figure 5.1) consists of an IDR comprising residues 1-121, a FHD comprising residues 122-152, a CCD comprising residues 158-250 and a BARAD comprising residues 230-431. The most variable region of Beclin 1 and Beclin 2 is the IDR. Within the Beclin 2 IDR, residues 88-111 are equivalent to the Beclin1 BH3D. However, the highly conserved Beclin 1 BH3D residue, L116, that is critical for binding to various Bcl-2 proteins (Oberstein et al., 2007, Sinha et al., 2008, Su et al., 2014), is not conserved in Beclin 2. Another Beclin 1 BH3D residue T119, which is phosphorylated by DAPK to promote dissociation of Beclin 1 from Bcl-2 (Zalckvar et al., 2009), is also not conserved in Beclin 2. The FHD-CCD-BARAD region of Beclin 1 and Beclin 2 is highly conserved, sharing 60.3 % identity, with the CCD sharing 53.8 % sequence identity.

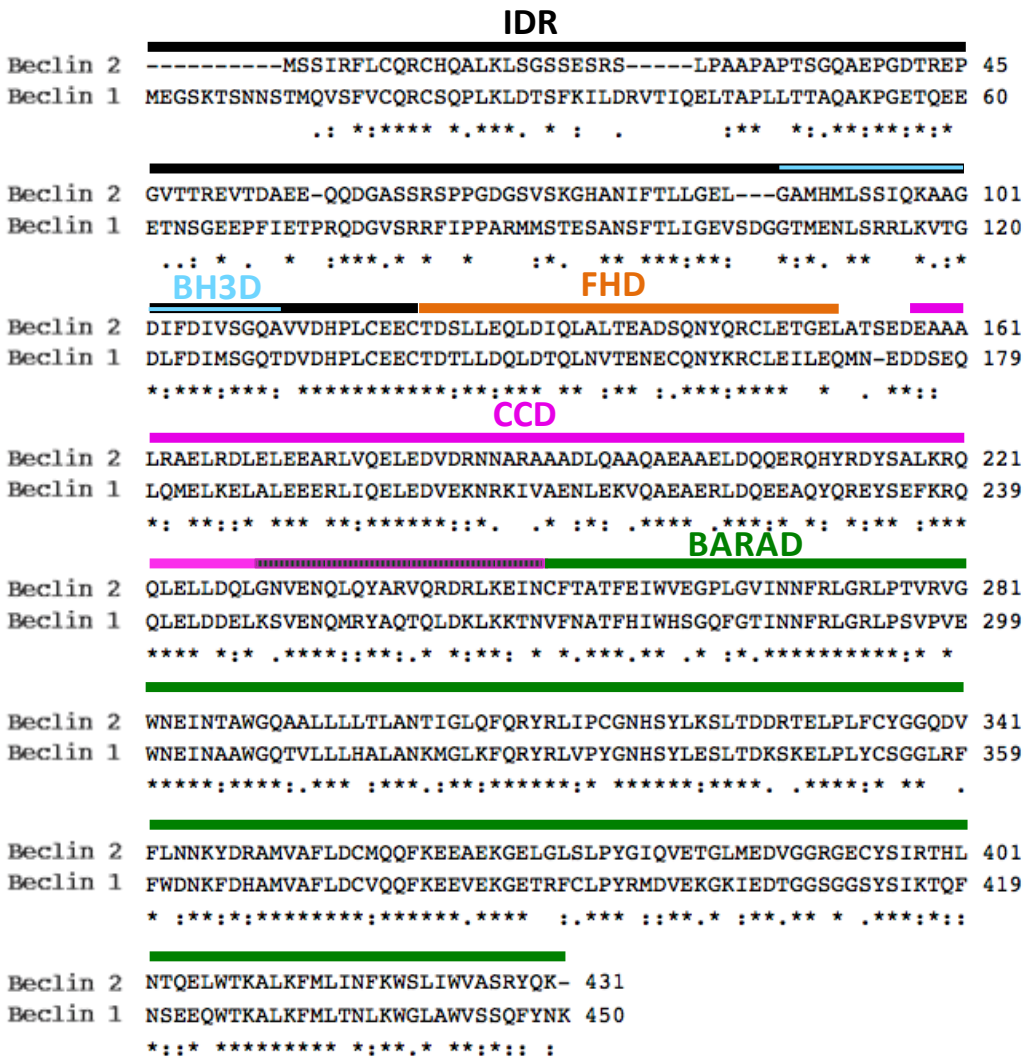

Figure 5.1: Sequence alignment of human Beclin 1 and Beclin 2. Asterisks represent identical residues, while double and single dots represent decreasing sequence conservation. Domain boundaries are displayed above the alignment with the black, cyan, orange, violet and green lines representing the IDR, BH3D, FHD, CCD and BARAD, respectively.

5.3.2. Expression and purification of full-length Beclin 2

In order to investigate the structure of Beclin 2 using X-ray crystallography, different constructs of Beclin 2, including full-length Beclin 2, Beclin 2 FHD-CCD-BARAD, Beclin 2 FHD-CCD, Beclin 2 CCD and three different Beclin 2 BARADs, were cloned, expressed and purified. Full-length Beclin 2 was expressed in *E. coli* BL21(DE3)*p*LysS cells as a MBP fusion protein, and soluble protein in the cell lysate was first purified by amylose affinity

chromatography and then further purified by SEC using a Superdex 200 10/300 GL column in tandem with a Superdex 75 10/300 GL column. The final SEC purification results are shown in Figure 5.2. SDS-PAGE indicates that (Figure 5.2 Lane 2 of SDS-PAGE gel) the protein sample obtained from amylose affinity purification was a mixture of proteins. A band of ~100 kD was observed which most likely corresponds to MBP-Beclin 2, which has an expected molecular weight of 92.1 kD. Unfortunately, this band only represents a small fraction of this sample. The majority of the protein comprised of multiple bands between the 37 kD and 75 kD markers, which were most likely degradation products of full-length Beclin 2. SEC was used to attempt to purify this sample further. The SEC profile combined with SDS-PAGE suggests that MBP-Beclin 2 aggregates, as all the MBP-Beclin 2 eluted in the void volume of the SEC column (Figure 5.2 Peak 1). Peak 2 and 3 contained only degradation products. Therefore, most of the MBP-Beclin 2 was already degraded before SEC purification and the remaining MBP-Beclin 2 full-length is aggregated, leaving no useful protein sample for crystallization.

Next, we will remove the first 120 residues which comprise the IDR, from the expression construct, hoping to reduce the degradation and aggregation.

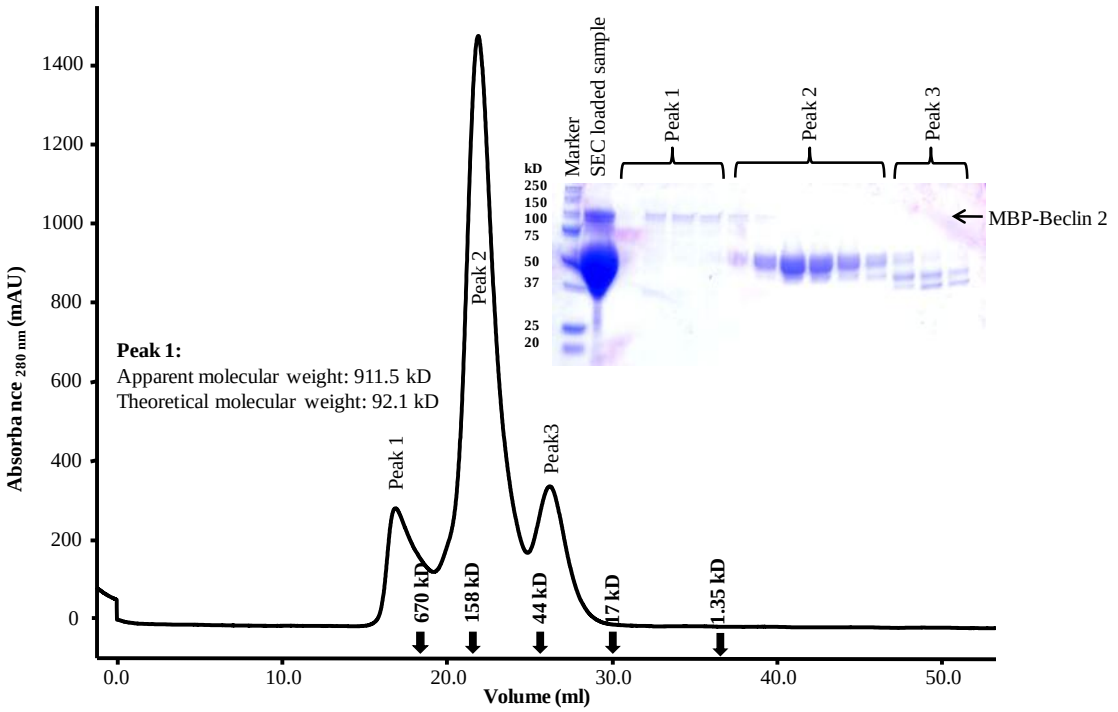

Figure 5.2: Size-exclusion chromatogram and the corresponding SDS-PAGE of MBP-Beclin 2.

5.3.3. Expression and purification of Beclin 2 FHD-CCD-BARAD

MBP-Beclin 2 FHD-CCD-BARAD was expressed in *E. coli* BL21(DE3)*p*LysS cells, and soluble protein from the cell lysate was purified, first by amylose affinity chromatography and then by SEC using tandem Superdex 200 10/300 GL and Superdex7510/300 GL columns. The final SEC purification results are shown in Figure 5.3. Much like the MBP-Beclin 2 purification, the protein obtained from amylose affinity purification of the MBP-Beclin 2 FHD-CCD-BARAD was a also a mixture of proteins (Figure 5.3, Lane 2 of the SDS-PAGE gel). The theoretical molecular weight of MBP-Beclin 2 FHD-CCD-BARAD is 79.6 kD. Therefore, the band that appears between 75 k D and 100 kD marker most likely represent MBP-Beclin 2 FHD-CCD-BARAD, although it accounts for only one-third of the protein in the amylose affinity eluate. Additionally, MBP-Beclin 2 FHD-CCD-BARAD appears to have degraded before SEC purification. As indicated by SEC and SDS-PAGE (Figure 5.3), the remaining intact MBP-

Beclin 2 FHD-CCD-BARAD could not be used for crystallization as it was aggregated and eluted in the void volume of the SEC column. Notably, a single Gaussian peak observed in SEC, Peak 2, eluting between the 44 kD and 158 kD marker (Figure 5.3), contains the major degradation product, which runs just above the 50 kD marker in SDS-PAGE. This is also the major degradation product observed during the purification of MBP-Beclin 2 and was stable enough to go through all the purification process. This degradation product has a molecular weight consistent with a MBP-Beclin 2 FHD-CCD fragment, suggesting that the FHD-CCD is a stable fragment of Beclin 2. To test this, we next attempted to express and purify the Beclin 2 FHD-CCD.

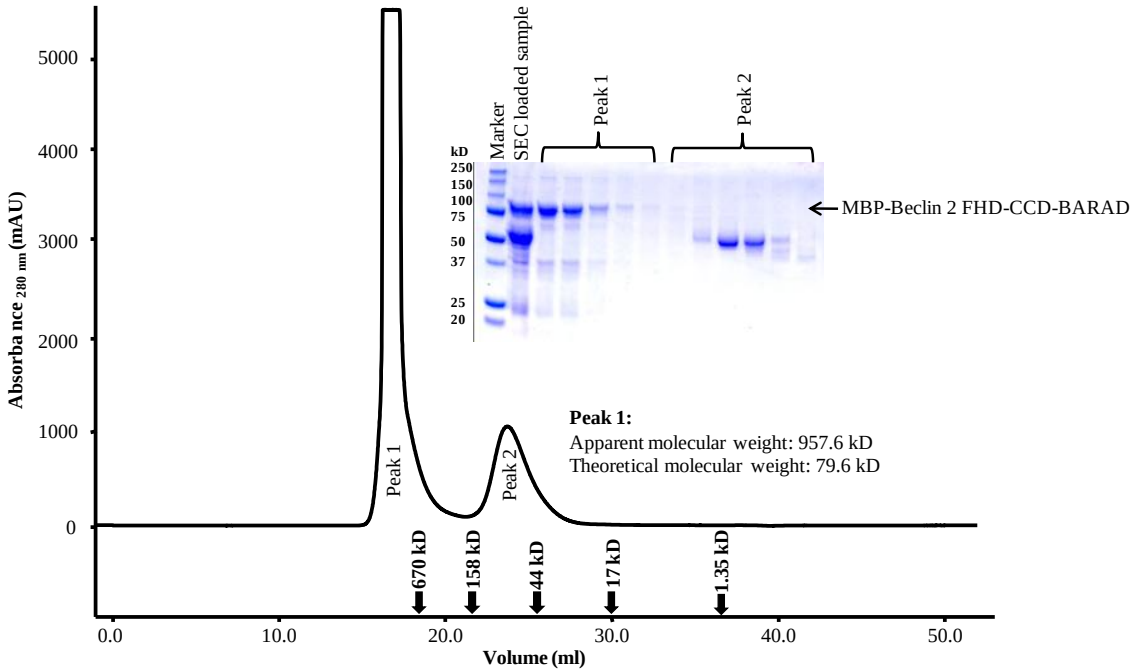

Figure 5.3: Size-exclusion chromatogram and the corresponding SDS-PAGE of MBP-Beclin 2FHD-CCD-BARAD.

5.3.4. Expression and purification of Beclin 2 FHD-CCD

MBP-Beclin 2 FHD-CCD was expressed in *E. coli* BL21(DE3)*p*LysS cells, and soluble protein in the cell lysate was first purified by amylose affinity chromatography. The MBP-Beclin 2 FHD-CCD was very stable, and so the MBP tag was removed by TEV cleavage to facilitate crystallization experiments. The cleaved protein was further purified by IEX and SEC. The final SEC purification results were shown in Figure 5.4. The sample loaded onto the SEC column (Figure 5.4 Lane 2 of SDS-PAGE gel) contained ~ 80% pure Beclin 2 FHD-CCD and some degradation products. Compared to full length Beclin 2 and Beclin 2 FHD-CCD-BARAD, the degradation of Beclin 2 FHD-CCD was significantly reduced. Unexpectedly, the Beclin 2 FHD-CCD, which has a theoretical molecular weight of 15.7 kD, runs along the 25 kD marker upon SDS-PAGE. The SEC profile (Figure 5.4) contains a single peak corresponding to the Beclin 2 FHD-CCD. Due to the presence of the CCD, the Beclin 2 FHD-CCD most likely forms a dimer. The apparent molecular weight of the Beclin 2 FHD-CCD, calculated from the elution volume of this single peak is 125.1 kD, which is much larger than the expected molecular weight of a Beclin 2 FHD-CCD dimer. However, since the Beclin 2 FHD-CCD is an elongated molecule due to the presence of the CCD, it distorts the SEC profile, making it almost impossible to calculate the oligomerization state of the Beclin 2 FHD-CCD based on the SEC profile. The leading edge of the peak (Figure 5.4 Lane 3 of the SDS-PAGE gel) contains the purest protein with almost no contaminants. These fractions were pooled and concentrated to 6.3 mg/ml and used for crystallization screening.

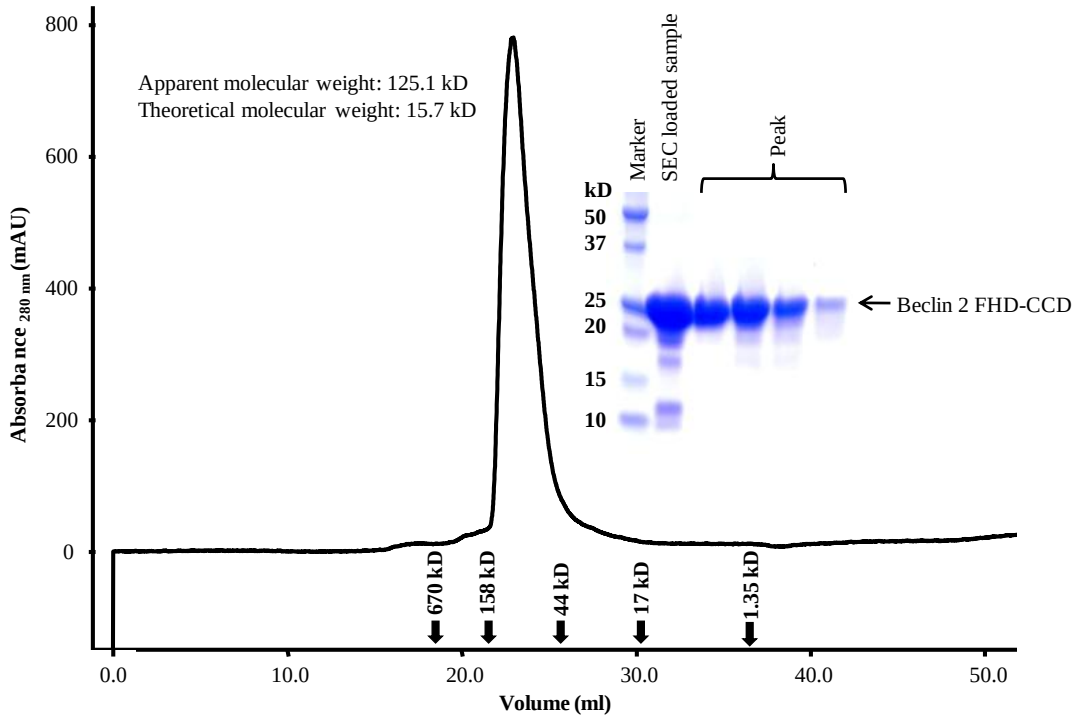

Figure 5.4: Size-exclusion chromatogram and the corresponding SDS-PAGE of Beclin 2FHD-CCD.

5.3.5. Expression and purification of Beclin 2 CCD

MBP-Beclin 2 CCD was expressed in *E. coli* BL21(DE3)*p*LysS cells, and soluble protein in the cell lysate was first purified by amylose affinity chromatography followed by on-column TEV cleavage to remove the MBP tag. The cleaved protein was further purified by IEX and SEC. The final SEC purification results are shown in Figure 5.5. The Beclin 2 CCD with a theoretical monomer molecular weight of 11.3 kD runs as expected between the 10 kD and 15 kD marker on SDS-PAGE. The sample loaded onto the SEC column (Figure 5.5 Lane 2 of SDS-PAGE gel) contained more than 90% pure Beclin 2 CCD. The SEC profile (Figure 5.5) contains a single peak that corresponds to the Beclin 2 CCD (Figure 5.5 SDS-PAGE gel). The apparent molecular weight calculated from the elution volume of this peak is 74.9, which is ~3-fold larger than the molecular weight of the Beclin 2 CCD dimer. This larger apparent molecular weight

estimated from SEC is likely a consequence of the rod-like shape of a typical CCD dimer. Notably, the shape of the peak (figure 5.5) was not an ideal symmetrical Gaussian distribution. The slope of the leading edge of the peak is less steep than the trailing edge, which may suggest that the Beclin 2 CCD forms a weak oligomer with the trailing edge of the peak representing monomers. The fractions from the single peak were collected, concentrated to 5.5 mg/ml and used for crystallization experiments.

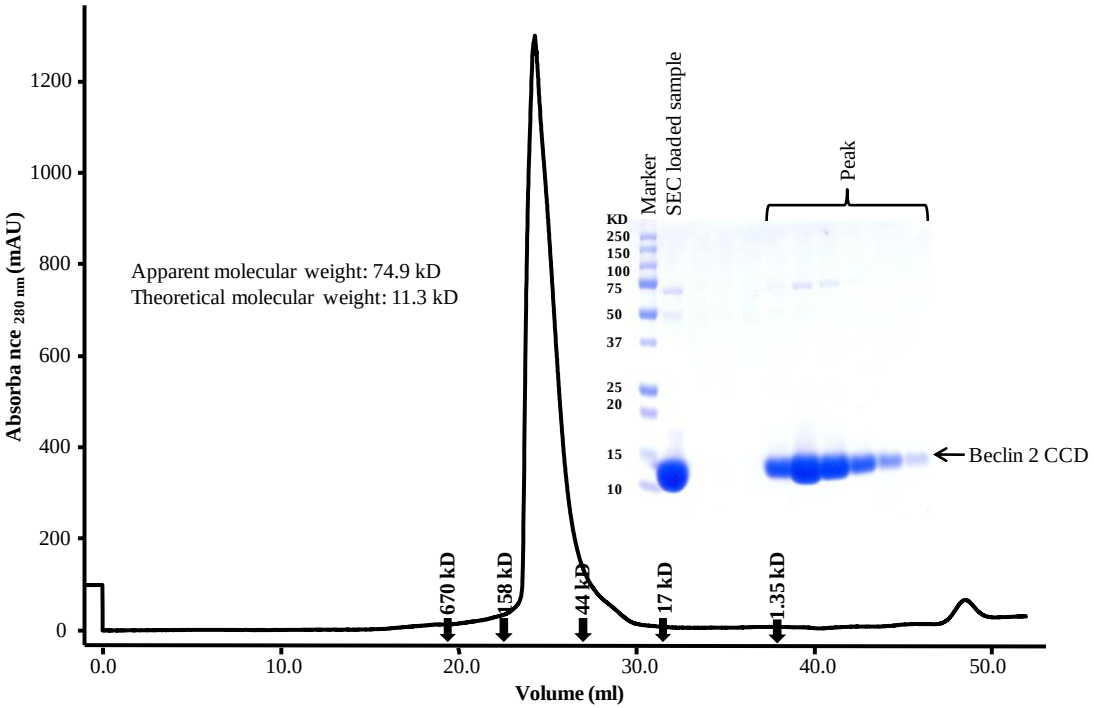

Figure 5.5: Size-exclusion chromatogram and the corresponding SDS-PAGE of Beclin 2 CCD.

5.3.6. Expression and purification of Beclin 2 BARAD

The crystal structure of human Beclin 1 (residues 248-450) includes residues 248-264 preceding the BARAD, which pack against the BARAD as an additional helix (Huang et al., 2012) that we call the "overlap helix". The overlap helix corresponds to the C-terminal four turns of the Beclin 1 CCD. Overlap helix residues that pack against the BARAD (Huang et al., 2012), also constitute the CCD homodimer interface (Mei et al., 2016b, Li et al., 2012). Therefore,

extensive steric clashes would prevent the overlap helix from simultaneously existing as part of both domains within a single molecule. The Beclin 1 BARAD was crystallized with this overlap helix, while the yeast homolog Vps30 BARAD was crystallized without it; therefore, it is still unclear whether the overlap helix also exists in Beclin 2, and whether the Beclin 2 BARAD is more stable with or without the presence of the overlap helix. In order to identify the most stable state of the BARAD, expression and purification of three different Beclin 2 BARAD constructs was tested for expression and purification: MBP-Beclin 2 BARAD (residues 230-431) which contains the overlap helix; Beclin 2 BARAD (residues 223-431) which contains seven additional residues corresponding to seven residues that were included in the Beclin 1 BARAD expression construct but were not ordered enough to be seen in the crystal structure; and MBP-Beclin 2 BARAD (residues 254-431) which does not contain the overlap helix. All three Beclin 2 BARAD constructs were expressed in *E. coli* BL21(DE3)*p*LysS cells.

MBP-BARAD (residues 223-431) was purified by amylose affinity chromatography followedby SEC. The final SEC purification results are shown in Figure 5.6. The MBP-Beclin 2 BARAD (residues 223-431) has a theoretical monomer molecular weight of 68.1 KD, and as expected, on SDS-PAGE, runs between the 50 kD and 75 kD marker. The sample loaded onto SEC column (Figure 5.6 Lane 2 of SDS-PAGE gel) contained ~60% MBP-BARAD (residues 223-431) along with multiple degradation products. During SEC purification, most of MBP-BARAD (residues 223-431) was present in Peak 1, which eluted in the SEC void volume, indicating most of the MBP-BARAD (residues 223-431) was aggregated.

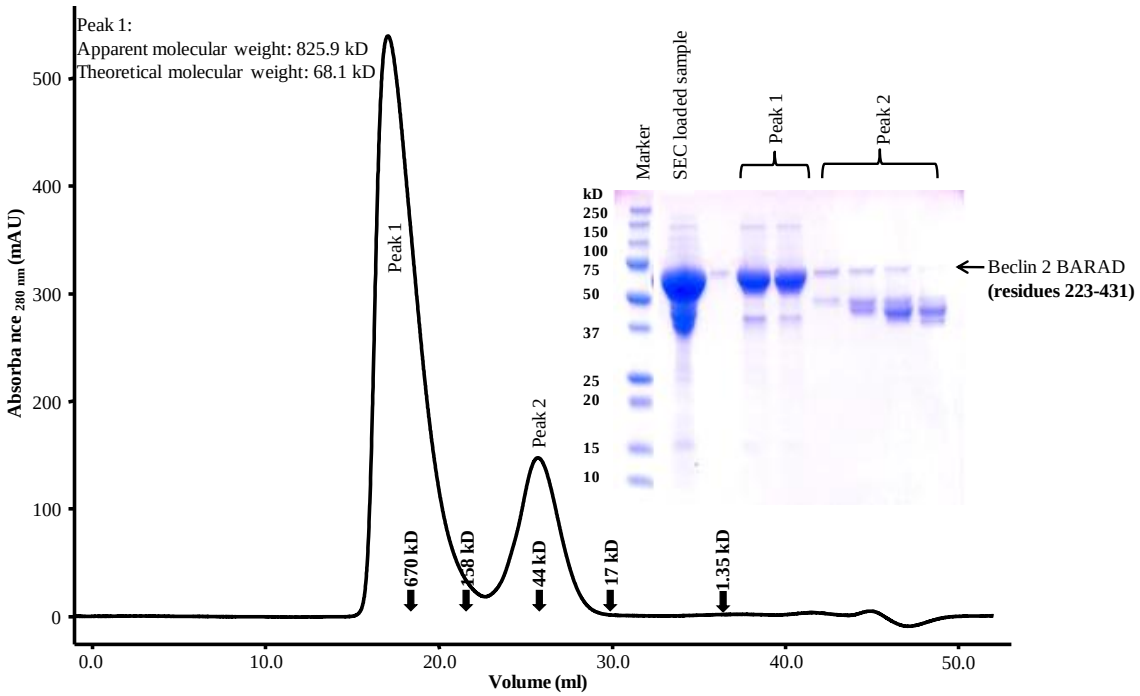

Figure 5.6: Size-exclusion chromatogram and the corresponding SDS-PAGE of Beclin 2 BARAD (residues 223-431).

Beclin 2 BARAD (residues 230-431) was purified as a MBP fusion protein by amylose affinity chromatography and SEC. Compared to MBP-Beclin 2 BARAD (residues 223-431), this protein has reduced degradation and aggregation. About 2 mg of MBP-Beclin 2 BARAD (residues 230-431) was obtained from 1 L of bacterial culture. In order to remove the MBP tag and the linker region between MBP and the Beclin 2 BARAD, to facilitate crystallization of Beclin 2 BARAD, on-column TEV cleavage was performed after amylose affinity purification. The cleavage product was further purified by IEX and SEC. To our surprise, IEX did not separate MBP (isoelectric point = 5.0) from the cleaved Beclin 2 BARAD (residues 230-431) (isoelectric point = 6.2). Approximately half the total protein content of the BARAD-containing fractions pooled after IEX was MBP (Figure 5.7 Lane 1 of SDS-PAGE gel). The cleaved protein ran as a single band of ~ 20 kD, ~4 kD smaller than its expected molecular weight. This impure

IEX pool was further purified by SEC. Two overlapping peaks were observed during SEC purification. Based on its elution volume, the protein eluted in Peak 1 was estimated to have an apparent molecular weight of 38.7 kD, close to the expected molecular weight of 43.2 kD for MBP; and SDS-PAGE indicates that this peak contains mostly MBP. The overlapping Peak 2, with an apparent molecular weight of 18.4 kD, contains both MBP and Beclin 2 BARAD (residues 230-431). Therefore, the molecular weight difference between MBP and BARAD was insufficient to separate the two proteins by SEC, even on tandem Superdex 200 and Superdex 75 columns. Therefore, although BARAD (residues 230-431) is more stable than BARAD (residues 223-431), this construct also did not result in protein of adequate quality for crystallization experiments.

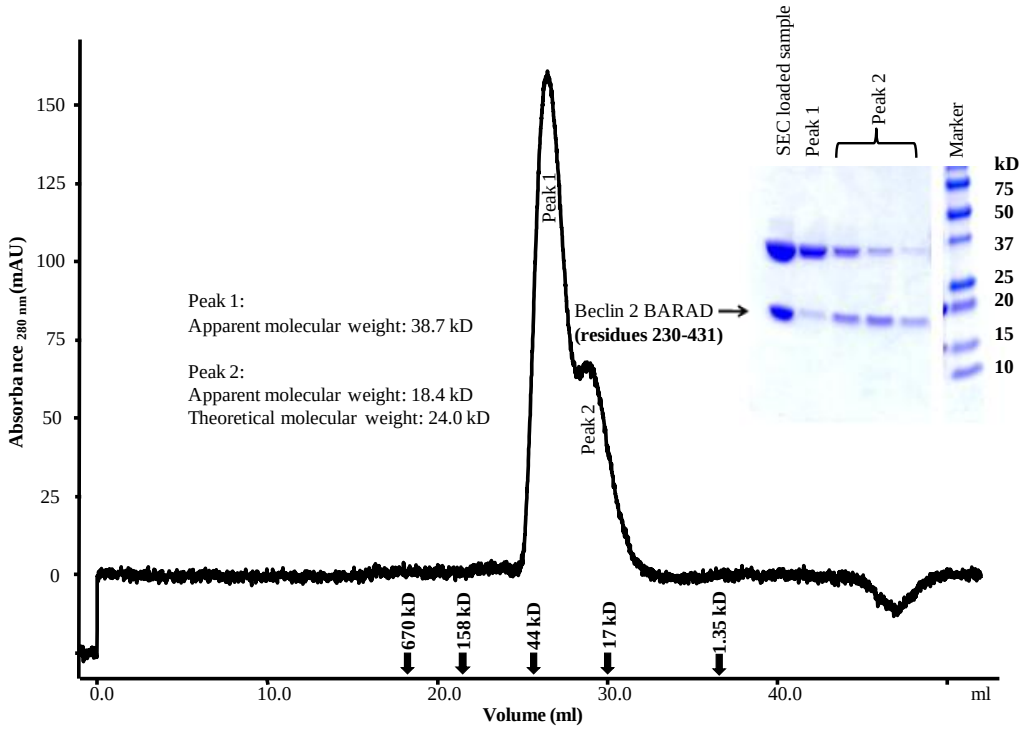

Figure 5.7: Size-exclusion chromatogram and the corresponding SDS-PAGE of Beclin 2 BARAD (residues 230-431).

Lastly, we expressed and purified Beclin 2 BARAD (residues 254-431) that lacks the overlap helix. MBP-Beclin 2 BARAD (residues 254-431) was the most stable Beclin 2 BARAD constructs among the three constructs tested. Only slight degradation was observed during purification. Although aggregation was observed at a level similar to that seen for MBP-BARAD (residues 230-431), pure and homogeneous MBP-BARAD (residues 254-431) can be obtain after SEC. In order to facilitate crystallization, MBP tag was removed by TEV cleavage. The cleaved protein was further purified by IEX and SEC. The cleaved protein ran as a single band between the 15 kD and 20 kD marker (Figure 5.8). The cleaved BARAD (residues 254-431) elutes from the SEC column as a single peak (Figure 5.8) with an apparent molecular weight of 12.4 estimated from its elution volume. Interestingly, both BARAD (residues 254-431) and BARAD (residues 230-431) behave like smaller proteins: they run faster than expected during SDS-PAGE and elute later during SEC, which may indicate important structural features of the Beclin 2 BARAD. BARAD (residues 254-431) from the single SEC elution peak (Figure 5.8) was pooled, concentrated to 3.7 mg/ml (as it precipitates at higher concentrations), and screened for crystallization.

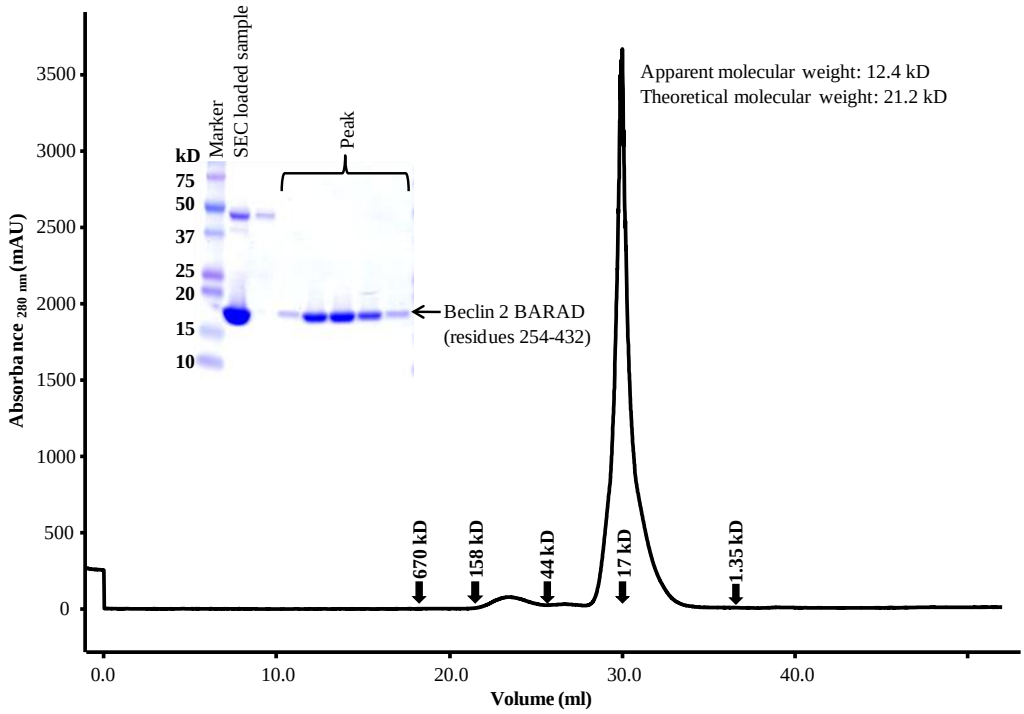

Figure 5.8: Size-exclusion chromatogram and the corresponding SDS-PAGE of Beclin 2 BARAD (residues 254-431).

5.3.7. Structural studies of Beclin 2 CCD, FHD-CCD, and BARAD

A total of 1152 different conditions, including the 384 different reservoir solution compositions provided by MCSG Suite along with three different protein:reservoir ratios, 3:1, 1:1 and 1:3,were used to screen each crystallization-quality protein purified: the Beclin 2 CCD, Beclin 2 FHD-CCD and Beclin 2 BARAD (residues 254-431), for crystallization. Unfortunately, no crystal hits were obtained for the Beclin 2 FHD-CCD and BARAD (residues 254-431).

Crystallization conditions for the Beclin 2 CCD were successfully optimized. Beclin 2 CCD crystals were grown at 20 ℃ by hanging drop vapor diffusion methods, from a 1:1 mixture of protein solution (5.5 mg/ml in 20 mM Tris, pH 8.0, 150 mM NaCl, 2 mM 2-mercaptoethanol) and well solution (0.1 M Bis-Tris, pH 6.5, 0.1 M NaCl and 1.5 M $(NH_4)_2SO_4$). Plate-shaped crystals grew to 50×50×10 in 7 days (Figure 5.9).

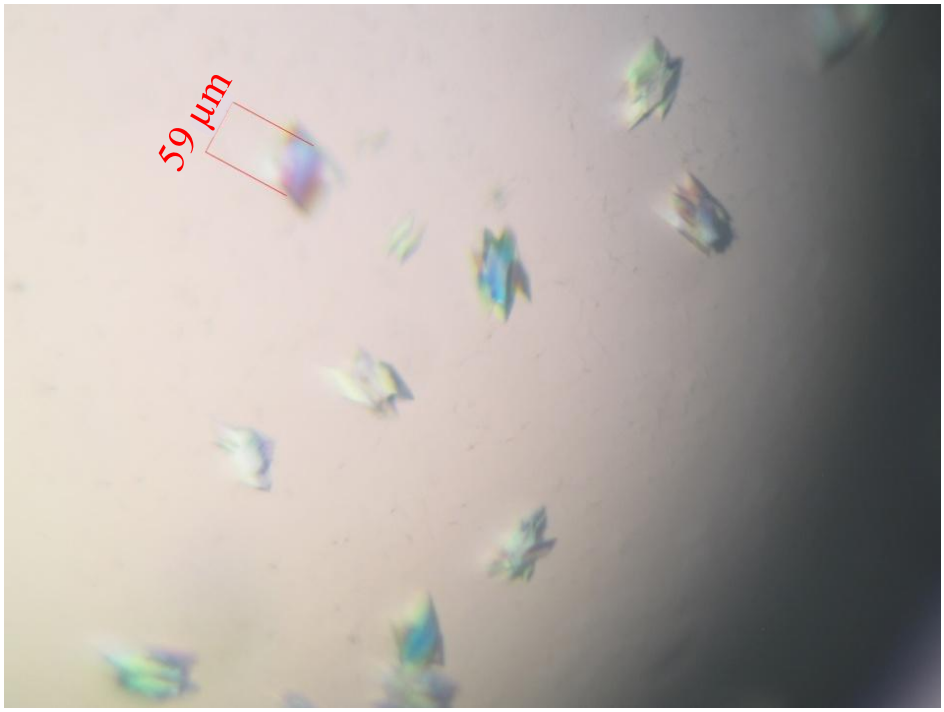

Figure 5.9: Typical Beclin 2 CCD crystals.

The crystals were harvested and cryoprotected in a cryosolution consisting of 0.1 M Bis-Tris, pH 6.5, 0.1 M NaCl and 1.5 M $(NH_4)_2SO_4$ and 25% v/v glycerol, and then immediately flash-frozen in liquid N_2. The data used to solve the Beclin 2 CCD structure were collected at an X-ray wavelength of 0.97920 Å in a 180 °sweep from a single crystalat at beamline 24-ID NE-CAT@APS, ANL, Chicago. Data were processed using MOSFLM (Leslie and Powell, 2007) and the data statistics are summarized in Table 5.2.

Table 5.2: Summary of X-ray data collection and refinement statistics.

Data collection:	
Wavelength (Å)	0.97920
Data range (Å)	40.33 - 2.19
Space group	I2
Unit cell parameters	a=95.46Å b=44.32Å c=97.96Å β=96.77 °
Average Mosaicity (°)	0.77
Unique reflections	17947 (1589)
Avg. multiplicity	3.4 (3.3)
Completeness (%)	84.6 (87.0)
CC1/2	0.997 (0.473)
[1]R_{meas}	0.11 (0.76)
I/σ_I	7.7 (2.6)
Refinement:	
Monomer A	87 residues
Monomer B	91 residues
Monomer C	86 residues
Monomer D	88 residues
Water molecules	139
Data Range (Å)	40.15 -2.30
[2]R_{work} (%)	22.1
[2,3]R_{free} (%)	23.6
Average B-values ($Å^2$)	43.5
Macromolecules	43.7
Water	37.7
RMSDs from target values:	
Bond Lengths (Å)	0.022
Bond Angles (°)	1.55
Ramachandran favored (%)	98.5
Ramachandranoutliers(%)	0

Values in parentheses pertain to the outermost shell of data.

[1] $R_{meas}= \sum_{hkl}(n/n-1)^{1/2}\sum_{h,i} |I_{hkl,i}-<I_{hkkl}>|/\sum_{hkl}\sum_{h,i}I_{hkl,i}$.

[2] R factor= $\sum_{h,} |F_{obs}-|F_{calc}|/\sum_{h}|F_{obs}|$.

[3] Test set for R_{free} consisted of 5% of data

The X-ray crystal structure of Beclin 2 CCD was solved to 2.3 Å resolution by MR using a search model extracted from Beclin 1 CCD (PDB code: 3Q8T). The crystallographic refinement statisticsare summarized in Table 5.2.

5.3.8. The Beclin 2 CCD is a curved, anti-parallel homodimer with multiple non-ideal interface interactions

The Beclin 2 CCD forms an anti-parallel coiled-coil homodimer in which two α-helices are coiled in a left-handed twist around each other (Figure 5.10 A & B). In each crystallographic asymmetric unit, there are two such CCD homodimers: one comprising chain A and chain B, and another comprising chain C and chain D. The AB dimer superimposes upon the CD dimer with an RMSD of 1.49 Å over 160 Cα atoms. Since the two pairs of dimers are almost identical, subsequent discussion focuses on the AB dimer, unless mentioned otherwise.

The average surface area buried upon homodimerization of the Beclin2 CCD is 2070 ± 37Å, constituting ~24% of the total surface per monomer. The surface area buried in the human Beclin 1 CCD homodimer interface is 2504 $Å^2$, which constitutes 27 % of the total surface per monomer (Mei et al., 2016b). The Beclin 2 CCD homodimer forms a curved coiled-coil with a 15 nm radius of curvature, in contrast to the Beclin 1 CCD homodimer, which is not curved (Figure 5.10 C). Like Beclin 1 (Mei et al., 2016b), the Beclin 2 surface CCD is mostly negatively charged as indicated by its surface electrostatic potential (Figure 5.10D), especially at the center of the convex face (Figure 5.10D, top panel).

Classical CCDs have heptad amino-acid repeats (*a-b-c-d-e-f-g*), with positions *a* and *d* usually occupied by hydrophobic residues, that enables the formation of a well-packed hydrophobic interface that holds the two chains together (Mason and Arndt, 2004). The Beclin 2 CCD homodimer interface consists of 26 pairs of interacting residues (or thirteen pairs of heptad

repeats), comprised of thirteen unique pairs related by molecular two-fold symmetry. Within these thirteen pairs of heptad repeats, the first heptad (residues 159-165) of one CCD packs against the thirteenth heptad (residues 243-249) of the partner CCD (Figure 5.10A), which is similar to Beclin 1. Within each pair of heptad repeats, residues at the *a* and *d* positions of one repeat interact with residues at the *d* and *a* positions respectively of the partner heptad. However, unlike classical CCD dimers, the Beclin 2 CCD has only six unique pairs of acceptable packing interactions: A159-L246, L166-A239, L169-L236, L176-L229, L180-L225, and A201-L204, including three ideal Leu pairs. Notably, these ideal packing interactions are conserved in the Beclin 1 CCD (Mei et al., 2016b).

The Beclin 2 CCD homodimer has seven pairs of non-ideal packing interactions wherein either the *a* or *d* position is occupied by either a charged or a bulky polar residue (Figure 5.10A, B & E).This includes four pairs where one partner bears a charged residue (L162-R243, E173-V232, L194-H211, A197-E208), and three pairs where one partner bears a bulky polar residue (V183-Q222, N187-L218, A190-Y215) at the *a* or *d* positions. Equivalent pairs in Beclin 1 also have similar non-ideal pairings that include charged or non-polar residues, except for the terminal L162-R243 pairs, which are ideal leucine pairs in Beclin 1(Mei et al., 2016b). Thus, six pairs of non-ideal packing interactions are conserved between Beclin 1 and Beclin 2.

Besides the hydrophobic interactions at the interface, the Beclin 2 CCD homodimer is also stabilized by two unique pairs of inter-chain polar interactions: Q222 is hydrogen bonded to D184 of the partner helix, and R240 makes a salt bridge to E170 of the partner helix. Notably, the Beclin 1 CCD has three unique pairs of inter-chain polar interactions. Beclin 2 Q222 is equivalent to Beclin 1 Q240, but other Beclin 1 residues contributing to polar interactions in Beclin 1 are not located at positions equivalent to those in Beclin 2. Thus, surface polar

interactions stabilize both the Beclin 1 and Beclin 2 CCD homodimers, but unlike the interface residues, these interactions are not well conserved between these paralogs.

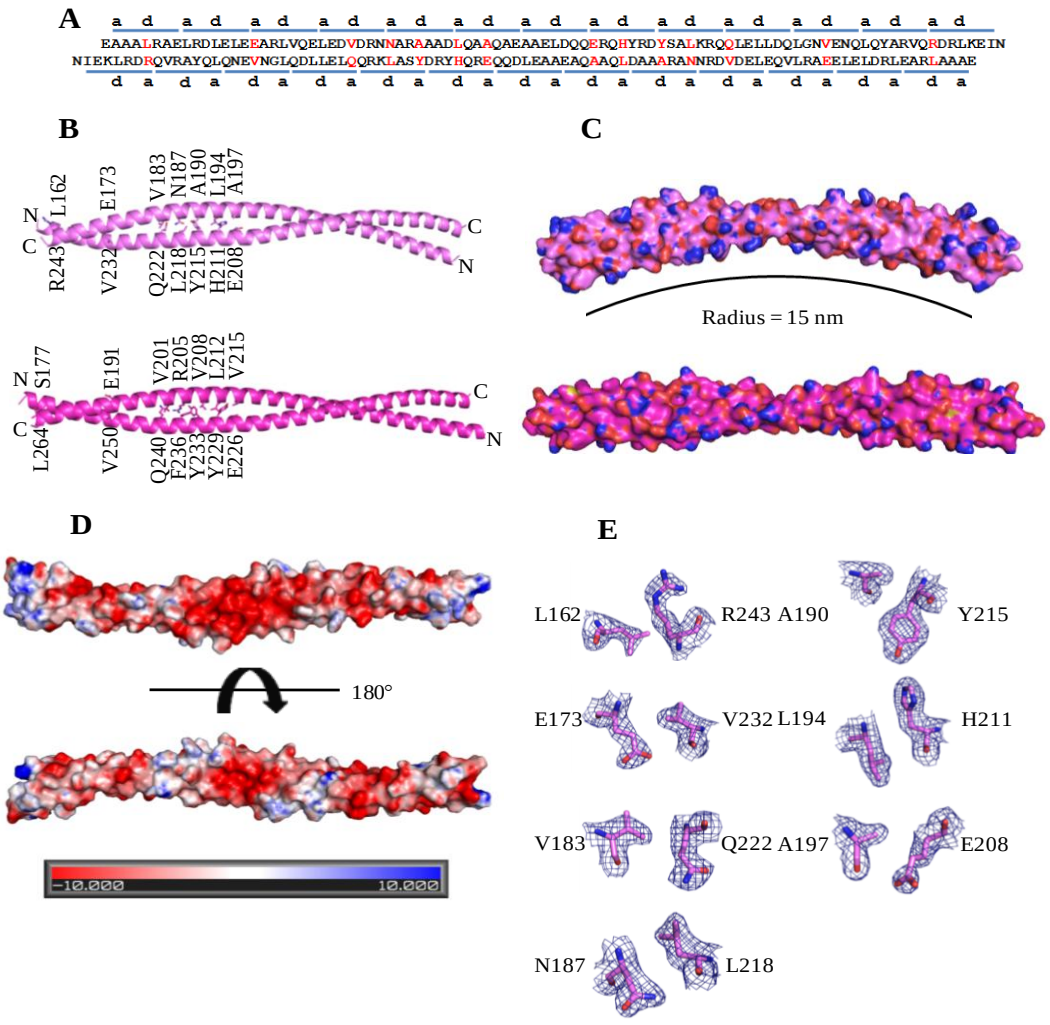

Figure 5.10: The Beclin 2 CCD. (A) Sequence presentation of the packing of the two anti-parallel monomers of Beclin 2 CCD homodimer. The blue bars on top or below the sequence indicate the heptad repeats of Beclin 2 CCD. The letters “a” and “d” indicate the residues at position *a* and *d* in the heptad repeats, respectively. The non-ideal interface residues are colored in red. (B) The X-ray crystal structures of Beclin 2 CCD (violet) and Beclin 1 CCD (magenta) anti-parallel homodimer. The side-chains of non-ideal packing residues are displayed in atomic detail with atoms colored by type – oxygen red, nitrogen blue, and carbon violet (Beclin 2 CCD) or magenta (Beclin 1 CCD). (C) Surface representation of the Beclin 2 CCD homodimer demonstrates that it is a curved molecule with a radius of 15 nm in contrast to the straight-rod-like Beclin 1 CCD (megenta). (D) Electrostatic surface of the Beclin 2 CCD homodimer generated by APBS. Top panel is the convex face & bottom panel is the concave face. (E) Atomic details of non-ideal packing residues, color-coded as in (B).The blue mesh represents 2Fo-Fc maps contoured at 1δ above the mean.

5.4. Discussion

In this study, we attempted to purify full-length Beclin 2 in order to investigate its structure by X-ray crystallography or other structural methods. However, the MBP-Beclin 2 degraded and aggregated severely during expression and purification. Even after the removal of the IDR region, the stability of the MBP-Beclin 2 FHD-CCD-BARAD did not improve compared to full-length Beclin 2. The recent reported phosphatidylinositol 3-kinase Vps34 complex, which includes the yeast homologs of phosphatidylinositol 3-kinase, p150, Beclin 1 and UVRAG, indicates that Vps30 (yeast Beclin 1) and Vps38 (yeast UVRAG) interact along the whole length of the molecule so that the FHD, CCD and BARAD of Vps30 pack against the CC1 (coiled-coil domain 1) , CCD and BARA2 of Vps38 (Rostislavleva et al., 2015). Therefore, perhaps Vps30/Beclin 1 is stable only in the context of a heterodimer complex with partners such as Vps38. In fact, in the same study, the Vps30:Vps38 complex was successfully purified and used to pull-down the Vps15/Vps34 complex (Rostislavleva et al., 2015). Our study suggests that by itself, Beclin 2 may not be stable enough to be purified for any *in vitro* studies. Therefore, in future studies, Beclin 2 should be tested for co-expression and purification with binding partners which may help to stabilize Beclin 2.

A very interesting observation during the purification of full-length Beclin 2 and Beclin 2 FHD-CCD-BARAD is that major degradation products of both constructs are similar in molecular weight and may correspond to the MBP-Beclin 2-FHD-CCD. Consistent with this, we find that the MBP-Beclin 2 FHD-CCD is stable enough to allow removal of the MBP tag and purification of untagged Beclin 2 FHD-CCD. Moreover, among the three BARAD constructs tested in this study, we find that the MBP-BARAD (residues 223-431) is stable, but the MBP-BARAD (residues 230-431) and MBP-BARAD (residues 254-431) are not and degrade severely.

This information suggests that in the absence of appropriate binding partners, Beclin 2 may be cleaved between residues 223-230. Despite the identification of Beclin 2 FHD-CCD and Beclin 2 BARAD as stable Beclin 2 protein fragments; we were unable to crystallize them.

The Beclin 2 CCD was successfully purified and crystallized, and its structure was solved to 2.3 Å. Unlike the Beclin 2 CCD which is straight, the Beclin 2 CCD is a curved anti-parallel homodimer with a radius of curvature of 15 nm. The curvature of the Beclin 2 CCD may imply an ability to interact with membranes of similar curvature or to induce curvature in membranes; however, the surface of Beclin 2 is more positively charged and there is no evidence suggesting that the CCDs of Beclin homologs associate directly with membranes. Unlike the ideal CCD structure, which contains mostly hydrophobic residues at the dimer interface that can help to hold the strands of helices together, the Beclin 2 CCD contains 7 pairs of non-ideal interface residues. Therefore, the Beclin 2 CCD may be a weaker homodimer compared to those ideal CCDs. In fact, the Beclin 1 CCD, which contains 7 pairs of non-ideal interface residues has been shown to be a weak homodimer with a dimer dissociation constant of 89 μM as measured by ITC (Li et al., 2012). The weak association of the Beclin 1 homodimer is important for binding to the CCDs of binding partners like Atg14 and UVRAG. Mutating the non-ideal interface residues of Beclin 1 CCD to leucine enhances self-association of the Beclin 1 CCD homodimer, but weakens or completely blocksits binding to CCDs of Atg14 and UVRAG (Li et al., 2012). The impact of the non-ideal interface residues on the self-association of Beclin 2 CCD and its ability to interact with Atg14 CCD will be investigated further in Chapter 6.

CHAPTER 6. BECLIN 2 INTERACTS WITH ATG14 THROUGH A METASTABLE CCD TO REGULATE AUTOPHAGY

6.1. Introduction

CCDs are common structural features of proteins. A CCD is usually formed by 2-5 α-helices wrapped around each other into a left-handed supercoil. The distortion imposed on each α-helix in each left-handed CCD makes it go through 3.5 residues per turn, instead of 3.6 residues per turn found in a regular α-helix. Thus, in CCDs, a heptad repeat occurs every two turns of the α-helix (Landschulz et al., 1988). This repeat is usually denoted as '*a-b-c-d-e-f-g*' in one helix and '*a*'-*b*'-*c*'-*d*'-*e*'-*f*'-*g*'' in the other helix. In an anti-parallel CCD, residues at position *a* and *d* are usually packed against residues at position *a'* and *d'*, respectively. Conversely, in a parallel CCD, residues at position *a* and *d* are usually packed against residues at position *d'* and *a'*, respectively. Most often, residues at position *a* and *d* are hydrophobic residues that hold the α-helix chains together and determine the overall stability of CCDs. In fact, the most stable CCDs are those have the most hydrophobic residues at the position *a* and *d*, like leucine zippers (Landschulz et al., 1988, Lau et al., 1984, Mason and Arndt, 2004).

The Beclin 1 CCD is found to be responsible for interacting with the Atg14 CCD (Li et al., 2012, Itakura et al., 2008, Sun et al., 2008). Co-IP assays demonstrate that any of the Atg14 fragments containing the CCD, including the CCD alone, immunoprecipitate Beclin 1, whereas Atg14 fragments that don't contain the CCD fail to immunoprecipitate Beclin 1, suggesting that Atg14 specifically binds to Beclin 1 via its CCD (Sun et al., 2008). The human Beclin 1 CCD has also been shown to bind to Atg14 CCD with an affinity of 4.44 μM by ITC measurements (Mei et al., 2016b). The interactions of Beclin 1 and Atg14 is important for autophagy as Beclin

1 CCD mutations that disrupt the interaction of Beclin 1 with Atg14 impair autophagy (Mei et al., 2016b)..

Similar to Beclin 1, Beclin 2 co-immunoprecipitates with each of the proteins in the PI3KC3 core complexes: PI3KC3, Atg14 and UVRAG; as well as with AMBRA1, a positive regulator of autophagy (Fimia et al., 2007); and with Bcl-2 homologs which negatively regulate autophagy (He et al., 2013). However, there are clear differences in the interactions of Beclin 1 and Beclin 2. Beclin 2 binds AMBRA1 more strongly than does Beclin 1. Further unlike Beclin 1, the Beclin 2:Bcl-2 interaction is not disrupted upon starvation (He et al., 2013). Lastly, Beclin 2 does not co-immunoprecipitate with Rubicon, a negative regulator of autophagy (Matsunaga et al., 2009).

In Chapter 5, we demonstrated that Beclin 2 contains a CCD similar to Beclin 1. The X-ray crystal structure of the Beclin 2 CCD revealed that, similar to the Beclin 1 CCD, Beclin 2 forms an anti-parallel homodimer with 7 pairs of non-ideal interface residues. As Beclin 2 also co-immunoprecipitates with Atg14, the Beclin 2 CCD is likely responsible for binding the Atg 14 CCD, although this interaction has not yet been demonstrated. In this study, we use structure-based mutations, CD and ITC to demonstrate that interface mutations that improve homodimerization of the Beclin 2 CCD also stabilize the homodimer structure, and mutations that adversely impact homodimerization, destabilize CCD structure. We have also solved the X-ray crystal structure of the N187L mutant Beclin 2 CCD to reveal how it homodimerizes better than WT Beclin 2. Further, we examine the effects of these mutations on Beclin 2 CCD heterodimerization with Atg14 using ITC, and show that these mutations also impact binding to Atg14. We have also built a model of the Beclin 2:Atg14 CCD heterodimer, which helps explain the impact of Beclin 2 CCD mutations on binding to Atg14. An *ab initio* bead model of the

Beclin 2:Atg14 CCD heterodimer generated by SAXS demonstrates that the two CCDs of the Beclin 2: Atg14 heterodimer are arranged in a parallel manner. Our results indicate that compared to the Beclin 1 CCD, the Beclin 2 CCD forms a weaker homodimer, but forms a stronger heterodimer with the Atg14 CCD.

6.2. Materials and Methods

6.2.1. Creation of expression constructs

The human Atg14 CCD (residue 88-178) was delineated based on the sequence alignment to the rat Atg14 CCD (Li et al., 2012), and cloned into the expression vector *p*MBP parallel 1 by Ms. Yang Mei in Dr. Sangita Sinha's lab here at North Dakota State University. A 6×His tag was then added to the C-terminus of Atg14 CCD by site directed mutagenesis. In general, the sense (primer S1) and antisense (primer A1) primers were designed to insert the 6×His during the PCR and their sequences are listed in Table 6.1. The reagents used for 50 μL of PCR reaction were as follows: 5 μL of 10 × reaction buffer, 1 μL of 10 mM dNTPs mixture, 2 μL of 10 ng/μL template, 2.5 μL of each 50 ng/μL primers, and 1 μL of 2.5 U/μL *Pfu* Ultra HF DNA polymerase and 37 μL nuclease-free H_2O. PCR was performed on the GeneAmp PCR System 9700 (Life Technologies) for 18 cycles under the following experimental conditions: initial denaturation at 95 ℃ for 30 sec, denaturation at 95 ℃ for 30 sec, annealing at 55 ℃ for 1 min, extension at 68 ℃ for 8 min, final extension at 68 ℃ for 7 min, and then hold at 4 ℃. 1 μL of DpnI was added to the reaction product to digest the template DNA at 37 ℃ for 1 hr. 1 μL of the digestion product was transformed into chemically competent Top10 cells. A single colony of recombinant *E. coli* cells was inoculated in 5 mL LB media supplemented with 100 μg/ml Ampicillin and grown overnight at 37 ℃. Plasmids were isolated using E.Z.N.A. Plasmid Mini Kit I (Omega Bio-tek). The insertion of the 6×His was confirmed by sequencing at MCLAB.

The creation of the WT Beclin 2 CCD expression construct was described in Chapter 5. All expression constructs of mutant Beclin 2 CCD were created by site directed mutagenesis using the WT Beclin 2 CCD construct as the template and followed the same mutagenesis method as described above. All the primers used are named the "mutant name" plus "S" for sense and "A" for antisense primers (Table 6.1).

Different constructs were used to obtain the Beclin 2: ATG14 CCD complex for SAXS analysis. The MBP-Atg14 CCD construct described above was modified by site directed mutagenesis to replace the long linker between the MBP tag and Atg14 CCD with a short linker of three alanine residues. A small ubiquitin-like modifier (SUMO)-His_6-Beclin 2 CCD construct was created by cloning the His_6-Beclin 2 CCD coding sequence into a modified *p*ET-28 vector with a SUMO coding sequence preceding the multiple cloning site using the Gibson Assembly cloning method (Gibson et al., 2009). In general, PCR was first employed to amplify the cDNA sequence corresponding to His_6-Beclin 2 CCD. Sequences complimentary to the target *p*ET-28 vector, and including BamHI and HindIII restriction site sequences were incorporated in the sense and antisense primers, respectively. The sense and antisense primers were named as S2 and A2 and their sequences were listed in Table 6.1. The reagents used for 50 μL of PCR reaction were as follows: 5 μL of 10 × *Pfu* Ultra AD DNA polymerase reaction buffer, 1 μL of 10 mM dNTPs mixture, 2 μL of 20 ng/μL template, 1 μL of each 25 μM primers, and 1 μL of 2.5 U/μL *Pfu* Ultra AD polymerase and 39 μL nuclease-free H_2O. PCR was performed on the GeneAmp PCR System 9700 (Life Technologies) for 25 cycles under the following experimental conditions: initial denaturation at 95 ℃ for 45 sec, denaturation at 95 ℃ for 30 sec, annealing at 67 ℃ for 45 sec, extension at 72 ℃ for 45 sec, final extension at 72 ℃ for 5 min, and then hold at 4 ℃. The PCR amplified DNA was gel purified using E.Z.N.A. Gel Extraction Kits (Omega

Bio-tek). The linearized *p*ET-28 vector was prepared by restriction digestion. The reagents used for the 20 μL restriction digestion reaction are: 1 μg of vector, 2 μL of 10 × CutSmart Buffer, 1 μL of BamHI (20 U/μL), 1 μL of HindIII (20 U/μL), and 15 μLof nuclease-free H_2O. The reaction mixture was incubated at 37 ℃ for 1 hr. The digestion products were gel purified using E.Z.N.A. Gel Extraction Kits (Omega Bio-tek). For the assembly reaction, a 1:6 molar ratio of gel purified vector and PCR product were added to 15 ul of Gibson Assembly Master Mix for a 20 μL reaction. The reaction mixture was incubated at 50 ℃ for 1 hr. The DNA present in the reaction mixture was transformed into chemically competent Top10 cells. A single colony of the recombinant *E. coli* cells was inoculated in 5 mL LB media supplemented with 15 μg/ml Kanamycin and grown overnight at 37 ℃. The recombinant plasmid was isolated using E.Z.N.A. Plasmid Mini Kit I (Omega Bio-tek). The cloning of the coding regions of the His_6-Beclin 2 CCD in the *p*ET-28 vector was confirmed by sequencing at MCLAB.

Table 6.1: Summary of primers used for creation of expression constructs.

Primers	5’ to 3’
S1	GCTGGTAGAAAAACACCACCACCACCACTGAAGCGGCCGC
A1	GCGGCCGCTTCAGTGGTGGTGGTGGTGGTGTTTTTCTACCAGC
S2	GAGGCTCACAGAGAACAGATTGGTGGATCCATGCACCACCAC CACCACCACTCC
A2	GTGGTGGTGCTCGAGTGCGGCCGCAAGCTTTCAGTTGATTTCC TTCAGCCGGTC
E173L-S	CCTGGAGCTGGAGCTGGCCAGGCTGGTGC
E173L-A	GCACCAGCCTGGCCAGCTCCAGCTCCAGG
N187L-S	GATGTGGACAGGAACCTGGCAAGAGCAGCGGCG
N187L-A	CGCCGCTGCTCTTGCCAGGTTCCTGTCCACATC
A190L-S	GGAACAATGCAAGACTGGCGGCGGATCTCCAG
A190L-A	CTGGAGATCCGCCGCCAGTCTTGCATTGTTCC
A197L-S	GCGGATCTCCAGGCACTGCAGGCAGAGGCTGCG
A197L-A	CGCAGCCTCTGCCTGCAGTGCCTGGAGATCCGC
E208L-S	GAGCTGGACCAGCAGCTGAGGCAGCACTACAGG
E208L-A	CCTGTAGTGCTGCCTCAGCTGCTGGTCCAGCTC
H211L-S	CAGCAGGAGAGGCAGCTGTACAGGGACTACAGTG
H211L-A	CACTGTAGTCCCTGTACAGCTGCCTCTCCTGCTG
Y215L-S	CAGCACTACAGGGACCTGAGTGCCTTGAAGCGG
Y215L-A	CCGCTTCAAGGCACTCAGGTCCCTGTAGTGCTG
Q222L-S	GCCTTGAAGCGGCAGCTGCTGGAACTGCTTGATC
Q222L-A	GATCAAGCAGTTCCAGCAGCTGCCGCTTCAAGGC
R243L-S	GCCAGGGTCCAGCTGGACCGGCTGAAG
R243L-A	CTTCAGCCGGTCCAGCTGGACCCTGGC

6.2.2. Protein expression and purification

All seven Beclin 2 CCD mutants were expressed and purified in a manner similar to the WT Beclin 2 CCD, as described in Chapter 5. The author would like to thank Ms.Yue Li in the Sinha Lab, NDSU, for expressing and purifying the E173L and R243L Beclin 2 CCD.

As a rotation student, under the guidance of the author, Mr. Shane Wyborny in the Colbert Lab, NDSU, optimized the expressioin conditions of MBP-Atg14 CCD-His_6. The best

expression condition was chosen and used in this study. In general, *E. coli* ArcticExpress chemically competent cells (Agilent Technologies) were transformed with pMBP-Atg14 (residues 88-178)-His_6 for the overexpression of MBP-Atg14 CCD-His_6. The transformed cells were grown in 2 ml LB supplemented with 100 µg / µL Ampicillin at 37 ℃ for overnight. The second day, the 2 ml overnight culture was used to inoculate 50 ml LB supplemented with 100 µg/µL Ampicillin and 20 µg/µL Gentamycin and grown further at 37 ℃ for 3 hrs. 8 ml of this culture was used to inoculate 1 L of LB supplemented with 100 µg/µL Ampicillin, and further grown at 37 ℃ until optical density of ~0.8 was reached at 600 nm. At this point, the overexpression of MBP-Atg14 CCD-His_6 was induced with 0.5 mM IPTG. The cells were grown further at 13 ℃ with a shaker speed of 220 rpm for ~20 hrs. Then the cells were harvested by centrifugation at 4000 rpm for 20 minutes at 4 ℃ and stored at -80 ℃ until needed. The cell pellet from a 6 L culture was suspended in 200 ml lysis buffer comprised of 50 mM HEPES, pH 7.5, 150 mM NaCl, 2 mM 2-mercaptoethanol with 3 tablets of cOmplete, EDTA-free protease inhibitor cocktail (Roche) and 1 mM EDTA. The cells were lysed by emulsification and the crude extract centrifuged at 20000 g for 40 min at 4 ℃ to remove the cellular debris. The resulting supernatant was loaded onto a gravity column containing 12 ml of amylose resin (New England Biolabs). After the supernatant had passed through the column completely, the column was washed with 120 ml lysis buffer to remove contaminating protein. 20 mM maltose in lysis buffer was used to elute the MBP-Atg14 CCD-His_6, and 5 ml elution factions were collected until OD_{280} of the elution sample reached ~0. The elution fractions were analyzed using SDS-PAGE and all elution fractions containing MBP-Atg14 CCD-His_6 were pooled and further purified by IMAC using 5 ml HisTrap HP column (GE Healthcare). The elution fractions were analyzed using SDS-PAGE and elution samples containing the purest MBP-Atg14 CCD-His_6

were pooled, concentrated to 15 mg/ml and further purified by SEC using a HiLoad Superdex 200 16/600 column (GE Healthcare). The SEC column was pre-equilibrated with SEC buffer comprising 50 mM HEPES, pH 7.5, 150 mM NaCl, 2 mM 2-mercaptoethanol. Each 2.5 ml of 15 mg/ml protein was loaded onto the SEC column and eluted with SEC buffer at a flow rate of 1 ml/min. The purity of samples eluted from SEC was evaluated using SDS-PAGE. Fractions from the single peak that contains pure MBP-Atg14 CCD-His_6 were pooled, concentrated to ~24 mg/ml, and stored in small aliquots at-80 ℃.

For co-expression of the Beclin 2:Atg14 CCD complex, MBP-Atg14 was first transformed into *E. coli* ArcticExpress chemically competent cells (Agilent Technologies). The transformed cells that contain MBP-Atg14 plasmids were then made chemically competent and SUMO-His_6-Beclin 2 CCD was transformd into these competent cells. The secondarily transformed cells were grown in 2 ml LB supplemented with 100 μg/μL Ampicillin and 15 μg/μL Kanamycin at 37 ℃ overnight. The next day, the 2 ml overnight culture was used to inoculate 50 ml LB supplemented with 100 μg/μL Ampicillin, 15 μg/μL Kanamycin and 20 μg/μL Gentamycin; and grown further at 37 ℃ for 3 hrs. 8 ml of this culture was used to inoculate 6 × 1 L of LB supplemented with 100 μg/μL Ampicillin and 15 μg/μL Kanamycin and grown further at 37 ℃, until OD_{600} of ~0.4 was reached. At this pointthe temperature control of the shaker was adjusted to 13 ℃ so that the temperature of the media cooled down to 13 ℃, while OD_{600} reached 0.8. Overexpression of Beclin 2:Atg14 CCD complex was then induced with 0.5 mM IPTG. The cells were grown further at 13 ℃ with a shaker speed of 220 rpm for ~20 hrs. Then the cells were harvested by centrifugation at 4000 rpm for 20 min at 4 ℃ and stored at -80 ℃ until usage. The cell pellet from a 6 L culture was suspended in 200 ml lysis buffer comprising 50 mM HEPES, pH 7.5, 150 mM NaCl, 25 mM Imidazole with 3 tablets of

cOmplete, EDTA-free protease inhibitor cocktail (Roche). The cells were lysed by emulsification and the crude extract was centrifuged at 20000 g for 40 min at 4 ℃ to remove the cellular debris. The resulting supernatant was first purified by immobilized metal affinity chromatography using a 5 ml HisTrap HP column (GE Healthcare). After all the supernatant had passed through the HisTrap column, the column was first washed with 150 ml of lysis buffer to remove most of the contaminants and then eluted with 100 ml of 200 mM Imidazole in lysis buffer. The elution fractions were analyzed using SDS-PAGE and all elution fractions containing Beclin 2:Atg14 CCD complex were pooled and further purified by amylose affinity chromatography using 10 ml of amylose resin in a gravity column. 20 mM maltose in a buffer comprised of 20 mM Tris, pH 8.0, 150 mM NaCl, 2 mM 2-mercaptoethanol, was used to elute the complex and each 5 ml faction was collected until OD_{280} of elution sample reached ~0. The elution fractions were analyzed again using SDS-PAGE, and all elution fractions containing the purest complex were pooled, concentrated to 8 mg/ml and purified further by SEC using a HiLoad Superdex 200 16/600 column (GE Healthcare). The column was pre-equilibrated with the SEC buffer comprised of 20 mM Tris, pH 8.0, 150 mM NaCl, 2 mM 2-mercaptoethanol. 1.5 ml aliquots of 8 mg/ml protein were loaded onto the SEC column and eluted with SEC buffer at a flow rate of 1 ml/min. The purity of samples eluted from SEC was evaluated using SDS-PAGE. The fractions from the single peak that contains pure Beclin 2:Atg14 CCD complex were pooled, concentrated to ~6 mg/ml, and stored in small aliquots in -80 ℃.

6.2.3. Crystallization and structure determination

N187L Beclin 2 CCD was crystallized at 20 ℃ by hanging-drop vapor diffusion from a 1:1 mixture of 12.2 mg/ml protein and reservoir solution comprised of 0.1 M $MgCl_2$ and 19 % PEG3350. Crystals were harvested and cryo-protected in the reservoir solution plus 25 %

glycerol and then immediately flash-frozen in liquid N_2. All diffraction data were collected at 100 K at the 24-ID NE-CAT beamline at APS, Argonne National Laboratory (ANL), Argonne, IL. Data were recorded in a 180° sweep from a single N187L Beclin 2 crystal, at 1 second exposure per 1 ° crystal rotation per image, at a crystal-to-detector distance of 310 mm. Diffraction data were processed using RAPD automated processing suite (https://rapd.nec.aps.anl.gov/rapd), which incorporates XDS for integration and scaling (Kabsch, 2010). The structure of the N187L mutant CCD was solved by molecular replacement using the WT Beclin 2 CCD AB homodimer as the search model, and using Phaser-MR in PHENIX (Adams et al., 2010). Refinement was performed in PHENIX (Adams et al., 2010). Crystallographic data collection and refinement statistics are summarized in Table 6.6. All molecular figures were prepared using the PyMOL Molecular Graphics System (Schrodinger, 2010). Buried surface area was analyzed using PISA (Krissinel and Henrick, 2007). The final refined structures of the N187L mutant Beclin 2 CCD is deposited in the PDB with code 5K9L.

6.2.4. ITC

ITC experiments were performed using a Low Volume Nano ITC (TA Instruments). All protein samples were dialyzed against the ITC buffer consisting of 50 mM HEPES, pH 7.5, 150 mM NaCl and 2 mM 2-mercaptoethanol. All ITC experiments were performed at 15 ℃ with 20 injections of 2.5 μL each, with at least three repeats per measurement. Data were analyzed using the NanoAnalyze Software (TA Instruments), with an independent model for the Beclin 2 CCD and Atg14 binding experiments and a dimer dissociation model for the Beclin 2 CCD self-dissociation experiments. For the Beclin 2 CCD and Atg14 CCD binding experiments, samples were loaded into separate dialysis cassettes, then co-dialyzed into the ITC buffer. The Atg14 CCD was loaded into the syringe and titrated into the cell containing the Beclin 2 CCD. Self-

dissociation experiments were performed by titrating protein into its dialysis buffer. Blank profiles obtained by titrating Atg14 into dialysis buffer or titrating buffer into buffer were subtracted from the experimental profiles of Beclin 2 CCD and Atg14 CCD binding experiments or Beclin 2 CCD self-dissociation experiments respectively.

6.2.5. CD

CD data were recorded from the WT and mutant Beclin 2 CCD at a concentration of 50 uM in a quartz cell with a 0.1 cm path length using a Jasco J-815 CD spectrometer. Each sample was dialyzed into CD buffer comprising 10 mM potassium phosphate, pH 7.5 and 100 mM ammonium sulfate. Thermal stability was assessed by recording CD signal at 222 nm, from 5 ℃ to 85 ℃ (or 85 ℃ to 5 ℃ for reverse measurements) at 1 degree intervals, with a ramp rate of 1 ℃ /min. Data were analyzed using OriginPro 8 (OriginLab). The mean residue molar ellipticity was plotted against temperature, and the T_m obtained by fitting data tothe Boltzman algorithm included in OriginPro 8. Full-length scanning spectra were collected between 200 and 250 nm at 4 ℃. Secondary structure content of each sample was estimated using CONTIN included within the CDPro program package (Sreerama et al., 2001).

6.2.6. SEC-SAXS

SEC-SAXS data were recorded at beamline 18-ID Bio-CAT at APS, ANL, Argonne, IL. Purified proteins in 20 mM Tris, pH 8.0, 150 mM NaCl and 2 mM 2-mercaptoethanol were loaded onto an inline Superdex 200 10/300 SEC column and eluted at 0.8 ml/ml. SAXS data was recorded by exposing the column eluate to the X-ray beam for one second with a periodicity of three seconds. The data were recorded on a Pilatus 1M detector at a sample-to-detector distance of 3.5 m, covering a momentum transfer range of $0.0036\ Å^{-1} < q < 0.4\ Å^{-1}$. Scattering data were normalized to the incident X-ray beam intensity, and buffer subtraction performed prior to

processing using the ATSAS program suite (Petoukhov et al., 2012).Within the ATSAS program suite, PRIMUS (Konarev et al., 2003) was used to scale and average data for further analysis. The linear Guinier region was estimated using PRIMUS, and the R_g was calculated from the Guinier extrapolation. The P(r) plot and Kratky plot were calculated using GNOM (Svergun, 1992). The P(r) plot was used to estimate R_g and D_{max}, and for the calculation of ten independent *ab initio* bead models using DAMMIF (Franke and Svergun, 2009) which were then sequentially modeled using DAMSEL, DAMSUP, DAMAVER (Volkov and Svergun, 2003) and DAMMFILT. The atomic structures of MBP (extracted from PDB code 4GGQ), SUMO (extracted from PDB code 1L2N) and Beclin 2:Atg14 CCD model were used in SASREF (Petoukhov and Svergun, 2005) to build a model to be fit into the corresponding SAXS data sets. FoXS (Schneidman-Duhovny et al., 2013, Schneidman-Duhovny et al., 2010) was used to compare theoretical scattering curves calculated for SUMO-His_6-Beclin 2:MBP-Atg14 CCD heterodimer models against the experimental SAXS scattering curve, while SUPCOMB (Kozin and Svergun, 2001) was used to superimpose the SUMO-His_6-Beclin 2:MBP-Atg14 CCD heterodimer models to the *ab initio* bead models.

6.2.7. Construction of an atomic model of the Beclin 2:Atg14 CCD heterodimer

Based on our SAXS data, the Beclin 2:Atg14 CCD heterodimer model was built as a parallel packed CCD. In order to determine a parallel Beclin 2:Atg14 CCD heterodimer packing pattern that has the most ideal packing interactions at the *a* and *d* positions of the Beclin 2 CCD and Atg14 CCD, CCBuilder (Wood et al., 2014) was first used to build a series of heterodimer models with different packing patterns by changing the *a* and *d* register along the Atg14 sequence. The packing pattern with the most pairs of hydrophobic interface residues was picked and $(PS)^2$ (Huang et al., 2015) was then used to further calculate a heterodimer model based on

the amino acid sequences of the Beclin 2 CCD and Atg14 CCD and the packing pattern obtained from CCBuilder.

6.3. Results

6.3.1. Expression and purification results of seven Beclin 2 CCD mutants

In order to study the impact of non-ideal packing interactions on the stability of the Beclin 2 CCD dimers, the seven pairs of non-ideal packing residues were mutated to more ideal leucine-leucine or leucine-valine pairs to create five single mutants and two double mutants: E173L, N187L, A190L+Y215L, A197L+E208L, H211L, Q222L and R243L. Relative to the WT CCD homodimer, the more-ideal interface mutants are expected to result in stronger hydrophobic interactions at the interface, leading to a more stable homodimer. The WT and mutant Beclin 2 CCDs were expressed as MBP fusion proteins in *E. coli* BL21(DE3)*p*LysS cells, and soluble protein in the cell lysate was first purified by amylose affinity chromatography followed by the on-column TEV cleavage to remove the MBP tag. The cleaved product was further purified by IEX and SEC. The final SEC purification results are shown in Figure 6.1. All WT and mutant Beclin 2 CCDs have a theoretical monomer molecular weight of ~11kD, and run as expected between the 10 kD and 15 kD marker. The SEC profiles combined with SDS-PAGE gels indicated that WT and mutant Beclin 2 CCDs were eluted from SEC as a single peak that contained pure proteins (Figure 6.1). The SEC peaks of N187L and A197L+E208L mutant were ideal symmetrical Gaussian distribution peaks. But for WT and other five mutant Beclin 2 CCDs, the slope of the trailing edge of the peak is less steep than the leading edge. Since the X-ray crystal structure of the WT Beclin 2 CCD indicates that it forms a homodimer (Chapter 5), this suggeststhat the WT and these five mutant Beclin 2 CCDs form weak homodimers with the trailing edge of the peak representing monomeric states of these CCDs. N187L and

A197L+E208L mutant Beclin 2 CCDs, on the other hand, formed stronger homodimers than WT Beclin 2 CCD. The purification yields of four of the Beclin 2 mutants, including N187L, A190L+Y215L, A197L+E208L and H211L, increases by two to five fold over the WT (Table 6.2), suggesting that these four mutants are stronger homodimers than the WT Beclin 2 CCD.

Table 6.2: Summary of purification yields of WT and mutant Beclin 2 CCDs.

Beclin 2 CCD	Yield (mg per liter of cells)
Wild type	0.9
E173L	0.8
N187L	3.8
A190L&Y215L	2.9
A197L&E208L	4.7
H211L	1.8
Q222L	0.6
R243L	0.6

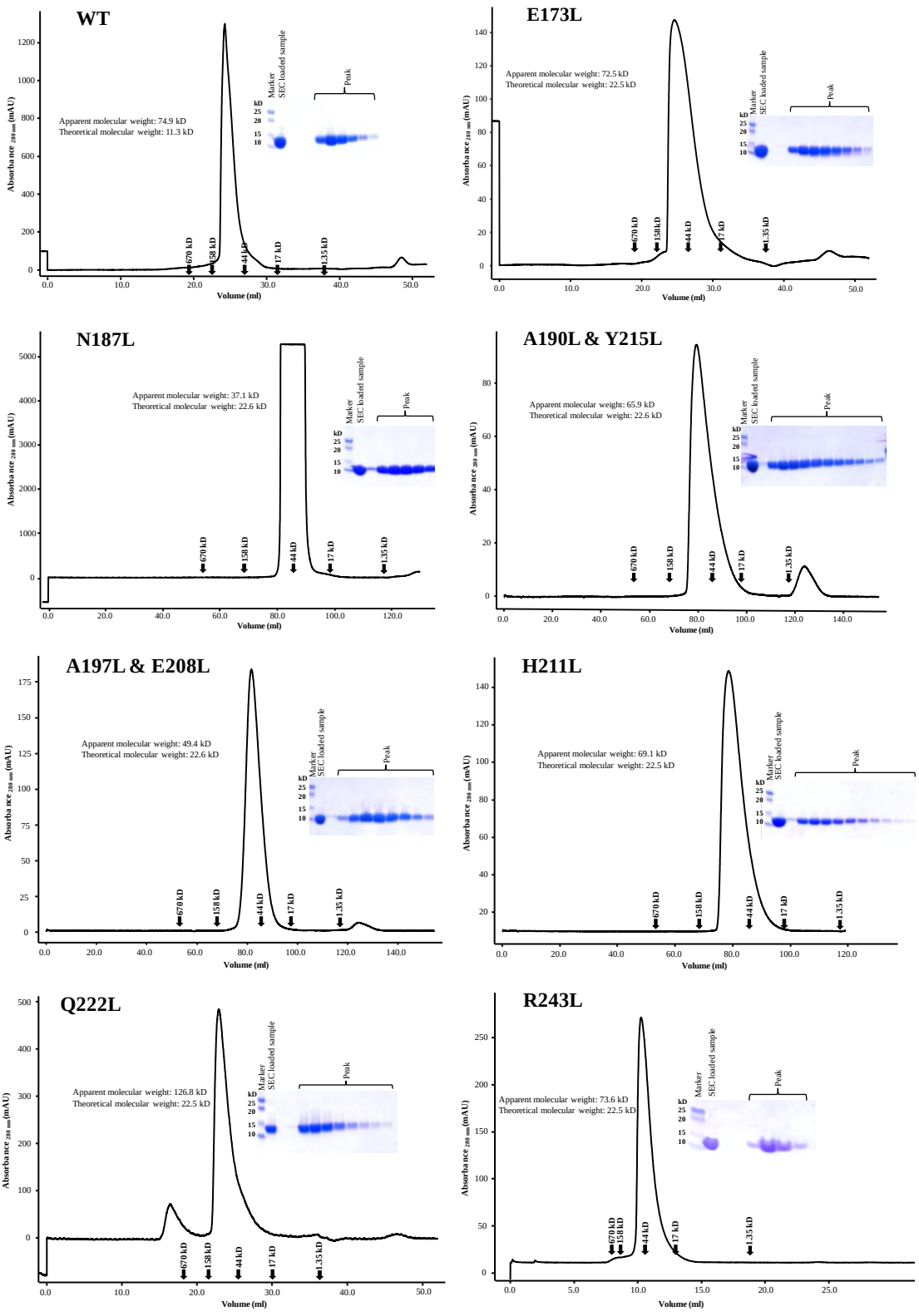

Figure 6.1: Size-exclusion chromatograms and corresponding SDS-PAGE gels of WT and mutant Beclin 2 CCDs.

6.3.2. The non-ideal packing interactions differentially impact the Beclin 2 CCD homodimerization

The K_d for the WT Beclin 2 CCD, quantified using ITC, indicates that it homodimerizes weakly, with a K_d of 138.3 μM, which is driven by entropy, not enthalpy (Figure 6.2, Table 6.3); consistent with the structural evidence that more than half the CCD homodimer interface interactions are non-ideal. The human Beclin 1 CCD homodimerizes with a K_d of 48 μM (Mei et al., 2016b), indicating that Beclin2 CCD forms a weaker homodimer compared to the Beclin 1 CCD. This is consistent with the structural differences in the interactions stabilizing the Beclin 2 and Beclin 1 CCD homodimers discussed in Chapter 5.

In order to study the impact of the non-ideal packing interactions on the stability of Beclin 2 CCD dimers, the seven pairs of non-ideal packing residues were mutated to more ideal leucine-leucine or leucine-valine pairs to create five single mutants and two double mutants, wherein both partners within the imperfect pair were altered (Figure 6.2 and Table 6.3). Relative to the WT CCD homodimer, the more ideal interface mutants were expected to result in stronger hydrophobic interactions at the interface, leading to a more stable homodimer..

We used ITC to quantify the self-dissociation constants of mutant Beclin 2 CCDs for comparison to WT. Consistent with the expectation of improved stability, we find that three of the seven Beclin 2 mutants associate more tightly as homodimers (Figure 6.2, Table 6.3). Amongst these three mutants, we find that the N187L mutant homodimerizes most tightly, with a K_d of 0.04 μM, which is ~3500 fold tighter than the WT Beclin 2 CCD. Homodimerization of the H211L mutant is ~10-fold tighter compared to the WT Beclin 2 CCD, while that of the A190L+Y215L mutant is only 1.3-fold tighter than WT.

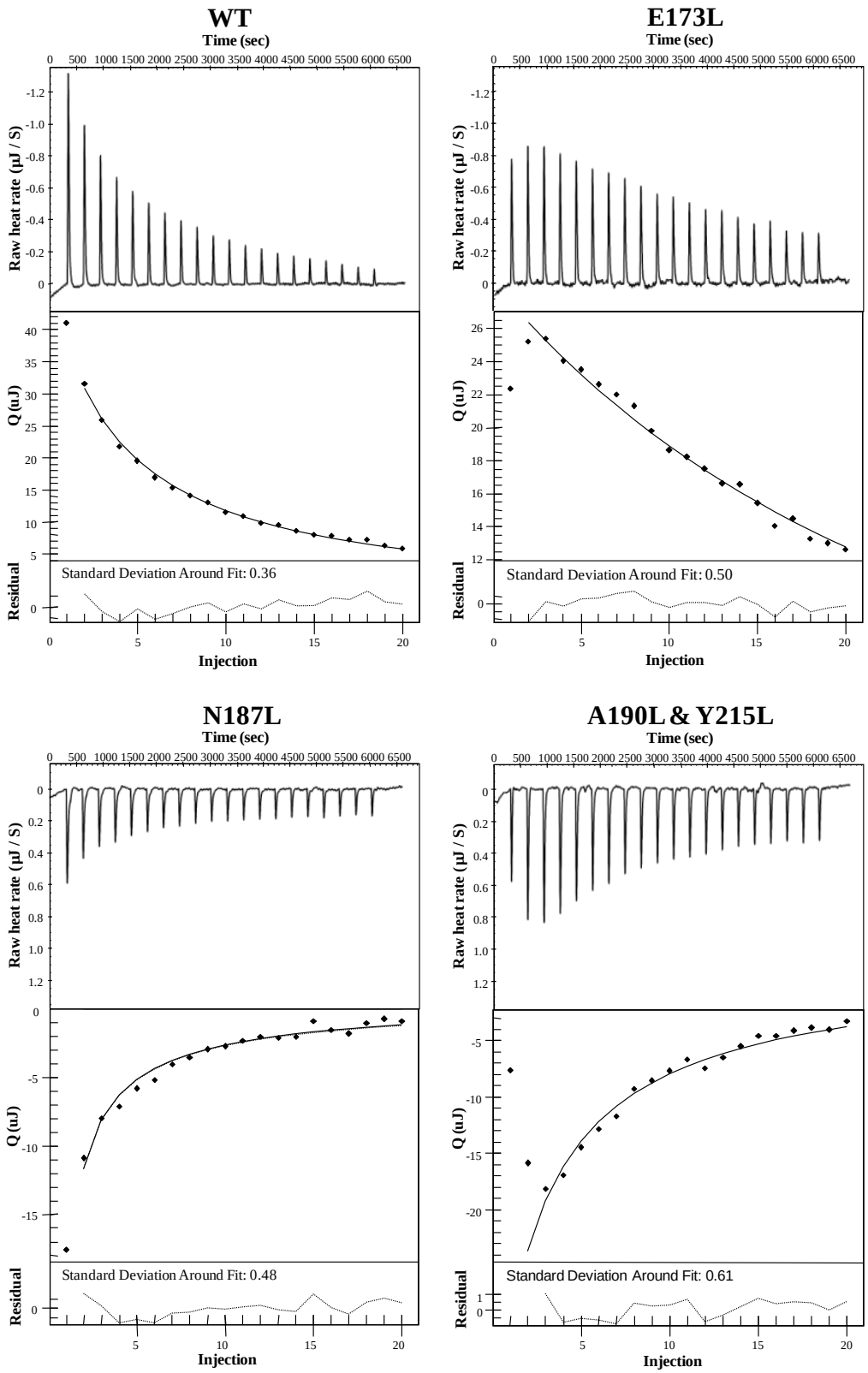

Figure 6.2: ITC titration profiles of WT and mutant Beclin 2 CCD dissociation measurements.

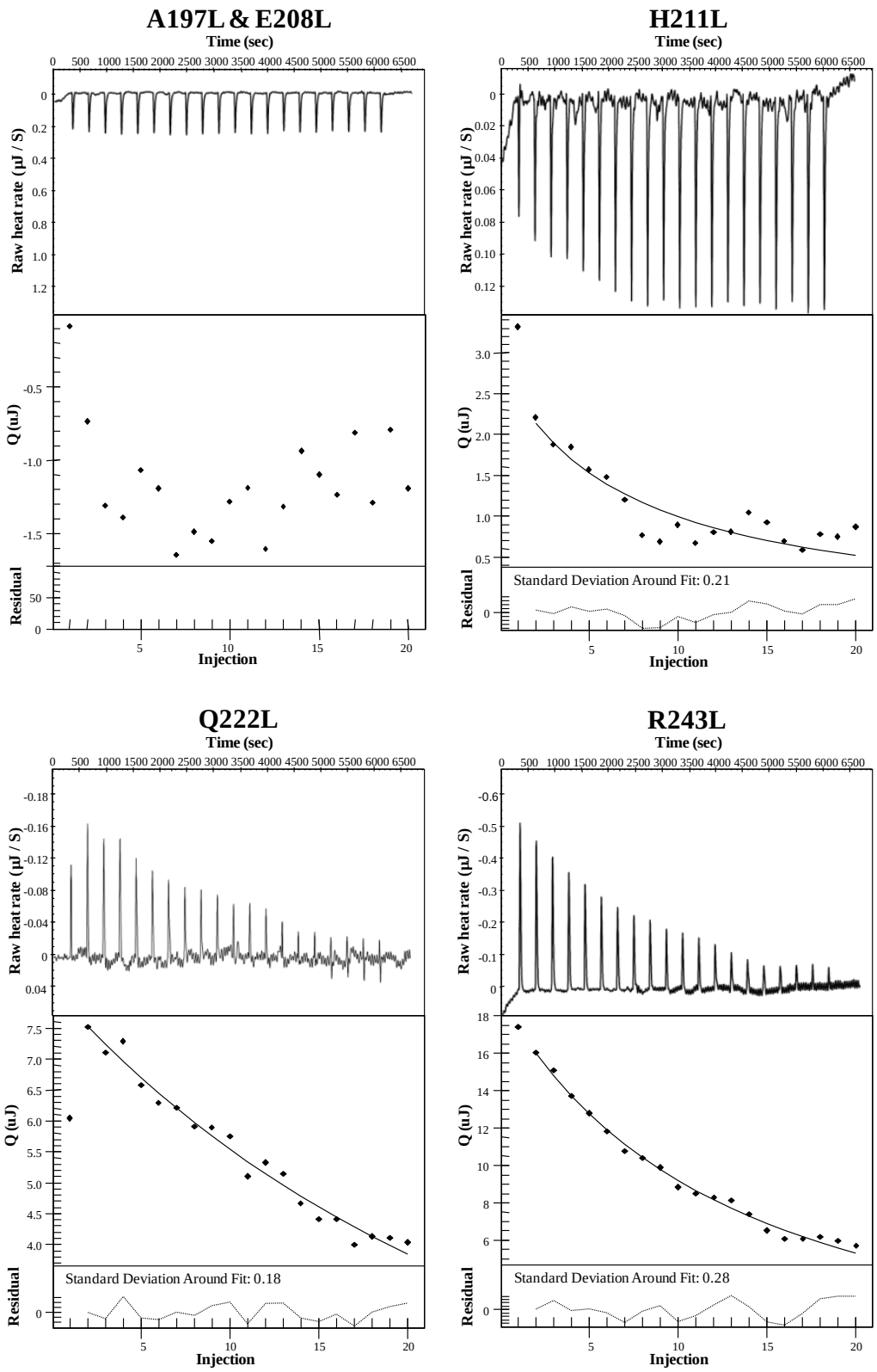

Figure 6.2: ITC titration profiles of WT and mutant Beclin 2 CCD dissociation measurements (continued).

Table 6.3: Summary of the self-dissociation constants of WT and mutant Beclin 2 CCD.

Beclin 2 CCD	Kd (uM)	dH(kJ/mol)	dS(J/K ▪mol)
WT	138.3 ± 6.5	120.7 ±7.4	492.7 ± 25.4
E173L	5176.0 ± 937.6	205.6 ± 12.4	757.2 ± 41.6
N187L	0.04 ± 0.01	-877.8 ± 89.9	-2904.7 ±
A190L+Y215L	104.5 ± 8.7	-85.4 ± 1.4	-220.0 ± 4.2
A197L+E208L	Not detected		
H211L	13.3 ± 2.2	168.2 ± 1.1	677.4 ± 5.1
Q222L	4804.3 ± 754.3	98.5 ±9.1	386.3 ± 32.6
R243L	325.5 ± 4.0	165.3 ± 7.6	640.6 ± 26.5

In addition to the three mutants with improved homodimer interfaces, we are unable to detect any self-dissociation of the A197L+E208L mutant, suggesting that either there is no detectable dissociation of the homodimer, or the heat generated during dissociation is too small to be detected by ITC, or possibly that this mutant does not homodimerize, and therefore does not self-dissociate. The dramatically improved purification yield for this mutant (Table 6.2), suggests that the first possibility is the most likely, and the A197L+E208L mutant forms the most stable homodimer.

In contrast to the mutants discussed above, and contrary to our initial expectations, the remaining three mutants, R243L, E173L and Q222L, homodimerize more weakly than the WT Beclin 2 CCD, with the latter two forming substantially weaker homodimers (Figure 6.2 and Table 6.3). In the WT Beclin 2 CCD homodimer, the Cα, Cβ and Cδ atoms of the aliphatic part of R243 pack against a Cδ atom of L162 of the partner helix; while the charged R243 guanidinium sticks out of the homodimer interface. Analysis of the modeled backbone-dependent rotamers of the leucine side chain of the R243L mutation indicates that L162 and L166 of the partner helix would sterically clash in 65% of the R243L conformations, thereby

weakening homodimerization. Similarly, in the WT Beclin 2 CCD homodimer, the E173 Cβ and Cγ pack against the L229 Cδ and V232 Cγ of the partner helix; but the E173 carboxylate is solvent-exposed. Mutation of E173 to leucine causes steric clashes with L229 or V232 of the partner in all backbone-dependent rotamer conformations, explaining the significantly weaker homodimerization of the E173L mutant compared to WT. Lastly, in the WT Beclin 2 CCD homodimer, the Q222 Cα and Cβ pack against the V183 Cγ atom of the partner helix, while the Q222 Cγ packs with the partner helix L180 Cδ atom. Further, the Q222 side-chain amide hydrogen bonds the D184 carboxylate of the partner helix, while the Q222 side-chain carbonyl oxygen makes an intra-chain hydrogen bond to the K219 NH_3^+ group. Mutation of Q222 to leucine would cause loss of these hydrogen bonds; and also, in all rotamer conformations, cause steric conflicts with V183, D184 or L180 of the partner helix. Thus, like the E173L mutant, the Q222L mutant makes a much weaker homodimer compared to WT.

6.3.3. Non-ideal packing interactions impact thermal stability of the Beclin 2 CCD

We used CD spectroscopy to assess the secondary structure of each WT and mutant Beclin 2 CCD. The CD spectra recorded for each protein show two minima at wavelength 208 nm and 222 nm, indicative of a α-helical conformation (Figure 6.3), consistent with expectations from the crystal structure.

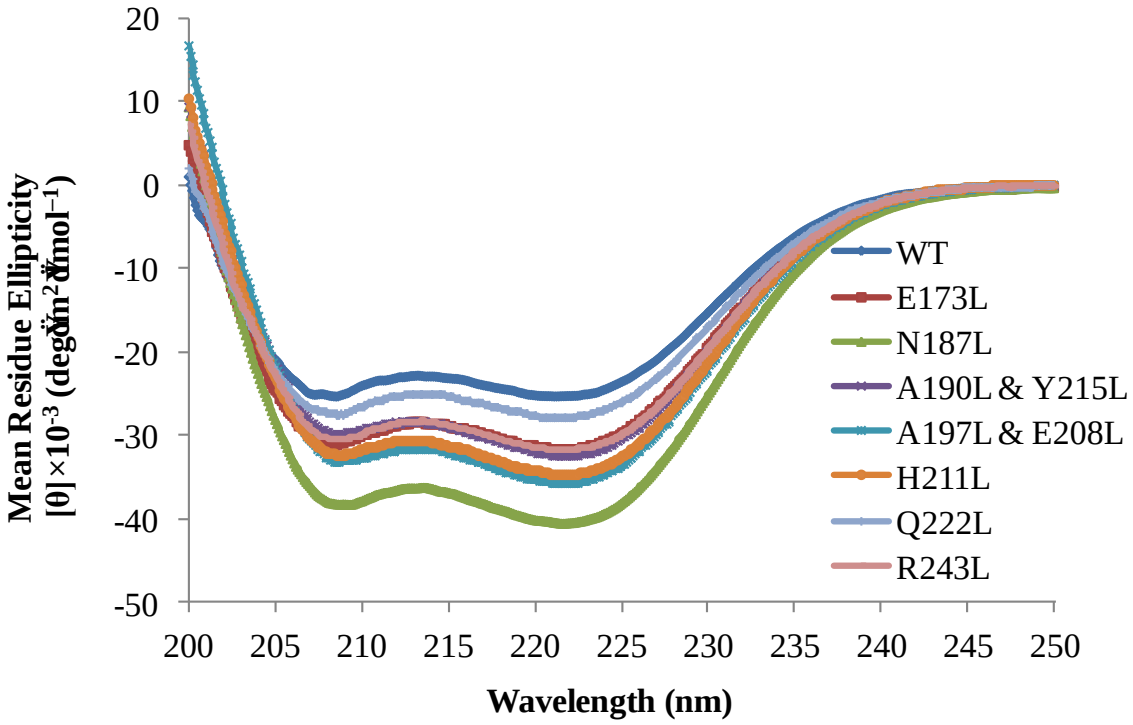

Figure 6.3: CD spectra of WT and mutant Beclin 2 CCDs at 4 ℃.

Further, a comparison of the secondary structure estimated from each spectra indicates that there is no significant reduction in the α-helical content of any of the mutants (Table 6.4).

Table 6.4: CD analysis of secondary structure content of WT and mutant Beclin 2 CCDs.

Beclin 2 CCD	Helix (residues)	Strand (residues)	Turn (residues)	Disordered (residues)	Total (residues)
WT	98	0	0	0	98
E173L	98	0	0	0	98
N187L	96	2	0	0	98
A190L+Y215	98	0	0	0	98
A197L+E208	96	2	0	0	98
H211L	98	0	0	0	98
Q222L	98	0	0	0	98
R243L	96	2	0	0	98

CCDs are unique in terms of protein folding, because their tertiary structure, and often their secondary structure as well, is coupled to their oligomerization (Sanchez et al., 2014). Therefore, we assessed and compared the structural stability of the WT and the seven mutant Beclin 2 CCD constructs by using thermal denaturation coupled to CD measurements at 222 nm to quantify T_m (Figure 6.4, Table 6.5). The relatively low T_m of 19.3 ℃ (Figure 6.4, Table 6.5) determined from the single transition melting curve of the WT Beclin 2 CCD indicates that the Beclin 2 CCD is a meta-stable dimer.

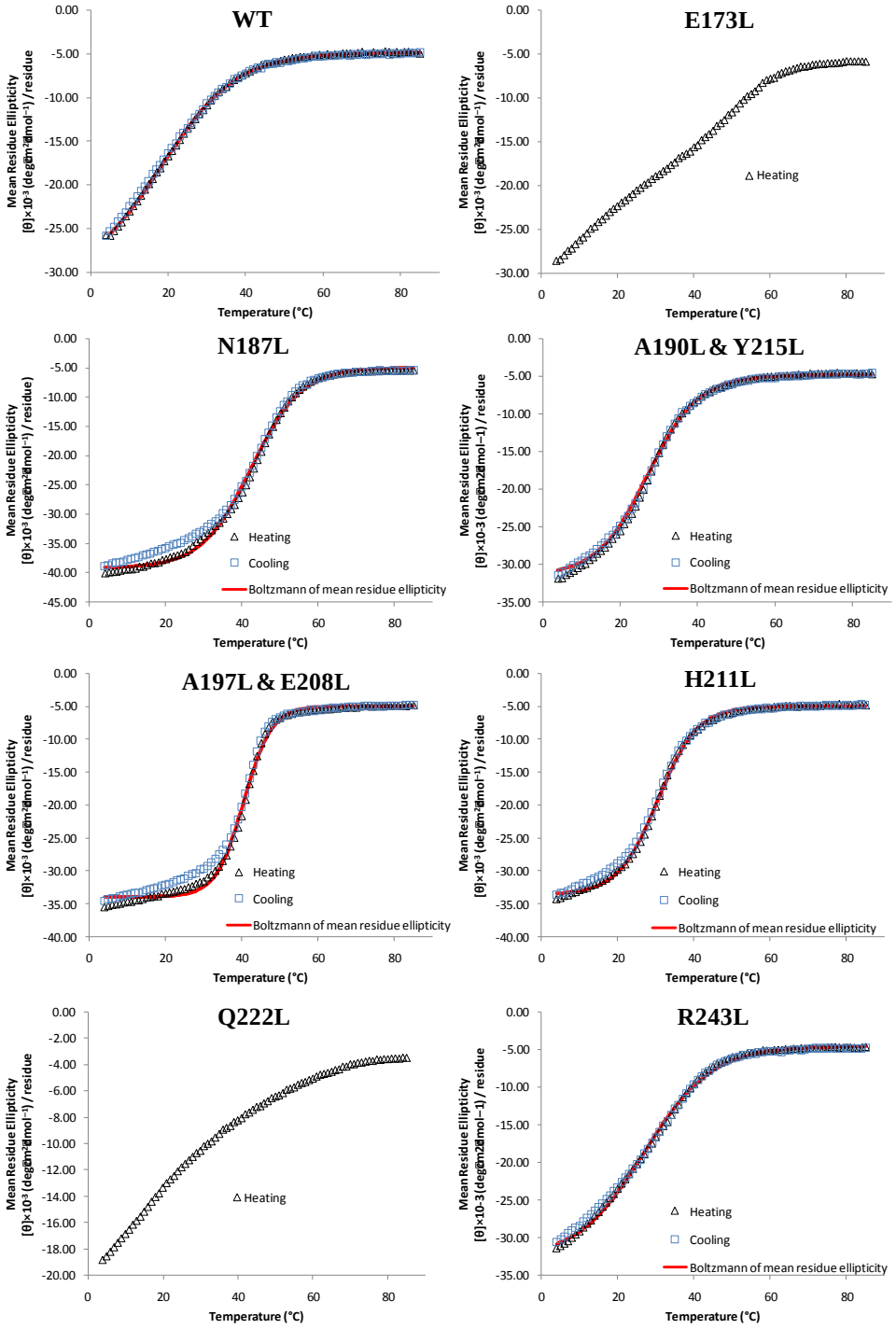

Figure 6.4: Temperature-dependent CD profiles of WT and mutant Beclin 2 CCDs. For each mutant, mean residue ellipticity was measured at 222 nm from 4 ℃ to 85 ℃ for the heating measurement (Δ) and from 85 °C to 4 °C for the cooling measurement (□). Boltzmann fitting of the heating measurement is shown in red curve. For E173L and Q222L mutant Beclin 2 CCD, only the heating measurements are present. Because the melting processes of these two mutants is not cooperative, no Boltzmann fitting was shown.

Table 6.5: Summary of T_ms of WT and mutant Beclin 2 CCDs.

Beclin 2 CCD	**T_m(℃)**
WT	19.3
E173L	----[a]
N187L	42.5
A190L+Y215L	27.2
A197L+E208L	40.5
H211L	30.5
Q222L	----[a]
R243L	26.9

[a]The $T_m$of these mutants can't be obtained using CD because the melting process is not cooperative.

All the mutants, except the two that formed significantly weaker homodimers, also have single transition melting curves, and strikingly, each of these has a T_m significantly higher than WT. Amongst all these mutants, the N187L and A197L+E208L mutants have the highest melting temperatures, a striking 21-23 ℃ higher than WT, and 10-12 ℃ higher than the other mutants (Table 6.5). Notably, the N187L Beclin 2 mutant has the tightest measured homodimerization, about ~3500 fold lower self-dissociation than WT, while no self-dissociation was detected for the A197L+E208L mutant. The dramatically improved thermal stability of the A197L+E208L mutant confirms that the non-detectable self-dissociation by ITC is the result of its strong homodimerization, rather than lack of dimerization or low heat of dissociation. The H211L mutant which homodimerizes ~10-fold tighter than the WT Beclin 2 CCD, also shows an improvement of 11 ℃ in thermal stability; while the A190L+E215L and R243L, which have homodimerization affinities comparable to WT, display a smaller, ~7 ℃ increase in thermal stability.

Melting temperatures of the remaining two mutants, E173L and Q222L, could not be quantified because their melting curves are non-cooperative. This may suggest that these two mutants are molten globules (Rantalainen et al., 2008). Significantly, these two mutants also resulted in the weakest homodimerization, which likely leads to reduced stability of the CCD secondary and tertiary structure. In sum, the stability of all Beclin 2 CCD mutants (Figure 6.4 and Table 6.5) appears to be co-related with their ability to form CCD homodimers (Table 6.3).

6.3.4. The N187L Beclin 2 CCD X-ray crystal structure reveals why it homodimerizes better than WT

In order to understand the impact of the N187L single mutation on the Beclin 2 CCD structure, we determined the 2.5 Å X-ray crystal structure of N187L Beclin 2 CCD mutant. Rod-shaped crystals grew to 100 μm×10 μm × 10 μm in 3 days (Figure 6.5).

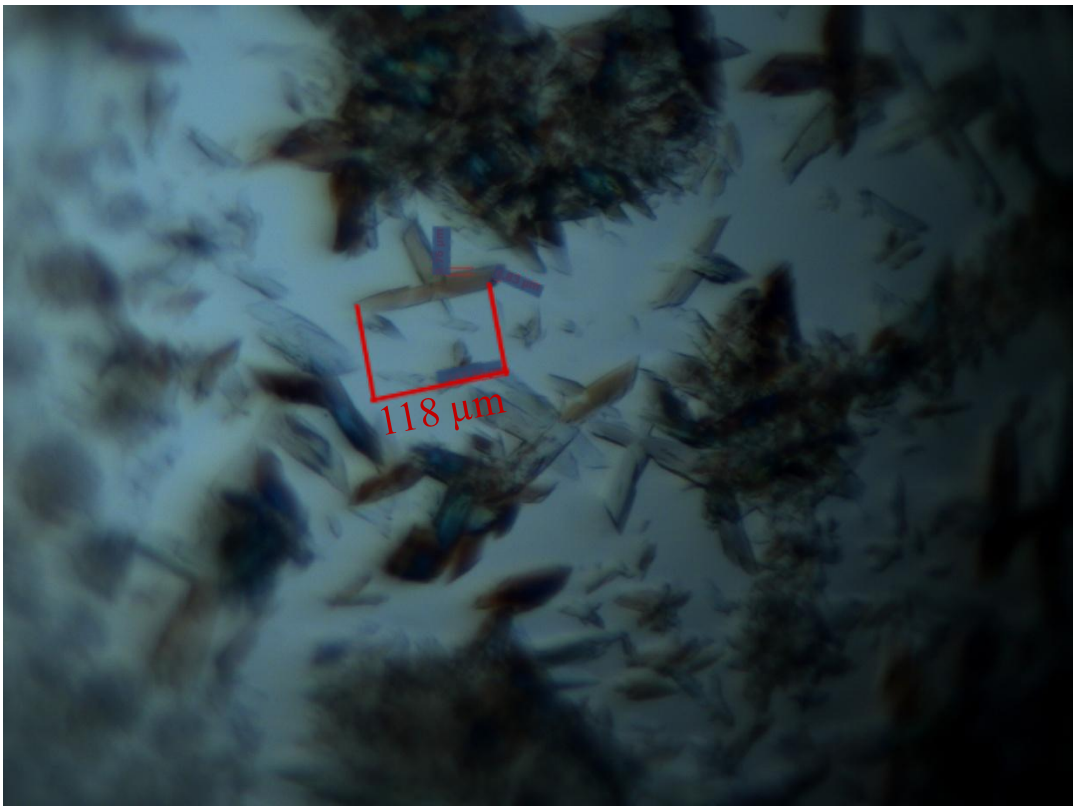

Figure 6.5: Typical N187L Beclin 2 CCD crystals.

The structure of N187L mutant CCD was solved by MR using the WT Beclin 2 CCD AB homodimer as the search model using Phaser-MR in PHENIX (Adams et al., 2010). All refinement was performed using phenix.refine (Adams et al., 2010). Crystallographic data collection and refinement statistics are summarized in Table 6.6.

Table 6.6: Summary of x-ray data collection and refinement statistics of N187L Beclin 2 CCD.

Data collection:	
Wavelength (Å)	0.97918
Data range (Å)	72.09 - 2.52
Space group	C2
Unit cell parameters	a= 127.97 Å b= 44.71 Å c= 94.90 Å β= 130.57 °
Average Mosaicity ( )	0.18
Unique reflections	13749 (1362)
Avg. multiplicity	3.7 (3.4)
Completeness (%)	97.1 (86.9)
CC1/2	0.991 (0.761)
[1]R_{meas}	0.26 (1.43)
I/σ_I	6.1 (1.1)
Refinement:	
Monomer A	89 residues
Monomer B	90 residues
Monomer C	89 residues
Monomer D	89 residues
Water molecules	60
Data Range (Å)	72.09 - 2.52
[2]R_{work} (%)	23.5
[2,3]R_{free} (%)	27.8
Average B-values ($Å^2$)	47.6
Macromolecules	47.8
Water	37.6
Bond Lengths (Å)	0.018
Bond Angles ( )	1.38
Ramachandran favored (%)	96.8
Ramachandran outliers(%)	0

Values in parentheses pertain to the outermost shell of data.

[1] $R_{meas}= \sum_{hkl}(n/n-1)^{1/2}\sum_{h,i} |I_{hkl,i}-<I_{hkkl}>|/\sum_{hkl}\sum_{h,i}I_{hkl,i}$.

[2] R factor= $\sum_{h,} |F_{obs}-|F_{calc}|/\sum_{h}|F_{obs}|$.

[3] Test set for R_{free} consisted of 5% of data

The N187L Beclin 2 CCD crystallized in a different space group than the WT (Table 6.6 and Chapter 5 Table 5.2), but like the WT, the crystallographic asymmetric unit contains two pairs of anti-parallel homodimers: AB and CD. The N187L Beclin 2 CCD AB homodimer superimposes on the CD homodimer with an RMSD of 1.49Å over 160 Cα atoms, indicating that the two homodimers are very similar. The Beclin 2 N187L dimers superimpose very well on the WT dimers, with an RMSD of 1.08 ± 0.58 Å over 160 Cα atoms (Figure 6.6A). Thus, overall, the structure of N187Lmutant and WT Beclin 2 CCD are very similar.

The N187L CCD homodimer interface has a total buried surface area of 2188 ± 30 $Å^2$, somewhat more than in the WT CCD. Except for the mutated residues, packing at the N187L Beclin 2 CCD homodimer interface, including the two pairs of inter-chain surface polar interactions, is similar to WT. The N187 in the WT structure (Figure 6.6B), as well as the leucine at position 187 in the mutant structure (Figure 6.6C) are clearly defined by electron density. The average buried surface area for the leucines from the four chains in the N187L CCD homodimer interface is 94.56 ± 3.06 $Å^2$. This is significantly more than the 80.44 ± 6.54 $Å^2$ calculated from N187 in the WT CCD interface. In the WT CCD structure, the N187 Cγ packs between side-chains of Y215 and L218 from the partner helix, while the polar end of the side chain is solvent-exposed. In the N187L CCD structure, the L187 Cγ atom packs similarly and the two leucine Cδ atoms make additional hydrophobic interactions with the partner helix via the L218, K219,Y215 side-chain atoms as well as the Y215 backbone C atoms.Thus, as expected, the N187L mutation results in increased hydrophobic interactions, leading to tighter homodimerization.

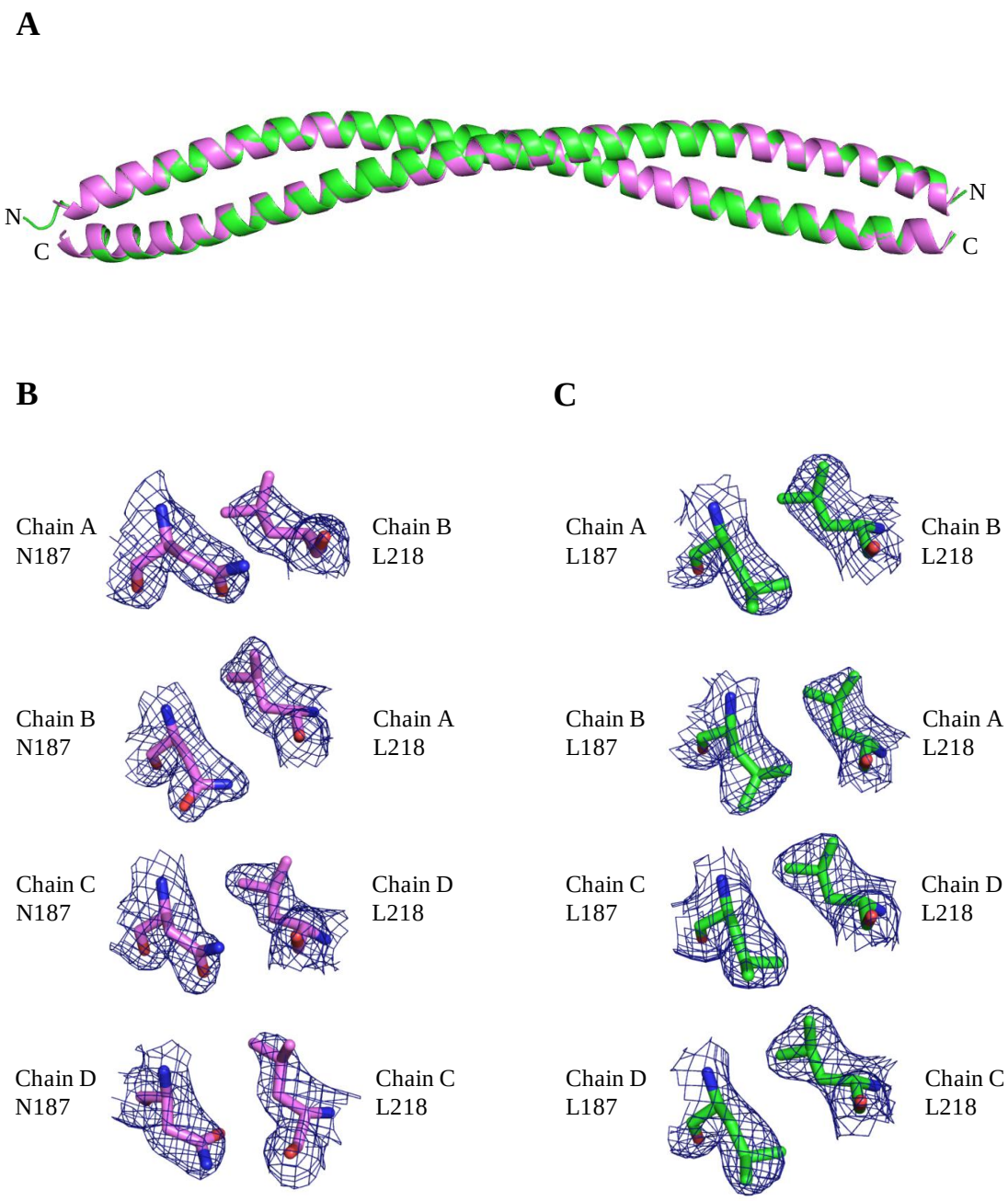

Figure 6.6: Superposition of WT and N187L Beclin 2 CCD structures. (A) Superposition of the N187L mutant (green) and WT (violet) Beclin 2 CCD homodimers. (B) Atomic details of N187 - L218 pair in the WT Beclin 2 CCD structure. The blue mesh represents 2Fo-Fc maps contoured at 1δ above the mean. (C) Atomic details of L187-L218 pair in the N187L Beclin 2 CCD structure. The blue mesh represents 2Fo-Fc maps contoured at 1δ above the mean.

6.3.5. The Beclin 2 and Atg14 CCD interaction is inversely related to the stability of Beclin 2 CCD homodimer

The imperfect interactions at the Beclin 2 homodimer interface that weaken the CCD homodimer, likely enable self-dissociation of the CCD homodimer to facilitate heterodimerization with other CCD containing autophagy proteins, such as Atg14. Consistent with this, the Beclin 2 CCD binds tightly to the Atg14 CCD, with a binding affinity of 0.22 uM, which is 20-fold tighter than association of the CCDs of Beclin 1 and Atg14.

All the mutants created to have more ideal packing interfaces, bind more weakly to the Atg14 CCD, although all binding affinities lie within ~10-fold of the WT (Figure 6.7, Table 6.7). Notably, the trend of increasing self-association of Beclin 2 CCD mutants (Table 6.3) correlates, although not perfectly, with the order of decreasing binding affinity for Atg14. For instance, the A197L+E208L Beclin 2 CCD mutant, which has no detectable self-dissociation, displays the weakest interaction, with ~9-fold lower binding affinity for the Atg14 CCD relative to WT. Similarly, the N187L and H211L mutants have significantly tighter self-association relative to WT and bind to the Atg14 CCD with ~3-fold lower affinity compared to WT. The A190L+Y215L mutant binds to the Atg14 CCD only slighter more weakly than to the Beclin 2 CCD WT, as it self-associates only slightly better than the WT. However, the E173L and Q222L, the two Beclin 2 CCD mutants that homodimerized very weakly and had non-cooperative melting curves, also bind 2.5 – 4 fold more weakly to the Atg14 CCD than WT Beclin 2 CCD. This is not entirely surprising, because heterodimerization with Atg14 also depends on factors other than homodimerization. Perhaps, the side-chain oxygen and hydrogen atoms of E173 and Q222 are involved in polar interactions with Atg14 residues, therefore mutating these residues to leucines does not improve the binding of Beclin 2 CCD to Atg 14 CCD. Thus, although all

mutations weaken binding of Beclin 2 CCD to Atg14 CCD, no mutation completely abrogates this interaction. Significantly, all the Beclin 2 interface mutations impact homodimerization more than heterodimerization.

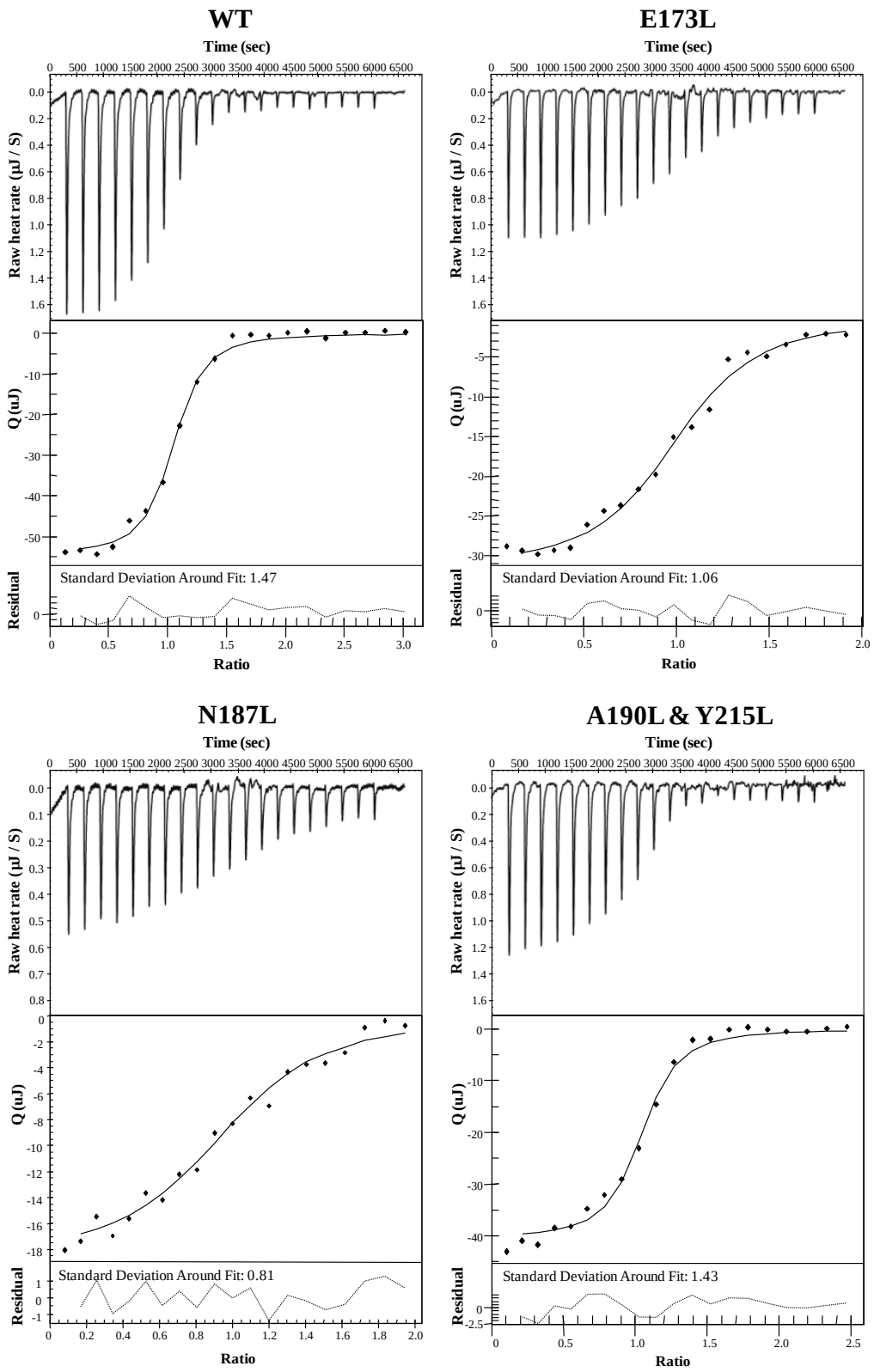

Figure 6.7: ITC titration profiles of Atg14 CCD binding to WT and mutant Beclin 2 CCDs.

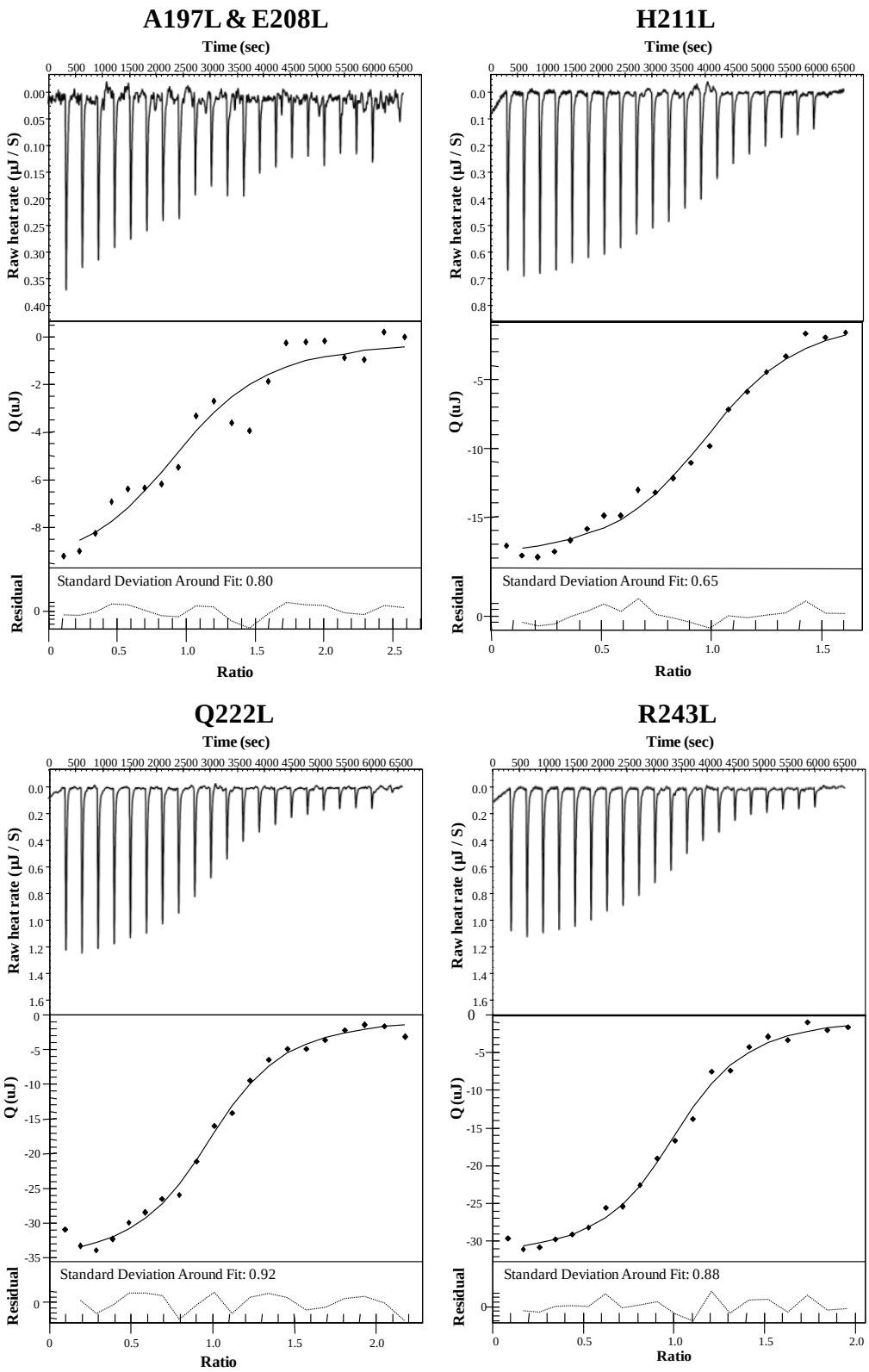

Figure 6.7: ITC titration profiles of Atg14 CCD binding to WT and mutant Beclin 2 CCDs (continued).

Table 6.7: Summary of thermodynamic parameters for binding of WT and mutant Beclin 2 CCDs to Atg14 CCD.

Beclin 2 CCD	Kd (uM)	dH(kJ/mol)	dS(J/K·mol)
Wild type	0.22 ± 0.04	-162.2 ±1.1	-435.4 ± 2.2
E173L	0.58 ± 0.14	-154.3 ±6.8	-416.0 ± 21.4
N187L	0.72 ± 0.11	-110.5 ± 16.1	-265.8 ± 57.1
A190L&Y215L	0.30 ± 0.02	-120.7 ± 3.9	-294.0 ± 13.8
A197L&E208L	1.23 ± 0.06	-61.7 ± 11.5	-100.9 ± 40.4
H211L	0.80 ± 0.18	-105.7 ± 3.0	-250.0 ± 12.2
Q222L	0.79 ± 0.01	-149.7 ± 0.1	-402.7 ± 0.2
R243L	0.54 ± 0.05	-148.7 ± 0.6	-396.0 ± 1.6

6.3.6. The Beclin 2 CCD and Atg14 CCD form a parallel heterodimer

We used SAXS to probe the structure of the Beclin2:Atg14 CCD homodimer in solution. To ensure that the SAXS data were collected from a homogeneous sample, SAXS was performed in tandem with size exclusion chromatography (SEC-SAXS). For this study, the Beclin 2 CCD was expressed and purified with an 11kD N-terminal SUMO-His_6-tag and the Atg14 CCD was expressed and purified with a 40 kD N-terminal MBP tag, so that the relative orientation of each protein in the complex could be extrapolated from the relative location of the tags in the low-resolution envelope. The SEC profile of the SUMO-His_6 –Beclin 2 CCD:MBP-Atg14 CCD complex comprises a single peak consistent with an elongated CCD dimer and indicates an absence of aggregated protein (Figure 6.8).

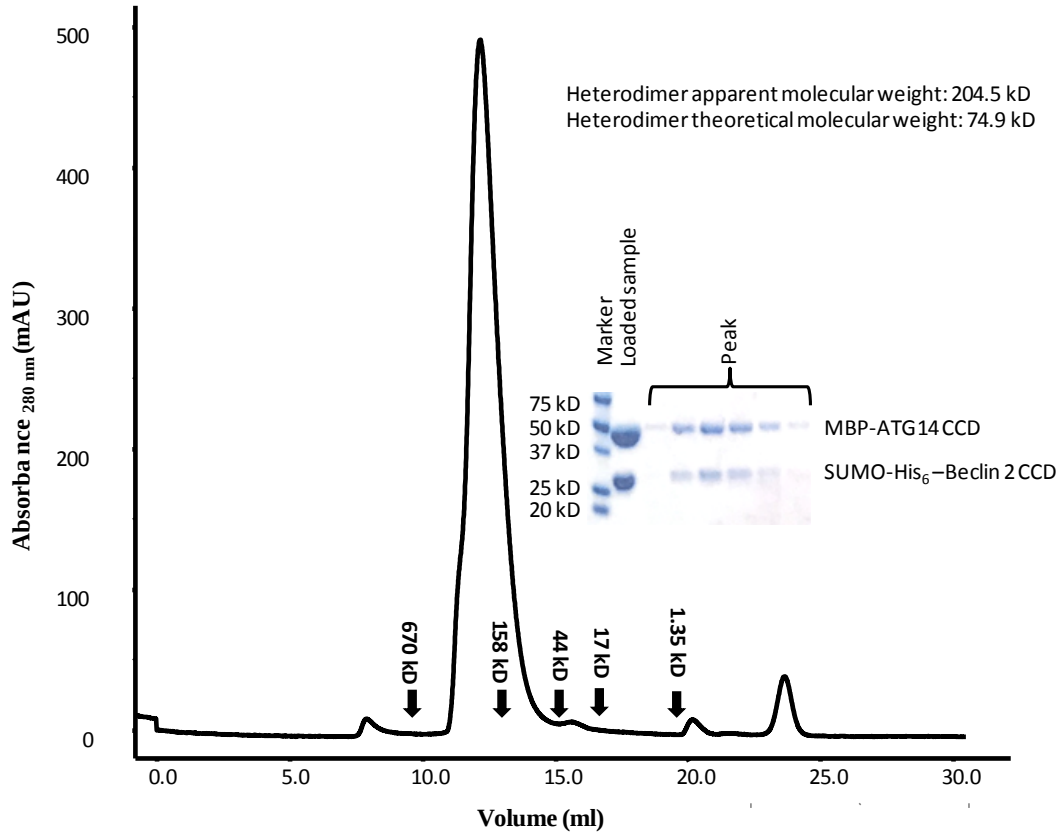

Figure 6.8: Gel filtration chromatogram and corresponding SDS-PAGE of SUMO-His_6 –Beclin 2 CCD:MBP-ATG14 CCD complex. The apparent molecular weight calculated from SEC is 204 kD and the theoretical molecular weight calculated from sequence is 74.9 kD.

The low q-range region in the Guinier plot is linear in the range of $q \times R_g < 1.3$ which confirms the absence of aggregation (Figure 6.9A). The Guinier plot indicates that the SUMO-His_6-Beclin 2:MBP-Atg14 CCD heterodimer has a R_g of 43 Å, which is similar to the R_g of 49 Å estimated from the P(r) distribution (Figure 6.9B). The D_{max} of the heterodimer estimated from the P(r) plotis 186 Å. The Kratky plot indicates that the heterodimer is well-folded (Figure 6.9C).The *ab initio* envelope calculated from the heterodimer SAXS data, was "lollipop-shaped", comprising of a long rod with a sphere at one end of the rod, which likely corresponds to the heterodimeric CCD and MBP+SUMO, respectively (Figure 6.9E). Therefore, the Beclin 2 CCD and Atg14 CCD most likely form a parallel heterodimer.

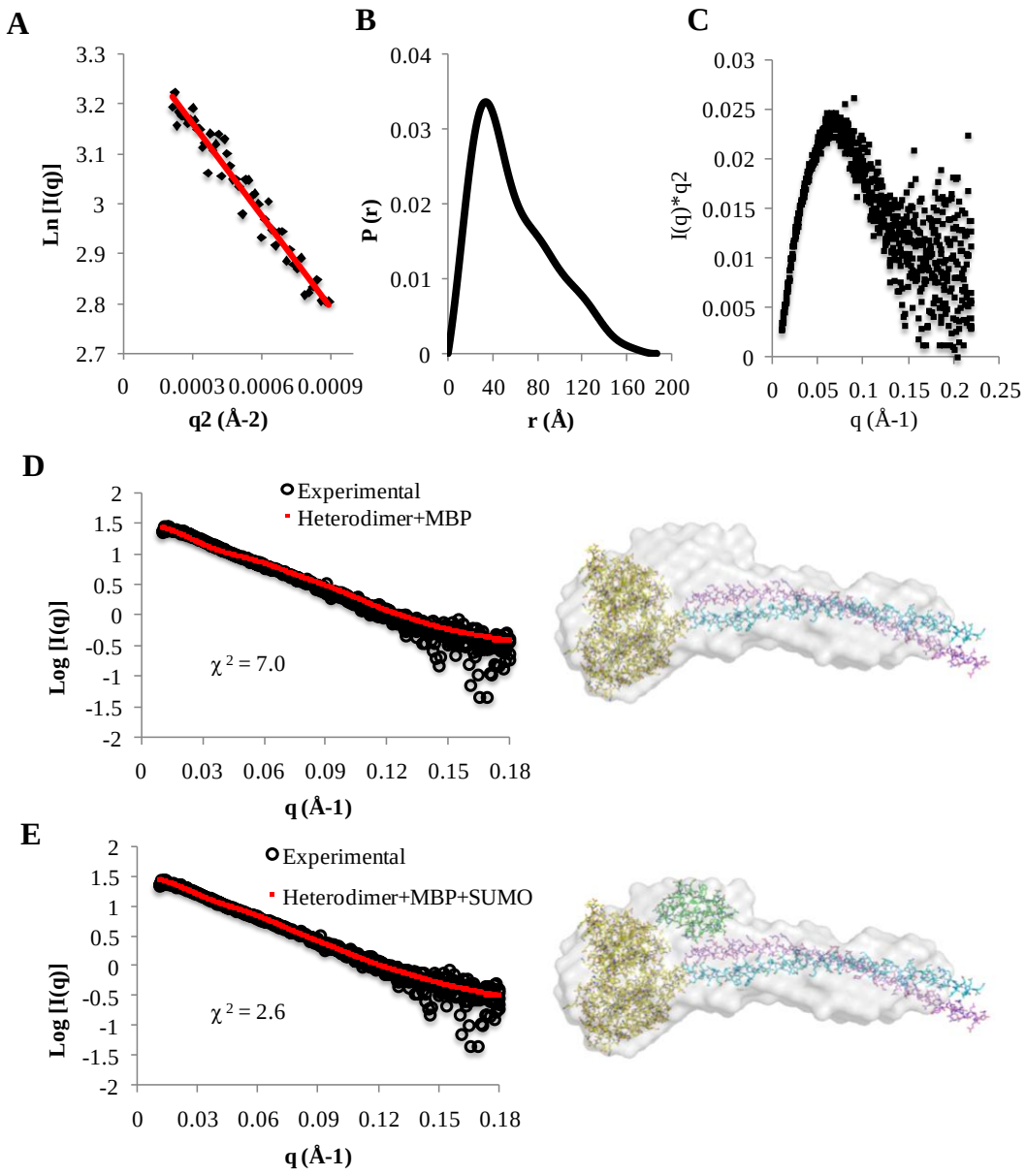

Figure 6.9: SEC-SAXS analysis of SUMO-His_6-Beclin 2: MBP-Atg14 CCD heterodimer. (A) Guinier plot.(B) P(r) pairwise distribution. (C) Kratky plot. (D) and (E) Fit of the pseudo-atomic Beclin 2:MBP-Atg14 CCD heterodimer models to the *ab initio* bead model and the experimental SAXS data (D) without SUMO-His_6 or (E) with SUMO-His_6 placed manually. The *ab initio* bead model is shown in grey and atomic structures used for heterodimer model construction are shown in atomic details with MBP colored yellow, SUMO colored green, the Beclin 2 CCD colored violet, and the Atg14 CCD colored cyan. The fits of theoretical scattering profiles (red dots) calculated from the corresponding heterodimer model to the experimental SAXS data (black circles) are shown on the right.

In order to further investigate structural details of the Beclin2:Atg14 CCD heterodimer, we built a parallel heterodimer model (Figure 6.10A).We first used CCBuilder (Wood et al., 2014) to determine the register of parallel Beclin 2 CCD and Atg14 CCD sequences that results in optimal packing interactions at the potential *a* and *d* positions of each CCD. Next, we used $(PS)^2$ (Huang et al., 2015) to calculate a pseudo-atomic heterodimer model based on the amino acid sequences of each CCD and the best packing register obtained from CCBuilder. Interestingly, the Beclin 2:Atg 14 CCD model is also curved, with a radius of curvature of 13 nm (Figure 6.10B), suggesting the heterodimer may be slightly more curved than the Beclin 2 CCD homodimer. Notably, the Beclin 2:Atg14 CCD heterodimer is less negtively charged compared to the Beclin 2 CCD homodimer (Figure 6.10B).

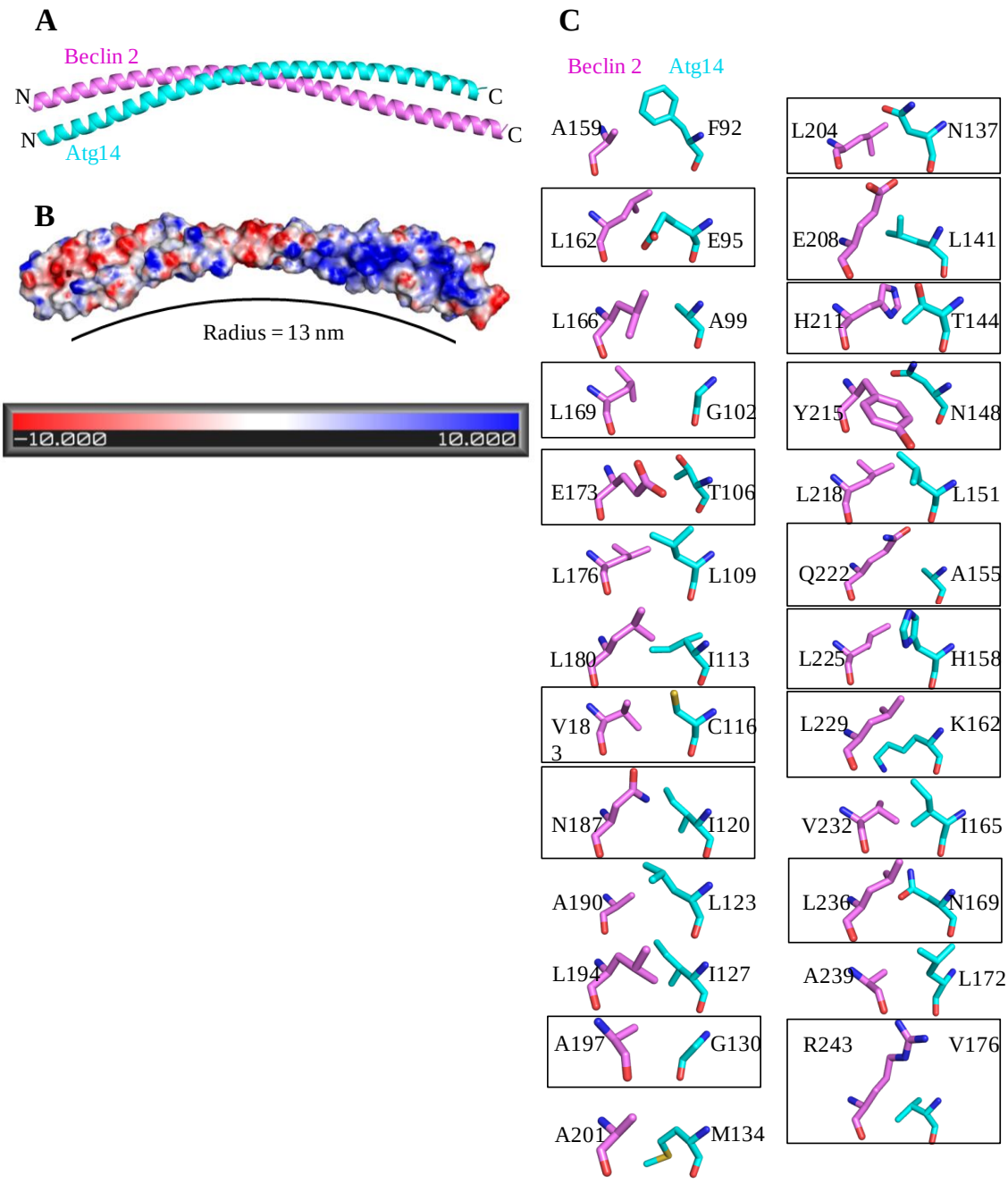

Figure 6.10: The Beclin 2:Atg14 CCD heterodimer. (A) The heterodimer model displayed in ribbon with Beclin2 in violet and ATG14 in cyan ribbon. (B) Molecular surface representation of the heterodimer. (C) Heterodimer interface residues displayed in stick colored as in Figure 1B, with Beclin 2 C in violet and Atg14 C in cyan. Non-ideal packing residues are boxed.

SASREF (Petoukhov and Svergun, 2005) was then used to construct a pseudo-atomic model that contains MBP and the Beclin 2:Atg 14 CCD heterodimer, which fit somewhat poorly,

with a χ^2 of 7.0 (Figure 6.9D), to the experimental SAXS curve. The CCD fits into the rod part of the "lollipop"-shaped envelope, while MBP is positioned in the head. Lastly, SUMO was manually placed into unoccupied space in the lollipop head that remained even after MBP had been positioned. This results in significantly improved agreement with the SAXS data as indicated by a χ^2 of 2.6 (Figure 6.9E). Therefore, MBP and SUMO are located on the same side of the rod-like part of the *ab initio* SAXS envelope, with no obvious unoccupied space on the other end of the envelope. Thus, the Beclin 2 CCD and Atg14 CCD form a parallel heterodimer, similar to that observed for the Beclin1:Atg14 CCD (Baskaran et al., 2014).

6.3.7. The Beclin 2:Atg14 CCD heterodimer interface

The total surface buried at the heterodimer interface is 1814 $Å^2$, accounting for 21.6% of the Beclin 2 CCD surface area and also 21.6% of the Atg14 CCD surface area. This buried area is less than the 2070 ± 37$Å^2$ found in the Beclin 2 CCD homodimer. Notably, all Beclin 2 CCD residues at the homodimer interface were modeled at the interface of the Beclin 2:Atg14 CCD heterodimer. Only 15 of a total 91 Atg14 CCD residues are leucine, valine or isoleucine and in the best-packed heterodimer model ten of these residues contribute to the heterodimer interface.

Since the Beclin 2 CCD and Atg14 CCD form a parallel heterodimer, Beclin 2 residues at *a* and *d* positions of the successive heptad repeats pack against the Atg14 CCD residues at *a'* and *d'* positions, respectively, resulting in 25 paired interactions (Figure 6.10C). Given the few hydrophobic residues contributed by Atg14, the heterodimer interface has only five pairs of ideal and five pairs of acceptable packing interactions, compared to the twelve pairs found in the Beclin 2 CCD homodimer. This is consistent with the smaller interface buried in the heterodimer model relative to the homodimer. However, Beclin 2:Atg14 CCD heterodimerization is > 600-fold tighter than Beclin 2 CCD self-association (Figure 6.7 and Table 6.7).

The heterodimer model helps explain the impact of mutating Beclin 2 interface residues on heterodimerization with the Atg14 CCD, as assessed by ITC (Figure 6.7 and Table 6.7). N187L and the A197L+E208L Beclin 2 CCD are the two mutants that self-associate most tightly. The N187L crystal structure provides evidence of improved packing of the mutant Beclin 2 CCD homodimer. In the heterodimer model, N187 packs against Atg14 I120. Therefore, mutating N187 to leucine also makes a more hydrophobic L187-I120 heterodimer interface. However, since heterodimerization depends on dissociation of the Beclin 2 CCD homodimer, the significantly improved homodimerization results in 3.5-fold lower heterodimerization.

The A197L+E208L mutant does not appear to self-dissociate. Based on the heterodimer model these mutations should also result in significantly better hydrophobic packing of a Beclin 2 L208–Atg14 L141 pair. Mutating A197 to leucine likely also improves packing against the partnered Atg14 glycine. However, while the A197L+E208L Beclin 2:Atg14 CCD heterodimer interface is likely better packed, the substantially decreased homodimer dissociation of the Beclin 2 CCD, negatively impacts the formation of the Beclin 2:Atg14 CCD heterodimer, such that overall K_d for heterodimerization remains approximately the same.

The H211L Beclin 2 CCD mutant also displays improved homodimerization. In the heterodimer model, H211 is involved in polar interactions with Atg14 T144; therefore mutating H211 to leucine merely results in a non-ideal L211-T144 pair, which is a worse pairing. As a result, although the H211L Beclin 2 CCD self-associates 60-fold more strongly than WT, the H211L mutant binds to Atg14 CCD with ~4-fold weaker affinity than the WT.

Both the E173L and Q222L Beclin 2 CCD form much weaker homodimers compared to WT, but they both also bind to the Atg14 CCD more weakly than WT. In the heterodimer model, E173 packs against Atg14 T106, while Q222 packs against A155. In each case, mutating the

interface Beclin 2 residue does not improve hydrophobic packing at the heterodimer interface. Indeed the E173 side-chain may interact better with the Atg14 T106. E173 and Q222 may both also help stabilize the WT heterodimer structure by polar interactions with the surrounding charged or polar residues. Thus, the absence of improved interactions likely prevents improved binding of E173L and Q222L Beclin 2 CCD to Atg14 CCD compared to WT, despite the substantially weakened homodimerization.

A190L+Y215L Beclin 2 CCD self-dissociation is similar to the WT Beclin 2 CCD. In the heterodimer model, A190 and Y215 pack against Atg14 L123 and N148 respectively. While mutating A190 to leucine makes an ideal L190-L123 interface pair, mutating Y215 to leucine may not improve the stability of the heterodimer. The Y215 side-chain packs hydrophobically with the N148 Cα and Cβ,and with carbon atoms of surrounding residues, while the Y215 hydroxyl may hydrogen bond with the polar Atg14 N148, or with other polar Atg14 residues. This may explain why the Atg14 CCD binds to the A190L+Y215L Beclin 2 CCD with a binding affinity similar to WT.

Lastly, relative to WT, the R243L Beclin 2 CCD forms a ~2.5-fold weaker homodimer and heterodimer with Atg14. In the heterodimer model, the aliphatic part of the R243 side-chain packs against Atg14 V176, while the charged guanidinium group may make polar interactions to surrounding charged Atg14 residues such as Atg14 E177. The loss of these polar interactions in the R243L mutant may explain the weaker heterodimerization of this mutant.

6.4. Discussion

Our detailed mutational, biophysical and structural analysis of Beclin 2 CCD homodimerization and heterodimerization with Atg14, suggests that these Beclin homologs are designed to associate and dissociate in the context of subtle cellular signals. Further, the

sequence of Beclin homologs is optimized to pair with partners such as Atg14 to form functionally active states, rather than to form homodimers, which may represent a functionally inactive reservoir within the cell.

Unlike canonical CCDs, such as leucine zippers, the Beclin 2 CCD homodimer is stabilized by a few ideally paired hydrophobic residues, some less well-packed hydrophobic residues, as well as non-canonical, inter-chain polar interactions; while being weakened by several non-ideal pairings of polar and hydrophobic interface residues. This results in weakly associating, meta-stable Beclin 2 homodimers that likely represent an autophagy inactive cellular reservoir of Beclin 2. This homodimer may be further stabilized by interactions with other proteins in the cell. For instance, the Beclin 1 homodimer appears to be stabilized by binding of Bcl-2 homologs.

Indeed, formation of a meta-stable homodimer appears to be a conserved feature of Beclin homologs, as many of the non-ideal interface pairs are conserved. Consistent with this hypothesis, cellular studies of the mammalian ortholog, Beclin 1, indicate that there is a stable cellular reservoir of homodimers; and structural and biophysical studies show that the Beclin 1 CCD also exists as a meta-stable homodimer (Noble et al., 2008, Adi-Harel et al., 2010). The weak homodimerization of Beclin homologs likely facilitates the dissociation of these homodimers upon induction of autophagy, to allow them to form heterodimers with the CCDs of other autophagy proteins like Atg14 and UVRAG.

Beclin 1 homologs are core components of quaternary complexes called PI3KC3 Complex I and II, which include PI3KC3, p150 and either Atg14 or UVRAG respectively. 28 Å Cryo-EM reconstructions of Complex I and Complex II indicate that these complexes have similar overall architecture and shape at that resolution. A more recent crystal structure of the

yeast equivalent of Complex II confirmed results from the Cryo-EM reconstructions and provided additional information regarding arrangement and interactions of different domains. Our SAXS results indicate that Beclin2 and Atg14 form a parallel heterodimer, similar to that deduced for Beclin 1 and Atg14 from the Cryo-EM reconstruction of Complex I and analogous to the arrangement of Beclin and UVRAG homologs in Complex II. However, compared to the Complex II, the curvature of the Beclin 2:Atg14 heterodimer is likely to alter the relative arrangement of membrane-binding domains of Beclin 1, PI3KC3 and Atg14 in Complex I. This may influence selection and binding to membranes of different curvature by Complex I and Complex II.

Beclin 2:Atg14 heterodimer formation is driven by the higher affinities of the Beclin2 CCD for the Atg14 CCD, than for another molecule of Beclin 2, corroborating earlier qualitative assessments of binding (He et al., 2013). Our heterodimer model indicates that this higher affinity is dictated by better pairing of residues at the heterodimer interface: while the number of hydrophobic pairs is similar, some polar Beclin 2 residues are paired with polar Atg14 residues, rather than with hydrophobic residues, resulting in better interactions. Strikingly, some of these polar pairings are conserved amongst homologs, providing yet another rationale for the presence of polar residues at the interface packing positions from each helix.

These conclusions are corroborated by our experiments assessing the impact of Beclin 2 mutagenesis on thermal stability of the homodimer as well as affinity of homodimerization and heterodimerization. Mutating the non-ideal Beclin 2 interface residues to ideal leucine-leucine or lecine-valine pairs, improves homodimer stability and self-association while adversely impacting binding to Atg14. However, binding to Atg14 is not completely abrogated, because these mutations often also improve interactions with Atg14. Exceptions to improved

homodimerization upon mutagenesis to Leu/Val primarily involve polar/charged residues where such mutations cause steric conflicts within the homodimer, and in one case the polar residues are stabilized by inter and/or intra-chain interactions. Thus, the sequence of Beclin homologs is optimized to prevent tight self-association, yet enable association with specific partners such as Atg14. This simultaneously prevents overly tight association with these partners thereby allow for dynamic exchange of partners for different functions.

Despite the overall similarity in the structure, interactions and function of the Beclin 1 and Beclin 2 CCDs, there are important differences. For example, selected single Beclin 1 CCD mutations of charged interface residues to leucine completely abrogate binding to the Atg14 CCD (Li et al., 2012). More recently, it has been shown that mutating the Beclin 1 CCD hydrophobic interface residues to alanine dramatically impairs interaction between full-length Beclin 1 and Atg14 and significantly diminishes starvation-induced autophagy (Mei et al., 2016b). In contrast, none of the mutations we made to the Beclin 2 CCD abrogate binding to the Atg14 CCD. Therefore, our study indicates that the interaction between the Atg14 CCD and Beclin 2CCD is more tolerant to point mutations in Beclin 2, relative to both, the self-association of Beclin 2 or the interaction of Atg14 and Beclin 1.

CHAPTER 7. CONCLUSION AND FUTURE DIRECTIONS

The work presented in this dissertation aims to obtain a structure-based understanding of the biological function of Bcl-2 proteins and Beclin homologs in regulating autophagy and apoptosis.

In this study, a mutational analysis of Beclin 1 was performed to identify differential selectivity determinants that prevent Bcl-X_L, but not M11, from binding to Beclin 1 and down-regulating autophagy. Based on this information, a G120E+D121A Beclin 1 BH3D peptide was designed and confirmed to bind specifically to M11, but not to Bcl-X_L. In order to elucidate the mechanism by which this double-mutant peptide specifically binds to M11, the X-ray crystal structure of the peptide bound to M11 complex was determined. Most importantly, a cell-permeable version of this peptide was designed that specifically inhibits M11-mediated, but not Bcl-X_L-mediated down-regulation of autophagy.

We also attempted to create BALF1 expression constructs that can over-express sufficient quantities of pure BALF1 for structural studies. Expression and purification of BALF1 from two available constructs was tested. Western blot, ESI-MS and Edman sequencing were employed to verify the expressed proteins. Unfortunately, no success was achieved in either constructs making or protein expression and purification, presumably due to the toxicity of BALF1.

Additionally, we investigated the interaction between Atg12 and Mcl-1. Although this interaction has been demonstrated by Co-IP previously (Rubinstein et al., 2011), in this study, no interaction was observed by either ITC or pull-down assays using purified Mcl-1 and Atg12 protein and chemically synthesized Atg12 BH3D peptide.

Lastly, in this study, different Beclin 2 expression constructs that express full-length, multi-domain fragments or individual domains of Beclin 2, were created and tested for expression. Amongst the seven different expression constructs, only the Beclin 2 CCD was successfully expressed, purified to homogeneity and yielded pure and homogeous protein that could be crystallized successfully. The structure of the Beclin 2 CCD revealed a curved anti-parallel coiled-coil dimer with seven pairs of non-ideal packing residues. Mutating these non-ideal packing residues to leucines generally increased the thermal stability and association constant of the CCD homodimer. Unlike the Beclin 1 CCD, Beclin 2 CCD mutants that form stronger homodimers, bind more weakly, but do not completely lose their ability to bind to Atg14 CCD. Moreover, the SAXS analysis suggested that, like Beclin 1,the Beclin 2 CCD forms a parallel heterodimer with Atg14.

As noted, in this study, a structural-based mutational analysis of Beclin 1 BH3D bound to M11 and Bcl-X_L led to the successful identification of a double-mutant Beclin1 BH3D-derived peptide inhibitor that prevents Bcl-X_L, but not M11, from binding to Beclin 1 and down-regulating autophagy. This method may be further applied to identify other selective inhibitors that target important human pathogen encoded Bcl-2 homologs, like KSHV Bcl-2 and BALF1, if the exact function of BALF1 can be elucidated in the near future.

Since autophagy and apoptosis are both cellular degradation pathways essential for organismal homeostasis, it is not surprising that both autophagy and apoptosis have been implicated in protecting organisms against a variety of diseases, including cancers (Lowe and Lin, 2000, Levine, 2006, Liu and Ryan, 2012). Researchers investigating the crosstalk between the two pathways will enable a complete understanding of the co-regulation of autophagy and apoptosis, which is essential for the rational design of successful anticancer therapeutics.

Therefore, it will also be of great interest to see if our peptide inhibitor can also selectively inhibit M11-mediated down regulation of apoptosis. If so, this peptide inhibitor will enable the inhibition of both M11-mediated down-regulation of autophagy and apoptosis. This peptide inhibitor can then be further used to study the potential of inhibition of both M11-mediated down-regulation of autophagy and apoptosis in γHV 68 infected mice. The information obtained from this study might enable the development of a therapeutic that can treat γHV infections and diseases associated with the expressions of γHV Bcl-2 proteins in future.

Recently, ABT-199 (Venclexta) was approved by the U.S. Food and Drug Administration to treat patients with chronic lymphocytic leukemia with a chromosomal abnormality called 17p deletion. Venclexta is the first treatment that targets Bcl-2 to be approved by the U.S. Food and Drug Administration (http://www.fda.gov/NewsEvents/Newsroom/PressAnnouncements/ucm495253.htm). ABT-199 binds to the Bcl-2 surface hydrophobic groove, which is also responsible for binding to BH3Ds from other proteins (Souers et al., 2013). ABT-199 was derived from ABT-263, which is a mimetic of BAD BH3D and was developed with the aim of inhibiting anti-apoptotic proteins to restore the natural process of apoptosis (Tse et al., 2008). However, since ABT-263 targets both Bcl-2 and Bcl-X_L, the concomitant on-target thrombocytopenia caused by Bcl-X_L inhibition limits the efficacy achievable with ABT-263 (Souers et al., 2013). The ABT-199 was then developed by analyzing the complex structure of Bcl-2 bound to ABT-263 and comparing to structures of Bcl-2 and Bcl-X_L. Therefore, regarding our research, in addition to the studies that can be performed using the double-mutant peptides as mentioned above, small compounds that mimics the conformation and function of our double-mutant peptide, can also be developed

based on the structures of double-mutant peptide:M11 complex, M11 and Bcl-X_L, following the same theory for the development of ABT-199.

While most γHVs only encode one Bcl-2 protein, EBV encodes two, or maybe three Bcl-2 proteins, depending on whether both BALF0 and BALF1 open reading frames are expressed by EBV. It is possible that only EBV encodes more than one Bcl-2 homolog, which makes EBV special amongst all the γHVs. However, it is also possible that additional viral Bcl-2 homologs exist in other γHVs and have not yet been identified.

As noted, it is still not clear whether both BALF0 and BALF1 are encoded by EBV, nor at what stages of virus life cycle they are expressed, which is important for understanding how the virus establishes latency in the normal host and the pathogenesis of γHV-associated malignancies. Reverse transcription polymerase chain reaction (RT-PCR) can be employed to address this question by assessing mRNA levels of BALF0 and BALF1 at both viral latency and lytic replication stages in EBV-positive cell lines.

But knowing the expression stage of BALF0 and/or BALF1 is not sufficient to determine if they have anti- or pro-apoptotic functions. While structural studies of BALF proteins, as discussed in Chapter 3, will likely provide important clues to their functions, other experiments may also help determine BALF0/1 protein function, one of which is to identify binding partners of BALF proteins using yeast two-hybrid assay. Anti-apoptotic Bcl-2 proteins accomplish their anti-apoptotic function by binding to and inhibiting the function of multi-domain pro-apoptotic Bcl-2 proteins BAX and/or BAK, while BH3-only proteins bind to anti-apoptotic Bcl-2 proteins to release the multi-domain pro-apoptotic Bcl-2 proteins from this inhibition. Therefore, identifying the binding partners will go a long way toward revealing the anti- or pro-apoptotic functions of BALF0/1 proteins.

Although, as discussed in Chapter 4, additional studies need to be carried out to confirm the interaction between Atg12 and Mcl-1 *in vitro*, in order to further characterize the structural details of the interaction between the two proteins (assuming they do interact), we expect that the interaction will be different from that between typical BH3D-containing proteins and Bcl-2 homologs, as the BH3D-like motif of Atg12 bears a proline, which would prevent it from forming an α-helix like other BH3Ds. Therefore, an understanding of the interaction between Atg12 and Mcl-1 will expand our knowledge of how BH3Ds bind to Bcl-2 proteins. The binding-associated transition of BH3Ds from a random coil to an α-helix may not be a universal feature that is required for binding to Bcl-2 proteins.

Notably, however, a second Atg12 binding site outside the BH3D-like motif has been shown to be required for the interaction. Moreover, to our surprise, although the Atg12 construct we used for detecting interaction between Atg12 and Mcl-1 did include both the BH3D-like motif and the second binding site, no interaction was observed. Therefore, additional binding sites, including Atg12 IDR and Mcl-1 PEST sequences that were not included in the expression constructs, may also be important for the interaction. It is possible that the inability of the Atg12 BH3D-like motif to form an α-helix upon binding weakens its binding to Mcl-1, and therefore, additional interactions are required to stabilize the interaction. In fact, it is also possible that the presence of additional interaction sites is not only restricted to Atg12-Mcl-2 interaction, but is common feature of BH3D-containing proteins that bind to Bcl-2 proteins. In fact, another BH3D-contaig protein, Beclin 1, may be an example. Compared to isolated BH3D (residues 105-130), Beclin 1 residues 1-135 bind with 5.5-fold higher affinity to M11. Although lots of interactions have been identified between pro-apoptotic BH3D-contaig proteins and anti-apoptotic Bcl-2 proteins, the studies are mostly restricted to interactions between isolated BH3Ds

and Bcl-2 proteins, which have undercovered critical features of these interactions. Therefore, additional studies of the interaction between larger constructs of BH3D-containing proteins and Bcl-2 proteins are needed to fully understand the interaction mechanism. This will add to our current understanding of the mechanism of regulation of apoptosis and autophagy and the crosstalk between the two pathways. Furthermore, this information may also be important for designing inhibitors of Bcl-2 proteins.

If the Atg12 IDR and Mcl-1 PEST sequences are required for interaction, it will be very difficult to purify the two proteins alone for the *in vitro* interaction characterization using ITC or pull-down assays, as the IDR and PEST sequences will destabilize proteins. In this case, Atg12 and Mcl-1 co-expression may help stabilize the IDR and PEST sequences of Atg12 and Mcl-1, respectively, and the complex structure could then be studied using X-ray crystallization if the complex is stable enough to crystallize, or using NMR.

As noted in Chapter 4, Mcl-1 only binds to free Atg12 but not to Atg12-Atg5 conjugates. Knockdown of endogenously expressed Atg12 down-regulates apoptosis upon treatment with apoptosis inducers, and down-regulates autophagy induced by starvation. Compared to WT Atg12, cells with overexpressed Bcl-2 binding-deficient Atg12 have increased autophagy levels upon starvation (Rubinstein et al., 2011). However, it is not yet known whether overexpression of Atg12 also affects apoptosis. More importantly, what decides the fate of Atg12 inside the cell? In other words, inside cells, is Atg12 mainly associated with Mcl-1 or with Atg5 or does it exist as an isolated protein until a suitable trigger occurs? It is possible these three states of Atg12 co-exist in equilibrium in normal cells to regulate basal levels of autophagy and apoptosis. Under stress conditions such as starvation and oxidative damage caused by ROS, the equilibrium is disrupted in order to up-regulate or down-regulate either or both apoptosis and autopahgy,

thereby deciding the fate of the cells. Much more research will need to be carried out in order to address these questions, which are also important for understanding the crosstalk between apoptosis and autophagy.

In Chapter 6, we pointed out that the 28 Å Cryo-EM reconstructions of PI3KC3 Complex I and II reveal nearly identical overall V-shaped envelopes (Baskaran et al., 2014). Compared to the recently reported 4.4 Å crystal structure of PI3KC3 Complex II that contains Beclin 1 (Rostislavleva et al., 2015), our structural studies reveal that the Beclin 2:Atg14 heterodimer has a different curvature, which may alter the relative arrangement of membrane-binding domains of Beclin 2, PI3KC3 and Atg14 in Complex I and lead to the differential selection and binding to membranes of different curvature by Complex I and Complex II. In order to test our hypothesis, it will be of great interest to solve the X-ray crystal structure of the PI3KC3 Complex I that includes Beclin 2. This crystal structure will not only confirm the curvature of the Complex I and the arrangement of each component inside the complex, but also provide more detailed structural information regarding residues important for assembling the complex and binding to membranes. Moreover, if we can purify a stable PI3KC3 Complex I for crystallization, this complex could be used to test binding to liposome of different sizes and lipid compositions, which may help elucidate the membrane/vesicle targeted by PI3KC3 Complex I.

Like Beclin 1, Beclin 2 has been shown to be important for both basal and starvation-induced autophagy (He et al., 2013). Surprisingly, in the same study, it was found that upon starvation, overexpressed Beclin 2 could still pull-down Bcl-2, while overexpressed Beclin 1 did not. The Beclin 1 BH3D residue T119 has been reported to be phosphorylated by DAPK and the phosphorylated Beclin 1 does not bind to Bcl-2/Bcl-X_L(Zalckvar et al., 2009). Notably, this threonine residue corresponds to an alanine in Beclin 2. Therefore, DAPK cannot phosphorylate

Beclin 2 to promote its dissociation form Bcl-2 proteins. Upon starvation, JNK-1 also phosphorylates Bcl-2 at residues within a non-structured loop, disrupting the interaction between Beclin 1 and Bcl-2 (Wei et al., 2008a). Unlike Beclin 1, the interaction between Beclin 2 and Bcl-2 may also not be affected by Bcl-2 phosphorylation. Therefore, it is possible that the dissociation of Beclin 2 from Bcl-2 is regulated by mechanisms different form that seen for Beclin 1 dissociation. Interestingly, the Beclin 1 BH3D residue L116 which is buried at the interface between Beclin 1 and Bcl-2 proteins and has been shown to be important for binding to various Bcl-2 proteins (Sinha et al., 2008, Oberstein et al., 2007, Mei et al., 2014, Su et al., 2014), corresponds to a glutamine in Beclin 2. The interaction between Beclin 2 BH3D and Bcl-2 is highly likely to be weakened by the presence of this glutamine, although more binding assays will need to be performed in order to demonstrate whether and to what extent this glutamine impacts the interaction between Beclin 2 and Bcl-2 proteins. However, if Beclin 2 does bind to Bcl-2 with a weaker binding affinity compared to Beclin 1, it is possible that the disruption of the interaction between Beclin 2 and Bcl-2 is due to the increased expression of another protein that can competitively bind to Bcl-2 and displace Beclin 2. Experiments showing that Beclin 2 binds to Bcl-2 even upon starvation involved overexpression of Beclin 2 (He et al., 2013), which would push the binding equilibrium towards the association of Beclin 2 and Bcl-2, even though cellular regulatory mechanisms push for dissociation. Nevertheless, more studies are needed to fully understand the interaction between Beclin 2 and Bcl-2 proteins and the roles of Bcl-2 proteins in regulating Beclin 2-dependent autophagy.

In addition to its function in regulating autophagy, Beclin 2 also regulates endolysosomal trafficking and degradation of a subset of GPCRs through its interaction with GASP1. This interaction is mediated through the interaction between Beclin 2 N-terminal residues 1-88 and

GASP1 C-terminal residues 899-1395 as suggested by yeast two-hybrid results (He et al., 2013). While our IUpred predictions indicate that this region of GASP1 is folded, residues 1-88 of Beclin 2 are part of the IDR as described in Chapter 5. Although it will be really interesting and important to elucidate the structural details of the interaction between Beclin 2 and GASP1, the extremely unstable structure of IDR will also make it very difficult to study. Optimization of the expression and purification strategy using different tags, *E. coli* strains, expression time and temperature, and etc, will need to be performed in order to obtain relatively stable Beclin 2 residues 1-88. The co-expression of Beclin 2 residues 1-88 with GASP1 residues 899-1395 may also help to stabilize the IDR. NMR may then be employed to characterize the interaction between Beclin 1 residues 1-88 and GASP1residues 899-1395.

REFERENCES

ADAMS, P. D., AFONINE, P. V., BUNKOCZI, G., CHEN, V. B., DAVIS, I. W., ECHOLS, N., HEADD, J. J., HUNG, L. W., KAPRAL, G. J., GROSSE-KUNSTLEVE, R. W., MCCOY, A. J., MORIARTY, N. W., OEFFNER, R., READ, R. J., RICHARDSON, D. C., RICHARDSON, J. S., TERWILLIGER, T. C. & ZWART, P. H. 2010. PHENIX: a comprehensive Python-based system for macromolecular structure solution. *Acta Crystallographica Section D-Biological Crystallography,* 66**,** 213-221.

ADI-HAREL, S., ERLICH, S., SCHMUKLER, E., COHEN-KEDAR, S., SEGEV, O., MIZRACHY, L., HIRSCH, J. A. & PINKAS-KRAMARSKI, R. 2010. Beclin 1 self-association is independent of autophagy induction by amino acid deprivation and rapamycin treatment. *Journal of Cellular Biochemistry,* 110**,** 1262-1271.

AFONSO, C. L., TULMAN, E. R., LU, Z., ZSAK, L., KUTISH, G. F. & ROCK, D. L. 2000. The genome of fowlpox virus. Journal of Virology, 74**,** 3815-31.

AFONSO, C. L., TULMAN, E. R., LU, Z., ZSAK, L., ROCK, D. L. & KUTISH, G. F. 2001. The genome of turkey herpesvirus. *Journal of Virology,* 75**,** 971-8.

ALTMANN, M. & HAMMERSCHMIDT, W. 2005. Epstein-Barr virus provides a new paradigm: A requirement for the immediate inhibition of apoptosis. *Plos Biology,* 3**,** 2148-2157.

ANNUNZIATO, L., AMOROSO, S., PANNACCIONE, A., CATALDI, M., PIGNATARO, G., D'ALESSIO, A., SIRABELLA, R., SECONDO, A., SIBAUD, L. & DI RENZO, G. F. 2003. Apoptosis induced in neuronal cells by oxidative stress: role played by caspases and intracellular calcium ions. *Toxicology Letters,* 139**,** 125-133.

BAKHSHI, A., JENSEN, J. P., GOLDMAN, P., WRIGHT, J. J., MCBRIDE, O. W., EPSTEIN, A. L. & KORSMEYER, S. J. 1985. Cloning the chromosomal breakpoint of T(14-18) human lymphomas - clustering around Jh on chromosome-14 and near a transcriptional unit on 18. *Cell,* 41**,** 899-906.

BANEYX, F. & MUJACIC, M. 2004. Recombinant protein folding and misfolding in Escherichia coli. *Nature Biotechnology,* 22**,** 1399-1408.

BASKARAN, S., CARLSON, L. A., STJEPANOVIC, G., YOUNG, L. N., KIM, D. J., GROB, P., STANLEY, R. E., NOGALES, E. & HURLEY, J. H. 2014. Architecture and dynamics of the autophagic phosphatidylinositol 3-kinase complex. *Elife,* 3.

BASU, A. & HALDAR, S. 2003. Identification of a novel Bcl-xL phosphorylation site regulating the sensitivity of taxol- or 2-methoxyestradiol-induced apoptosis. *Febs Letters,* 538**,** 41-47.

BELLOWS, D. S., CHAU, B. N., LEE, P., LAZEBNIK, Y., BURNS, W. H. & HARDWICK, J. M. 2000. Antiapoptotic herpesvirus Bcl-2 homologs escape caspase-mediated conversion to proapoptotic proteins. *Journal of Virology,* 74**,** 5024-5031.

BELLOWS, D. S., HOWELL, M., PEARSON, C., HAZLEWOOD, S. A. & HARDWICK, J. M. 2002. Epstein-Barr virus BALF1 is a BCL-2-like antagonist of the herpesvirus antiapoptotic BCL-2 proteins. *Journal of Virology,* 76**,** 2469-2479.

BENEDICT, C. A., NORRIS, P. S. & WARE, C. F. 2002. To kill or be killed: viral evasion of apoptosis. *Nature Immunology,* 3**,** 1013-1018.

BOISE, L. H., GONZALEZGARCIA, M., POSTEMA, C. E., DING, L. Y., LINDSTEN, T., TURKA, L. A., MAO, X. H., NUNEZ, G. & THOMPSON, C. B. 1993. Bcl-X, a Bcl-2-related gene that functions as a dominant regulator of apoptotic cell-death. *Cell,* 74**,** 597-608.

BOYD, J. M., GALLO, G. J., ELANGOVAN, B., HOUGHTON, A. B., MALSTROM, S., AVERY, B. J., EBB, R. G., SUBRAMANIAN, T., CHITTENDEN, T., LUTZ, R. J. & CHINNADURAI, G. 1995. Bik, a novel death-inducing protein shares a distinct sequence motif with Bcl-2 family proteins and interacts with viral and cellular survival-promoting proteins. *Oncogene,* 11**,** 1921-1928.

BRUN, A., RODRIGUEZ, F., ESCRIBANO, J. M. & ALONSO, C. 1998. Functionality and cell anchorage dependence of the African swine fever virus gene A179L, a viral bcl-2 homolog, in insect cells. *Journal of Virology,* 72**,** 10227-33.

BRUNE, B. 2003. Nitric oxide: NO apoptosis or turning it ON? *Cell Death and Differentiation,* 10**,** 864-869.

BRUNGER, A. T. 1992. Free R-value - a novel statistical quantity for assessing the accuracy of crystal-structures. *Nature,* 355**,** 472-475.

BRUNGER, A. T., ADAMS, P. D., CLORE, G. M., DELANO, W. L., GROS, P., GROSSE-KUNSTLEVE, R. W., JIANG, J. S., KUSZEWSKI, J., NILGES, M., PANNU, N. S., READ, R. J., RICE, L. M., SIMONSON, T. & WARREN, G. L. 1998. Crystallography & NMR system: A new software suite for macromolecular structure determination. *Acta Crystallographica Section D-Biological Crystallography,* 54**,** 905-921.

BRUNGER, A. T., ADAMS, P. D. & RICE, L. M. 1997. New applications of simulated annealing in X-ray crystallography and solution NMR. *Structure,* 5**,** 325-336.

BYRNE, G. I. & OJCIUS, D. M. 2004. Chlamydia and apoptosis: Life and death decisions of an intracellular pathogen. *Nature Reviews Microbiology,* 2**,** 802-808.

CABRAS, G., DECAUSSIN, G., ZENG, Y., DJENNAOUI, D., MELOULI, H., BROULLY, P., BOUGUERMOUH, A. M. & OOKA, T. 2005. Epstein-Baff virus encoded BALF1 gene

is transcribed in Burkitt's lymphoma cell lines and in nasopharyngeal carcinoma's biopsies. *Journal of Clinical Virology,* 34**,** 26-34.

CHAYEN, N. E. 1998. Comparative studies of protein crystallization by vapour-diffusion and microbatch techniques. *Acta Crystallographica Section D: Biological Crystallography,* 54**,** 8-15.

CHEN, L., WILLIS, S. N., WEI, A., SMITH, B. J., FLETCHER, J. I., HINDS, M. G., COLMAN, P. M., DAY, C. L., ADAMS, J. M. & HUANG, D. C. S. 2005. Differential targeting of prosurvival Bcl-2 proteins by their BH3-only ligands allows complementary apoptotic function. *Molecular Cell,* 17**,** 393-403.

CHENG, E. H., NICHOLAS, J., BELLOWS, D. S., HAYWARD, G. S., GUO, H. G., REITZ, M. S. & HARDWICK, J. M. 1997a. A Bcl-2 homolog encoded by Kaposi sarcoma-associated virus, human herpesvirus 8, inhibits apoptosis but does not heterodimerize with Bax or Bak. *Proceedings of the National Academy of Sciences of the United States of America,* 94**,** 690-4.

CHENG, E. H. Y., KIRSCH, D. G., CLEM, R. J., RAVI, R., KASTAN, M. B., BEDI, A., UENO, K. & HARDWICK, J. M. 1997b. Conversion of Bcl-2 to a Bax-like death effector by caspases. *Science,* 278**,** 1966-1968.

CHENG, E. H. Y., NICHOLAS, J., BELLOWS, D. S., HAYWARD, G. S., GUO, H. G., REITZ, M. S. & HARDWICK, J. M. 1997c. A Bcl-2 homolog encoded by Kaposi sarcoma-associated virus, human herpesvirus 8, inhibits apoptosis but does not heterodimerize with Bax or Bak. *Proceedings of the National Academy of Sciences of the United States of America,* 94**,** 690-694.

CLEM, R. J., CHENG, E. H. Y., KARP, C. L., KIRSCH, D. G., UENO, K., TAKAHASHI, A., KASTAN, M. B., GRIFFIN, D. E., EARNSHAW, W. C., VELIUONA, M. A. & HARDWICK, J. M. 1998. Modulation of cell death by Bcl-x(L) through caspase interaction. *Proceedings of the National Academy of Sciences of the United States of America,* 95**,** 554-559.

COLE, C., BARBER, J. D. & BARTON, G. J. 2008. The Jpred 3 secondary structure prediction server. *Nucleic Acids Research,* 36**,** W197-201.

CRAWFORD, D. H. 2001. Biology and disease associations of Epstein-Barr virus. *Philosophical Transactions of the Royal Society of London Series B-Biological Sciences,* 356**,** 461-473.

CRIGHTON, D., WILKINSON, S., O'PREY, J., SYED, N., SMITH, P., HARRISON, P. R., GASCO, M., GARRONE, O., CROOK, T. & RYAN, K. M. 2006. DRAM, a p53-induced modulator of autophagy, is critical for apoptosis. *Cell,* 126**,** 121-134.

CRIGHTON, D., WOIWODE, A., ZHANG, C., MANDAVIA, N., MORTON, J. P., WARNOCK, L. J., MILNER, J., WHITE, R. J. & JOHNSON, D. L. 2003. p53 represses

RNA polymerase III transcription by targeting TBP and inhibiting promoter occupancy by TFIIIB. *Embo Journal,* 22**,** 2810-2820.

CUCONATI, A. & WHITE, E. 2002. Viral homologs of BCL-2: role of apoptosis in the regulation of virus infection. *Genes & Development,* 16**,** 2465-78.

CZABOTAR, P. E., LEE, E. F., THOMPSON, G. V., WARDAK, A. Z., FAIRLIE, W. D. & COLMAN, P. M. 2011. Mutation to Bax beyond the BH3 domain disrupts interactions with pro-survival proteins and promotes apoptosis. *Journal of Biological Chemistry,* 286**,** 7123-7131.

CZABOTAR, P. E., LEE, E. F., VAN DELFT, M. F., DAY, C. L., SMITH, B. J., HUANG, D. C. S., FAIRLIE, W. D., HINDS, M. G. & COLMAN, P. M. 2007. Structural insights into the degradation of Mcl-1 induced by BH3 domains. *Proceedings of the National Academy of Sciences of the United States of America,* 104**,** 6217-6222.

CZABOTAR, P. E., LESSENE, G., STRASSER, A. & ADAMS, J. M. 2014. Control of apoptosis by the BCL-2 protein family: implications for physiology and therapy. *Nature Reviews Molecular Cell Biology,* 15**,** 49-63.

CZABOTAR, P. E., WESTPHAL, D., DEWSON, G., MA, S., HOCKINGS, C., FAIRLIE, W. D., LEE, E. F., YAO, S. G., ROBIN, A. Y., SMITH, B. J., HUANG, D. C. S., KLUCK, R. M., ADAMS, J. M. & COLMAN, P. M. 2013. Bax crystal structures reveal how BH3 domains activate Bax and nucleate its oligomerization to induce apoptosis. *Cell,* 152**,** 519-531.

DAY, C. L., CHEN, L., RICHARDSON, S. J., HARRISON, P. J., HUANG, D. C. S. & HINDS, M. G. 2005. Solution structure of prosurvival Mcl-1 and characterization of its binding by proapoptotic BH3-only ligands. *Journal of Biological Chemistry,* 280**,** 4738-4744.

DAY, C. L., SMITS, C., FAN, F. C., LEE, E. F., FAIRLIE, W. D. & HINDS, M. G. 2008. Structure of the BH3 domains from the p53-inducible BH3-only proteins Noxa and Puma in complex with Mcl-1. *Journal of Molecular Biology,* 380**,** 958-971.

DE LIMA, B. D., MAY, J. S., MARQUES, S., SIMAS, J. P. & STEVENSON, P. G. 2005. Murine gammaherpesvirus 68 bcl-2 homologue contributes to latency establishment in vivo. *Journal of General Virology,* 86**,** 31-40.

DEBARTOLO, J., DUTTA, S., REICH, L. & KEATING, A. E. 2012. Predictive Bcl-2 family binding models rooted in experiment or structure. *Journal of Molecular Biology,* 422**,** 124-144.

DONNELLY, M. I., STEVENS, P. W., STOLS, L., SU, S. X. Y., TOLLAKSEN, S., GIOMETTI, C. & JOACHIMIAK, A. 2001. Expression of a highly toxic protein, Bax, in Escherichia coli by attachment of a leader peptide derived from the GroES cochaperone. *Protein Expression and Purification,* 22**,** 422-429.

DOSZTANYI, Z., CSIZMOK, V., TOMPA, P. & SIMON, I. 2005. IUPred: web server for the prediction of intrinsically unstructured regions of proteins based on estimated energy content. *Bioinformatics,* 21**,** 3433-3434.

DOSZTANYI, Z., MESZAROS, B. & SIMON, I. 2009. ANCHOR: web server for predicting protein binding regions in disordered proteins. *Bioinformatics,* 25**,** 2745-6.

EDLICH, F., BANERJEE, S., SUZUKI, M., CLELAND, M. M., ARNOULT, D., WANG, C. X., NEUTZNER, A., TJANDRA, N. & YOULE, R. J. 2011. Bcl-x(L) Retrotranslocates Bax from the mitochondria into the cytosol. *Cell,* 145**,** 104-116.

ELMORE, S. 2007. Apoptosis: a review of programmed cell death. *Toxicol Pathol,* 35**,** 495-516.

EMSLEY, P., LOHKAMP, B., SCOTT, W. G. & COWTAN, K. 2010. Features and development of Coot. *Acta Crystallographica Section D-Biological Crystallography,* 66**,** 486-501.

ERLICH, S., MIZRACHY, L., SEGEV, O., LINDENBOIM, L., ZMIRA, O., ADI-HAREL, S., HIRSCH, J. A., STEIN, R. & PINKAS-KRAMARSKI, R. 2007. Differential interactions between Beclin 1 and bcl-2 family members. *Autophagy,* 3**,** 561-568.

EVANS, P. & MCCOY, A. 2008. An introduction to molecular replacement. *Acta Crystallographica Section D-Biological Crystallography,* 64**,** 1-10.

EWINGS, K. E., HADFIELD-MOORHOUSE, K., WIGGINS, C. M., WICKENDEN, J. A., BALMANNO, K., GILLEY, R., DEGENHARDT, K., WHITE, E. & COOK, S. J. 2007a. ERK1/2-dependent phosphorylation of Bim(EL) promotes its rapid dissociation from Mcl-1 and Bcl-x(L). *Embo Journal,* 26**,** 2856-2867.

EWINGS, K. E., WIGGINS, C. M. & COOK, S. J. 2007b. Bim and the pro-survival bcl-2 proteins - Opposites attract, ERK repels. *Cell Cycle,* 6**,** 2236-2240.

FENG, W., HUANG, S., WU, H. & ZHANG, M. 2007. Molecular basis of Bcl-xL's target recognition versatility revealed by the structure of Bcl-xL in complex with the BH3 domain of Beclin-1. *Journal of Molecular Biology,* 372**,** 223-35.

FENG, Z., ZHANG, H., LEVINE, A. J. & JIN, S. 2005. The coordinate regulation of the p53 and mTOR pathways in cells. *Proceedings of the National Academy of Sciences of the United States of America,* 102**,** 8204-9.

FENG, Z. H. 2010. p53 Regulation of the IGF-1/AKT/mTOR pathways and the endosomal compartment. *Cold Spring Harbor Perspectives in Biology,* 2.

FIMIA, G. M., STOYKOVA, A., ROMAGNOLI, A., GIUNTA, L., DI BARTOLOMEO, S., NARDACCI, R., CORAZZARI, M., FUOCO, C., UCAR, A., SCHWARTZ, P., GRUSS, P., PIACENTINI, M., CHOWDHURY, K. & CECCONI, F. 2007. Ambra1 regulates autophagy and development of the nervous system. *Nature,* 447**,** 1121-U14.

FIRE, E., GULLA, S. V., GRANT, R. A. & KEATING, A. E. 2010. Mcl-1-Bim complexes accommodate surprising point mutations via minor structural changes. *Protein Science,* 19**,** 507-519.

FOGHSGAARD, L. & JAATTELA, M. 1997. The ability of BHRF1 to inhibit apoptosis is dependent on stimulus and cell type. *Journal of Virology,* 71**,** 7509-7517.

FOLLIS, A. V., CHIPUK, J. E., FISHER, J. C., YUN, M. K., GRACE, C. R., NOURSE, A., BARAN, K., OU, L., MIN, L., WHITE, S. W., GREEN, D. R. & KRIWACKI, R. W. 2013. PUMA binding induces partial unfolding within BCL-xL to disrupt p53 binding and promote apoptosis. *Nature Chemical Biology,* 9**,** 163-168.

FRANKE, D. & SVERGUN, D. I. 2009. DAMMIF, a program for rapid ab-initio shape determination in small-angle scattering. *Journal of Applied Crystallography,* 42**,** 342-346.

FREYER, M. W. & LEWIS, E. A. 2008. Isothermal titration calorimetry: Experimental design, data analysis, and probing Macromolecule/Ligand binding and kinetic interactions. *Biophysical Tools for Biologists: Vol 1 in Vitro Techniques,* 84**,** 79-113.

FU, Z. & TINDALL, D. J. 2008. FOXOs, cancer and regulation of apoptosis. *Oncogene,* 27**,** 2312-2319.

FURUYA, N., YU, F., BYFIELD, M., PATTINGRE, S. & LEVINE, B. 2005. The evolutionarily conserved domain of Beclin 1 is required for Vps34 binding, autophagy and tumor suppressor function. *Autophagy,* 1**,** 46-52.

GANGAPPA, S., VAN DYK, L. F., JEWETT, T. J., SPECK, S. H. & VIRGIN, H. W. 2002. Identification of the in vivo role of a viral bcl-2. *Journal of Experimental Medicine,* 195**,** 931-940.

GARCÍA-FUENTES, L., TÉLLEZ-SANZ, R., QUESADA-SORIANO, I. & BARÓN, C. 2011. Thermodynamics of molecular recognition by calorimetry. *Thermodynamics - Physical Chemistry of Aqueous Systems.*

GENG, J. F. & KLIONSKY, D. J. 2008. The Atg8 and Atg12 ubiquitin-like conjugation systems in macroautophagy. *Embo Reports,* 9**,** 859-864.

GERMAIN, M., MILBURN, J. & DURONIO, V. 2008. MCL-1 inhibits BAX in the absence of MCL-1/BAX interaction. *Journal of Biological Chemistry,* 283**,** 6384-6392.

GIANSANTI, V., TORRIGLIA, A. & SCOVASSI, A. I. 2011. Conversation between apoptosis and autophagy: "Is it your turn or mine?". *Apoptosis,* 16**,** 321-333.

GIBSON, D. G., YOUNG, L., CHUANG, R. Y., VENTER, J. C., HUTCHISON, C. A. & SMITH, H. O. 2009. Enzymatic assembly of DNA molecules up to several hundred kilobases. *Nature Methods,* 6**,** 343-U41.

GONZALEZ-GARCIA, M., PEREZ-BALLESTERO, R., DING, L., DUAN, L., BOISE, L. H., THOMPSON, C. B. & NUNEZ, G. 1994. bcl-XL is the major bcl-x mRNA form expressed during murine development and its product localizes to mitochondria. *Development,* 120**,** 3033-42.

GREENFIELD, N. J. 2006a. Using circular dichroism collected as a function of temperature to determine the thermodynamics of protein unfolding and binding interactions. *Nature Protocols,* 1**,** 2527-2535.

GREENFIELD, N. J. 2006b. Using circular dichroism spectra to estimate protein secondary structure. *Nature Protocols,* 1**,** 2876-2890.

GURKAR, A. U., CHU, K., RAJ, L., BOULEY, R., LEE, S. H., KIM, Y. B., DUNN, S. E., MANDINOVA, A. & LEE, S. W. 2013. Identification of ROCK1 kinase as a critical regulator of Beclin1-mediated autophagy during metabolic stress. *Nature Communications,* 4.

HAN, J., GOLDSTEIN, L. A., GASTMAN, B. R. & RABINOWICH, H. 2005. Disruption of Mcl-1/Bim complex in granzyme B-mediated mitochondrial apoptosis. *Faseb Journal,* 19**,** A363-A363.

HARDWICK, J. M. 1998. Viral interference with apoptosis. *Seminars in Cell & Developmental Biology,* 9**,** 339-349.

HE, C. C., WEI, Y. J., SUN, K., LI, B. H., DONG, X. N., ZOU, Z. J., LIU, Y., KINCH, L. N., KHAN, S., SINHA, S., XAVIER, R. J., GRISHIN, N. V., XIAO, G. H., ESKELINEN, E. L., SCHERER, P. E., WHISTLER, J. L. & LEVINE, B. 2013. Beclin 2 functions in autophagy, degradation of G Protein-Coupled Receptors, and metabolism. *Cell,* 154**,** 1085-1099.

HENDERSON, S., HUEN, D., ROWE, M., DAWSON, C., JOHNSON, G. & RICKINSON, A. 1993. Epstein-Barr virus-coded BHRF1 protein, a viral homologue of Bcl-2, protects human B cells from programmed cell death. *Proceedings of the National Academy of Sciences of the United States of America,* 90**,** 8479-83.

HOCKENBERY, D., NUNEZ, G., MILLIMAN, C., SCHREIBER, R. D. & KORSMEYER, S. J. 1990. Bcl-2 is an inner mitochondrial-membrane protein that blocks programmed cell-death. *Nature,* 348**,** 334-336.

HUANG, Q., PETROS, A. M., VIRGIN, H. W., FESIK, S. W. & OLEJNICZAK, E. T. 2002. Solution structure of a Bcl-2 homolog from Kaposi sarcoma virus. *Proceedings of the National Academy of Sciences of the United States of America,* 99**,** 3428-33.

HUANG, Q. L., PETROS, A. M., VIRGIN, H. W., FESIK, S. W. & OLEJNICZAK, E. T. 2003. Solution structure of the BHRF1 protein from Epstein-Barr virus, a homolog of human Bcl-2. *Journal of Molecular Biology,* 332**,** 1123-1130.

HUANG, T. T., HWANG, J. K., CHEN, C. H., CHU, C. S., LEE, C. W. & CHEN, C. C. 2015. (PS)(2): protein structure prediction server version 3.0. *Nucleic Acids Research,* 43**,** W338-W342.

HUANG, W., CHOI, W., HU, W., MI, N., GUO, Q., MA, M., LIU, M., TIAN, Y., LU, P., WANG, F. L., DENG, H., LIU, L., GAO, N., YU, L. & SHI, Y. 2012. Crystal structure and biochemical analyses reveal Beclin 1 as a novel membrane binding protein. *Cell Research,* 22**,** 473-89.

ICHIMURA, Y., KIRISAKO, T., TAKAO, T., SATOMI, Y., SHIMONISHI, Y., ISHIHARA, N., MIZUSHIMA, N., TANIDA, I., KOMINAMI, E., OHSUMI, M., NODA, T. & OHSUMI, Y. 2000. A ubiquitin-like system mediates protein lipidation. *Nature,* 408**,** 488-92.

ISHIDA, T. & KINOSHITA, K. 2007. PrDOS: prediction of disordered protein regions from amino acid sequence. *Nucleic Acids Research,* 35**,** W460-4.

ITAKURA, E., KISHI, C., INOUE, K. & MIZUSHIMA, N. 2008. Beclin 1 forms two distinct phosphatidylinositol 3-kinase complexes with mammalian Atg14 and UVRAG. *Molecular Biology of the Cell,* 19**,** 5360-5372.

ITAKURA, E. & MIZUSHIMA, N. 2009. Atg14 and UVRAG mutually exclusive subunits of mammalian Beclin 1-PI3K complexes. *Autophagy,* 5**,** 534-536.

KABSCH, W. 2010. Xds. *Acta Crystallographica Section D-Biological Crystallography,* 66**,** 125-132.

KANG, R., ZEH, H. J., LOTZE, M. T. & TANG, D. 2011. The Beclin 1 network regulates autophagy and apoptosis. *Cell Death & Differentiation,* 18**,** 571-80.

KIHARA, A., KABEYA, Y., OHSUMI, Y. & YOSHIMORI, T. 2001a. Beclin-phosphatidylinositol 3-kinase complex functions at the trans-Golgi network. *EMBO Reports,* 2**,** 330-5.

KIHARA, A., NODA, T., ISHIHARA, N. & OHSUMI, Y. 2001b. Two distinct Vps34 phosphatidylinositol 3-kinase complexes function in autophagy and carboxypeptidase Y sorting in Saccharomyces cerevisiae. *Journal of Cell Biology,* 152**,** 519-530.

KIKHNEY, A. G. & SVERGUN, D. I. 2015. A practical guide to small angle X-ray scattering (SAXS) of flexible and intrinsically disordered proteins. *Febs Letters,* 589**,** 2570-2577.

KISSINGER, C. R., GEHLHAAR, D. K. & FOGEL, D. B. 1999. Rapid automated molecular replacement by evolutionary search. *Acta Crystallographica Section D-Biological Crystallography,* 55**,** 484-491.

KONAREV, P. V., VOLKOV, V. V., SOKOLOVA, A. V., KOCH, M. H. J. & SVERGUN, D. I. 2003. PRIMUS: a Windows PC-based system for small-angle scattering data analysis. *Journal of Applied Crystallography,* 36**,** 1277-1282.

KOZIN, M. B. & SVERGUN, D. I. 2001. Automated matching of high- and low-resolution structural models. *Journal of Applied Crystallography,* 34**,** 33-41.

KOZOPAS, K. M., YANG, T., BUCHAN, H. L., ZHOU, P. & CRAIG, R. W. 1993. Mcl1, a gene expressed in programmed myeloid cell-differentiation, has sequence similarity to Bcl2. *Proceedings of the National Academy of Sciences of the United States of America,* 90**,** 3516-3520.

KRISSINEL, E. & HENRICK, K. 2007. Inference of macromolecular assemblies from crystalline state. *Journal of Molecular Biology,* 372**,** 774-797.

KU, B., LIANG, C. Y., JUNG, J. U. & OH, B. H. 2011. Evidence that inhibition of BAX activation by BCL-2 involves its tight and preferential interaction with the BH3 domain of BAX. *Cell Research,* 21**,** 627-641.

KU, B., WOO, J. S., LIANG, C., LEE, K. H., HONG, H. S., E, X., KIM, K. S., JUNG, J. U. & OH, B. H. 2008a. Structural and biochemical bases for the inhibition of autophagy and apoptosis by viral BCL-2 of murine gamma-herpesvirus 68. *Plos Pathogens,* 4**,** e25.

KU, B., WOO, J. S., LIANG, C., LEE, K. H., JUNG, J. U. & OH, B. H. 2008b. An insight into the mechanistic role of Beclin 1 and its inhibition by prosurvival Bcl-2 family proteins. *Autophagy,* 4**,** 519-520.

KURIBAYASHI, K. & EL-DEIRY, W. S. 2008. Regulation of programmed cell death by the p53 pathway. *Programmed Cell Death in Cancer Progression and Therapy,* 615**,** 201-221.

KVANSAKUL, M., WEI, A. H., FLETCHER, J. I., WILLIS, S. N., CHEN, L., ROBERTS, A. W., HUANG, D. C. S. & COLMAN, P. M. 2010. Structural Basis for Apoptosis Inhibition by Epstein-Barr Virus BHRF1. *Plos Pathogens,* 6.

LANDSCHULZ, W. H., JOHNSON, P. F. & MCKNIGHT, S. L. 1988. The leucine zipper: a hypothetical structure common to a new class of DNA binding proteins. *Science,* 240**,** 1759-64.

LARKIN, M. A., BLACKSHIELDS, G., BROWN, N. P., CHENNA, R., MCGETTIGAN, P. A., MCWILLIAM, H., VALENTIN, F., WALLACE, I. M., WILM, A., LOPEZ, R., THOMPSON, J. D., GIBSON, T. J. & HIGGINS, D. G. 2007. Clustal W and Clustal X version 2.0. *Bioinformatics,* 23**,** 2947-8.

LAU, S. Y., TANEJA, A. K. & HODGES, R. S. 1984. Synthesis of a model protein of defined secondary and quaternary structure. Effect of chain length on the stabilization and

formation of two-stranded alpha-helical coiled-coils. *Journal of Biological Chemistry,* 259**,** 13253-61.

LEE, E. F., PERUGINI, M. A., PETTIKIRIARACHCHI, A., EVANGELISTA, M., KEIZER, D. W., YAO, S. G. & FAIRLIE, W. D. 2016. The BECN1 N-terminal domain is intrinsically disordered. *Autophagy,* 12**,** 460-471.

LESLIE, A. G. W. & POWELL, H. R. 2007. Processing diffraction data with MOSFLM. *Evolving Methods for Macromolecular Crystallography,* 245**,** 41-51.

LETAI, A., BASSIK, M. C., WALENSKY, L. D., SORCINELLI, M. D., WEILER, S. & KORSMEYER, S. J. 2002. Distinct BH3 domains either sensitize or activate mitochondrial apoptosis, serving as prototype cancer therapeutics. *Cancer Cell,* 2**,** 183-192.

LEVINE, B. 2006. Unraveling the role of autophagy in cancer. *Autophagy,* 2**,** 65-66.

LEVINE, B. & KLIONSKY, D. J. 2004. Development by self-digestion: molecular mechanisms and biological functions of autophagy. *Developmental Cell,* 6**,** 463-77.

LEVINE, B. & KROEMER, G. 2008. Autophagy in the pathogenesis of disease. *Cell,* 132**,** 27-42.

LEVINE, B., SINHA, S. & KROEMER, G. 2008. Bcl-2 family members - Dual regulators of apoptosis and autophagy. *Autophagy,* 4**,** 600-606.

LI, H., WANG, P., YU, J. & ZHANG, L. 2011. Cleaving Beclin 1 to suppress autophagy in chemotherapy-induced apoptosis. *Autophagy,* 7**,** 1239-1241.

LI, X., HE, L., CHE, K. H., FUNDERBURK, S. F., PAN, L., PAN, N., ZHANG, M., YUE, Z. & ZHAO, Y. 2012. Imperfect interface of Beclin1 coiled-coil domain regulates homodimer and heterodimer formation with Atg14L and UVRAG. *Nature Communications,* 3**,** 662.

LIANG, X. H., JACKSON, S., SEAMAN, M., BROWN, K., KEMPKES, B., HIBSHOOSH, H. & LEVINE, B. 1999. Induction of autophagy and inhibition of tumorigenesis by beclin 1. *Nature,* 402**,** 672-676.

LIANG, X. H., KLEEMAN, L. K., JIANG, H. H., GORDON, G., GOLDMAN, J. E., BERRY, G., HERMAN, B. & LEVINE, B. 1998. Protection against fatal Sindbis virus encephalitis by beclin, a novel Bcl-2-interacting protein. *Journal of Virology,* 72**,** 8586-96.

LIANG, X. H., YU, J., BROWN, K. & LEVINE, B. 2001. Beclin 1 contains a leucine-rich nuclear export signal that is required for its autophagy and tumor suppressor function. *Cancer Research,* 61**,** 3443-3449.

LIU, E. Y. & RYAN, K. M. 2012. Autophagy and cancer - issues we need to digest. *Journal of Cell Science,* 125**,** 2349-2358.

LIU, G. H., POPPE, L., AOKI, K., YAMANE, H., LEWIS, J. & SZYPERSKI, T. 2014. High-quality NMR structure of human anti-apoptotic protein domain Mcl-1(171-327) for cancer drug design. *PLoS One,* 9.

LIU, Q., MOLDOVEANU, T., SPRULES, T., MATTA-CAMACHO, E., MANSUR-AZZAM, N. & GEHRING, K. 2010. Apoptotic regulation by MCL-1 through heterodimerization. *Journal of Biological Chemistry,* 285**,** 19615-19624.

LIU, X., DAI, S., ZHU, Y., MARRACK, P. & KAPPLER, J. W. 2003. The structure of a Bcl-xL/Bim fragment complex: implications for Bim function. *Immunity,* 19**,** 341-52.

LOH, J., HUANG, Q. L., PETROS, A. M., NETTESHEIM, D., VAN DYK, L. F., LABRADA, L., SPECK, S. H., LEVINE, B., OLEJNICZAK, E. T. & VIRGIN, H. W. 2005. A surface groove essential for viral Bcl-2 function during chronic infection in vivo. *Plos Pathogens,* 1**,** 80-91.

LOWE, S. W. & LIN, A. W. 2000. Apoptosis in cancer. *Carcinogenesis,* 21**,** 485-495.

LUO, S. Q., GARCIA-ARENCIBIA, M., ZHAO, R., PURI, C., TOH, P. P. C., SADIQ, O. & RUBINSZTEIN, D. C. 2012. Bim inhibits autophagy by recruiting Beclin 1 to microtubules. *Molecular Cell,* 47**,** 359-370.

MACCARRONE, M., GASPERI, V., CATANI, M. V., DIEP, T. A., DAINESE, E., HANSEN, H. S. & AVIGLIANO, L. 2010. The endocannabinoid system and its relevance for nutrition. *Annual Review of Nutrition, Vol 30,* 30**,** 423-440.

MAITY, A., YADAV, S., VERMA, C. S. & DASTIDAR, S. G. 2013. Dynamics of Bcl-xL in water and membrane: Molecular Simulations. *PLoS One,* 8.

MAIURI, M. C., LE TOUMELIN, G., CRIOLLO, A., RAIN, J. C., GAUTIER, F., JUIN, P., TASDEMIR, E., PIERRON, G., TROULINAKI, K., TAVERNARAKIS, N., HICKMAN, J. A., GENESTE, O. & KROEMER, G. 2007a. Functional and physical interaction between Bcl-X(L) and a BH3-like domain in Beclin-1. *Embo Journal,* 26**,** 2527-39.

MAIURI, M. C., ZALCKVAR, E., KIMCHI, A. & KROEMER, G. 2007b. Self-eating and self-killing: crosstalk between autophagy and apoptosis. *Nature Reviews Molecular Cell Biology,* 8**,** 741-752.

MARSHALL, W. L., YIM, C., GUSTAFSON, E., GRAF, T., SAGE, D. R., HANIFY, K., WILLIAMS, L., FINGEROTH, J. & FINBERG, R. W. 1999. Epstein-Barr virus encodes a novel homolog of the bcl-2 oncogene that inhibits apoptosis and associates with Bax and Bak. *Journal of Virology,* 73**,** 5181-5185.

MASON, J. M. & ARNDT, K. M. 2004. Coiled coil domains: stability, specificity, and biological implications. *Chembiochem,* 5**,** 170-6.

MASSA, W. 2004. *Crystal structure determination,* Berlin ; New York, Springer.

MATLASHEWSKI, G., BANKS, L., PIM, D. & CRAWFORD, L. 1986. Analysis of human p53 proteins and mRNA levels in normal and transformed cells. *European Journal of Biochemistry,* 154**,** 665-72.

MATSUNAGA, K., SAITOH, T., TABATA, K., OMORI, H., SATOH, T., KUROTORI, N., MAEJIMA, I., SHIRAHAMA-NODA, K., ICHIMURA, T., ISOBE, T., AKIRA, S., NODA, T. & YOSHIMORI, T. 2009. Two Beclin 1-binding proteins, Atg14L and Rubicon, reciprocally regulate autophagy at different stages. *Nature Cell Biology,* 11**,** 385-U69.

MAZUMDER, S., CHOUDHARY, G. S., AL-HARBI, S. & ALMASAN, A. 2012. Mcl-1 phosphorylation defines ABT-737 resistance that can be overcome by increased NOXA expression in leukemic B cells. *Cancer Research,* 72**,** 3069-3079.

MCREE, D. E. 1993. *Practical protein crystallography,* San Diego, Academic Press.

MEI, Y., RAMANATHAN, A., GLOVER, K., STANLEY, C., SANISHVILI, R., CHAKRAVARTHY, S., YANG, Z., COLBERT, C. L. & SINHA, S. C. 2016a. Conformational flexibility enables the function of a BECN1 region essential for starvation-mediated autophagy. *Biochemistry,* 55**,** 1945-1958.

MEI, Y., SU, M., SANISHVILI, R., CHAKRAVARTHY, S., COLBERT, C. & SINHA, S. 2016b. Structure-based identification of BECN1 and ATG14 CCD residues important for starvation-induced autophagy. *Biochemistry,* Accepted.

MEI, Y., SU, M. F., SONI, G., SALEM, S., COLBERT, C. L. & SINHA, S. C. 2014. Intrinsically disordered regions in autophagy proteins. *Proteins-Structure Function and Bioinformatics,* 82**,** 565-578.

MIZUSHIMA, N. 2007. Autophagy: process and function. *Genes & Development,* 21**,** 2861-2873.

MIZUSHIMA, N., NODA, T. & OHSUMI, Y. 1999. Apg16p is required for the function of the Apg12p-Apg5p conjugate in the yeast autophagy pathway. *Embo Journal,* 18**,** 3888-96.

MIZUSHIMA, N., NODA, T., YOSHIMORI, T., TANAKA, Y., ISHII, T., GEORGE, M. D., KLIONSKY, D. J., OHSUMI, M. & OHSUMI, Y. 1998. A protein conjugation system essential for autophagy. *Nature,* 395**,** 395-398.

MOLDOVEANU, T., LIU, Q., TOCILJ, A., WATSON, M., SHORE, G. & GEHRING, K. 2006. The X-ray structure of a BAK homodimer reveals an inhibitory zinc binding site. *Molecular Cell,* 24**,** 677-688.

MOLL, U. M., WOLFF, S., SPEIDEL, D. & DEPPERT, W. 2005. Transcription-independent pro-apoptotic functions of p53. *Current Opinion in Cell Biology,* 17**,** 631-636.

MORONI, M. C., HICKMAN, E. S., DENCHI, E. L., CAPRARA, G., COLLI, E., CECCONI, F., MULLER, H. & HELIN, K. 2001. Apaf-1 is a transcriptional target for E2F and p53. *Nature Cell Biology,* 3**,** 552-558.

MOROY, G., MARTIN, E., DEJAEGERE, A. & STOTE, R. H. 2009. Molecular basis for Bcl-2 homology 3 domain recognition in the Bcl-2 protein family: identification of the conserved hot spot interactions. *Journal of Biological Chemistry,* 284**,** 17499-17511.

MUCHMORE, S. W., SATTLER, M., LIANG, H., MEADOWS, R. P., HARLAN, J. E., YOON, H. S., NETTESHEIM, D., CHANG, B. S., THOMPSON, C. B., WONG, S. L., NG, S. L. & FESIK, S. W. 1996. X-ray and NMR structure of human Bcl-xL, an inhibitor of programmed cell death. *Nature,* 381**,** 335-41.

MULLER, M., WILDER, S., BANNASCH, D., ISRAELI, D., LEHLBACH, K., LI-WEBER, M., FRIEDMAN, S. L., GALLE, P. R., STREMMEL, W., OREN, M. & KRAMMER, P. H. 1998. p53 activates the CD95 (APO-1/Fas) gene in response to DNA damage by anticancer drugs. *Journal of Experimental Medicine,* 188**,** 2033-2045.

MURALIDHAR, S., VEYTSMANN, G., CHANDRAN, B., ABLASHI, D., DONIGER, J. & ROSENTHAL, L. J. 2000. Characterization of the human herpesvirus 8 (Kaposi's sarcoma-associated herpesvirus) oncogene, Kaposin (ORF K12). *Journal of Clinical Virology,* 16**,** 203-213.

MURSHUDOV, G. N., VAGIN, A. A. & DODSON, E. J. 1997. Refinement of macromolecular structures by the maximum-likelihood method. *Acta Crystallographica Section D-Biological Crystallography,* 53**,** 240-255.

NOBLE, C. G., DONG, J. M., MANSER, E. & SONG, H. W. 2008. Bcl-x(L) and UVRAG cause a monomer-dimer switch in Beclin1. *Journal of Biological Chemistry,* 283**,** 26274-26282.

NODA, N. N., KOBAYASHI, T., ADACHI, W., FUJIOKA, Y., OHSUMI, Y. & INAGAKI, F. 2012. Structure of the novel C-terminal domain of Vacuolar Protein Sorting 30/Autophagy-related Protein 6 and its specific role in autophagy. *Journal of Biological Chemistry,* 287**,** 16256-16266.

NUNEZ, S., VENHORST, J. & KRUSE, C. G. 2012. Target-drug interactions: first principles and their application to drug discovery. *Drug Discovery Today,* 17**,** 10-22.

O'CONNOR, L., STRASSER, A., O'REILLY, L. A., HAUSMANN, G., ADAMS, J. M., CORY, S. & HUANG, D. C. S. 1998. Bim: a novel member of the Bcl-2 family that promotes apoptosis. *Embo Journal,* 17**,** 384-395.

OBERSTEIN, A., JEFFREY, P. D. & SHI, Y. 2007. Crystal structure of the Bcl-XL-Beclin 1 peptide complex: Beclin 1 is a novel BH3-only protein. *Journal of Biological Chemistry,* 282**,** 13123-32.

OBRADOVIC, Z., PENG, K., VUCETIC, S., RADIVOJAC, P. & DUNKER, A. K. 2005. Exploiting heterogeneous sequence properties improves prediction of protein disorder. *Proteins,* 61 Suppl 7**,** 176-82.

OHSUMI, Y. 2001. Molecular dissection of autophagy: two ubiquitin-like systems. *Nature Reviews Molecular Cell Biology,* 2**,** 211-6.

OJALA, P. M., TIAINEN, M., SALVEN, P., VEIKKOLA, T., CASTANOS-VELEZ, E., SARID, R., BIBERFELD, P. & MAKELA, T. P. 1999. Kaposi's sarcoma-associated herpesvirus-encoded v-cyclin triggers apoptosis in cells with high levels of cyclin-dependent kinase 6. *Cancer Research,* 59**,** 4984-4989.

OTWINOWSKI, Z. & MINOR, W. 1997. Processing of X-ray diffraction data collected in oscillation mode. *Macromolecular Crystallography, Pt A,* 276**,** 307-326.

PASTORINO, J. G., CHEN, S. T., TAFANI, M., SNYDER, J. W. & FARBER, J. L. 1998. The overexpression of Bax produces cell death upon induction of the mitochondrial permeability transition. *Journal of Biological Chemistry,* 273**,** 7770-7775.

PATTINGRE, S., BAUVY, C., LEVADE, T., LEVINE, B. & CODOGNO, P. 2009. Ceramide-induced autophagy: to junk or to protect cells? *Autophagy,* 5**,** 558-60.

PATTINGRE, S., TASSA, A., QU, X., GARUTI, R., LIANG, X. H., MIZUSHIMA, N., PACKER, M., SCHNEIDER, M. D. & LEVINE, B. 2005a. Bcl-2 antiapoptotic proteins inhibit Beclin 1-dependent autophagy. *Cell,* 122**,** 927-39.

PATTINGRE, S., TASSA, A., QU, X. P., GARUTI, R., LIANG, X. H., MIZUSHIMA, N., PACKER, M., SCHNEIDER, M. D. & LEVINE, B. 2005b. Bcl-2 antiapoptotic proteins inhibit Beclin 1-dependent autophagy. *Cell,* 122**,** 927-939.

PENG, K., RADIVOJAC, P., VUCETIC, S., DUNKER, A. K. & OBRADOVIC, Z. 2006. Length-dependent prediction of protein intrinsic disorder. *BMC Bioinformatics,* 7**,** 208.

PENNARUN, B., MEIJER, A., DE VRIES, E. G. E., KLEIBEUKER, J. H., KRUYT, F. & DE JONG, S. 2010. Playing the DISC: Turning on TRAIL death receptor-mediated apoptosis in cancer. *Biochimica Et Biophysica Acta-Reviews on Cancer,* 1805**,** 123-140.

PETOUKHOV, M. V., FRANKE, D., SHKUMATOV, A. V., TRIA, G., KIKHNEY, A. G., GAJDA, M., GORBA, C., MERTENS, H. D. T., KONAREV, P. V. & SVERGUN, D. I. 2012. New developments in the ATSAS program package for small-angle scattering data analysis. *Journal of Applied Crystallography,* 45**,** 342-350.

PETOUKHOV, M. V. & SVERGUN, D. I. 2005. Global rigid body modeling of macromolecular complexes against small-angle scattering data. *Biophysical Journal,* 89**,** 1237-1250.

PETROS, A. M., NETTESHEIM, D. G., WANG, Y., OLEJNICZAK, E. T., MEADOWS, R. P., MACK, J., SWIFT, K., MATAYOSHI, E. D., ZHANG, H. C., THOMPSON, C. B. &

FESIK, S. W. 2000. Rationale for Bcl-x(L)/Bad peptide complex formation from structure, mutagenesis, and biophysical studies. *Protein Science,* 9**,** 2528-2534.

PUTHALAKATH, H., HUANG, D. C. S., O'REILLY, L. A., KING, S. M. & STRASSER, A. 1999. The proapoptotic activity of the Bcl-2 family member Bim is regulated by interaction with the dynein motor complex. *Molecular Cell,* 3**,** 287-296.

PUTNAM, C. D., HAMMEL, M., HURA, G. L. & TAINER, J. A. 2007. X-ray solution scattering (SAXS) combined with crystallography and computation: defining accurate macromolecular structures, conformations and assemblies in solution. *Quarterly Reviews of Biophysics,* 40**,** 191-285.

PYO, J. O., JANG, M. H., KWON, Y. K., LEE, H. J., JUN, J. I., WOO, H. N., CHO, D. H., CHOI, B., LEE, H., KIM, J. H., MIZUSHIMA, N., OSHUMI, Y. & JUNG, Y. K. 2005. Essential roles of Atg5 and FADD in autophagic cell death: dissection of autophagic cell death into vacuole formation and cell death. *Journal of Biological Chemistry,* 280**,** 20722-9.

RADOSHEVICH, L., MURROW, L., CHEN, N., FERNANDEZ, E., ROY, S., FUNG, C. & DEBNATH, J. 2010. ATG12 conjugation to ATG3 regulates mitochondrial homeostasis and cell death. *Cell,* 142**,** 590-600.

RAHMANI, M., AUST, M. M., ATTKISSON, E., WILLIAMS, D. C., FERREIRA-GONZALEZ, A. & GRANT, S. 2012. Inhibition of Bcl-2 antiapoptotic members by obatoclax potently enhances sorafenib-induced apoptosis in human myeloid leukemia cells through a Bim-dependent process. *Blood,* 119**,** 6089-6098.

RAJAH, R., VALENTINIS, B. & COHEN, P. 1997. Insulin like growth factor (IGF)-binding protein-3 induces apoptosis and mediates the effects of transforming growth factor-beta 1 on programmed cell death through a p53- and IGF-independent mechanism. *Journal of Biological Chemistry,* 272**,** 12181-12188.

RAJAN, S., CHOI, M., BAEK, K. & YOON, H. S. 2015. Bh3 induced conformational changes in Bcl-X-l revealed by crystal structure and comparative analysis. *Proteins-Structure Function and Bioinformatics,* 83**,** 1262-1272.

RANTALAINEN, K. I., UVERSKY, V. N., PERMI, P., KALKKINEN, N., DUNKER, A. K. & MAKINEN, K. 2008. Potato virus A genome-linked protein VPg is an intrinsically disordered molten globule-like protein with a hydrophobic core. *Virology,* 377**,** 280-288.

REUTER, S., EIFES, S., DICATO, M., AGGARWAL, B. B. & DIEDERICH, M. 2008. Modulation of anti-apoptotic and survival pathways by curcumin as a strategy to induce apoptosis in cancer cells. *Biochemical Pharmacology,* 76**,** 1340-1351.

RHODES, G. 1993. *Crystallography made crystal clear : a guide for users of macromolecular models,* San Diego, Academic Press.

ROHN, T. T., WIRAWAN, E., BROWN, R. J., HARRIS, J. R., MASLIAH, E. & VANDENABEELE, P. 2011. Depletion of Beclin-1 due to proteolytic cleavage by caspases in the Alzheimer's disease brain. *Neurobiology of Disease,* 43**,** 68-78.

ROIZMAN, B. *Family Herpesviridae: A Brief Introduction*.

ROSTISLAVLEVA, K., SOLER, N., OHASHI, Y., ZHANG, L. F., PARDON, E., BURKE, J. E., MASSON, G. R., JOHNSON, C., STEYAERT, J., KTISTAKIS, N. T. & WILLIAMS, R. L. 2015. Structure and flexibility of the endosomal Vps34 complex reveals the basis of its function on membranes. *Science,* 350**,** 178-U81.

ROULSTON, A., MARCELLUS, R. C. & BRANTON, P. E. 1999. Viruses and apoptosis. *Annual Review of Microbiology,* 53**,** 577-628.

RUBINSTEIN, A. D., EISENSTEIN, M., BER, Y., BIALIK, S. & KIMCHI, A. 2011. The autophagy protein Atg12 associates with antiapoptotic Bcl-2 family members to promote mitochondrial apoptosis. *Molecular Cell,* 44**,** 698-709.

RUPPERT, S. M., LI, W. Q., ZHANG, G., CARLSON, A. L., LIMAYE, A., DURUM, S. K. & KHALED, A. R. 2012. The major isoforms of Bim contribute to distinct biological activities that govern the processes of autophagy and apoptosis in interleukin-7 dependent lymphocytes. *Biochimica Et Biophysica Acta-Molecular Cell Research,* 1823**,** 1877-1893.

RUSSO, J. J., BOHENZKY, R. A., CHIEN, M. C., CHEN, J., YAN, M., MADDALENA, D., PARRY, J. P., PERUZZI, D., EDELMAN, I. S., CHANG, Y. & MOORE, P. S. 1996. Nucleotide sequence of the Kaposi sarcoma-associated herpesvirus (HHV8). *Proceedings of the National Academy of Sciences of the United States of America,* 93**,** 14862-7.

SANCHEZ, J. G., OKREGLICKA, K., CHANDRASEKARAN, V., WELKER, J. M., SUNDQUIST, W. I. & PORNILLOS, O. 2014. The tripartite motif coiled-coil is an elongated antiparallel hairpin dimer. *Proceedings of the National Academy of Sciences of the United States of America,* 111**,** 2494-2499.

SARID, R., SATO, T., BOHENZKY, R. A., RUSSO, J. J. & CHANG, Y. 1997. Kaposi's sarcoma-associated herpesvirus encodes a functional Bcl-2 homologue. *Nature Medicine,* 3**,** 293-298.

SATTLER, M., LIANG, H., NETTESHEIM, D., MEADOWS, R. P., HARLAN, J. E., EBERSTADT, M., YOON, H. S., SHUKER, S. B., CHANG, B. S., MINN, A. J., THOMPSON, C. B. & FESIK, S. W. 1997. Structure of Bcl-x(L)-Bak peptide complex: Recognition between regulators of apoptosis. *Science,* 275**,** 983-986.

SCHNEIDMAN-DUHOVNY, D., HAMMEL, M. & SALI, A. 2010. FoXS: a web server for rapid computation and fitting of SAXS profiles. *Nucleic Acids Research,* 38**,** W540-W544.

SCHNEIDMAN-DUHOVNY, D., HAMMEL, M., TAINER, J. A. & SALI, A. 2013. Accurate SAXS profile computation and its assessment by contrast variation experiments. *Biophysical Journal,* 105**,** 962-974.

SCHRODINGER, LLC 2010. The PyMOL Molecular Graphics System, Version 1.3r1.

SHEFFIELD, P., GARRARD, S. & DEREWENDA, Z. 1999. Overcoming expression and purification problems of RhoGDI using a family of "parallel" expression vectors. *Protein Expression and Purification,* 15**,** 34-39.

SHIMIZU, S., EGUCHI, Y., KAMIIKE, W., ITOH, Y., HASEGAWA, J., YAMABE, K., OTSUKI, Y., MATSUDA, H. & TSUJIMOTO, Y. 1996. Induction of apoptosis as well as necrosis by hypoxia and predominant prevention of apoptosis by Bcl-2 and Bcl-X(L). *Cancer Research,* 56**,** 2161-2166.

SHINTANI, T., MIZUSHIMA, N., OGAWA, Y., MATSUURA, A., NODA, T. & OHSUMI, Y. 1999. Apg10p, a novel protein-conjugating enzyme essential for autophagy in yeast. *Embo Journal,* 18**,** 5234-5241.

SHOJI-KAWATA, S., SUMPTER, R., LEVENO, M., CAMPBELL, G. R., ZOU, Z. J., KINCH, L., WILKINS, A. D., SUN, Q. H., PALLAUF, K., MACDUFF, D., HUERTA, C., VIRGIN, H. W., HELMS, J. B., EERLAND, R., TOOZE, S. A., XAVIER, R., LENSCHOW, D. J., YAMAMOTO, A., KING, D., LICHTARGE, O., GRISHIN, N. V., SPECTOR, S. A., KALOYANOVA, D. V. & LEVINE, B. 2013. Identification of a candidate therapeutic autophagy-inducing peptide. *Nature,* 494**,** 201-206.

SINHA, S., COLBERT, C. L., BECKER, N., WEI, Y. & LEVINE, B. 2008. Molecular basis of the regulation of Beclin 1-dependent autophagy by the gamma-herpesvirus 68 Bcl-2 homolog M11. *Autophagy,* 4**,** 989-97.

SINHA, S. & LEVINE, B. 2008. The autophagy effector Beclin 1: a novel BH3-only protein. *Oncogene,* 27 Suppl 1**,** S137-48.

SMYTH, M. S. & MARTIN, J. H. J. 2000. x Ray crystallography. *Journal of Clinical Pathology-Molecular Pathology,* 53**,** 8-14.

SOLSTAD, T., BULL, V. H., BREIVIK, L. & FLADMARK, K. E. 2008. Identification of protein interaction partners by immunoprecipitation: Possible pitfalls and false positives. *Experimental & Clinical Hepatology,* 4**,** 7.

SOUERS, A. J., LEVERSON, J. D., BOGHAERT, E. R., ACKLER, S. L., CATRON, N. D., CHEN, J., DAYTON, B. D., DING, H., ENSCHEDE, S. H., FAIRBROTHER, W. J., HUANG, D. C. S., HYMOWITZ, S. G., JIN, S., KHAW, S. L., KOVAR, P. J., LAM, L. T., LEE, J., MAECKER, H. L., MARSH, K. C., MASON, K. D., MITTEN, M. J., NIMMER, P. M., OLEKSIJEW, A., PARK, C. H., PARK, C. M., PHILLIPS, D. C., ROBERTS, A. W., SAMPATH, D., SEYMOUR, J. F., SMITH, M. L., SULLIVAN, G. M., TAHIR, S. K., TSE, C., WENDT, M. D., XIAO, Y., XUE, J. C., ZHANG, H. C.,

HUMERICKHOUSE, R. A., ROSENBERG, S. H. & ELMORE, S. W. 2013. ABT-199, a potent and selective BCL-2 inhibitor, achieves antitumor activity while sparing platelets. *Nature Medicine,* 19**,** 202-208.

SREERAMA, N., VENYAMINOV, S. Y. & WOODY, R. W. 2001. Analysis of protein circular dichroism spectra based on the tertiary structure classification. *Analytical Biochemistry,* 299**,** 271-274.

SREERAMA, N. & WOODY, R. W. 2004. Computation and analysis of protein circular dichroism spectra. *Methods in Enzymology.* Academic Press.

STACK, J. H., HERMAN, P. K., SCHU, P. V. & EMR, S. D. 1993. A membrane-associated complex containing the Vps15 protein kinase and the Vps34 PI 3-kinase is essential for protein sorting to the yeast lysosome-like vacuole. *Embo Journal,* 12**,** 2195-204.

SU, M., MEI, Y., SANISHVILI, R., LEVINE, B., COLBERT, C. L. & SINHA, S. 2014. Targeting gamma-herpesvirus 68 Bcl-2-mediated down-regulation of autophagy. *Journal of Biological Chemistry,* 289**,** 8029-40.

SU, M., MEI, Y. & SINHA, S. 2013. Role of the crosstalk between autophagy and apoptosis in cancer. *Journal of Oncology,* 2013**,** 14.

SUBRAMANIAN, T., KUPPUSWAMY, M., GYSBERS, J., MAK, S. & CHINNADURAI, G. 1984. 19-Kda tumor-antigen coded by early region E1b of Adenovirus-2 is required for efficient synthesis and for protection of viral-DNA. *Journal of Biological Chemistry,* 259**,** 1777-1783.

SUI, X. B., JIN, L. J., HUANG, X. F., GENG, S. M., HE, C. & HU, X. T. 2011. p53 signaling and autophagy in cancer A revolutionary strategy could be developed for cancer treatment. *Autophagy,* 7**,** 565-571.

SUN, Q. M., FAN, W. L., CHEN, K. L., DING, X. J., CHEN, S. & ZHONG, Q. 2008. Identification of Barkor as a mammalian autophagy-specific factor for Beclin 1 and class III phosphatidylinositol 3-kinase. *Proceedings of the National Academy of Sciences of the United States of America,* 105**,** 19211-19216.

SUZUKI, M., YOULE, R. J. & TJANDRA, N. 2000. Structure of Bax: coregulation of dimer formation and intracellular localization. *Cell,* 103**,** 645-654.

SUZUKI, N. N., YOSHIMOTO, K., FUJIOKA, Y., OHSUMI, Y. & INAGAKI, F. 2005. The crystal structure of plant ATG12 and its biological implication in autophagy. *Autophagy,* 1**,** 119-126.

SVERGUN, D. I. 1992. Determination of the regularization parameter in indirect-transform methods using perceptual criteria. *Journal of Applied Crystallography,* 25**,** 495-503.

TAKAHASHI, Y., KARBOWSKI, M., YAMAGUCHI, H., KAZI, A., WU, J., SEBTI, S. M., YOULE, R. J. & WANG, H. G. 2005. Loss of Bif-1 suppresses Bax/Bak conformational change and mitochondrial apoptosis. *Molecular and Cellular Biology,* 25**,** 9369-9382.

TANIDA, I., MIZUSHIMA, N., KIYOOKA, M., OHSUMI, M., UENO, T., OHSUMI, Y. & KOMINAMI, E. 1999. Apg7p/Cvt2p: A novel protein-activating enzyme essential for autophagy. *Molecular Biology of the Cell,* 10**,** 1367-1379.

TARAKANOVA, V. L., SUAREZ, F., TIBBETTS, S. A., JACOBY, M. A., WECK, K. E., HESS, J. L., SPECK, S. H. & VIRGIN, H. W. 2005. Murine gammaherpesvirus 68 infection is associated with lymphoproliferative disease and lymphoma in BALB beta 2 microglobulin-deficient mice. *Journal of Virology,* 79**,** 14668-14679.

TARODI, B., SUBRAMANIAN, T. & CHINNADURAI, G. 1994. Epstein-Barr virus BHRF1 protein protects against cell death induced by DNA-damaging agents and heterologous viral infection. *Virology,* 201**,** 404-7.

TAYLOR, R. C., CULLEN, S. P. & MARTIN, S. J. 2008. Apoptosis: controlled demolition at the cellular level. *Nature Reviews Molecular Cell Biology,* 9**,** 231-241.

THEODORAKIS, P., DSAEIPPER, C., SUBRAMANIAN, T. & CHINNADURAI, G. 1996. Unmasking of a proliferation-restraining activity of the anti-apoptosis protein EBV BHRF1. *Oncogene,* 12**,** 1707-1713.

THOMAS, A., GIESLER, T. & WHITE, E. 2000. p53 mediates Bcl-2 phosphorylation and apoptosis via activation of the Cdc42/JNK1 pathway. *Oncogene,* 19**,** 5259-5269.

THOMAS, L. W., LAM, C. & EDWARDS, S. W. 2010. Mcl-1; the molecular regulation of protein function. *Febs Letters,* 584**,** 2981-2989.

TONG, Q. S., ZHENG, L. D., WANG, L., LIU, J. & QIAN, W. 2004. BAK overexpression mediates p53-independent apoptosis inducing effects on human gastric cancer cells. *Bmc Cancer,* 4.

TSE, C., SHOEMAKER, A. R., ADICKES, J., ANDERSON, M. G., CHEN, J., JIN, S., JOHNSON, E. F., MARSH, K. C., MITTEN, M. J., NIMMER, P., ROBERTS, L., TAHIR, S. K., MAO, Y., YANG, X. F., ZHANG, H. C., FESIK, S., ROSENBERG, S. H. & ELMORE, S. W. 2008. ABT-263: A potent and orally bioavailable Bcl-2 family inhibitor. *Cancer Research,* 68**,** 3421-3428.

TSUJIMOTO, Y., GORHAM, J., COSSMAN, J., JAFFE, E. & CROCE, C. M. 1985. The T(14,18) Chromosome translocations involved in B-Cell neoplasms result from mistakes in Vdj joining. *Science,* 229**,** 1390-1392.

UCHIDA, H., KIYOKAWA, N., TAGUCHI, T., HORIE, H., FUJIMOTO, J. & TAKEDA, T. 1999. Shiga toxins induce apoptosis in pulmonary epithelium-derived cells. *Journal of Infectious Diseases,* 180**,** 1902-1911.

UPRETI, M., GALITOVSKAYA, E. N., CHU, R., TACKETT, A. J., TERRANO, D. T., GRANELL, S. & CHAMBERS, T. C. 2008. Identification of the major phosphorylation site in Bcl-xL induced by microtubule inhibitors and analysis of its functional significance. *Journal of Biological Chemistry,* 283**,** 35517-35525.

VAN DELFT, M. F., WEI, A. H., MASON, K. D., VANDENBERG, C. J., CHEN, L., CZABOTAR, P. E., WILLIS, S. N., SCOTT, C. L., DAY, C. L., CORY, S., ADAMS, J. M., ROBERTS, A. W. & HUANG, D. C. S. 2006. The BH3 mimetic ABT-737 targets selective Bcl-2 proteins and efficiently induces apoptosis via Bak/Bax if Mcl-1 is neutralized. *Cancer Cell,* 10**,** 389-399.

VIRGIN, H. W., LATREILLE, P., WAMSLEY, P., HALLSWORTH, K., WECK, K. E., DALCANTO, A. J. & SPECK, S. H. 1997. Complete sequence and genomic analysis of murine gammaherpesvirus 68. *Journal of Virology,* 71**,** 5894-5904.

VOLKOV, V. V. & SVERGUN, D. I. 2003. Uniqueness of ab initio shape determination in small-angle scattering. *Journal of Applied Crystallography,* 36**,** 860-864.

WANG, G. H., GARVEY, T. L. & COHEN, J. I. 1999. The murine gammaherpesvirus-68 M11 protein inhibits Fas- and TNF-induced apoptosis. *Journal of General Virology,* 80**,** 2737-2740.

WANG, Y. L., CAO, R., LIU, D. X., CHERVIN, A., YUAN, J., AN, J. & HUANG, Z. W. 2007. Oligomerization of BH4-truncated Bcl-X-L in solution. *Biochemical and Biophysical Research Communications,* 361**,** 1006-1011.

WEI, M. C., ZONG, W. X., CHENG, E. H. Y., LINDSTEN, T., PANOUTSAKOPOULOU, V., ROSS, A. J., ROTH, K. A., MACCREGOR, G. R., THOMPSON, C. B. & KORSMEYER, S. J. 2001. Proapoptotic BAX and BAK: A requisite gateway to mitochondrial dysfunction and death. *Science,* 292**,** 727-730.

WEI, Y., PATTINGRE, S., SINHA, S., BASSIK, M. & LEVINE, B. 2008a. JNK1-mediated phosphorylation of Bcl-2 regulates starvation-induced autophagy. *Mol Cell,* 30**,** 678-88.

WEI, Y. J., SINHA, S. & LEVINE, B. 2008b. Dual role of JNK1-mediated phosphorylation of Bcl-2 in autophagy and apoptosis regulation. *Autophagy,* 4**,** 949-951.

WEINRAUCH, Y. & ZYCHLINSKY, A. 1999. The induction of apoptosis by bacterial pathogens. *Annual Review of Microbiology,* 53**,** 155-187.

WENG, C. J., LI, Y., XU, D., SHI, Y. & TANG, H. 2005. Specific cleavage of Mcl-1 by caspase-3 in tumor necrosis factor-related apoptosis-inducing ligand (TRAIL)-induced apoptosis in Jurkat leukemia T cells. *Journal of Biological Chemistry,* 280**,** 10491-10500.

WILLIS, S. N., CHEN, L., DEWSON, G., WEI, A., NAIK, E., FLETCHER, J. I., ADAMS, J. M. & HUANG, D. C. S. 2005. Proapoptotic Bak is sequestered by Mcl-1 and Bcl-x(L),

but not Bcl-2, until displaced by BH3-only proteins. *Genes & Development,* 19**,** 1294-1305.

WINN, M. D., BALLARD, C. C., COWTAN, K. D., DODSON, E. J., EMSLEY, P., EVANS, P. R., KEEGAN, R. M., KRISSINEL, E. B., LESLIE, A. G. W., MCCOY, A., MCNICHOLAS, S. J., MURSHUDOV, G. N., PANNU, N. S., POTTERTON, E. A., POWELL, H. R., READ, R. J., VAGIN, A. & WILSON, K. S. 2011. Overview of the CCP4 suite and current developments. *Acta Crystallographica Section D-Biological Crystallography,* 67**,** 235-242.

WINN, M. D., ISUPOV, M. N. & MURSHUDOV, G. N. 2001. Use of TLS parameters to model anisotropic displacements in macromolecular refinement. *Acta Crystallographica Section D-Biological Crystallography,* 57**,** 122-133.

WIRAWAN, E., VANDE WALLE, L., KERSSE, K., CORNELIS, S., CLAERHOUT, S., VANOVERBERGHE, I., ROELANDT, R., DE RYCKE, R., VERSPURTEN, J., DECLERCQ, W., AGOSTINIS, P., VANDEN BERGHE, T., LIPPENS, S. & VANDENABEELE, P. 2010. Caspase-mediated cleavage of Beclin-1 inactivates Beclin-1-induced autophagy and enhances apoptosis by promoting the release of proapoptotic factors from mitochondria. *Cell Death & Disease,* 1.

WISEMAN, T., WILLISTON, S., BRANDTS, J. F. & LIN, L. N. 1989. Rapid measurement of binding constants and heats of binding using a new titration calorimeter. *Analytical Biochemistry,* 179**,** 131-137.

WOOD, C. W., BRUNING, M., IBARRA, A. A., BARTLETT, G. J., THOMSON, A. R., SESSIONS, R. B., BRADY, R. L. & WOOLFSON, D. N. 2014. CCBuilder: an interactive web-based tool for building, designing and assessing coiled-coil protein assemblies. *Bioinformatics,* 30**,** 3029-3035.

YANG, J. Y., ZONG, C. S., XIA, W. Y., YAMAGUCHI, H., DING, Q. Q., XIE, X. M., LANG, J. Y., LAI, C. C., CHANG, C. J., HUANG, W. C., HUANG, H., KUO, H. P., LEE, D. F., LI, L. Y., LIEN, H. C., CHENG, X. Y., CHANG, K. J., HSIAO, C. D., TSAI, F. J., TSAI, C. H., SAHIN, A. A., MULLER, W. J., MILLS, G. B., YU, D. H., HORTOBAGYI, G. N. & HUNG, M. C. 2008. ERK promotes tumorigenesis by inhibiting FOXO3a via MDM2-mediated degradation. *Nature Cell Biology,* 10**,** 138-U22.

YAOITA, Y. & NAKAJIMA, K. 1997. Induction of apoptosis and CPP32 expression by thyroid hormone in a myoblastic cell line derived from tadpole tail. *Journal of Biological Chemistry,* 272**,** 5122-5127.

YIN, X. C., CAO, L. Z., PENG, Y. H., TAN, Y. F., XIE, M., KANG, R., LIVESEY, K. M. & TANG, D. L. 2011. A critical role for UVRAG in apoptosis. *Autophagy,* 7**,** 1242-1244.

YOUSEFI, S., PEROZZO, R., SCHMID, I., ZIEMIECKI, A., SCHAFFNER, T., SCAPOZZA, L., BRUNNER, T. & SIMON, H. U. 2006. Calpain-mediated cleavage of Atg5 switches autophagy to apoptosis. *Nature Cell Biology,* 8**,** 1124-U146.

ZALCKVAR, E., BERISSI, H., MIZRACHY, L., IDELCHUK, Y., KOREN, I., EISENSTEIN, M., SABANAY, H., PINKAS-KRAMARSKI, R. & KIMCHI, A. 2009. DAP-kinase-mediated phosphorylation on the BH3 domain of beclin 1 promotes dissociation of beclin 1 from Bcl-X-L and induction of autophagy. *Embo Reports,* 10**,** 285-292.

ZHA, J. P., HARADA, H., OSIPOV, K., JOCKEL, J., WAKSMAN, G. & KORSMEYER, S. J. 1997. BH3 domain of BAD is required for heterodimerization with BCL-X-L and pro-apoptotic activity. *Journal of Biological Chemistry,* 272**,** 24101-24104.

ZHOU, X. D., KINI, R. M. & SIVARAMAN, J. 2011. Application of isothermal titration calorimetry and column chromatography for identification of biomolecular targets. *Nature Protocols,* 6**,** 158-165.